The Effect of Siderophores on the Aqueous Chemistry of Uranium VI: A Combined Experimental and Computational Approach

By Matthew Edward Kirby

Thesis Submitted for

the Degree of Doctor of Philosophy

Department of Earth Science and Engineering

Imperial College London

2019

I hereby declare that the research presented in this thesis is my own work and that all mention to work carried out by others is appropriately referenced

Abstract

Understanding aqueous uranium VI (U^{VI}) chemistry in alkaline environments (pH >10) is crucial as radioactive waste can be stored and disposed in these conditions. Naturally occurring organic molecules can interact with U^{VI}, modifying its aqueous chemistry and subsequent groundwater facilitated transport. The aim of this research project is to characterise the effect of the (tris)hydroxamate siderophore desferrioxamine B (DFOB) on U^{VI} aqueous chemistry in alkaline solutions. Initially, the physico-chemical properties of U^{VI} precipitates were characterised in solutions containing 42 μM U^{VI} and 0.1 M NaCl. U^{VI} formed 640 ± 111 and 837 ± 142 nm diameter $Na_6U_7O_{24}$ precipitates at pH 10.5 and 11.5 respectively. These were usually physically immobilised in quartz sand columns. When ≥130 μM DFOB was simultaneously added with U^{VI} to pH 11.5, 0.1 M NaCl solutions, U^{VI} quantitatively passes through 0.2 μm filter membranes. This could be due to the formation of an aqueous U^{VI}-DFOB complex as observed below pH 10. To further explore complex formation, a density functional theory protocol was established. The protocol predicts the stability constants (log β) of U^{VI}-organic ligand complexes with root mean square deviation of 1.19 log β units after calibration against experimental data collected in acidic solutions. The relative stability series for U^{VI} complexes with key siderophore functional groups calculated using the fitting equation is: α-hydroxycarboxylate bound via the α-hydroxy and carboxylate groups (log β_{110} = 17.08), α-hydroxyimidazolate (log β_{110} = 16.55), catecholate (log β_{110} = 16.43), hydroxamate (log β_{110} = 9.00), hydroxy-phenyloxazolonate (log β_{110} = 8.43) and α-aminocarboxylate (log β_{110} = 4.73). Finally the DFT protocol was adapted so that the stability of U^{VI}-hydroxamate complexes can be approximated at pH 11.5. This suggests DFOB complexes in a monodentate fashion via one hydroxamate group. These results highlight the significant effect siderophores can play on aqueous U^{VI} chemistry.

Acknowledgments

First and foremost, I would like to thank my supervisors, Professor Dominik Weiss and Dr Sam Krevor for keeping me grounded during my PhD and teaching me a great deal about science. I would like to thank all members of the Environmental Geochemistry and the Subsurface CO_2 group for providing me with great feedback and advice in numerous group meetings. In particular, thanks to Dr Chaipat Lapinee for teaching me how to do lab work, and thanks to Dr Alexandra Simperler and Dr Jason Sonnenberg for teaching me about Density Functional Theory. Thanks to Dr Jonathan Watson for teaching me how to use the ICP-MS.

The work presented during my PhD used a wide variety of experimental techniques which I would not have been able to use successfully on my own. I would like to thank members of the Natural History Museum for their technical support: Dr Javier Cuadros and Dr Jens Najorka for helping me conduct the XRD analysis of the quartz and uranium minerals, and Dr Amy Burton for analysis my samples for Si with ICP-AES. Thanks to members of Imperial College for technical support: Dr Mahmoud Ardakani for helping analyse the samples with TEM and EDS. Dr Pete Lai and Dr Ed Day for doing CT imaging of the columns and Dr Qingyang Lin and Dr Tom Bultreys for extracting the grain volume and pore/pore throat radii respectively. I would like to thank Dr Alexandra Porter for access to DLS, and Dr Matthew Jackson for access to Ion Chromatography.

Thank you to Professor Scott Fendorf and Dr Guangchao Li for making my research trip to Stanford University possible. A big thank you to NERC, RWM, EA, and STFC for sponsoring me during my PhD, and to the NSCCS and Imperial College for access to the slater and cx1 super computers respectively. Thanks to Dr Simon Norris from RWM and Dr Gavin Thomson from the EA for periodically reviewing my work and providing me with advice.

Last but not least, thanks to my family, Gary, Ann and Sam for supporting me during my PhD. I couldn't have reached this stage without their unending support.

Publications

Published – PhD Related

1. Kirby, M.E., Simperler, A., Krevor, S. Weiss, D.J.*, Sonnenberg J.L.*, 2018, Computational Tools for Calculating log β Values of Geochemically Relevant Uranium Organometallic Complexes, *Journal of Physical Chemistry A*, 122, 8007-8019.

2. Kenney J.P.L., Kirby M.E., Cuadros J., Weiss D.J.*, 2017, A conceptual model to predict uranium removal from aqueous solutions in water-rock systems associated with low-and intermediate-level radioactive waste disposal, *RSC Advances*, 7, 7876-7884.

Submitted/in preparation – PhD Related

3. Kirby, M.E., Watson, J., Najorka, J., Krevor, S., Weiss D.J.* Uranium (U^{VI}) particle formation, characterisation and transport through quartz sand between pH 10.5 and 12.5 in 0.1 M sodium chloride solutions, *Journal of Colloid and Interface Science*

4. Kirby, M.E., Sonnenberg J.L., Simperler, A., Krevor, S. Weiss, D.J*, A Stability Series for Uranium (U^{VI}) Complexes Containing Siderophore Functional Groups in Acidic Solutions. *Physical Chemistry Chemical Physics*

5. Kirby, M.E., Watson, J., Weiss D.J.* Inhibition of Uranium (U^{VI}) Precipitation by the Siderophore Desferrioxamine B. *Geochemical Perspective Letters*

Revisions and resubmit – Teaching during PhD

6. Kirby, M.E.*, Bullen, J.C., Hanif, MD, Heiba, H.F., Fengjie, L., Northover, G.H.R., Resongles, E., Weiss, D.J.* Effect of pH on Iron Oxidation Kinetics in Aquatic Environments: an Educational Approach, *Journal of Chemical Education*

List of Contents

List of Tables

List of Figures

Chapter 1 - Introduction

The United Kingdom has a large quantity of legacy radioactive waste which has been accumulating since the 1940's during the UK's pursuit of nuclear energy.[3] The need for a low carbon emitting energy source which can provide a large, stable base load of electricity is revitalising the nuclear industry and has led to the recent UK Government Nuclear Sector Deal.[4] This means radioactive waste will continue to accumulate over the next century. Other radioactive waste is generated through industrial, agricultural defence, medicine and research activities.[3, 5] Humans and the environment need to be protected from this waste. The time frame the radioactive waste needs to be isolated and contained from humans and the environment is dependent on the radioactivity and composition of the waste. This can be up to one million years for the disposal of High Level Waste (HLW), Intermediate Level Waste (ILW) and Long Lived Low Level Waste (LL-LLW).[6] This provides an unprecedented timescale for a human project, with significant engineering, scientific and societal challenges.

Following a recommendation from the House of Lords in 1999, the UK Government launched the Managing Radioactive Waste Safely (MRWS) Consultation in 2001 which led to the establishment of the Committee on Radioactive Waste Management (CoRWM) in 2003.[7, 8] The Committee systematically reviewed the possible options for radioactive waste disposal such as disposal in space, sub-seabed disposal and placement in subduction zones.[8] The Committee concluded that disposal of ILW and HLW in a Geological Disposal Facility (GDF) was the most appropriate method. They recommended the GDF to the UK Government, and England, Wales and Northern Ireland adopted the GDF into their policy.[9] The is in line with international policy.[6, 10] The waste will be disposed of in a GDF using a multi-barrier system comprised of a series of engineered and natural barriers designed to reduce the migration of radionuclides from the disposal facility to the environment [6, 10, 11] Scotland, who has a simpler waste inventory (no HLW or spent fuel) has opted to manage their radioactive waste in surface stores or in near surface facilities.[12]

Uranium (U) is present in large quantities in intermediate level waste (ILW). In the UK ILW, the total activity of U amounts to 20.65 TBq, corresponding to approximately 1.38 million kg (1380 tU), and 5.8 million mol of U.[13] This type of waste will be disposed of as a grouted wasteform in a cement backfilled facility.[5] There is also a significant quantity of U, approximately 200,000 tU, which is classed as a zero-value asset radioactive material rather than radioactive waste. It is classed as zero-asset radioactive material because it can potentially be used in different applications, for example in mixed oxide fuels, or to manufacture military gun shells. This is known collectively as depleted, natural and low enriched uranium (DNLEU) and will likely be disposed in the same way as ILW.[3, 14]

Leaching of the grout wasteform and cement backfill by groundwater will lead to a set of unique chemical conditions (pH 9-14, ionic strength ≤0.2M) which will evolve over time as different cement phases dissolve.[11, 13] High pH and ionic strength conditions can also be found in cement-free systems. For example, at Hanford, high level liquid radioactive waste has been collected from reprocessing Pu for nuclear weapons. These tanks contain 5.2 to 13.4 M Na and 130 µM U in pH 13 solutions.[15-17] At Sellafield, spent fuel rods are stored in high pH solutions (pH > 10) adjusted with NaOH.[18] High pH conditions can be found for U mine tailings (pH 10) such as at the Deilmann pit in Canada.[19] Alkaline and saline conditions can also occur in natural systems such as at Maqarin, Jordan (pH 12.5)[20, 21] and the Allas Springs, Cyprus (pH 9.25-11.71).[22] These unique conditions may play an important role on the aqueous chemistry and subsequent mobility of U. These conditions may also influence U interactions with other groundwater components such as organic molecules.

The aim of the research presented in this thesis is to advance our understanding of the effect of siderophores, a class of naturally occurring organic molecules, on the aqueous chemistry of U when U is in its VI oxidation state (U^{VI}). A special focus is placed on alkaline and saline solutions. To address this, a multidisciplinary approach has been taken which combines computational chemistry with experimental techniques. The outline of the thesis is provided below:

- Chapter 2 presents a review of the literature.
- Chapter 3 outlines the methods employed to explore the aqueous chemistry of U^{VI}.
- Chapter 4 reports results which use a variety of experimental techniques to characterise the U^{VI} precipitate formation, the physico-chemical properties of the precipitates, and subsequent transport of U^{VI} through quartz sand in the absence of siderophores. The solutions contained 42 µM U^{VI} and 0.1 M NaCl at pH 10.5, 11.5 and 12.5.
- Chapter 5 reports the development and validation of a Density Functional Theory (DFT) protocol to predict the stability constants of U^{VI} complexes containing organic molecules. The method was validated in acidic conditions because of the lack of experimental data in alkaline solutions.
- Chapter 6 uses the DFT protocol developed in chapter 6 to establish the relative stability series for U^{VI} complexes with the functional groups found within siderophores in acidic solutions.
- Chapter 7 uses a combined experimental and DFT approach to explore the effect of DFOB on U^{VI} precipitation in pH 11.5 solutions containing 42 µM U^{VI} and 0.1 M NaCl, and to test whether the hydroxamate functional groups of the siderophore can complex with U^{VI}.
- Chapter 8 summarises key findings from the research.
- Chapter 9 highlights future research requirements.
- Several appendices are added at the end of the thesis:
  i) Appendix A outlines the initial column experiment design for U^{VI} particle transport, and requirements which led to the redesigned experiments which are used in chapter 5.
  ii) Appendix B provides the numerical data for the experiments employed in chapter 4 and 7.

iii) Appendix C provides the thermodynamic data (Gibbs energy, entropy, and enthalpy) of the complexes.

iv) Appendix D provides the structural data (bond lengths and angles) calculated using the DFT protocol.

v) Appendix E provides figures of the structures used in the ligand training set in chapter 6.

Chapter 2 - Background

The aim of this chapter is to provide background information relevant to the work presented in the thesis. These include:

- A brief overview of U including its natural abundance, isotopes and redox chemistry.
- Introduction to the aqueous chemistry of U^{VI} including hydrolysis reactions and formation of complexes with inorganic and organic ligands. This specifically focusses on U^{VI} complexes containing siderophores and siderophore functional groups. The generation of siderophores by bacteria is also discussed.
- Mechanisms for U^{VI} precipitation and mechanisms controlling the mobility of these precipitates in porous media.
- An introduction to DFT, including the major protocol components: density functional approximation, basis set, effective core potential, solvation model, concentration corrections and ionic strength corrections.

2.1. Introduction to Uranium

Uranium (U) is the heaviest naturally occurring element with typical abundances of 4-13 µM in the Earth's crust.[23] Its atomic number is 92. U has no stable isotopes but has multiple radioactive isotopes. The isotopes which occur naturally are U^{238} (99.2739-0.992752%) U^{235} (0.07198-0.07207%) and U^{234} (0.0050-0.0059%).[24] The U^{235} content is enriched in nuclear fuel typically to 3-5% as this is the fissile isotope used in nuclear reactions.[25] U^{232}, U^{233} U^{236} and U^{237} isotopes are produced artificially in nuclear reactors,[26] of which U^{232}, U^{233} U^{236} are present in UK radioactive waste.[27]

Uranium has four oxidation states, U^{III}, U^{IV}, U^{V} and U^{VI}. The U^{III} and U^{V} oxidation states are unstable with U^{III} oxidizing to the U^{IV} state, and U^{V} oxidising to U^{VI} or reducing to U^{IV} depending on the reduction potential (Eh) of the system.[23] When U is present as U^{IV}, U typically precipitates from

solution as uraninite.[23] U^{VI} can be reduced to U^{IV} in anoxic conditions inorganically, for example by reduction by Fe^{II}, [28] or biologically.[29] These typically have a low solubility, for example uraninite (UO_2) has a solubility product (K_{s0}) of $1x10^{-4.8}$.[30]

2.2. Aqueous U^{VI} chemistry

2.2.1. The uranyl dication (UO_2^{2+})

When U is present as U^{VI} in aqueous solutions, it hydrolyses to form the linear dication UO_2.[23] The U-O bonds are short (1.764-1.790 Å)[31-34] with bond order of three.[35] Therefore the dication is highly stable and most aqueous uranyl species will contain O=U=O. The U^{VI} atom can bind with other ligands in the plane 90˚ to the O=U=O axial plane (equatorial plane). The equatorial plane of U^{VI} is co-ordinated with water molecules in acidic solutions (pH <4). Following a series of experimental and computational studies, it is broadly accepted that there are five bound water molecules bound in the equatorial plane of the U^{VI} atom.[33, 34, 36-40] These have much weaker bonds than the O=U bonds in the axial plane[35] and can be replaced by different inorganic and organic ligands.

2.2.2. U^{VI} Hydrolysis reactions

As pH increases, a series of hydrolysis reactions occur which form a wide variety of monomeric and polymeric U^{VI} hydroxide species.[23] The generalised reaction for the formation of the hydrolysis complexes is provided in Equation 2.1.[41] For simplicity, this equation ignores H_2O (e.g. UO_2^{2+} is $[UO_2(H_2O)_5]^{2+}$. The speciation of the U^{VI} hydrolysis complexes are provided in Figure 2.1. The speciation was calculated using the PHREEQC geochemical software[42] in combination with the ANDRA Thermochimie "SIT" database.[43] During the hydrolysis reactions, the co-ordination number decreases from five to four in the monomeric species. The repulsion from OH^- groups forces a water molecule out from the structure. DFT calculations show this occurs for the $[UO_2(OH)_3]^-$ and $[UO_2(OH)_4]^{2-}$ species.[44] This is also supported by Extended X-ray Absorption spectroscopic (EXAFS) measurements of $[UO_2(OH)_4]^{2-}$ crystals.[45]

$$\mathrm{p}[\mathrm{UO_2}]^{2+} + \mathrm{qH_2O} = [(\mathrm{UO_2})_\mathrm{p}(\mathrm{OH})_\mathrm{q}]^{(2\mathrm{p}-\mathrm{q})} + \mathrm{qH}^+ \qquad (2.1)$$

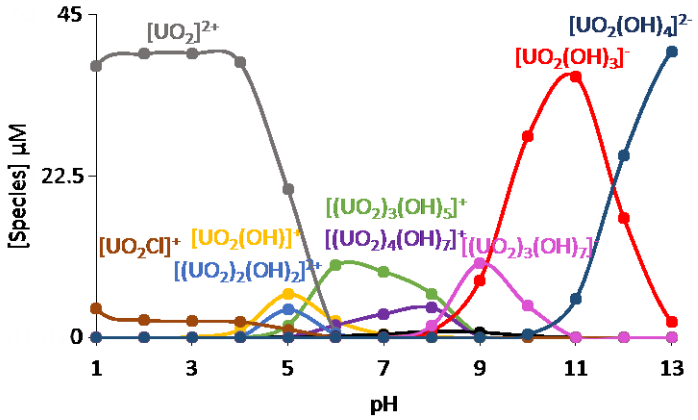

Figure 2.1. Speciation diagram for U^{VI} which was created using PHREEQC and the SIT database. For simplicity water molecules are removed from the species. The chemical conditions are: 42 µM U^{VI}, 0 µM $\Sigma[CO_2]$, 0.1 M NaCl, dissolved oxygen was equilibrated with the atmosphere partial pressure (0.2 atm). The solution is charge balanced with Cl^- and Na^+ by assuming HCl and NaOH was added to adjust pH.

In the alkaline conditions (pH >10) of interest here, Time-resolved Laser-induced Fluorescence Spectroscopy (TRLFS) measurements suggest one prevalent species formed between pH 10-12, at 10^{-5} to 10^{-6} M U^{VI}.[46] The authors assigned the $[UO_2(OH)_3]^-$ species based on thermodynamic calculations. A second species could also be detected, which became more prevalent as the U^{VI} concentration increased from $1x10^{-6}$ M to $1x10^{-4}$ M. The authors suggested it could be $[UO_2(OH)_2]^-$ or $[(UO_2)_3(OH)_7]^-$. A more recent TRLFS study observed that $[UO_2(OH)_3]^-$ and a second species was present at pH 11.[47, 48] They assign the second species as $[(UO_2)_3(OH)_7]^-$ based on Eliet *et al.*[46] although Eliet *et al.* were unsure whether this corresponded to $[UO_2(OH)_2]^-$ or $[(UO_2)_3(OH)_7]^-$. Only $[UO_2(OH)_3]^-$ was identified at pH 12 and only $[UO_2(OH)_4]^{2-}$ was found at pH ≥13.[47, 48] Thermodynamic modelling using the SIT database[42, 43] indicate that the two monomeric hydroxide species $[UO_2(OH)_3]^-$ and $[UO_2(OH)_4]^{2-}$ dominate speciation above pH 10 when 42 µM U^{VI} is present (Figure 2.1).

2.2.3. U^{VI} complex formation with inorganic ligands

In natural systems, a variety of inorganic ligands can complex with uranyl in the equatorial plane of the U^{VI} atom. Common inorganic ligands include SO_4^{2-}, Cl^-, OH^-, PO_4^{3-}, NO_3^- and CO_3^{2-} .[44, 45, 49-54] The stability of these complexes can be compared by calculating the equilibrium constant (K). K is the

ratio of the concentration of products over the concentrations of the reactants at equilibrium. This is illustrated in Equation 2.2 for the formation of a 1:1 metal-ligand complex where $M(Sol)_m$, L, and Sol are the aqueous metal complex, ligand, and solvent respectively. The initial metal aqua complex contains m water molecules. n is the number of solvent molecules released during the reaction. K spans orders of magnitude and is usually reported as a log value (log K).

$$M(Sol)_m + L \leftrightharpoons ML(Sol)_{m-n} + nSol \qquad K = \frac{[ML(Sol)_{m-n}]}{[M(Sol)_m][L]} \tag{2.2}$$

Since metal ions have multiple coordination sites, complexation reactions often involve more than one ligand that bind in a series of reactions. The resulting stepwise equilibrium constants are multiplied together and reported as the stability constant, β. The subscripts of the stability constants represent the number of metal and ligands participating in the reaction to create the product complex. The subscript varies depending on the textbook and research article. In popular textbooks only the number of metals x, and ligands y are reported.[55] However, protons participate in some reactions and papers use x,y,z subscripts to represent the numbers of metal, proton and ligands[56] or metal, ligand and protons[57] in the product complex. Throughout the remainder of this thesis, the x,y,z formalism will be used to represent the metal, ligand and proton respectively unless otherwise stated. The reaction of one metal with one ligand is denoted β_{110}. This is illustrated in Equation 2.3.

$$\log\ \beta_{110} = \log\ K = \log \frac{[ML(Sol)_{m-n}]}{[M(Sol)_m][L]} \tag{2.3}$$

CO_3^{2-} is often an important divalent inorganic ligand controlling U^{VI} speciation because it is commonly found in groundwater due to the dissolution of atmospheric CO_2, dissolution of carbonate rocks, and microbial release of CO_2 into solution.[58] A series of uranyl carbonate complexes can form including $[UO_2(CO_3)]^0$, $[UO_2(CO_3)_2]^{2-}$ and $[UO_2(CO_3)_3]^{4-}$. $[UO_2(CO_3)]^0$ can be found as a precipitate.

Upon addition of monovalent cations (e.g. Na, K, Cs), $M_2[UO_2(CO_3)_2]$ and $M_4[UO_2(CO_3)_3]$ precipitates from solution where M is the monovalent cation.[51, 52, 59] Polynuclear complexes such as $[(UO_2)_2(CO_3)(OH)_3]^-$ can also be found.[51, 60] These carbonate containing complexes control aqueous U^{VI} speciation above pH 6, until the concentration of OH^- has increased sufficiently to out compete CO_3^{2-} for the co-ordination sites in the equatorial plane of U^{VI}. This can be seen in Figure 2.2 for typical total CO_2 concentrations ($\Sigma[CO]_2$) measured during the column experiments reported in chapter 4 of this thesis. Carbonate can significantly alter the speciation of U^{VI}, therefore it is important to characterise $\Sigma[CO_2]$ in experiments because of the dissolution of atmospheric CO_2 and the use of analytical grade chemicals which may contain CO_3^{2-}.

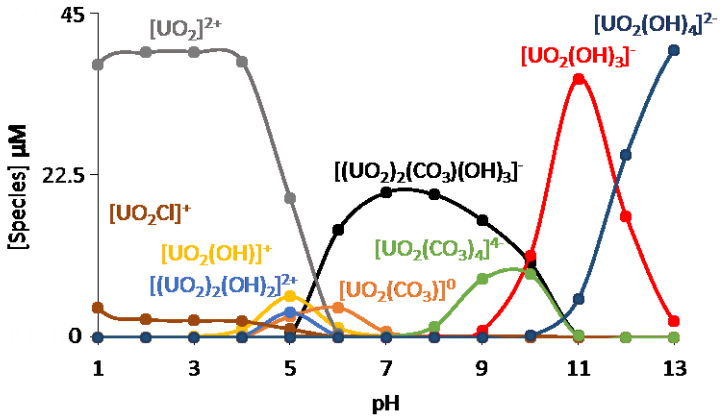

Figure 2.2. Specia Γ database. The chemical conditions are: 42 µM U^{VI}, 220 µM $\Sigma[CO_2]$ and 0.1 M NaCl., Dissolved oxygen was equilibrated with the partial pressure of atmospheric oxygen (0.21 atm). The solution is charge balanced with Cl and Na by assuming HCl and NaOH was added to adjust pH. 220 µM $\Sigma[CO_2]$ was the average $\Sigma[CO_2]$ measured during the quartz sand column experiments reported in chapter 4.

2.3. Siderophores: A class of naturally occurring organic molecules

A variety of organic ligands can complex with U^{VI}, [23, 41] including a class of organic molecules called siderophores.[61] Siderophores have been extensively reviewed[62-67] and only a brief introduction is provided here before focussing on U^{VI}-siderophore interactions. Siderophores are a class of low molecular weight organic molecules released by plants, bacteria and fungi.[62, 63, 67] Most siderophores contain catecholate (1), hydroxamate (2) or α-hydroxycarboxylate (3) functional groups [63, 64] and less

commonly the α-aminocarboxylate (4), hydroxyl-phenyloxazolonate (5) and α-hydroxyimidazolate (6) functional groups (Figure 2.3).[62]

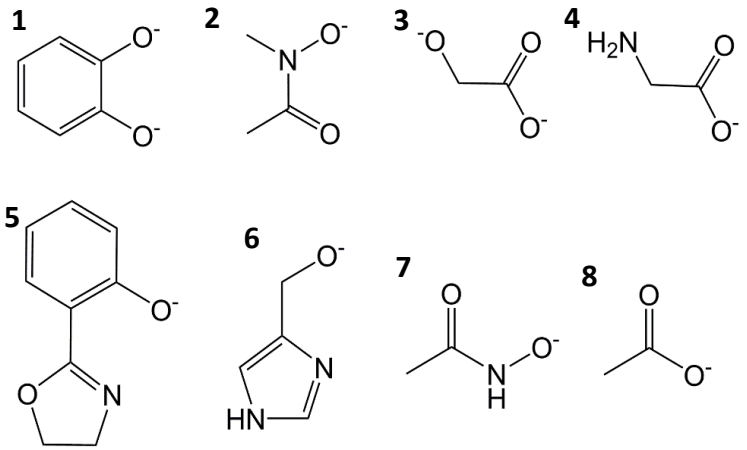

Figure 2.3. The key functional groups found in siderophores. These are 1 catecholate, 2 hydroxamate, 3 α-hydroxycarboxylate, 4 α-aminocarboxylate, 5 hydroxy-phenyloxazolonate, and 6 α-hydroxyimidazolate. Structures 7 and 8 are acetohydroxamate and acetate respectively. These two structures are often used as analogues for hydroxamate and carboxylate functional groups and are discussed in sections 2.3.3.2 and 2.3.3.3 respectively.

Siderophores were first isolated in 1949 to 1952 and to date over 500 siderophores have been identified.[62] They form highly stable complexes with Fe^{III} (log β up to 52, Table 2.1).[68-71] The structure of some common siderophores are provided in Figure 2.4. Siderophores are also produced in greater quantities in Fe deficient environments.[72-74] Fe is a key nutrient for a variety of metabolic processes.[67, 75, 76] For micro-organisms, Fe is important because it acts as a catalyst in enzymatic processes, oxygen metabolism, electron transfer, DNA synthesis and RNA synthesis. It also is important for the development of biofilms by stabilising the polysaccharide matrix.[63] In aerobic, neutral to alkaline solutions, Fe^{II} rapidly oxidises[77] and precipitates from solution as a variety of Fe^{III} oxides and hydroxides which have low solubility's. For example the K_{s0} of $Fe(OH_3)$ is $2.79x10^{-39}$.[78] Consequently, bacteria, plants, and fungi developed mechanisms to solubilise Fe^{III}. The primary purpose of siderophores was identified as solubilising Fe^{III} and transporting it back to the plant, bacteria or fungi.[67] Therefore they were named siderophores, Greek for iron (sidero) and carriers (phore).[67]

Table 2.1. Log β for Fe –siderophore complexes, including a hydroxamate (desferrioxamine B) [71] a catecholate (enterobactin),[68, 69] and carboxylate (rhizoferrin)[70] type-siderophore.

Siderophore	log β
Desferrioxamine B	30.6
Enterobactin	49
Rhizoferrin	25.3-36.9

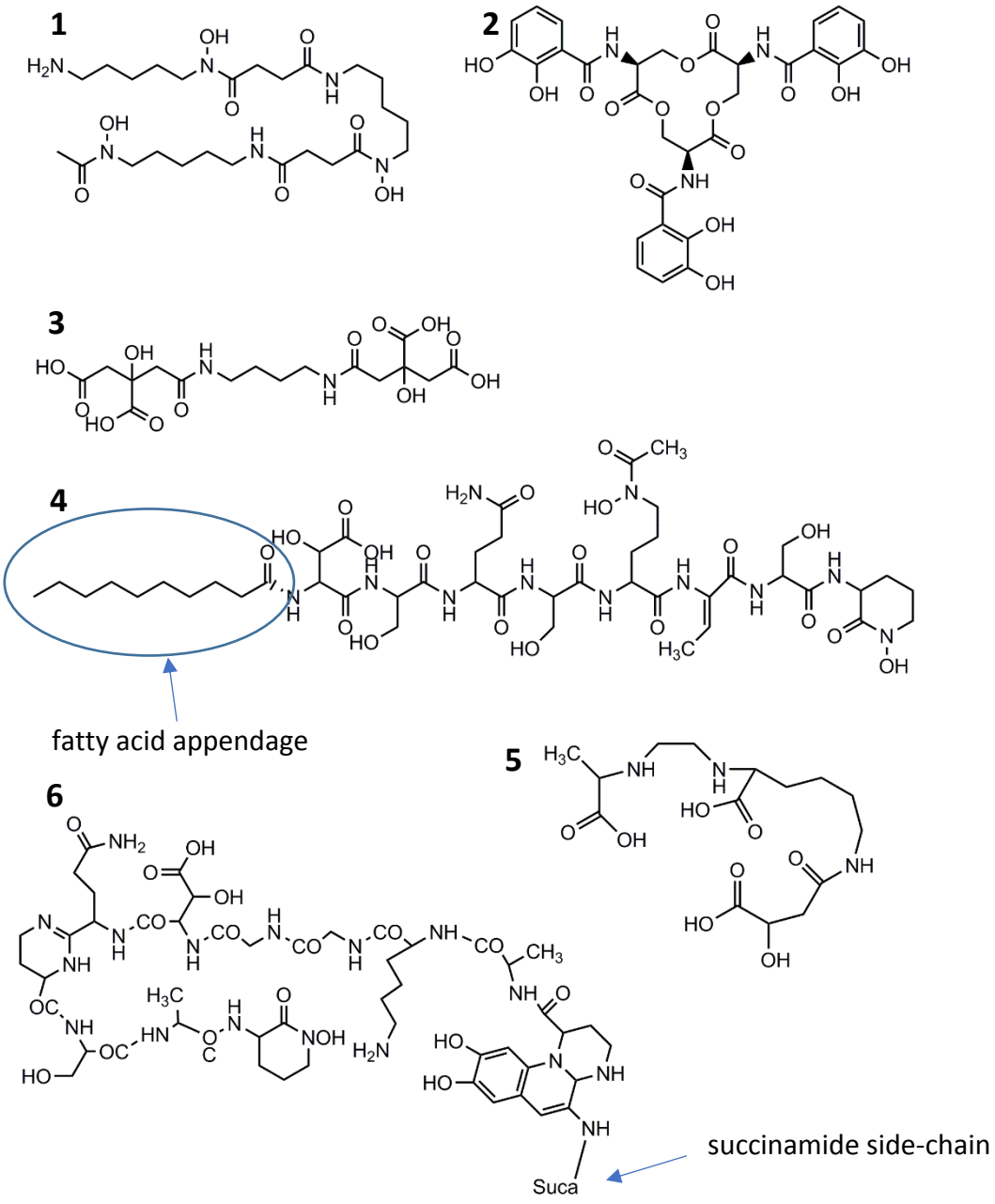

Figure 2.4. Structures of some common siderophores. These are: **1** desferrioxamine B ($C_{25}H_{48}N_6O_8$),[1] **2** enterobactin ($C_{30}H_{27}N_3O_{15}$),[79] **3** rhizoferrin ($C_{16}H_{24}N_2O_{12}$),[70] **4** loihichelins A ($C_{44}H_{72}N_{11}O_{19}$) which contains a fatty acid appendage composed of 10 carbon and an O atom,[80] **5** rhizobactin ($C_{15}H_{26}N_3O_8$),[81] **6** pyoverdin A($C_{50}H_{70}N_{17}O_{17}$) with a side-chain composed of succinamide units ($C_4H_5NO_2$).[57]

Siderophores undergo a stepwise deprotonation of their functional groups, giving the siderophores increased formal negative charge as the pH of the solution increases from circumneutral to pH ≥ 10. For example the pK_a's of the common hydroxamate siderophore desferrioxamine B (DFOB, $C_{25}H_{48}N_6O_8$, structure 1 in Figure 2.4) are 8.32, 8.97 and 9.52 and 10.84 [71] and the pK_a's of the common α-hydroxycarboxylate siderophore rhizoferrin ($C_{16}H_{24}N_2O_{12}$, structure 3 in Figure 2.4) are 2.86, 3.05, 4.21, 5.25, 10.05 and 11.3.[70] The aqueous U^{VI} species at pH ≥ 10.5 are the negatively charged $[UO_2(OH)_3]^-$ and $[UO_2(OH)_4]^{2-}$ complexes and the interaction between the negatively charged U^{VI} species and the negatively charged siderophores could be limited. However organic ligands with multiple functional groups produced from cellulose degradation (α-isosaccharinic) and cement degradation (D-gluconate) can complex with U^{VI} at pH 12-13.[82-84] These are similar to siderophores and could indicate that U^{VI} can complex with siderophores in alkaline solutions, impacting aqueous U^{VI} chemistry. In alkaline solutions, some siderophores can degrade, for example the ester linkages in enterobactin ($C_{30}H_{27}N_3O_{15}$, structure 2 in Figure 2.4) can undergo base-catalysed hydrolysis, fragmenting the siderophore along the carbonyl bond. [67] This potentially limits the impact of siderophores on aqueous U^{VI} chemistry in alkaline solutions.

2.3.1. Production of siderophores by bacteria

The synthesis of siderophores by bacteria is energetically costly, requiring many steps to be produced. As an example, the synthesis pathway of enterobactin is shown in Figure 2.5.[85-87] To overcome the expensive energetic cost of producing siderophores, bacterial communities co-operate and release siderophores together to increase the chance that each bacteria comes into contact with and Fe^{III}-siderophore complex.[88] Therefore with decreasing biological activity, siderophore production will decrease because there are less bacteria around, and because there is less chance for the bacteria to come into contact with an Fe^{III}-siderophore complexes through co-operation of the microbial community.[89] Siderophore concentrations can be < 10 μM in rocks and up to 1 mM in the rhizosphere in organic rich conditions.[90-92]

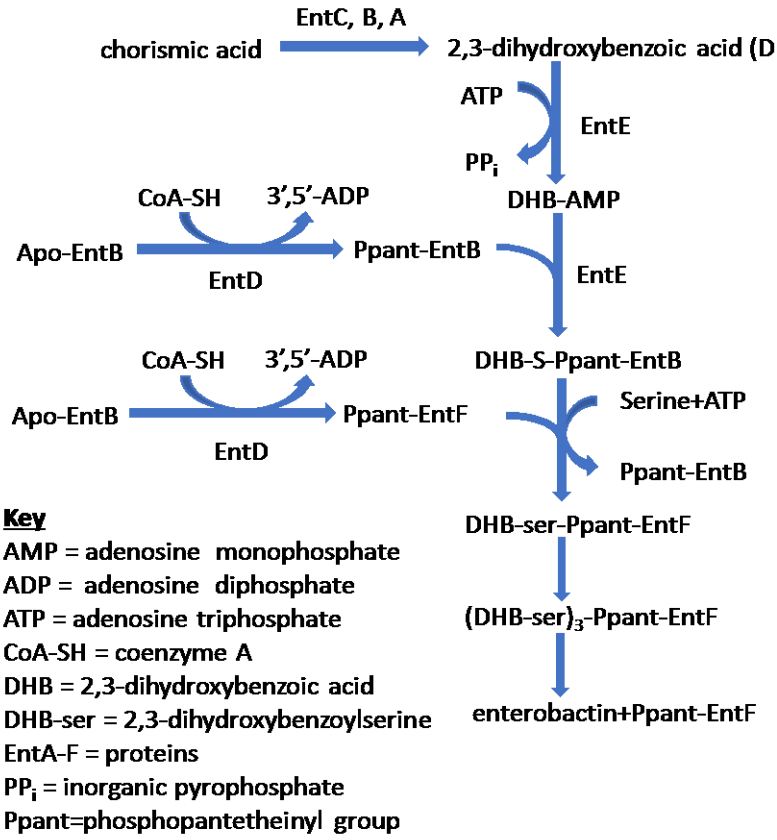

Figure 2.5. Biosynthesis pathway of enterobactin.[85-87] 2,3-dihydroxybenzoic acid (DHB) is synthesised from chorismic acid using the proteins EntA, B and C. 2,3-dihydroxybenzoylserine (DHB-ser) is synthesis by condensing DHB and serine by using the proteins Ent D,E and F. EntD and EntF are used to adenylylate DHB and serine respectively. EntF carries DHB-ser which is attached to EntF through the phosphopantetheinyl (Ppant) cofactor. This is passed onto the active site on an adjacent thioesterase domain in EntF. Continued additions of DHB and serine repeat the process twice more with each DHB-ser added onto thioesterase domain to form a linear trimer. This is cyclised to become enterobactin, detaching from the pPant and the EntF protein.

Bacteria that produce siderophores tend to be those found in Fe deficient environments. For example, siderophores are produced by a wide range of bacteria including bacteria in marine environments where Fe concentrations are 0.01-2 nM,[93, 94] and terrestrial bacteria found in the rhizosphere and bulk soil in aerobic, neutral-alkaline pH values where the solubility of Fe is very low (K_{s0} of $Fe(OH_3)$ is 2.79×10^{-39}). [78, 95] Typical siderophores produced by marine bacteria are composed of a peptide head-group appended to fatty acids with such as loihichelins A ($C_{44}H_{72}N_{11}O_{19}$, structure 4 in Figure 2.4).[80, 94] The peptide head-group contains functional groups such as α-hydroxycarboxylate, hydroxamate and catecholate. [80, 94] Terrestrial bacteria can produce a variety of siderophores such as

the hydroxamate containing desferrioxamine B (structure 1 in Figure 2.4), α-hydroxycarboxylate containing enterobactin (structure 2 in Figure 2.4), carboxylate containing rhizobactin ($C_{15}H_{26}N_3O_8$, structure 5 in Figure 2.4), and siderophores containing a mixture of functional groups such as pyoverdine A ($C_{50}H_{70}N_{17}O_{17}$, structure 6 in Figure 2.4).[2, 57, 63, 81, 96]

The biological activity in alkaline (pH ≥ 10.5) and saline solutions (ionic strength ≥ 0.1 M) relevant to radioactive waste storage and disposal facilities is limited due to the physiological challenges associated with bacterial growth. The cytoplasm pH of bacterial cells are between pH 7.4 to 7.8, and significant differences between the pH of the cytoplasm and the external solution prevent bacteria from maintaining the cytoplasm circumneutral pH.[97-99] When this happens proteins within the cell denature leading to DNA damage.[100, 101] It also causes protons to be pumped out of the cell rather than into the cell effecting energy production and respiration.[98] High ionic strengths limit, in general, bacterial growth due to effects of changing the osmotic gradient. Osmosis occurs where water moves from high water activity to low water activity through a semi-permeable membrane. In high ionic strength solutions the activity of water decreases leading to water molecules being released from the bacteria into the surrounding aqueous solution. This causes the bacteria cell to dehydrate reducing its volume and changing its shape.[102, 103] Therefore microbiological activity will likely be limited to haloalkalophiles such in the near field downstream of the waste storage and disposal facility.

Research into whether bacteria produce siderophores in alkaline solutions is limited. Alkaphilic bacteria including species of *Bacillus* have been observed to produce siderophores in iron deficient conditions at pH 9-10.[104] *C. thermarum*, *B. alcalophilus*, and *B. pseudofirmus* produce catechol-type siderophores while *C. thermarum* and *B. halodurans* produce siderophores which contain at least one hydroxamate functional group. A recent study showed that out of 80 bacterial isolates grown from a culture at an initial pH of 10.5, 17 were observed to release hydroxamate and catechol type

siderophores. However, the pH dropped to 7.5 and it is unclear whether the siderophores are produced at the initial pH.[105] A further study explored siderophore production for six isolates, four of which were studied at pH 10.6. In this study five of the six isolates generated siderophores which could complex with Ga. *Halomonas* sp. were found to produce siderophores at pH 9.0 in 0.86 M NaCl, representative of the chemical conditions at Soap Lake, Washington.[106] These were amphiphilic type siderophores containing α-hydroxcarboxylate functional groups. Overall there is evidence that siderophores are produced in alkaline solutions at approximately pH 10.5, however, further research is needed to explore whether this is the case at higher pH values.

Siderophores will be generated upstream of the radioactive waste storage or disposal facility where groundwater will have a circumneutral pH. The steel used within the construction of the facility will corrode, whereby Fe^0 undergoes an oxidation process to Fe^{II}.[107] At surface facilities, oxygen in the oxic groundwater will further oxidise Fe^{II} to Fe^{III} to form $Fe(OH)_3$ limiting the bioavailability of Fe, and bacteria will continue to release siderophores.[77, 108] In a geological disposal facility where conditions are anaerobic, Fe^{II} may be present as a cation limiting the need for siderophores, or present as green rust when pH >7, reducing the bioavailability of Fe and potentially inducing the release of siderophores.[28, 107, 109] There will be competition between Fe and U as well as with other cations, although before exploring this competition we need to know whether siderophores can complex with U^{VI} in these high pH conditions through a series of simple batch experiments and begin to gain mechanistic insights into U^{VI}-siderophore interactions.

2.3.2. U^{VI} siderophore complexes

Siderophores can form stable complexes with a wide variety of transition metals including Cu, Zn, Mn, V, Mo, Ni, and Pb.[70, 71, 110-114] As siderophores universally form stable complexes with metals, they could have high binding affinities with U^{VI}, influencing its aqueous chemistry and subsequent groundwater mobility.

To the best of my knowledge, research on U interactions with siderophores is limited to two areas. The first is an effort to understand the role of siderophores in the microbial leaching of U from the closed down Ranstad mine in Sweden. These studies focus on the mixed functional group class of siderophores called pyoverdines. The second area of research focusses on U^{IV} and U^{VI} interactions with desferrioxamine B (DFOB). This siderophore is used as a model because it is commercially available, while most other siderophores need to be isolated from bacteria, plants and fungi, or synthesised.

2.3.2.1. Siderophore enhanced microbial leaching of U from the Ranstad Mine

Microbial leaching of U was explored for ores collected at the Ranstad mine in Sweden. This was motivated by the presence of heavy metals in solution which could not be fully explained by abiotic processes, and by early research which found that U^{VI} could complex with pyoverdine A[115, 116] The initial research focussed on the effects of three strains of bacteria, *Pseudomonas fluorescens*, *Pseudomonas stutzeri* and *Shewanella putrefaciens,* on the mobilisation of heavy metals, including U, from naturally leached ore and unleached ore collected from the Ranstad mine.[115] The pH was initially 4.5 due to leaching of sulphate from the ores to form sulphuric acid (H_2SO_4). The pH increased over time, correlating with cell density, increasing the greatest to pH 9.3 for *P. fluorescens*. *P. fluorescens* was the only strain which thrived in the ore containing systems and only *P. fluorescens* increased the dissolved U concentration. After eight days the aqueous U concentration in the solutions containing the pre-leached shale ore was 5 ± 0.4 nM and 60 ± 20 nM in the absence and presence of the bacteria respectively. After five days, the aqueous U concentration in the unleached shale ore experiment was 90 ± 10 nM and 34 ± 2 µM in the absence and presence of the bacteria respectively. The authors suggest that the increased U concentration is due to siderophore production as the assay test show significant siderophore production in ore-free solutions within several hours.

Following this, another study focussed on the effect of *P. fluorescens* on U mobilisation from a naturally leached ore, acid leached ore and unleached ore from Ranstad.[117] The results of this study observed no significant change in pH in the absence of the ores, but the presence of the ore increased pH up to 9.3 and U concentrations were elevated. The authors concluded U could be mobilised by the formation of U-pyoverdine complexes or because of the formation of soluble uranyl carbonate complexes at the elevated pH. To explore whether it could be due to the siderophore, the research group isolated the siderophore from a *P. fluorescens* strain collected from the Aspo hard rock laboratory, and tested whether it could complex with U^{VI} using Ultraviolet-Visible light spectroscopy (UV-VIS).[57] The ultra-visible light spectra were dominated by the pyoverdin A (structure 6 in Figure 2.4). The pyoverdin formed complexes with U^{VI} with log β_{112} = 30.00 ± 0.64 and log β_{111} = 26.00 ± 0.85 in 0.1 M $NaClO_4$ solutions, representing $[UO_2(H_2PYV)]^0$ and $[UO_2(HPYV)]^-$ respectively, where PYV is short for pyoverdine. The siderophore contains catecholate, hydroxamate and α-hydroxycarboxylate functional groups, but there is no computational or experimental evidence which provides the binding mode of the siderophore.

2.3.2.2. Uranium interactions with the model siderophore, Desferrioxamine B

Deferrioxamine B (structure 1 on Figure 2.4) is a linear hydroxamate type siderophore which contains three hydroxamate functional groups with average protonation constants (pK_a) values of 8.32, 8.97 and 9.52 and an amine group with an average pK_a of 10.84.[71] The siderophore is produced by soil and marine bacteria.[118] The siderophore can be commercially purchased as a mesylate salt, where the mesylate (CH_3SO_3H) counter ion binds to the deprotonated amine group.

Spectrophotometric titrations conducted between pH 3.5-10 in 0.1 M $NaClO_4$ ionic media have shown that DFOB complexes with U^{VI}.[1] Three U^{VI}-DFOB species were observed with log β_{111} = 22.9 ± 0.1, log β_{110} = 17.1 ± 0.4 and log β_{11-1} = 22.8 ± 0.3 dominating speciation at pH 3.5-5.5, pH 5.5-8 and

pH 8-10 respectively. The authors suggest the species are $[UO_2(H_2DFOB)]^+$, $[UO_2(HDFOB)]^0$ and $[UO_2(OH)(HDFOB)]^-$ for log β_{112}, log β_{111} and log β_{11-1} respectively, where H_4DFOB represents the fully protonated ligand and mesylate group.

The high binding affinities suggest DFOB could have a significant effect on the mobility of U^{VI} in groundwater. This is supported by a series of batch experiments which have shown that 237-241 µM DFOB mobilises 40-60% of 50 µM U^{VI} adsorbed to the surface of goethite. The experiments were conducted at pH 6 in a 0.01 M ionic media at 25 °C.[119] The authors proposed DFOB mobilised U^{VI} from goethite at 25°C via indirect desorption as only 3% of DFOB adsorbed to the mineral surface. This is where DFOB complexes with U^{VI} in solution causing the concentrations of surface-bound U^{VI} and free aqueous U^{VI} (UO_2^{2+}) to not be in equilibrium. This causes U^{VI} to desorb from the goethite surface. The same researchers explored U^{VI} desorption by DFOB on Na-kaolinite under the same experimental conditions employed during the goethite experiments and came to the same conclusion.[120] Up to 70% of 55 µM U^{VI} sorbed to the surface of Na-kaolinite, all of which was desorbed by DFOB when its concentration is ≥146 µM.

Desferrioxamine B can also dissolve the highly insoluble U^{IV} mineral, uraninite, under reducing conditions.[121] Continuous flow tank reactors containing 1 g/L uraninite and 0.01 M $NaClO_4$ showed significant increases in dissolution rates. The net proton dissolution at pH 7-7.5 was 3 nmol/h.m^2 while DFOB was calculated to dissolve uraninite at a net rate of 64 nmol/h.m^2 when assuming the uraninite minerals surfaces were fully saturated with the siderophore.

The experimental work in this thesis expands our understanding of U^{VI}-DFOB interactions to pH 11.5 in 0.1 M NaCl solutions. Although the experiments only explore one siderophore, the outcome from the DFOB experiments should be representative of the hydroxamate type siderophores as they contain the same functional group. The functional group provides a significant amount of stability of

the complex.[122] The stability of U^{VI}-hydroxamate complexes is less than that of U^{VI}-catecholate and U^{VI}-α-hydroxycarboxylate as shown in section 2.3.2 and by the results presented in chapter 6. Therefore the stability of U^{VI}-siderophore complexes containing these key functional groups will likely be more stable than those of U^{VI}-DFOB and further reduce U^{VI} precipitation in pH 11.5 solutions containing 42 µM U^{VI} and 0.1 M NaCl.

2.3.3. U^{VI} complexes with siderophore functional groups

Although the available literature for U^{VI}-siderophore interactions is limited, one of the most important factors controlling the stability and selectivity of metal-siderophore interactions are the functional groups which bind with U^{VI}.[122] Understanding the stability and structures of U^{VI} complexes containing siderophore functional groups can help focus research by identifying which class of siderophores will likely form the most stable complexes with U^{VI}. The six siderophore functional groups are provided in Figure 2.3.

2.3.3.1. Catecholate ($C_6H_4(OH)_2$)

The catecholate ligand is composed of a 6 carbon ring (benzene) with two phenol groups in ortho position. The stability data is provided in Table 2.2. The pKa's for the two phenol groups are 9.2 and 13.0 respectively.[123] Catecholate can form highly stable complexes with U^{VI} due to the high binding ability of its two deprotonated phenol groups. Spectrophometric measurements suggest several different complexes form: $[ML]^0$, $[M(HL)]^+$, $[ML(HL)]^-$ and $[ML(HL)_2]^{2-}$ complexes, where M is $[UO_2]^{2+}$, L is the fully deprotonated ligand and HL is the ligand with one protonated O atom.[123, 124]

The experimental stability constant for a 1:1 U^{VI}-L complex in 0.1 M ionic media is 15.9 log K units.[123] A computational study also indicates the fully deprotonated catecholate ligand forms a bidentate complex with U^{VI}.[125] However, the formation of monodentate complexes were not studied. Extended X-ray Absorption Fine Structure Spectroscopy measurements in $1x10^{-3}$ M U^{VI} and $5x10^{-2}$ M catecholate, 0.1 M $NaClO_4$ solutions at pH 5 were also interpreted as bidentate complexation, and

observe the same type of binding at pH 10.[126] However speciation modelling from the same EXAFS study indicate that at pH 10 the species should be $[ML(HL)_2]^{2-}$. Therefore only one of the functional groups should form a bidentate complex, with the remaining two ligands binding in a monodentate fashion.

Table 2.2 Stability constant data for the uranyl catecholate complexes measured using spectrophotometry in 0.1 M $NaClO_4$.[123, 124] The difference between the stability constants for the same product ML complex between Ref. 123 and Ref. 124 is that Ref. 124 calculate log β when the reacting ligand is fully protonated. The pH data is taken from Ref. 124.

Reaction	pK_a/log β	pH
	Ref. 123	
$L^{2-} + H^+ = HL^-$	12.99	
$HL^- + H^+ = H_2L^0$	9.19	
$M^{2+} + HL^- = M(HL)^+$	6.2	3.3-5
$M^{2+} + L^{2-} = ML^0$	15.8	3.3-5
$ML^0 + HL^- = ML(HL)^-$	4.9	5-6.5
$ML(HL)^- + HL^- = ML(HL)_2^{2-}$	3.7	6.5-8
	Ref. 124	
$M^{2+} + H_2L^0 = M(HL)^+ + H^+$	-3.2	3.3-5
$M^{2+} + H_2L^0 = ML^0 + 2H^+$	-7.1	3.3-5
$ML^0 + H_2L^0 = ML(HL)^- + H^+$	-4.4	5-6.5
$ML(HL)^- + H_2L^0 = ML(HL)_2^{2-} + H^+$	-5.6	6.5-8

2.3.3.2. Hydroxamate (RC(O)N(OH)R' where R and R'= CH3)

Acetohydroxamic acid ($C_2H_5NO_2$, structure 7 in Figure 2.3) is often used to represent the functional group of DFOB because it is the simplest hydroxamic acid.[127] The stability of U^{VI} complexes with acetohydroxamic acid has been studied using spectrophotometric titrations in 1 M $NaClO_4$ solutions and the log β values are provided in Table 2.3.[128] The pK_a of the hydroxyl group was determined to be 9.15 ± 0.04 log K units. U^{VI} was observed to form a 1:1 and 1:2 U^{VI}-L complex with log β of 7.22 ± 0.01 and 14.89 ± 0.02 with stoichiometry $[ML]^+$ and $[ML_2]^0$ species respectively. The $[ML]^+$ species was observed to form at the starting pH of 1.12. Above pH 6 an orange precipitate forms which is likely due to the formation of the charge balanced ML_2^0 complex and its precipitation from solution. The ligand is generally assumed to form a chelate via its two oxygen atoms.[129]

Table 2.3. Stability data for U^{VI}-L complexes with AHA and NMAH.[128, 130] Spectrophotometric measurements in 1 M $NaClO_4$ were carried out for AHA. Potentiometry and spectrophotometry on 0.1 M KNO_3 was used from NMAH.

Reaction	pK_a/Log β	pH
	AHA-Ref. 128 (1 M $NaClO_4$)	
$L^- + H^+ = HL^0$	9.15 ± 0.04	
$M^{2+} + L^- = ML^+$	7.22 ± 0.011	1.12-6.00
$M^{2+} + 2L^- = ML^0$	14.89 ± 0.018	1.12-6.00
	NMAH-Ref. 130 (0.1 M KNO_3)	
$L + H^+ = HL^0$	8.68	
$M^{2+} + L^- = ML^+$	7.76[a], 7.81[b]	ca. 1.50-5.00
$ML^+ + L = ML_2$	6.14[a], 6.47[b]	ca. 4.00-5.00
$M^{2+} + 2L^- = ML^0$	13.90[a], 14.28[b]	ca. 4.00-5.00

[a]determined by potentiometric titrations, [b]determined spectrophotometrically

The hydroxamate functional group is represented by structure 2 in Figure 2.3, where the two R components are represented by CH_3. This is N-methylacetohydroxamic acid (NMAH).[130] The formation of U^{VI}-L complexes with NMAH was explored recently in 0.1 M KNO_3 solutions.[130] The pK_a of the hydroxyl group in NMAH was calculated as 8.68 log K units. The stepwise log K for the $[ML]^+$ and $[ML_2]^0$ complexes were 7.76 and 6.14 respectively when measured via glass-electrode potentiometry, and 7.81 and 6.47 respectively when measured spectrophotometrically. When pH increased past 5.5, an orange precipitate formed which was attributed to the precipitation of $[ML_2]^0$ from solution. This is similar to earlier findings for AHA.[128, 129] Crystals of the $[ML]^+$ and $[ML_2]^0$ complex have been isolated and their analysis indicate the ligand binds in a bidentate fashion for both complexes.[131] DFT calculations also indicated that a third protonated NMAH could bind to an axial oxygen of water via the protonated hydroxyl group, and to the U^{VI} atom via the carbonyl oxygen in the gas phase.[132]

2.3.3.3. α-hydroxycarboxylate ($OHCH_2C(O)OH$)

α-hydroxycarboxylate also known as glycolate (structure 3, Figure 2.3) is a simple carboxylate ligand similar to acetate with the exception that the CH_3 group in acetate is replaced with a hydroxyl group (α-OH). This means it could potentially form complexes with higher stability than acetate as it contains two oxygen atoms which have high electrodensities when deprotonated in solution. The

pK_a's of α-hydroxycarboxylate are 3.59 ± 0.01 and >17 for the carboxylate and α-hydroxy group respectively in solutions containing 1 M $NaClO_4$ and are provided in Table 2.4.[133]

Table 2.4. Stability data for the U^{VI} α-hydroxycarboxylate complexes,[133, 134] and U^{VI} acetate complexes.[135] The pH ranges for α-hydroxycarboxylate were obtained from the speciation diagram presented in the supplementary information of Ref. 134. All measurements were carried out using potentiometry in 1 M $NaClO_4$.

Reaction	Log β	pH
	α-hydroxycarboxylate – Ref. 133	
$H^+ + L^{2-} = HL^-$	3.59 ± 0.01	
$H^+ + HL^- = H_2L^0$	17-20	
$M^{2+} + HL^- = ML^0 + H^+$	-1.26 ± 0.07	<6
$M^{2+} + 2HL^- = ML(HL)^- + H^+$	0.19 ± 0.09	<6
$M^{2+} + 2HL^- = ML_2^{2-} + 2H^+$	-4.17 ± 0.04	>4.5
	α-hydroxycarboxylate – Ref. 134	
$M^{2+} + HL^- = M(HL)^+$	2.42 ± 0.02	<5
$M^{2+} + 2HL^- = M(HL)_2^0$	3.96 ± 0.03	<5
$M^{2+} + 3HL^- = M(HL)_3^-$	4.20 ± 0.05	<5
	acetate- Ref. 135	
$H^+ + L^- = HL^0$	4.59 ± 0.01	
$M^{2+} + L^- = ML^+$	2.58 ± 0.03	<3.85
$M^{2+} + 2L^- = ML_2^0$	4.37 ± 0.14	<3.85
$M^{2+} + 3L^- = ML_3^-$	6.86 ± 0.04	≥3.85

During potentiometric titrations in 1 M $NaClO_4$, stability constants for three U^{VI} α-hydroxycarboxylate complexes were observed with log β of 2.42 ± 0.02, 3.96 ± 0.03 and 4.20 ± 0.05 units respectively.[134] These represent $[M(HL)]^+$, $[M(HL)_2]^0$ and $[M(HL)_3]^-$ complexes where H represents the ligand with its α-hydroxy group protonated. In this case, the ligand binds via the two O atoms within the carboxylate group of the ligand.[133] When α-hydroxycarboxylate is co-ordinated with U^{VI}, the pK_a of the α-hydroxy group decreases from >17 to 3.64, and above pH 5 bidentate complexes form where the ligand binds to U^{VI} through a carboxylate O atom and the deprotonated α-hydroxy group.[133] Recent EXAFS data[136] supports this theory, which indicated $[M(HL)]^+$, $[M(HL)_3]^-$ and $[ML_2]^{2-}$ predominates at pH 2, pH 3.7, and pH>5 respectively. The EXAFS data also shed further light on the binding mode of the $[M(HL)]^+$ to $[M(HL)_3]^-$ complexes. No U-C bond distances were observed for these complexes suggesting the ligand binds in a monodentate fashion with an oxygen from the carboxylate end of the molecule when the alpha hydroxyl group was protonated.

In comparison, acetate (CH_3COO, structure 8 in Figure 2.3) forms 1:1, 1:2 and 1:3 U^{VI}-L complexes where each acetate ligand complexes in a bidentate fashion.[31] The pK_a of acetate calculated in 1 M $NaClO_4$ solutions using potentiometry was 4.59 ± 0.01 while log β for the $[ML]^+$, $[ML_2]^0$ and $[ML_3]^-$ complexes were 2.58 ± 0.03, 4.37 ± 0.14 and 6.86 ± 0.04 respectively.[135] These log β values are greater than those reported for the α-hydroxycarboxylate $[M(HL)]^+$ to $[M(HL)_3]^-$ complexes. In these complexes the decreased stability of the α-hydroxycarboxylate can be attributed to the differences in binding mode at the carboxylate end of the ligands, which is monodentate for α-hydroxycarboxylate and bidentate for acetate.

2.3.3.4. α-aminocarboxylate ($NH_3CH_2C(O)OH$)

α-aminocarboxylate, also called glycine (structure 4, Figure 2.3) has a similar structure to α-hydroxycarboxylate, but the α-hydroxyl group has been replaced by an amine group (NH_3). This is a zwitterion, an organic molecule with atoms carrying both a formal negative charge and a formal positive charge. The atom carrying the negative charge is the deprotonated O atom in the carboxylate group, while the positive charge is carried by the third H atom bound to the N atom.[56] The two pK_a's for the organic molecule were calculated as 2.38 ± 0.04 and 9.58 ± 0.04 in 0.1 M ionic media, corresponding to the species $[HL]^0$ and $[H_2L]^+$ respectively.[56]

Two complexes were observed to form, $[M(HL)]^{2+}$ and $[M(HL)_2]^{2+}$. The log β of the $[M(HL)]^{2+}$ and $[M(HL)_2]^{2+}$ complexes are 10.84 ± 0.10 and 21.19 ± 0.13 respectively when measured using TRLFS in 0.1 M $NaClO_4$ media.[56] These log β values assumed the ligand was fully deprotonated, and that the amine group protonated upon reaction. The log β values calculated when assuming the amine group was protonated in the reactant ligand were 1.26 ± 0.10 and 2.03 ± 0.13 for $[M(HL)]^{2+}$ and $[M(HL)_2]^{2+}$. The log β values were also determined in 0.5 M $NaClO_4$ using both using UV-VIS and TRLFS, providing similar stability constants to those obtained with TRLFS in 0.1 M $NaClO_4$ ionic media. These are

reported in Table 2.5. The experimental study[56] indicated α-aminocarboxylate complexed in a bidentate fashion with U^{VI}, which is supported by a recent detailed DFT study.[137]

Table 2.5. Stability data for the U^{VI} α-aminoxycarboxylate complexes measured using TRLFS in 0.1 M $NaClO_4$.[56]

Reaction	pK_a/log β	pH
α-aminocarboxylate – Ref. 54		
$H^+ + L^- = HL^0$	9.58 ± 0.04	
$H^+ + HL^0 = H_2L^+$	2.38 ± 0.04	
$M^{2+} + L^- + H^+ = M(HL)^{2+}$	10.84 ± 0.10	2-4
$M^{2+} + 2L^- + 2H^+ = M(HL)_2^{2+}$	21.19 ± 0.13	2-4

2.3.3.5. hydroxy-phenyloxazolonate ($C_6H_4(OH)C_3H_2NO$) and α-hydroxyimidazolate (C_3N_2HCOH)

To the best of my knowledge, there is no log β or structural data for the hydroxy-phenyloxazolonate and α-hydroxyimidazolate functional groups, which are structures 5 and 6 in Figure 2.3 respectively. Hydroxy-phenyloxazolonate has one hydroxyl group with pK_a of 9.0, and complexes with metals in a bidentate fashion via the deprotonated O atom and the lone pair of the N in the oxazolone ring.[62] α-hydroxyimidazolate contains two pK_a's corresponding to the hydroxyl group and deprotonation of the pyrrole-like-N atom within the imidazole ring, giving the ligand a -2 formal charge. The reported pK_a's are 6.00 and 14.52, where the latter pK_a represents that of the pyrrole-like-N atom.[62, 138] The ligand can complex to U^{VI} through the deprotonated O atom. Alternatively the ligand can complex to U^{VI} through the deprotonated pyrrole-like-N atom or through the lone pair in the pyridine-like-N atom. The formation of a direct U^{VI}-N co-ordination bond is supported by the formation of a U^{VI} complex directly through the N atoms of a similar ligand, 1-methylimidazole.[139]

2.3.4. Bacterial processes competing with uranium-siderophore complexation

Uranium interactions with organic materials are not limited to siderophores. A variety of processes occur including sorption, mineralisation, reduction and accumulation in contact with micro-organisms.[29] Micro-organisms contain functional groups on the outside of the cell wall such as

phosphate and carboxylate.[29, 140] These could compete with the siderophores to complex with U^{VI} and the success of the competition will depend on the log β of the siderophore and the bacteria. The stability of 1:1 U^{VI}-siderophore complexes can be between 17-30 log β units in 0.1 M $NaClO_4$ solutions.[1, 57] The stability of common functional groups on bacterial cell walls are typically less stable than this. For example the log β is 11.28 for the U^{VI} phosphate complex $[UO_2(PO_4)]^-$ in 0.5 M $NaClO_4$ solutions[49] and the log β values are 2.58, 4.37 and 6.86 for 1:1, 1:2 and 1:3 U^{VI} acetate complexes, respectively, in 1 M $NaClO_4$ solutions.[135] Therefore it is likely that siderophores will outcompete the common functional groups on bacteria cell walls, and the U^{VI}-siderophore complex will remain in aqueous solution. Any excess aqueous free U^{VI} could then complex with the bacteria cell wall.[140]

Uranium can precipitate by forming complexes with ligands produced by microorganisms, a process known as biomineralisation. The ligands generated are similar to the ones found on the cell walls of bacteria (e.g. phosphate, carboxylate, amines).[29] Uranium-phosphate precipitates have been observed which often occur within the bacterial cells, indicating transport and bioaccumulation of U^{VI} in the bacterial cells.[140-142] As for biosorption, the success of this mechanism depends on whether the ligands can displace the siderophore around U^{VI}. As the stability constants of the U^{VI}-phosphate complex is less than that of U^{VI}-siderophore complexes, it seems likely U^{VI}- siderophores complexes will remain stable, with excess free U^{VI} undergoing biomineralisation.

U^{VI} reduction to U^{IV} occurs at a similar redox potential as Fe^{III} reduction to Fe^{II}, and bacteria can reduce U^{VI} to U^{IV} to gain energy which can be used for metabolism.[143] Reducing U^{VI} to U^{IV} leads to precipitation from solution as biogenic uraninite (UO_2) or as a U^{IV}-L precipitate.[29, 144] A U^{VI}-DFOB complexation study did not observe reduction of U^{VI} in the siderophore complex[1] and Fe^{III} first needs to be removed from the siderophore and transported into the bacteria before it can be reduced.[62] Therefore it is unlikely that U^{VI} is reduced when it is complexed with a siderophore. If free aqueous

U^{VI} is bioreduced, the introduction of siderophores could potentially lead to remobilisation of uranium as DFOB has been observed to dissolve uraninite under anaerobic conditions.[121]

Siderophores could work synergistically with biosorption, bioaccumulation and bioreduction. Gram-negative bacteria have a cell wall composed of an inner and outer membrane. The pores in the outer membrane are too small for Fe^{III}-siderophore complexes to permeate through. Therefore these bacteria contain hydrophobic aromatic aminoacids on the extracellular surface of the outer membrane which bind the Fe^{III}-siderophore complex. Proteins with high binding affinities then outcompete the siderophore and bring Fe^{III} into the cell where it is reduced to Fe^{II}.[62] Gram-positive bacteria, which only has one membrane, is also expected to have similar mechanisms for removing Fe^{III} from the siderophore complex.[62] Therefore although U^{VI} may not directly biosorb to the surface of bacteria through functional groups such as carboxylate and phosphate, the U^{VI}-siderophore complex could bind instead, immobilising it on the bacteria surface. If the protein shuttles have high binding affinities with U^{VI} as they do with Fe^{III} then these shuttles could transport U^{VI} into the microorganism, leading to bioaccumulation and potentially bioreduction.

2.4. Factors controlling the mobility of U^{VI} precipitates

2.4.1. U^{VI} minerals

U^{VI} can precipitate from solution as a wide variety of minerals depending on the chemical composition of the solution. The change in Gibbs free energy of reaction ($\Delta_r G$), and subsequently the stability, of the precipitates is provided in Equation 2.4. R, T, K_{s0}, IAP and SI are the gas constant, absolute temperature, solubility product, the ion activity product, and the saturation index respectively. K_{s0} is the equilibrium constant (i.e. Equation 2.2) of a mineral dissolving in the aqueous phase. The change in concentration of the precipitate is considered to be insignificant, therefore it has no effect on the stability of the reaction and its value is 1. The IAP has the same form as K_{s0} except it is the actual concentration of the aqueous species measured in solution, rather than the

concentration at equilibrium. If the SI is positive, then the actual concentration of the dissolved species (IAP) is greater the concentration of the dissolved species at equilibrium (K), and the solution is oversaturated with respect to the mineral. If SI is negative the solution is undersaturated with respect to the mineral phase. [55, 145]

$$\Delta_r G = RT\ln\left(\frac{IAP}{K_{s0}}\right) = RT\ln(SI) \quad (2.4)$$

The precipitates can form homogenously in solution. This occurs when the Gibbs energy of the mineral plus that of the surrounding solvent is less than that of the Gibbs energy of the solution containing the dissolved mineral constituent ions. The Gibbs energy of the precipitate can be split into the bulk (G_{bulk}) and surface (G_{surf}) contributions. The G_{bulk} of the mineral has a lower energy than that of the G_{surf} as ions in the bulk of the ion cluster has stronger covalent and ionic type bonds than ion constituents on the surface of the cluster which has weaker hydrogen bonds with the surrounding solvent. Once the cluster of constituent ions is big enough, G_{bulk} plays a greater part in the energy of the cluster, reducing the overall energy of the system, allowing the mineral to precipitate out from solution.[145] The precipitation can also occur heterogeneously. This is where a surface (e.g. mineral surface) acts a nucleation point for the precipitates. The mineral surface can form stronger bonds with the critical cluster molecules compared to solvation bonds. This reduces the interfacial free energy, which makes it easier for the mineral to precipitate from solution and increasing the precipitation rate.[145]

A variety of U^{VI} minerals can be found in nature or form due to the corrosion of spent nuclear fuel. These minerals have been comprehensively reviewed,[146] and the thermodynamics of some common U^{VI} containing minerals have been reported.[147] These include U^{VI} oxides, peroxides, hydroxides, carbonates, phosphates, silicates and salts containing alkali and alkaline earth elements such as Na^+, K^+, and Ca^{2+}.

In the literature, mineral particles are called colloids when the particles have a diameter of 1 nm to 1 μm in one or more dimensions and are distributed in a second phase such as water.[55, 148] Particles containing U^{VI} have been observed to form in high pH and ionic strength conditions relevant to radioactive waste disposal. For example, U^{VI} precipitation was characterised in a synthetic cement leachate containing 0.19 M KOH, 0.19 M NaOH and 0.27 mM $Ca(OH)_2$ at pH 13.1.[149] The U^{VI} precipitates were 1.5-1.8 nm diameter crystals consisting of a clarkeite-type phase containing Ca, K and Na. These crystals aggregated to form 20 to 60 nm diameter colloids when 4.2-42 μM U^{VI} was present, and ≥ 0.22 μm precipitates when 252 μM U^{VI} was present in the cement leachate. The precipitates remained stable over the 32 months the experiments were conducted. Precipitation was also confirmed in a pH 13.3 cement leachate containing 0.092 M KOH, 0.95 M NaOH and 0.14 mM $Ca(OH)_2$.[150] When 42 μM U^{VI} was present, the U^{VI} was not removed by the calcite surface and was suspended in solution as 0.76 nm crystals which aggregate to 21.7 nm as a uranyl oxyhydroxide mineral similar to bequelerite ($Ca(UO_2)_6O_4(OH)_6 \bullet 8(H_2O)$). Precipitation of U^{VI} was observed in batch sorption experiments in solutions at pH ≥ 10 which contain 28.5 μM U^{VI} and Na containing solutions (0.01-0.05 M $NaClO_4$) often used in batch sorption studies, although the size of the precipitates were not characterised.[151, 152]

The formation of mineral particles can lead to U^{VI} being either highly mobile or immobile depending on their physical and chemical properties as discussed in sections 2.4.2 to 2.4.5. If the particles are immobile in the host rock of the facility then the integrity of the facility with respect to U^{VI} particles is upheld. However if the U^{VI} particles are highly mobile the safety of the facility could be compromised. The safety case of the radioactive waste storage and disposal site will need further consideration to determine the quantities of U^{VI} which could reach receptors at the surface through this exposure pathway. If the risk of fatality to humans increases above 1 in a million[153] after

reassessing this exposure pathway then the facilities need to be redesigned to prevent these particles from forming and exiting the facility.

2.4.2. Particle transport to the surface of porous media grains

Particle transport to the surface of a porous media grain and its subsequent attachment is described by the clean bed filtration theory. Small particles (<1 µm diameter) can be transported to the surface through Brownian diffusion while large (>1 µm diameter) and dense (>1 g/cm^3) particles are transported through interception and sedimentation respectively (Figure 2.6).[154-156] Brownian diffusion is the random motion of the particles due to being hit by other molecules in solution. This can bring the particle into contact with the mineral surface. Interception occurs when the size of the travelling particles leads to contact with the porous media when travelling around the grains. Sedimentation occurs when the travelling particles are too dense to follow the same trajectory as water around the porous media due to the influence of gravity, leading to contact with the grains. These processes can help transport the particles from the bulk solution to the quartz sand surface, enhancing the likelihood of particle attachment.[154, 155]

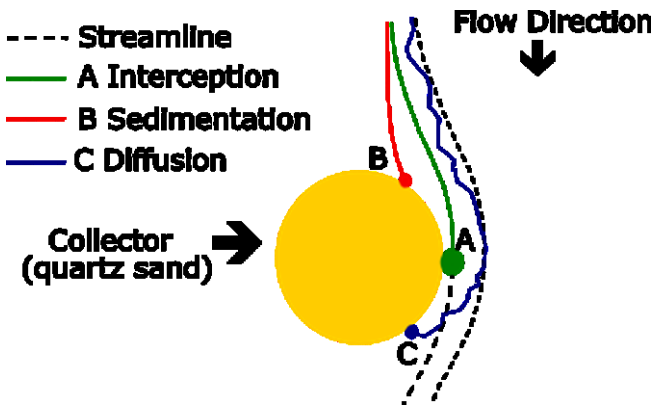

Figure 2.6. The three types of motion that can lead to uranium particle contact with quartz sand, redrawn from Yao *et al*.[154] A (green line) represents interception, B (red line) represents sedimentation, and C (blue line) represents Brownian diffusion. The streamline shows the path water takes around the sand grain.

2.4.3. Derjaguin, Landau, Verwey and Overbeek (DLVO) theory

The mobility of particles through porous media can be affected by Van der Waals and electrostatic forces acting between the travelling particle and the mineral surface. When the surfaces of the travelling particles and mineral grains are oppositely charged, electrostatic and Van der Waals forces attach the particles to the mineral grain surface. When the surfaces of the travelling particles and mineral grains have the same effective surface charge, short range electrostatic repulsion acts as a barrier to chemisorption, however, long range Van der Waals forces allow for weak attraction of the particles to the mineral grain surface. When the surfaces have a neutral charge, electrostatic repulsion and attraction will be minimised, and the particles will attach to the mineral grain surface by van der Waals attraction.[157, 158] These interactions are described by the Derjaguin, Landau, Verwey and Overbeek (DLVO) theory, [159, 160] and have been observed in laboratory column experiments.[161-164] These interactions are controlled by pH, ionic strength, electrolyte type (valence), colloid size and flow velocity.[155, 157, 158] Mineral surface roughness and charge heterogeneity can enhance precipitate immobilisation by van der Waals and electrostatic attraction respectively.[162, 165-168] Recent evidence suggests charge heterogeneity and surface roughness can potentially enhance particle mobilisation too. [169]

2.4.4. Particle Straining

Particle straining plays an important role in the mobility of particles through porous media. If the particles are bigger than the pores, mechanical filtration occurs (complete straining). If the particles are within a critical size of the pores, then incomplete particle straining occurs, and the particles remain trapped within grain to grain contacts (e.g. at pore throats) [155, 170-172]. The potential for particle straining has been examined by transporting fluorescent latex colloids (0.45-5.1 μm diameter) in homogenous quartz sand. Straining has been detected when the ratio of mean colloid size to median grain size (d_p:d_{50}) is >0.002 and becomes a significant removal mechanism when this ratio increases to >0.005-0.008.[156, 173] Therefore, straining increases with larger particle diameters

and smaller porous media grain sizes.[156, 170, 173, 174] Straining has also been shown to increase with ionic strength, with d_p:d_{50} decreasing to 0.0017 when ionic strength is to 0.2 M (NaCl).[171]

The physical properties of the porous media can affect particle removal by DLVO forces. The narrowing of the pore space into the pore throat reduces the distance the particles need to be transported to be able to intercept the porous media surface. This enhances the likelihood the particles can be removed from the mineral surface, a process known as particle wedging.[158]

2.4.5. Exclusion processes

The chemical and physical processes described by DLVO and particle straining can also significantly enhance the mobility of particles. The particles can be transported more rapidly than a conservative tracer. This is a tracer which does not interact with the mineral surfaces at all. This is due to differences in the flow paths the particles and non-reactive tracer takes. The non-reactive tracer molecules are small enough (nm size) to be transported through small pores, but particles which are several orders of magnitude greater in diameter cannot pass through the small pores because of their physical size. Therefore the particles will transport through fewer pore networks reducing the amount of dispersion, and these pore networks will tend to have a higher velocity, enhancing mobility.[156, 175] Particles will also tend to be transported near the centre of the pore where velocities are greater. This is due to electrostatic repulsive forces preventing the particles from coming close to the porous media grains. On the other hand, the non-reactive tracer can be transported through a much greater portion of the pore space and will have a slower velocity on average.[156]

2.5. Density Functional Theory

This section provides a brief introduction to Density Functional Theory (DFT) and the model chemistry components used in the calculations (functional, basis set, effective core potential, and solvation model). A computational method was selected as it can be used to understand the

thermodynamics and structural properties of U^{VI}-ligand interactions in chemical conditions which can be difficult and time consuming to explore experimentally. The aim of the research presented in this thesis is to develop a cost-effective computational method to predict the log β of U^{VI}-ligand complexes. DFT was selected over Hartree-Fock (HF) because it provides more accurate energetics while scaling with a similar computational cost for a given system size N (HF scales formally as N^4).[176] Density Functional Theory was selected over Moller-Plesset perturbation theory (e.g. MP2, scales as N^5) and coupled cluster methods (CCSD, scales N^6) as the latter two methods are increasingly computationally costly with respect to DFT.[176] DFT was used over molecular dynamics (MD) because it does not calculate the electronic energy of the system which is required to calculated the Gibbs energy and subsequently the log β of a reaction.[176]

Density Functional Theory has multiple assumptions and limitations which lead to systematic errors in calculating G which are discussed in more detail throughout this section. Electronic methods including DFT calculates the energy of a molecule assuming it acts as an ideal gas at 1 atm, so large differences in pressure (e.g. water pressure is 1354 atm) can lead to errors.[177] The harmonic oscillator and rigid rotor approximations are employed when calculating the G of a molecule.[177] Density functional approximations do not include the full exact electron correlation energy.[178] Basis sets have a finite number of functions rather than an infinite number.[176] Implicit solvation models struggle to represent local solute-solvent interactions. [176] However, the systematic error in $\Delta_r G$, and subsequently log β, for unknown complexes caused by these assumptions and limitations can be corrected by fitting the calculated values for a set of U^{VI}-ligand complexes against experimental data.[125]

The log β for U^{VI} complexes containing siderophores can be determined by calculating $\Delta_r G$ through the relationship shown in Equation 2.5 where R and T are the gas constant and absolute temperature respectively.

$$\log \beta_{110} = \log\left(\frac{-\Delta_r G}{2.303RT}\right) \quad (2.5)$$

The $\Delta_r G$ is calculated by subtracting the sum of the Gibbs free energy (G) of the reactant species from that of the product species as shown in Equation 2.6 for the formation of 1:1 M-L complex where G(ML(Sol)), G(M(Sol)) and G(L) are the Gibbs free energy of the ML, M and L complexes respectively. The subscript *m* represent the number of solvent molecules in the M(Sol) complex and *n* represents the number of solvent molecules released during the reaction.[55]

$$\Delta_r G = G(ML(Sol)_{m-n}) + nG(Sol) - G(M(Sol)_m) - G(L) \quad (2.6)$$

2.5.1. Calculating the electronic energy of a molecule by solving the Schrodinger equation

G can be calculated for molecules in the ground state by using the time independent Schrodinger equation shown in Equation 2.7, and by applying a series of energy corrections. In Equation 2.7, $\hat{H}$ is the Hamiltonian operator, Ψ is the wave function across the positions of the electrons $(\vec{r})$ and nuclei $(\vec{R})$ and E is the ground state energy. [179]

$$\hat{H}\Psi(\vec{r},\vec{R}) = E\Psi(\vec{r},\vec{R}) \quad (2.7)$$

Electronic structure methods aim to solve the Schrodinger equation by providing an initial guess for Ψ and then applying $\hat{H}$ onto Ψ, until a Ψ which has the lowest E is obtained. The $\hat{H}$ contains all the components of energy and is described by Equation 2.8. $\hbar$ is the Planck's constant divided by 2π, m_e is the mass of the electron, m_A is the mass of the nuclei, ∇_i^2 is the laplacian for the electrons, ∇_A^2, is the laplacian for the nuclei, e is the charge of the electron, Z is the charge of the nuclei. r_{iA}, r_{ij}, r_{AB} are the distances between the electron and nuclei, the two electrons and the two nuclei respectively.[179]

$$\hat{H} = -\sum_{i}^{electrons} \frac{\hbar^2}{2m_e}\nabla_i^2 - \sum_{A}^{nuclei} \frac{\hbar^2}{2m_A}\nabla_A^2 - \sum_{i}^{electrons}\sum_{A}^{nuclei} \frac{e^2 Z_A}{r_{iA}} + \sum_{i>j}^{electrons} \frac{e^2}{r_{ij}} + \sum_{A>B}^{nuclei} \frac{e^2 Z_A Z_B}{r_{AB}} \quad (2.8)$$

electron kinetic energy | nucleus kinetic energy | electron-nucleus attraction | electron-electron repulsion | nucleus-nucleus repulsion

The $\hat{H}$ can be simplified by employing the Born-Oppenheimer approximation. The mass of the electron (9.109×10^{-31} kg) is much smaller than that of a nuclei containing protons (1.673×10^{-27} kg) and neutrons (1.675×10^{-27} kg). Therefore the motion of the nuclei can be considered to be zero with respect to the motion of the electrons. The Schrodinger equation can then be split into an electronic Schrodinger equation and a nuclear potential equation. The electronic Schrodinger equation solves Ψ and E for a given set of stationary nuclei co-ordinates by setting the kinetic energy of the nuclei to zero, by employing the Born-Oppenheimer approximation. The nucleus-nucleus interaction energy is calculated separately in a second equation based on the stationary nuclei co-ordinates and charge of the nuclei (term five). The electronic energy methods aim to solve the electronic Schrodinger equation by calculating terms one, three and four in Equation 2.8. Once this energy is calculated, the nucleus-nucleus interaction energy is added to it to obtain the electronic energy of the system. The electronic energy can be calculated for a series of different nuclei co-ordinates. Plotting the electronic energy versus nuclei co-ordinates provides the potential energy surface (PES). [176, 179]

Density functional theory solves the Schrodinger equation by using the electron density (ρ) of the system. This can be done as the electronic energy can be determined based on the electron density as proven by Hohenberg and Kohn. This theorem states that i) the integral of the electron density determines the number of electrons, ii) the cusp in electron density defines the locations of the nuclei and iii) the height of the cusp gives the charge of the nuclei. This is illustrated in Figure 2.7. As a result, the electron density provides us with the number of nuclei and electrons, the locations of

the nuclei and electrons (based on probability distribution), and the charge of the nuclei, all the unknown information needed to calculate the energy of the system. This is given by the energy functional E[ρ], which is a function of ρ which is in turn a function of space and time. However, we can assume the functional is time independent as we are not looking at electron excitation where the energies of the electrons change with time.[176]

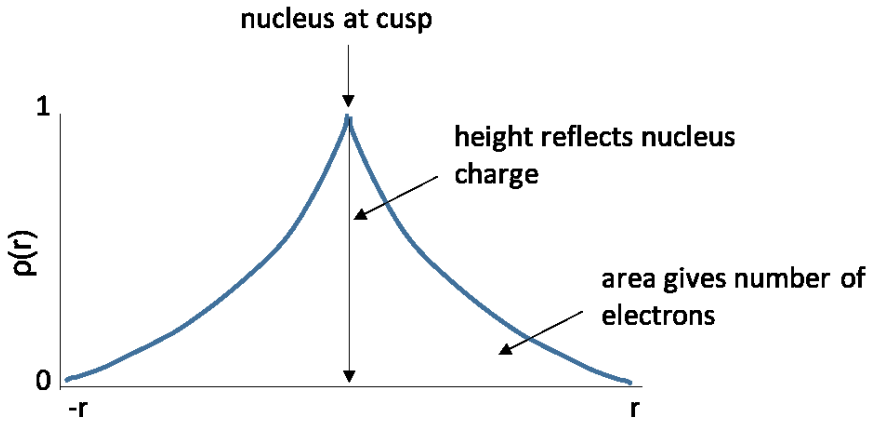

Figure 2.7. Key information obtained from the electron density (ρ(r)) for a given co-ordinate (r) using a slater type orbital.

2.5.2. Converting the electronic energy to the Gibbs free energy

Once the electronic energy (E) of the system has been calculated, a number of corrections need to be employed to convert E to G. The first correction is to add the zero point energy (ZPE) which takes into account that molecules can vibrate at 0 K. The second correction (E_{TOT}) takes into account the thermal effects on the translational (E_t), rotational (E_r), vibrational (E_v) and electronic (E_e) motion of the molecule and includes the ZPE (Equation 2.9).

$$E_{TOT} = ZPE + E_t + E_r + E_v + E_e \quad (2.9)$$

The enthalpy correction (H_{corr}) converts E_{TOT} to enthalpy (H) by adding k_BT. This is presented in Equation 2.10 where k_B and T are the Boltzman constant and temperature (K) respectively.

$$H_{corr} = E_{TOT} + k_B T \quad (2.10)$$

Finally the Gibbs energy correction (G_{corr}) adds TS_{TOT} to H_{corr}. S_{TOT} is the total entropy of the system, made up of translational, vibrational, rotational and electronic components (Equation 2.11).

$$G_{corr} = H_{corr} - TS_{TOT} \quad (2.11)$$

The Gibbs energy of a molecule can then be calculated by adding G_{corr} to E (Equation 2.12). [177]

$$G = E + G_{corr} \quad (2.12)$$

These calculations use the harmonic oscillator and rigid rotor approximations.[177] Energy contributions due to vibrational motion are calculated using the harmonic oscillator approximation. This assumes that the energy increases proportionally with increasing deviation from the equilibrium bond distance of two atoms.[180] Energy contributions due to rotational motion are taken into account by the rigid rotor approximation. This assumes that the bond length between two atoms is fixed during rotation.[181] These approximations do not take into account anharmonic contributions which lead to changes in bond distances during rotation, and deviations from proportionality at large and small atom separation distances. For example, the rotation across a bond can have an energy barrier which needs to be overcome and the rotation becomes hindered. At low vibrational frequencies hindered rotations causes the harmonic oscillator to break down and therefore hindered rotation corrections need to be included.[182] However, taking into account hindered rotation caused no difference in Gibbs energy compared to when hindered rotors were not taken into account for.

The numerical integration grid size used during the DFT calculations can also effect the entropic energies of low vibrational frequencies which are independent of the harmonic oscillator. Typical

grid sizes used in DFT calculations use 75 radial shells with 302 angular points per shell, however this leads to errors of up to 21 kJ/mol in Gibbs free energies. Using an integration grid of 99 radial shells, with 590 angular points per shell reduces this error to ≤ 4 kJ/mol and this integration grid is used in this thesis.[183]

The entropy contribution caused by a vibrational frequency increases exponentially as the frequency decreases often because of computational artefacts. The entropy contribution increases from approximately 0.3 kcal/mol at 150 cm^{-1} to approximately 2.7 kcal/mol at 0 cm^{-1} when the temperature is 298.15 K.[184] The entropy contribution also increases as temperature increases.[184] Therefore small variations in the frequency near 0 cm^{-1} can cause significant changes in the vibrational entropy. To account for this entropy contributions from vibrational frequencies ≤150 cm^{-1} can be deleted from the total entropy term.[184] Alternatively entropy contribution due to a frequency mode below a set value (e.g. 100 cm^{-1}) can be replaced by the entropy contribution at that set value (100 cm^{-1}). [184, 185]

2.5.3. The energy functional and density functional approximations

The energy functional, E[ρ], can be split into several functionals (Equation 2.13) where $T_s[\rho]$ represents the kinetic energy of non-interacting electrons, $E_{ne}[\rho]$ represents the electron-nuclei attraction energy, J[ρ] represents the electron-electron coulomb interaction energy, and $E_{xc}[\rho]$ represents the exchange-correlation energy. [176, 186]

$$E[\rho] = T_S[\rho] + E_{ne}[\rho] + J[\rho] + E_{xc}[\rho] \quad (2.13)$$

The $E_{ne}[\rho]$ term can be solved exactly however the electron kinetic energy and the electron-electron repulsion energy cannot be. The Kohn and Shams theorem is employed so that the kinetic energy of the electrons can be calculated. This theorem splits the electron kinetic energy into two

components. The first term calculates the electron kinetic energy assuming the electrons do not interact with each other, $T_s[\rho]$. This term can be calculated exactly and accounts for the majority of the energy term. The second term is a correction to take into account that the electrons will interact with each other, called the kinetic correlation energy. Likewise, most of the electron-electron interaction energy is due to the classical Coulomb energy, J[ρ], which can be calculated exactly. Two correction terms need to be included to take into account quantum mechanical effects for the electron-electron interaction energy. The first takes into account that two electrons cannot be in the same place (exchange energy). The second term takes into account that two electrons in the same orbital will move around to avoid each other, minimising Coulomb repulsion (correlation energy).[176, 186] The corrections for the electron kinetic energy and electron-electron interaction energy is given by the exchange-correlation energy $E_{xc}[\rho]$, as shown in Equation 2.14 where $\mathrm{T}[\rho]$ is the total kinetic energy, $\mathrm{T_S}[\rho]$ is the kinetic energy of non-interacting electrons $\mathrm{E_{ee}}[\rho]$ is the total electron-electron interaction energy and $\mathrm{J}[\rho]$ is the classical Coulomb interaction energy.

$$\mathrm{E_{xc}}[\rho] = (\mathrm{T}[\rho] - \mathrm{T_S}[\rho]) + (\mathrm{E_{ee}}[\rho] - \mathrm{J}[\rho]) \qquad (2.14)$$

There are wide variety of different density functional approximations (DFA) which can be used in the DFT calculations, all of which will calculate $T_s[\rho]$, $E_{ne}[\rho]$ and J[ρ] using the same equations but use different equations for $E_{xc}[\rho]$. Although there are a huge variety of different DFAs, they can be grouped into five classes, illustrated by Jacobs ladder (Figure 2.8). DFAs on higher rungs of the ladder increase the accuracy of $E_{xc}[\rho]$ and increase in computational cost.[178]

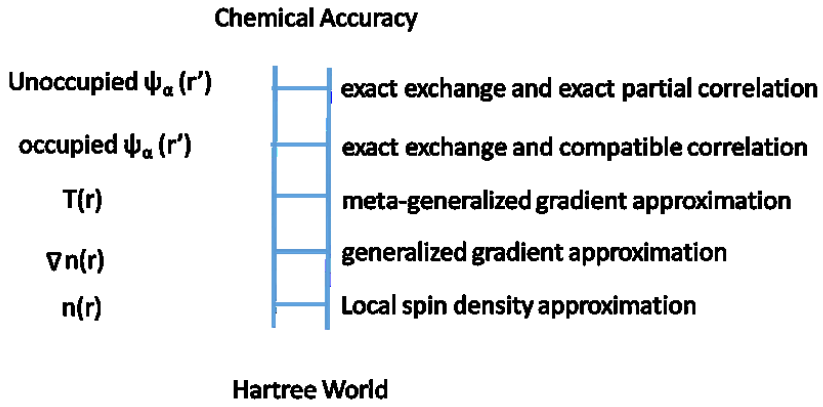

Figure 2.8. Jacob's Ladder redrawn from Perdew and Schmidt.[178] DFAs on higher rungs calculate the exchange correlation energy by using more complex equations, increasing the chemical accuracy of the calculations but leading to greater computational cost.

The least computationally demanding and least accurate class of DFAs employ the local spin density approximation (LDA) method. The LDA method assumes that the electron density can be treated locally as a uniform electron gas. The next class of DFAs employ the Generalised Gradient Approximation (GGA) method (e.g. PW91) which begins to represent a non-uniform electron gas by including the first derivative of the electron density as a variable. The meta-GGA method (e.g. TPSSTPSS) allows the exchange and correlation DFAs to depend on higher order derivatives, such as the second order laplacian ($\nabla^2\rho$) or by including the orbital kinetic energy density (τ). Density functional approximations using the hybrid method combine exact exchange energy using the Hartree Fock method (e.g. B3) with a GGA functional for calculating the correlation energy (e.g. LYP), i.e. B3LYP. The exact exchange energy is a nonlocal functional of the Kohn-Sham orbitals. For the correlation DFA to be compatible with the exact exchange energy it must also be a nonlocal functional of the occupied Kohn-Sham orbitals.[178] The final level on the Jacobs ladder is a hybrid functional where the correlation energy DFA also includes unoccupied Kohn-Sham orbitals.[178] This should improve van der Waal interactions.[176]

Zhao and Truhlar[187] benchmarked 30 DFAs using the def2-QVZP[188, 189] basis set. This included the TPSS,[190] B3LYP[191] and M06[192] DFAs. The mean unsigned error of the TPSS, B3LYP and M06 DFAs were

10-51 kJ/mol, 32-64 kJ/mol and 15-31 kJ/mol respectively. The reaction enthalpy's calculated using one LDA, four GGA including PW91,[193] two meta-GGA including TPSS[190] and six hybrid functionals including B3LYP[191] were benchmarked against experimental data of five gas phase reactions containing U^{VI}, $[UF_6]$, $[UO_3]$, $[UO_2F_2]$ and $[UO_2(OH)_2]$.[194] The Stuttgart MWB60[195] ECP was used for uranium and a Toulouse pseudopotential combined with a polarised double zeta basis set for ligand atoms.[196] The mean error decreased in the order LDA (90 kJ/mol), meta-GGA (76-78 kJ/mol), GGA (60-70 kJ/mol) and hybrid functional (25-45 kJ/mol). The experimental error was typically 15-30 kJ/mol, suggesting the hybrid functionals were close to the experimental error. The effect of the DFA on the molecular geometries of $[UO_2]^{2+}$ and $[UF_6]$ was explored for one LDA, three GGA and three hybrid GGA functionals[197] while using the MWB60 ECP[195, 198] and the aug-cc-PVDZ and aug-cc-PVTZ for oxygen and fluorine.[199, 200] The bond lengths for $[UO_2]^{2+}$ was compared to the Dirac-Hartree-Fock coupled-cluster singles, doubles, and perturbative triples (DHF-CCSD(T)) data due to the lack of experimental data and the results for all DFT functionals employed was observed to be within 1% of the DHF-CCSD(T) data. The DFT calculated bond lengths were also observed to be within 1% of the experimental data for UF_6 for all tested DFAs. This has also been observed in a later study using a GGA and Hybrid DFA for UO_2^{2+} and UF_6.[201]

The DFA tested during the thesis is the GGA functional PW91,[193] the meta-GGA functional TPSS,[190] and the hybrid functionals B3LYP[191] and M06.[192] Dispersion corrections can improve reaction energetics, for example benchmarking of the dispersion corrected D-B3LYP DFA provided MUE of 32-41 kJ/mol compared to MUE of 32-64 kJ/mol for B3LYP.[187] However, the M06 DFA is parameterised to include medium-range dispersion effects.[192] This DFA provides similar mean errors in reaction energetics to long-range dispersion corrected DFAs (<5 kJ/mol) [202] and can a provide more accurate energies (MUE = 15-31 kJ/mol) than the dispersion corrected hybrid functional D-B3LYP (MUE 32-41 kJ/mol).[187] Therefore the M06 DFA was tested rather than a separate dispersion correction add-on.

2.5.4. Basis Sets

A basis set is composed of functions which describe the density of an electron for a series of x, y, z co-ordinates, and represent the atomic orbitals. A linear combination of atomic orbitals (LCAO) can be used to characterise the Kohn-Sham molecular orbitals employed in DFT. To exactly describe a molecular orbital, the electron distributions need to be characterised infinitely in all directions, which requires an infinite number of basis functions. Inevitably a finite number of basis functions will be used in a basis set. The computational cost typically increases by a minimum of $1x10^4$ per basis function.[176] The basis function type used in this thesis are Gaussian type orbitals (GTO). These model the electron density as a Gaussian curve.

Basis sets can contain different numbers of basis functions. A minimum basis set (Z) uses the minimum number of basis functions required to represent the molecular orbitals (*s*, *p*, *d*, *f*, and *g*) for the system. Double (DZ), triple (TZ) and quadruple zeta (QZ) basis sets contain two, three and four times the number of basis functions required for the number of electrons in the system. This allows the basis set to use multiple exponential decay values for the change in electron distribution with distance from the nucleus. This means the basis set can model different electron distributions for different bond types in a molecule. For example the carbon atom in a molecule such as H-C=N will have a different electron distribution in the H-C bond than the C=N bond.[176] Basis sets that use the minimum number of basis functions to represent the core electrons and double, triple or quadruple the number of basis functions to represent the valence electrons are called split valence basis sets.[176]

Extra basis functions with higher angular momentum quantum numbers can be added to change the shape of a molecular orbital described by other basis functions. These can be added to reflect that the shape of an orbital can change when it interacts with another orbital during chemical bonding. For example, hydrogen will only contain an *s* orbital, however a *p* function can be added to the basis

set. The effect of adding a *p* function is highlighted in Figure 2.9. The wavefunction describing an electron orbital has a positive and negative phase. The regions of positive phase (red) which overlap between the *s* function and *p* function presented in Figure 2.9 reinforce each other leading to expansion of the orbital. Regions of negative phase (blue) of the *p* orbital cancel out with the positive regions in the *s* function leading to a contraction of the orbital towards the nucleus.[176] Diffuse functions can also be added to basis sets. These are *s* and *p* type functions with a small exponent which allow the molecular orbital to cover a much greater region of space. This is important when electrons are far away from the nucleus, such as anions.[176, 179]

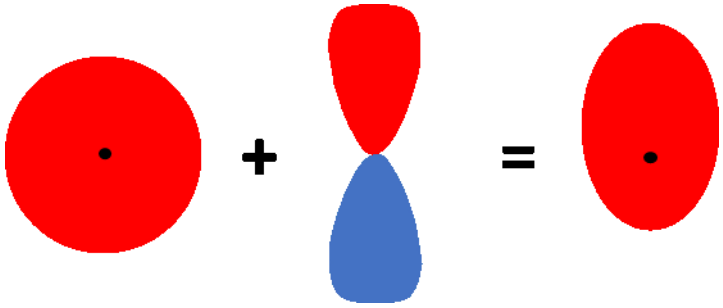

Figure 2.9. Distortion of the electron distribution of an *s* orbital by addition of a *p* orbital. Red represent positive phase of the wavefunction and blue represents the negative phase of the wavefunction. The positive phase of the *s* and *p* orbitals are constructive leading to an extension of the orbital, while the negative lobe of the *p* orbital cancels out the positive phase of the *s* orbital, leading to a contraction of the *s* orbital.

A number of basis functions can be linearly combined and be bracketed with one variational coefficient. This reduces computational cost compared to basis sets which treat each basis function separately with their own variational coefficient. Basis sets composed of these linear combination of basis functions are called contracted basis sets. The basis functions which are contained within the linear combination are called primitive basis functions, and one linear combination of primitive basis functions represents one basis function. This improves the computational cost of the basis set. [176]

Pople's 6-31g(d,p) basis set is a split valence basis set tested in chapter 5.[203, 204] Six primitive basis functions are used to represent the basis function for the core electrons. The two numbers after the dash indicate the valence electrons are treated as a double zeta basis set. One basis function is

comprised of three primitive basis functions while the second basis function set is composed of one primitive basis function. The (d,p) indicates that six uncontracted *d* polarisation functions have been added to heavy elements and three uncontracted *p* polarisation functions have been added to hydrogen.

The second type of basis set tested in chapter 5 is Dunning's aug-cc-pVnZ basis sets.[199, 200, 205] The aug means the basis set has been augmented with diffuse functions, the cc-p stands for correlation consistent polarised, while VnZ indicates a valence only basis set where nZ is double (D), triple (T) or quadruple (Q). The primitive basis functions and their contracted form is provided in Table 2.6. The contracted basis sets in Table 2.6 includes the polarisation functions. For hydrogen the polarisation functions are (1*p*), (2*p*, 1*d*) and (3*p*, 2*d*, 1*f*) for the cc-pVDZ, cc-pVTZ and cc-pVQZ basis sets respectively. For the first row elements the polarisation functions are (1*d*), (2*d*, 1*f*) and (3*d*, 2*f*, 1*g*) for the cc-pVDZ, cc-pVTZ and cc-pVQZ basis sets respectively.[200] An extra function is added to the basis sets for each orbital. For example the aug-cc-pVDZ contracted basis set becomes 4*s*3*p*2*d*.[199] These basis sets are called correlation consistent (cc) basis sets because they are designed to return significant quantities of the correlation energy. The aug-cc-pVDZ, aug-cc-pVTZ and aug-cc-pVQZ recover approximately 91%, 95% and 98% of the correlation energy for first row elements respectively.[199] They are also designed to systematically improve as the basis set increases in size. If a structure is optimised with enough different cc-pVnZ basis sets, the resulting electronic energy can be extrapolated to the complete basis set limit (i.e. infinite basis set) which is useful if high precision is required.[206]

Table 2.6. The primitive and contracted basis functions used in Dunning's correlation consistent-polarised (cc-pVnZ) basis sets. The contracted basis set includes the polarisation functions.

Basis set	Hydrogen		First row elements (C, N, O)	
	Primitive	Contracted	Primitive	Contracted
cc-pVDZ	4*s*	2*s*1*p*	9*s*4*p*	3*s*2*p*1*d*
cc-pVTZ	5*s*	3*s*2*p*1*d*	10*s*5*p*	4*s*3*p*2*d*1*f*
cc-pVQZ	6*s*	4*s*3*p*2*d*1*f*	12*s*6*p*	5*s*4*p*3*d*2*f*1*g*

2.5.5. Effective Core Potential

For heavy elements, such as uranium, relativistic effects are important. There are two relativistic effects, scalar relativistic and spin-orbit coupling effects. Scalar relativistic effects are due to the relativistic change in mass of the electron. The velocity of electrons in the *s* and *p* orbitals will be increased due to the highly charged uranium nucleus. This causes the electron mass to increase reducing the effective Bohr radius, leading to contracted *s* and *p* electron orbitals.[176, 207, 208] The contracted s and p orbitals increase the shielding of electrons in the *d* and *f* orbitals which are not close to the nucleus, leading to expansion of *d* and *f* electron orbitals, and increased energy of the electrons within these orbitals.[176, 208]

The second relativistic effect is spin-orbit coupling. The spin-orbit coupling is the interaction of the electron spin magnetic moment and the external magnetic field created by other charged particles in the system. It leads to the splitting of *p*, *d* and *f* orbitals of uranium into two separate shells with different shapes and orbital energies.[209] Inclusion of spin orbit effects impacts bond distances by 0.001-0.002 Å and frequencies by 1-3 cm^{-1}, when compared to scalar relativistic approaches, which is within the error of the contracted basis set employed for the calculations (0.002 Å, 1-2 cm^{-1}).[210] This indicate spin-orbit effects play a minor effect on the structure of the U^{VI} complexes.[210] Hydration reactions for U^{III}, U^{IV}, U^{V} and U^{VI} find spin-orbit effects contribute between 2-9 kJ/mol to the total reaction energy. This contribution is approximately 3 kJ/mol for the hydration of bare UO_2^{2+} with five water molecules and is within chemical accuracy (4 kJ/mol).[211] This indicates that if the number of uranium atoms remain consistent across a reaction the spin-orbit effects cancel out.[211]

Relativistic effects can be taken into account using all electron calculations employing the Dirac-Hartree-Fock (DHF) equation.[212] The relativistic wavefunction corresponding to application of the DHF Hamiltonian is four component, where two components are large for electronic states (called large components) and two components are large for positronic states (called small components).[213]

The DHF Hamiltonian can be expanded to include the Dirac-Coulomb correction (DC) which takes into account the nonrelativistic coulombic interaction between two electrons.[213, 214] The DC can be augmented with the Breit correction (DC + B) which takes into account magnetic interactions between two electrons, and the retardation of the magnetic interaction due to the finite velocity of light.[213] The root mean square deviation (rmsd) between DC and DC + B is 0.109 eV (11 kJ/mol) highlighting the importance of including the Breit correction.[215] The DHF Hamiltonian can be simplified by removing the small components as they only have a small effect on the electronic states (ca. 1% of the total charge), leading to the quasi-relativistic two-component Wood-Boring Hamiltonian.[213, 216]

To save on computational cost and take into account relativistic effects, the core electrons are modelled with an effective core potential (ECP). This potential includes the non-relativistic atomic orbital energies of the electrons plus relativistic energy corrections.[176] The relativistic effects are included implicitly within the ECP by parameterising and calibrating the ECP along with the corresponding basis set against a dataset which were calculated using an all-electron (AE) relativistic method for all oxidation states of uranium.[195, 213, 215]

In chapter 5 the MWB60[195, 198] and MDF60[215] ECP's are tested for uranium. The MDF60 ECP is calibrated against reference data that has been obtained using the multiconfiguration (MC) Dirac-Hartree-Fock/ Dirac-Coulomb-Breit (DHF/DC+B) Hamiltonian.[217] The MWB60 ECP is calibrated against reference data that has been obtained using the quasi-relativistic Wood-Boring (WB) Hamiltonian.[216] In both ECPs the inner 60 electrons are included within the ECP, while the remaining 32 electrons are treated explicitly with basis functions that has been optimised for use with the ECP. Therefore 26 core electrons have been described explicitly using basis functions on top of the 6 valence electrons. This is because the spatial extent of the ECP overlaps with the valence electrons which are described by the basis functions. Explicitly describing electrons with quantum number ≥5

prevents this spatial overlap reducing the error to < 0.01 eV (1 kJ/mol) compared to the all-electron reference data.[215] The basis functions used to describe the remaining U^{VI} electrons for MWB60 and MDF60 is provided in Table 2.7. This also includes the correlation consistent-polarised basis set which can replace the standard MDF60 basis set. This includes the 1*d*, 1*f* and 1*g* polarisation functions for 6*p*6*s*, 6*d* and 5*f* electrons respectively.

Table 2.7. The primitive and contracted basis functions used for valence electrons when using the MWB60, MDF60 and cc-pVDZ-PP basis sets. The polarisation functions of cc-PVDZ-PP are included within both the primitive and contracted notation.

Basis set	Primitive	contracted
MWB60	14*s*13*p*10*d*8*f*6*g*	10*s*9*p*5*d*4*f*3*g*
MDF60	14*s*13*p*10*d*8*f*6*g*	6*s*6*p*5*d*4*f*3*g*
cc-pVDZ-PP	14*s*13*p*9*d*8*f*1*g*	5*s*5*p*4*d*3*f*1*g*

2.5.6. Solvation Methods

The effects of solvation need to be considered when calculating the thermodynamic properties of chemical reactions in aqueous systems. These are a mixture of long range and short range interactions. Long range interactions are non-specific (they will always occur) and include polarisation and changes in dipole orientation due to changes in electrodensity in individual water molecules. Short range interactions are specific to the solute being explored, and include hydrogen bonding, van der Waals interaction, solvent-shell structure (i.e. number and geometry of water molecules bound to the metal), solvent-solute dynamics, charge transfer effects and hydrophobic effects.[176]

Solvation effects can be included into DFT calculations using three different methods. The first method is to use a continuum solvation model which considers the solvent as a uniform polarizable continuum with a dielectric constant, ε (ca. 80 for water). In this system the solute is placed in a cavity which is then placed into the continuum solvation model. The partial charges of the different

atoms in the solute decay outwards until it reaches the interface of the cavity where the remainder of the charge polarises the continuum. The continuum then polarises the solute, and the process repeats until the charge (a vector) is balanced in magnitude and direction. The apparent surface charge (ASC) is given by a series of point charges spread across the surface of the cavity. This is a self-consistent reaction field (SCRF) method and models that employ this method are called polarisable continuum models (PCM). [176, 179] The energy of solvation which is calculated by the model will include several components (Equation 2.15): An increase in energy due to adding a cavity into the solvent (ΔG_{cavity}); decrease in energy due to stabilisation through van der Waals forces ($\Delta G_{dispersion}$); decrease in energy due to electrostatic interactions between the solute and the bulk solvent ($\Delta G_{electrostatic}$). This last term is the energy given by the polarisation of the solute and the continuum solvation model by each other, discussed above.[176]

$$\Delta G_{solvation} = \Delta G_{cavity} + \Delta G_{dispersion} + \Delta G_{electrostatic} \quad (2.15)$$

There are several different versions of the PCM which can be employed including the Dielectric model (DPCM),[218] the conductor-like polarisable model (CPCM),[219] the integral equation formulism model polarisable continuum model (IEFPCM),[220] the universal solvation model (SMD)[221] and the self-consistent isodensity polarisable continuum model (SCIPCM).[222]

The DPCM is the original PCM described above. The CPCM model adjusts ε from a finite value to ε = ∞ corresponding to that of a conductor.[219] The values of the point charges on the cavity surface are selected so that the potential of the solute and solvent on the cavity surface cancels out.[218] The IEF model redefines the electrostatic potential as a series of integral equations. This also leads to the potential of the solute and solvent on the cavity surface to cancel out. Both the CPCM and IEFPCM models reduce issues associated with charge leaking from the cavity vacuum into the solvent.[220] In these three solvation models the cavity is built of interlocking spheres. The size of these spheres can be assigned based on the van der Waal radii generated through the universal force field method

(UFF),[223] or Pauling[224] and Bondi[225] method. The size of the spheres can also be defined using the United Atom Topological Model (UATM). These include the UAHF[226] and UAKS[222] where the UATM applied on the radii are optimised for the HF/6-31G(d) and PBE1PBE/6-31G(d) level of theory respectively. It also includes the UA0[223] method where the model is optimised based on radii generated for heavy elements using the UFF method. In all three UATM methods the hydrogen atoms are enclosed within the spheres of the heavy element they are bound to. The SCIPCM model generates it cavity based on a contour of constant isodensity which is defined by the user.

The implicit solvation model is good at representing the electrostatic energy but poorly represent short-range solute-solvent interactions included in the cavitation and dispersion energy contributions. [176] The $\Delta G_{solvation}$ for neutral molecules tend to be close to the experimental data when only using PCM models but errors increase significantly for ions due to stronger short-range solute-solvent interactions.[227] Attempts have been made to improve the description of non-electrostatic energies. For example the SMD model is a version of the IEFPCM model which has been parameterised and optimised against experimental data to better incorporate non-electrostatic effects.[221] The second option is to model the water molecules explicitly. This will provide a better representation of the short-range interactions, however it may require hundreds of water molecules to fully account for solvation effects which is computationally demanding.[176]

The third option is to use a mixed solvation approach where a few water molecules are modelled explicitly in the vicinity of the solute in combination with the implicit solvation model for the bulk solvent. Typically, the number of water molecules added explicitly to charged metal centres are the number required to saturate the co-ordination bonds of the metal as these aqua ligands have the strongest interaction with the metal centre.[113, 228-230] For U^{VI}, the five uranyl bound aqua ligands tend to be modelled explicitly when calculating $\Delta_r G$.[125] Fewer water molecules are explicitly added to anions. For example Kelly *et al*. [231] found that adding one water molecule per donor O atom to the

conjugate bases of acids generally increased the accuracy of the calculated pK_a values versus experimental data while using the SM6 implicit solvation model. Pliego and Riveros[232] observed that adding two or three explicit water molecules in combination with the PCM and SM5.42R solvation models reduced the root mean square deviation from 7 pk_a units to 2.2 pK_a units compared to when just using the implicit solvation models. It has also been found that modelling explicit water molecules not bound directly to U^{VI} is required for increased accuracy in the structure geometries, highlighting the effect the highly charged U atom has on the surrounding solvent shells.[38, 211, 233] For example, Gutowksi and Dixon[38] found that adding one water molecule per hydrogen atom of the uranyl bound aqua ligand, $[H_2O(H_2O)_2]$, improved the structure geometries of $[UO_2]^{2+}$, and reduced the reliance on the implicit solvation model to calculate accurate Δ_rG for water exchange reactions with uranyl. This approach has been applied to exploring Δ_rG for lanthanides such a Ce^{III}.[234]

The volume of the solute cavity plays an important role for calculating $\Delta G_{solvation}$. The larger the volume of the cavity, the greater the solute charge dissipates before reaching the cavity surface, reducing the solvation energy correction which is calculated by the model.[38] When only the U^{VI} bound aqua ligands are explicitly modelled (i.e. $[UO_2(H_2O)_5]^{2+}$) smaller cavity volumes which generate larger solvation corrections such as UAKS and UAHF produced more accurate solvation energies than those with larger cavity volumes generated by the UFF method,[211] and this was also observed for transition metals such as Hg^{II}.[228] This however was not observed with lanthanides such as Ce^{III} where the greater solvation energy corrections obtained from smaller cavity volumes shifted the solvation reactions from the experimentally determined exergenic reaction to an endergenic reaction.[234]

Adding explicit water molecules hydrogen-bonded to the uranyl bound-aqua ligands also changes the most accurate cavity type for the IEFPCM implicit solvation model. Large solvation cavities were found to produce the most accurate solvation energies, because adding the extra explicit water

molecules reduces the solvation energy correction required to reach experimental values.[211, 234] The UFF solvation cavity was found to be the most accurate cavity type for all oxidation states of U and for Ce^{III} when modelling the second hydration sphere.[211, 234] Surface area of the cavity also plays an important role as it defines the amount of point charges used by the model. In general cavities with large surface areas were observed to have large under and overestimations of the solvation energies of uranium solvation reactions. This error reduced as the cavity surface area decreased.[211]

In chapter 5 the UFF cavity is used for the IEFPCM model to build upon previous research developing practical DFT protocols for predicting stability constants of U^{VI}-L complexes,[125] and because it provides the most accurate solvation energies when explicit water molecules are hydrogen-bonded to the uranyl aqua ligands.[211, 234] The SMD model is also used because this is currently the recommended method for calculating solvation energies,[179] and the practical DFT protocol by Vukovic *et al*.[125] has been adapted recently to use this solvation model for U^{VI}-L log β calculations.[235, 236] The radii used to generate the spheres were 1.860, 1.520 and 1.200 Å for the U, O and H atom for the SMD model. The radii for U, O and H atoms are 1.698, 1.750 and 1.443 Å leading to a cavity surface area 234.618 $Å^2$ of and cavity volume of 217.618 $Å^3$ for the IEFPCM-UFF model.

A reaction is isodesmic when the type and number of bonds which are broken during a chemical reaction are the same as the type and number of bonds which forms during the chemical reaction. If the reaction is non-isodesmic, extra bonds are being formed or broken which do not participate directly in the ligand exchange reaction, and this can affect $\Delta_r G$.[237] When an organic ligand such as acetate complexes with U^{VI}, two water molecules which are directly bound to the U^{VI} metal centre are replaced by the ligand. When only the five water molecules directly complexed to U^{VI} are modelled explicitly ($[UO_2(H_2O)_5]^{2+}$), two water molecules are released as monomers on the product side of the chemical reaction and the reaction remains isodesmic. However, when extra water molecules are added to the second hydration sphere (e.g. $[UO_2(H_2O)_5(H_2O)_{10}]^{2+}$), hydrogen bonds

between the water molecules may not necessarily break when the acetate ligand complexes with U^{VI}. Instead the water molecules may be released as a cluster with the number of hydrogen bonds occurring between the water molecules being preserved.

Water clusters were tested in chapter 5 of my thesis to explore the effect of isodesmicity on $\Delta_r G$ for the formation of 1:1, 1:2 and 1:3 U^{VI}-acetate complexes when U^{VI} was modelled as $[UO_2(H_2O)_5(H_2O)_{10}]^{2+}$.[38] During the stepwise 1:1 and 1:2 reactions, six water molecules are released per acetate molecule. During the formation of the 1:3 complex, only three water molecules are released. There are a large number of possible configurations for the hexamer water cluster with the most stable being called prism, book, cage, cyclic bag and boat.[238, 239] These structures are shown in Figure 2.10.

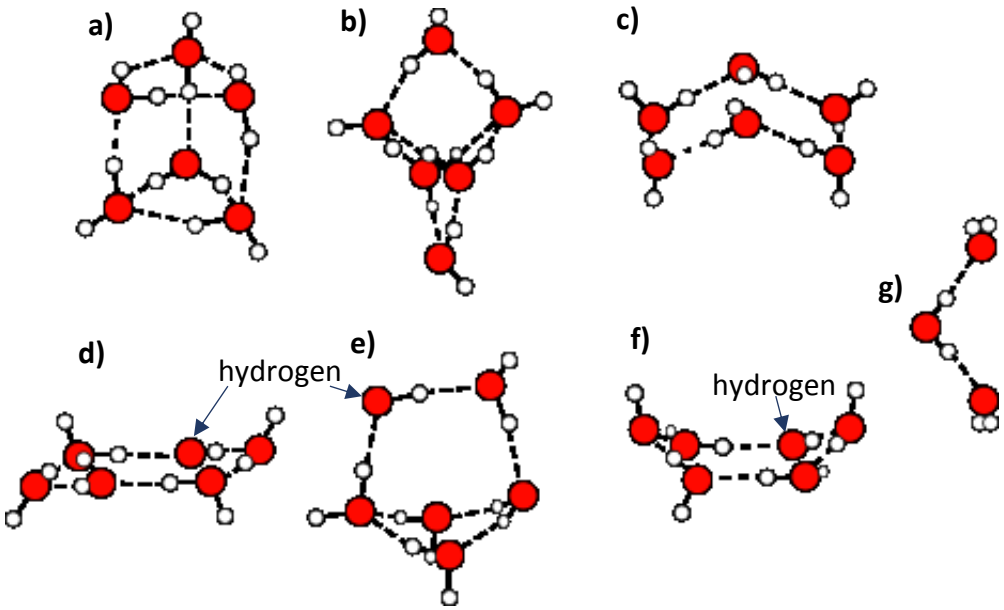

Figure 2.10. The six water clusters with configuration prism, cage, book, cyclic, bag and boat are shown in parts a-f respectively. The cyclic 6 water cluster presented in part d) was used in chapter 5. The trimer water cluster used in chapter 5 is shown in part g). The $(H_2O)_6$ structures are redrawn from Bates *et al*.[239]

CCSD(T) calculations at complete basis set limit indicate the structures decrease in stability in the order prism > cage > book > cyclic > bag > boat with the relative electronic energy between the prism and boat structures being 5 -18 kJ.mol.[239-241] Although the cyclic and boat structures are not

the most stable configuration, they were the only structures with the same number of hydrogen bonds as the cluster of six water molecules which are displaced by the acetate ligand during the formation of the 1:1 and 1:2 U^{VI}-acetate complexes. Therefore the cyclic structure was tested in chapter 5 as this is more stable than the boat structure. A water trimer was used for the 1:3 U^{VI}-acetate complex (Figure 2.10g).

2.5.7. Corrections to the calculated Gibbs energy

There are several corrections to the calculated $\Delta_r G$ that need to be conducted depending on the method employed to optimise the geometries of the complexes. There are two common methods which can be employed. Method 1 geometrically optimises the structure in the gas phase and then uses this geometry to calculate the solvation energy by conducting a single point energy and frequency calculation on the structure while using an implicit solvation model. Method 2 optimises the structure directly with the implicit solvation model. The corrections are presented in Table 2.8.

Table 2.8. Standard state and translational entropy corrections employed during the calculations. The standard state correction is applied to all reactant and product species. The entropy correction is applied to the single water molecule (H_2O) and water clusters (($H_2O)_3$ and ($H_2O)_6$). The entropy correction needs to be applied for each individual water molecule and cluster on the reactant and product side of the reaction.

Correction type	Energy correction (kJ/mol)		
	H_2O	$(H_2O)_3$	$(H_2O)_6$
Method 1 – energy optimisation in gas phase			
Standard state (all reactants and products)		+7.91	
Translational entropy (per water molecule/cluster)	+9.96	+3.32	+1.66
Method 2 – energy optimisation in implicit solvation model			
Standard state (all reactants and products)		0	
Translational entropy (per water molecule/cluster)	+17.87	+5.96	+2.98

If the geometries are optimised in the gas phase (method 1) then a standard state correction needs to be employed. Implicit solvation models such as the universal solvation model (SMD)[221] calculate the solvation energy at 1 M solvent concentration, however the gas phase electronic energy is calculated at 1 atm which corresponds to 24.46 L/mol (0.041 M). Therefore the gas phase energies for reactant and product structure need to be corrected from 24.46 mol/L to 1 M by using the equation RTln(24.46) where R and T correspond to the gas constant and absolute temperature respectively. This correction is +7.91 kJ/mol (i.e. +1.89 kcal/mol) at T = 298.15 K.[179, 242] This correction needs to be employed for all reactant and product species.

A further correction needs to be employed for explicit water molecules in the reaction. The standard concentration of water is 55.34 M at 298.15 K.[242] However, as discussed above, the concentration of the bulk solvent is 1 M when the solvation correction is applied to gas-phase optimised structures. Therefore the concentration of water is significantly higher, reducing the translational entropy of the solute water molecule.[38] This can be corrected using -*m*RTln(PH_2O/P°) where *m* is the number of water molecules, PH_2O is the pressure of water at 55.5 M and P° is the standard state pressure.[243, 244] The pressure of 55.34 M and 1 M water calculated using the ideal gas law is 1354 atm and 24.47 atm respectively. The equation then becomes –*m*RTln(55.34) and leads to a correction of 9.96 kJ/mol (i.e. -2.38 kcal/mol) to Δ_rG per explicit water molecule on the reactant side of the equation. If the water molecules are released as a product then +9.96 kJ/mol per explicit water molecule is added to the Δ_rG. If water clusters are employed, the entropy correction changes from -*m*RTln(PH_2O/P°) to -*m*RTln(PH_2O/P°)/*n* where *n* is the number of water molecules in the cluster. The correction to Δ_rG then decreases from -9.96 kJ/mol per single explicit water molecule to -1.66 kJ/mol (i.e. -0.40 kcal/mol) per $(H_2O)_6$ cluster on the reactant side of the equation.[242]

If the structures are optimised directly in the implicit solvation model (method 2), the standard state correction is not applied,[221] however the entropy correction needs to be applied for each explicit

reactant and product water molecule. In Gaussian the Gibbs energies are reported at 1 atm and so the correction equation -*m*RTln(PH_2O/P°) becomes -*m*RTln(1354). This leads to a correction of -17.87 kJ/mol (i.e. -4.27 kcal/mol) to Δ_rG per explicit water molecule on the reactant side of the equation. If the water molecules are released as a product then +17.87 kJ/mol per explicit water molecule is added to the Δ_rG. The entropy correction for a water cluster shifts to -*m*RTln(PH2O/P˚)/*n* and the correction to Δ_rG becomes -2.98 kJ/mol (i.e. -0.71 kcal/mol) per $(H_2O)_6$ cluster on the reactant side of the equation, and +2.98 kJ/mol per $(H_2O)_6$ cluster on the product side of the reaction.

2.5.8. Ionic Strength Corrections to Experimental log β values

So far the stability constant has been calculated from the concentrations of the products and reactants. However, the relationship in Equation 2.5 only holds for infinitely dilute solutions which act in an ideal fashion. An ideal solution is one in which different aqueous species do not interact with each other, removing potential energy caused by interacting aqueous-species.[55] Experiments use various concentrations of a background electrolyte (e.g. $NaClO_4$). The concentrations used in the experimental data which is subsequently used to validate the DFT model are typically 0.1 and 1 M. The ions in solution can interact with each other and with the solvent leading to an interaction energy and subsequently a different effective concentration to the formal concentration which is calculated theoretically. The effective concentration is called the activity (α). The relationship between Δ_rG and log β_{110} is actually given by the log ratio of the activity of the products and reactants, not the concentration. If the activity can be corrected to the same value as the formal concentration (i.e. activity at infinite dilution), then the relationship between Δ_rG and log β_{110} holds. This is highlighted in Equation 2.16 where β_{110}, K, ML(Sol), M(sol), L, Δ_rG, R, T are the stability constant, equilibrium constant, metal-ligand complex, metal complex, ligand, Gibbs free energy of reaction, the gas constant and absolute temperature respectively. The subscript *m* represents the number of solvent molecules in the M(Sol) complex, and *n* represents the number of solvent

molecules released during the reaction The concentrations and activities of the species are denoted by [ ] and { } respectively.[55]

$$\log \beta_{110} = \log\ \mathrm{K} = \log \frac{[\mathrm{ML(Sol)_{m-n}}]}{[\mathrm{M(Sol)_m}][\mathrm{L}]} \approx \log \frac{\{\mathrm{ML(Sol)_{m-n}}\}}{\{\mathrm{M(Sol)_m L}\}} = (\log_{10} \mathrm{e}) \frac{-\Delta_r \mathrm{G}}{\mathrm{RT}} = \frac{-\Delta_r \mathrm{G}}{2.303\mathrm{RT}} \quad (2.16)$$

The relationship between activity and the formal concentration is provided in Equation 2.17 where c_A is the formal concentration and f is the activity coefficient. f goes to one as the concentration of all solutes decreases to zero.[245]

$$\alpha = \mathrm{f} * \mathrm{c_A} \quad (2.17)$$

The relationship to log β is then expanded in Equation 2.18 where f_{ml}, f_m and f_L represents the activity coefficient for the ML, M and L complexes respectively. The ° represents the log β value calculated by using the activity at zero ionic strength. The [ ] and { } represent the concentration and activity of the species respectively.[245]

$$\log \beta^\circ = \log \frac{\{\mathrm{ML}\}}{\{\mathrm{M}\}\{\mathrm{L}\}} = \log \frac{[\mathrm{ML}]}{[\mathrm{M}][\mathrm{L}]} + \log \frac{\mathrm{f_{ML}}}{\mathrm{f_M f_L}} \quad (2.18)$$

There are a variety of different equations used to calculate f including the Debye-Hückel, Extended Debye-Hückel, Güntelberg, Davies, SIT and Pitzer theory. They are only valid for certain ionic strength ranges.[55, 246] The Davies equation is derived empirically from experimental data collected at different ionic strengths and is based upon the Debye-Hückel equation. It calculates an activity coefficient at a given ionic strength which takes into account electrostatic interactions between the charged species in solution. The Davies equation is presented in Equation 2.19 where Z_M, Z_L and Z_{ML} is the charge of the metal, ligand and metal-ligand complex, I is the ionic strength and A and B are constants with values of 0.509 and -0.2 $kg^{1/2}.mol^{-1/2}$ at 25°C and 1 bar respectively.[55]

$$\log \frac{f_{ML}}{f_M f_L} = -A * (Z_{ML}^2 - (Z_M^2 + Z_L^2)(\frac{\sqrt{I}}{1+\sqrt{I}} + BI) \quad (2.19)$$

The Davies equation was employed to extrapolate the experimental log β to zero ionic strength (log β°) for experimental data collected at ionic strength between 0.1 - 0.5 M. This can be done by substituting Equation 2.19 for $\log \frac{f_{ML}}{f_M f_L}$ in Equation 2.18, resulting in Equation 2.20.[55, 245]

$$\log \beta^\circ = \log \beta_{110} - A * (Z_{ML}^2 - (Z_M^2 + Z_L^2)(\frac{\sqrt{I}}{1+\sqrt{I}} + BI) \quad (2.20)$$

In solutions with increasing ionic strengths, short-range, non-electrostatic interactions need to be taken into account when correcting to zero ionic strength.[246, 247] The size of the ions and their effects on the dielectric constant also need to be included.[248] The Davies equation does not have parameters which can account for these effects, limiting its usefulness to ≤0.1 M ionic strengths.[246] Therefore experimental log β collected in solutions with ionic strengths > 0.1 M were adjusted to zero ionic strength using the Specific Ion Theory (SIT).[246] The SIT theory includes the Debye-Hückel equation to take into account the electrostatic interaction through the electrostatic charge of the species (Z) for a set of given solution properties (ionic strength, dielectric constant and temperature). It uses the Debye length equation to take into account how close two hydrated ions can come to each other at a given ionic strength and therefore how strong electrostatic-interactions can be. It takes into account the short-range, non-electrostatic interactions through an ion-interaction coefficient (ε_j) which is experimentally derived from equilibrium constants collected at different ionic strengths. The SIT theory sets the ion-interaction coefficient is zero for like charged and neutral species by assuming that these species will tend to be far away from each other in solution limiting short-range effects, although this may not be the case for neutral species.[246]

The SIT equation for calculating the log of the activity coefficient is presented in Equation 2.21 where f, Z_M, Z_L and Z_{ML} D, $\Delta\varepsilon_j$ and I_m is the activity coefficient, charge of the metal, charge of the ligand, charge of the metal-ligand complex, Debye length, change in ion-interaction coefficients and ionic strength in molality respectively.[246]

$$\log \frac{f_{ML}}{f_M f_L} = -(Z_{ML}^2 - (Z_M^2 + Z_L^2)D + \Delta\varepsilon_j I_m \quad (2.21)$$

The Debye length equation is presented in Equation 2.22. The Debye length contains temperature and pressure dependant constants A (0.509 $kg^{1/2}.mol^{-1/2}$ at 25˚C and 1 bar) and B. B has a value of 1.5 $kg^{1/2}.mol^{-1/2}$ at 25˚C and 1 bar when combined with an ion size parameter, α_j.[246]

$$D = \left(\frac{AI_m^{\frac{1}{2}}}{1+B\alpha_j I_m^{\frac{1}{2}}}\right) \quad (2.22)$$

$\Delta\varepsilon_j$ is the difference between the sum of the interaction coefficients for the products and reactants given by Equation 2.23. The ion interaction coefficients were taken from the Nuclear Energy Agency (NEA) database .[246] When experimental values were not available, they were estimated based on similar charged complexes and the values were kept constant.[246]

$$\Delta\varepsilon^2 = (\varepsilon_{ML}^2 - (\varepsilon_M^2 + \varepsilon_L^2) \quad (2.23)$$

Equation 2.21 can then be substituted for $\log \frac{f_{ML}}{f_M f_L}$ in Equation 2.18, resulting in Equation 2.24. [246]

$$\log \beta^\circ = \log \beta - \log (Z_{ML}^2 - (Z_M^2 + Z_L^2)D + \Delta\varepsilon_j I_m \quad (2.24)$$

Chapter 3 – Materials and Methods

3.1. Chemicals and Materials

All chemicals were analytical grade and all solutions were prepared with 15 MΩ.cm de-ionised water (Merck Millipore). NaOH pellets (VWR) and distilled 6 M HCl were used to prepare 1 M NaOH and HCl solutions for pH adjustment. 15.5 M HNO_3 (VWR) was used to prepare a 4.5 M HNO_3 solution which was used to dissolve the U^{VI} mineral to characterise the quartz sand column retention profiles. NaCl (VWR) was used to control ionic strength. A 1000 mg/L U PerkinElmer Pure Plus standard solution was used to prepare all U^{VI} solutions, and Induced Coupled Plasma Mass Spectrometry (ICP-MS) standards. NaBr (Sigma-Aldrich) was used as a non-reactive tracer. Na_2CO_3 and NaOH (Sigma-Aldrich) was used to prepare the anion eluent for Ion Chromatography. A 997 ± 4 mg/L Si standard (Tracecert, Fluka) was used to prepare Induced Coupled Plasma Atomic Emission Spectroscopy (ICP-AES) standards. Desferrioxamine mesylate salt powder (≥92.5%) from Sigma-Aldrich was used as is.

Washed and calcined quartz fine granular sand, diameter ≥40% 0.2-0.8 mm (Merck Millipore) was used as the porous media in the columns. The sand was cleaned with a series of acid and base washes using a similar procedure presented in the literature to remove any impurities on the mineral surface.[173] The sand was heated in 15.5 M HNO_3 at 60˚C for 24 hours, rinsed with DI water and then cleaned in a 1 M NaOH solution placed on a shaking tray. This procedure was repeated three times. In preparation for analysing the zeta potential of the sand with DLS, the sand was crushed using a mortar and pestle until its diameter was approximately 1 µm, and the cleaning procedure was then repeated.

3.2. Analytical Techniques

3.2.1. pH and dissolved CO_2 measurements

The solution pH was measured using a Metrohm pH meter calibrated at three (pH 4, 7 and 10) or four points (pH 4, 7, 10, 13). The three point calibrated meter was checked with a pH 13 glycine buffer

(Sigma Aldrich). This was within ± 0.04 pH units of the pH 13 buffer, and had a precision of ± 0.015. A typical four point pH calibration curve is provided in Figure 3.1a. The statistics were calculated using the least squares function by employing the LINEST keyword in Ms Excel. The standard error on the slope, intercept and pH is 5.02×10^{-5}, 1.06×10^{-2} and 1.93×10^{-2} for the calibration curve presented in Figure 3.1a. Typically the standard error for the measured pH was 0.05 units.

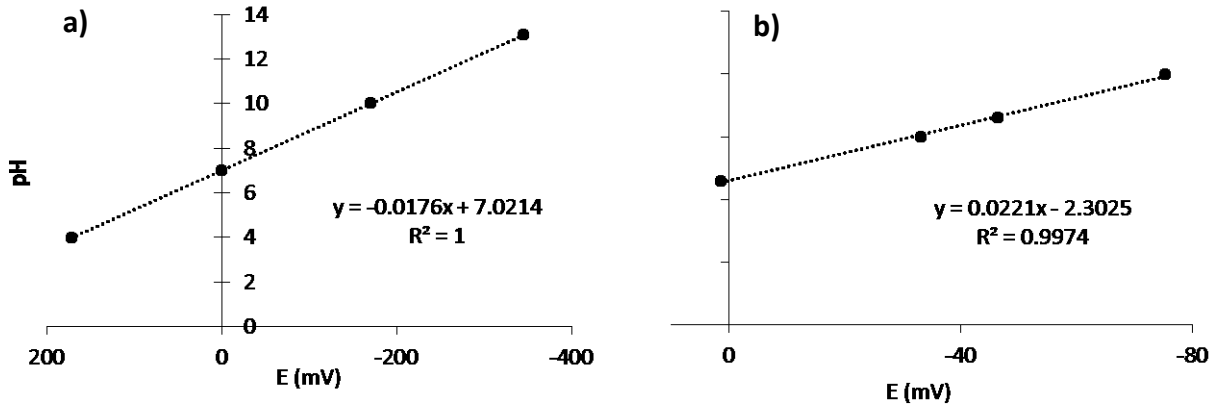

Figure 3.1. Part a) is a typical four point calibration curve of the pH electrode at pH 4, 7, 10 and 13. E is the electrode potential (mV). Part b) is a typical calibration curve for the CO_2 ion sensing electrode.

The dissolved $\Sigma[CO_2]$ was measured during the column experiments and long term organic batch experiments using an Orion CO_2 sensing electrode. This was done as the analytical grade chemicals may contain carbonate, and because atmospheric CO_2 could dissolve into the solutions which could affect aqueous U^{VI} speciation. The electrode was calibrated using at least three points with 0.1 to 5 mM $NaHCO_3$ solutions. The standard error in slope, intercept and log $\Sigma[CO_2]$ for the calibration curve presented in Figure 3.1b is 8.01×10^{-4}, 3.78×10^{-2} and 4.41×10^{-2} respectively. The subsequent error in $\Sigma[CO_2]$ is approximately 11% for this calibration curve, and is typically 14%. Three 5 ml samples were collected from the column input solutions at the beginning and end of injection to provide representative $\Sigma[CO_2]$. A single 5 ml sample was collected per week during the long term organic batch experiments. An Orion CO_2 buffer solution (0.5 ml) was added to the samples to reduce pH to ca. 4.8 so that all the aqueous carbonate species were converted to aqueous CO_2.

3.2.2. Chemical Analysis

U^{VI} concentrations were analysed using an Agilent Technologies, 7900 ICP-MS. 1 ml aliquots from the batch and column experiments were diluted 8-10 times using 2(v/v)% HNO_3 and analysed using ICP-MS. External calibration was carried out between 1 ppb (4.2 nM) and 2 ppm (8.4 µM) at the start and end of sample measurement, and a Bi internal standard was used to correct for drift. The concentrations were calculated automatically by the ICP-MS. However, a manual calibration curve of the ratio of U/Bi counts versus U^{VI} concentration is provided in Figure 3.2. The standard error in slope, intercept for this calibration curve is 0.92, 12.98 respectively resulting in a standard error in U^{VI} concentration of 122 nM (1.45%). A 1 ppm (4.2 µM) U standard prepared from 1000 ppm (4.2 mM) stock solution was measured multiple times throughout analysis. This gave a typical procedural error of ± 5%, and reproducibility of ± 2% (1 S.D.). Samples were measured three times giving typical relative standard deviation percentage (RSD%) of 1%. A blank was measured after the 4.2 µM standard to determine U carry over. Typical values for carry over are 12.60 ± 0.08 nM (0.3%).

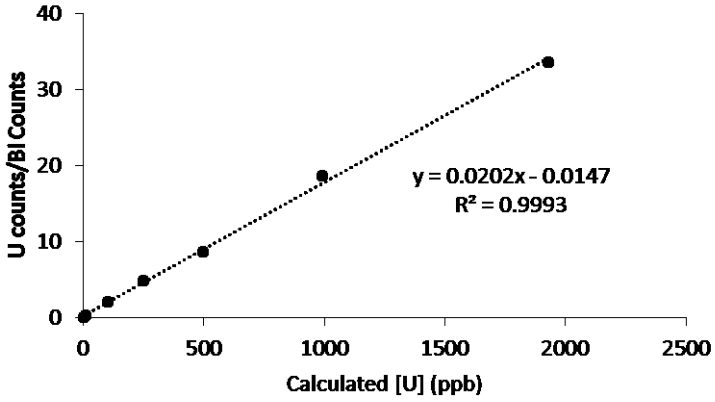

Figure 3.2. An example calibration curve during ICP-MS analysis. The U counts are corrected for drift by dividing by the counts of the internal Bi standard.

Silicon concentrations were analysed using a Thermo Scientific iCap 6500 duo view ICP-AES at the Natural History Museum, UK. It was calibrated between 50 ppb (1.78 µM) and 5 ppm (178 µM). The limit of quantification is 1.78 µM. Repeat analysis (7 times) of an in-house standard gives a typical RSD% of 0.909. The accuracy of the in-house standard measured 9 times was ± 6.5% (1 S.D.).

Bromide concentrations were analysed using a Metrostep a supp 16 150/4.0 6.1031.420 anion chromatography column in a 930 compact ic flex. 858 system calibrated between 0.2-100 ppm (2.5 µM-1.52 mM) for the pH 12.5 column experiment. The samples were diluted ten times with DI water and analysed with ICP-MS calibrated between 0.1-125 ppm (1.3 µM-1.56 mM) for the pH 10.5 and 11.5 column experiments.

3.2.3. Dynamic Light Scattering

Dynamic Light Scattering (DLS) was used to analyse the size distribution and zeta potential (Z_p) of the U^{VI} precipitates and quartz sand. The hydrodynamic diameter was calculated from the translational diffusion co-efficient of the particles, while the Z_p was calculated from the electrophoretic mobility of the particles resulting from the application of an electric field by using the Smoluchowski approach. [249, 250] Triplicate samples were created and measured 48 hours after production. The U^{VI} solutions were prepared in 15 ml test tubes and left stationary so that it represents the batch experiment conditions. The test tubes were sealed to prevent dust influx. Solutions containing the crushed quartz was prepared at a quartz concentration of 10 ppm and these were placed on a rotary device for 48 hours. The samples were shaken by hand immediately before analysis, and a 1 ml aliquot was placed in a cuvette. Each sample was measured three times using a ZEN5600 Malvern Zetasizer Nano ZSP with detection range of 0.3 nm to 10 µm. The number of scans for each size distribution measurement was at least 10. The precision based on 1 S.D for the averaged measurement is ± 127 nm. A 12.8˚ scattering angle was used for the quartz samples and U^{VI} samples at pH 10.5 and pH 11.5 as large particles scatter greater amounts in the forward direction. A 173˚ was used to measure the samples at pH 12.5 to try to detect smaller U^{VI} precipitates. Blank samples were measured at all pH values and the average derived count rates are less than 1% of the quartz and U^{VI} samples. The Z_p were measured three times for each sample, and each measurement was composed of 20 scans. The precision of the Z_p is typically within ± 2.5 mV based on 1 S.D of three independent measurements of a sample.

3.2.4. Transmission Electron Microscopy

A 42 µM U^{VI} sample containing 0.1 M NaCl, with initial pH of 10.5 and 11.5 were imaged with Transmission Electron Micrsoscopy (TEM). The particles were left to settle at the bottom of the test tube and the solution was pipetted out until approximately 1.5 ml remained. The sample was shaken by hand and a drop was pipetted onto a copper stack with carbon membrane (forvard film Cu-TEM grid). The pH 10.5 sample was analysed with a Jeol JEM 2001-plus TEM, while a Jeol JEM 2100F was used to analyse the pH 11.5 sample. Both instruments were operated at 200 kV. Energy dispersive x-ray spectroscopy (EDS) was used to confirm the precipitates contained U^{VI}. The analyses were carried out with an operating voltage of 200 kV. The detection limit for each element was 1 wt%.

3.2.5. X-Ray Powder Diffraction

XRD analysis was conducted at the Natural History Museum, UK. XRD was used to check the purity of the quartz sand. The quartz sand was crushed with a mortar and pestle and then analysed to check its composition. The quartz sand was analysed for several hours using an ENRAF NONIUS FR590 Diffractometer, with a Cu source operating at 35 mA and 40 kV. The incident X-ray beam was confined to pure Cu Ka1 radiation using a Germanium (111) monochromator in combination with horizontal slits set at 0.25 mm. Measurements were carried out in reflection using a fixed beam-sample-detector geometry. The diffracted x-rays were collected with an INEL 120º curved position sensitive detector. The angular linearity of the detector was calibrated with silicon and silverbehenate standards and a 2θ linearization was carried out using a least-squares cubic spline function. The diffraction patterns were compared to datasets in the PDF4 ICDD 2014 database. Additional measurements were performed without a sample on the sapphire substrate to evaluate the contribution of the zero-background holder, which showed no peaks.

XRD analysis was also performed to identify the U^{VI} bearing phase for precipitates initially formed in 15 ml solutions containing 10 mg/L U^{VI} and 0.1 M NaCl at pH 10.5 and 11.5. These conditions were chosen to see whether a change in pH could lead to a different U^{VI} phase. The precipitates were

allowed to settle at the bottom of the test tube before being pipetted onto a glass slide, and left at room temperature until the sample had dried. 15 MΩ.cm water was periodically applied to the dried U^{VI} bearing mineral, and removed with paper, to remove excess NaCl which could interfere with the XRD patterns. The dried precipitates were then scraped onto a sapphire substrate zero-background holder and analysed overnight using the same operational parameters as employed for the quartz sand. The diffraction patterns were compared to datasets in the PDF4 ICDD 2014 database.

3.2.6. X-Ray Computed Tomography

Three dimensional images of a representative quartz sand column were acquired using X-ray CT. The X-ray CT scans were taken with a Zeiss Xradia Versa 500 system. The X-ray source was operated with the anode voltage at 50 kV and power at 4 W. The X-rays were polychromatic and had a maximum energy of 50 keV. No source filter was used and the projections were collected on a CCD camera with a pixel count of 2048 × 2048. A 4x objective was used to achieve a resolution of 3.5 µm per voxel; 2200 projections were taken as the sample was rotated through 180° around an axis perpendicular to the X-ray beam. The exposure length was determined such that 9000 counts were obtained through the centre of the projection. The grain, pore, and pore throat size distributions were extracted from the CT images. Approximations for grain diameter was determined by extracting grain volume using Avizo 9.3,[251] followed by calculating the spherical radius of the particles, while pore and pore throat radius were extracted using a pore network model.[252]

3.3. Experiments

All of the data points are included in the figures of batch and column experiments throughout the thesis. The error bars shown are the standard deviation of the analytical error (± 5%) propagated to take into account division of one sample by another. This error is typically ± 7%. The same amount of U^{VI} is usually removed by all filter membrane sizes therefore it appears there is only one membrane pore size presented in the figures. The numerical data presented in the batch and

column experiments are provided in Appendix B, including the numbers for all filter membrane sizes. The specific tables in the appendix are referenced in the relevant sections of chapter 5 and 7.

3.3.1. Static Batch Experiments

Batch experiments were conducted for up to seven days to characterise the effects of pH on U^{VI} precipitation, in the absence of quartz sand and stirring. The batch experiments were repeated twice. 200 ml solutions with 42 µM U^{VI} and 0.1 M NaCl were created at pH 10.5, 11.5 and 12.5. An approximately 180 ml solution containing the NaCl was initially created and adjusted to the appropriate pH so that a 5 ml representative blank could be collected. 42 µM U^{VI} was then added to the solution by diluting the 4.2 mM U^{VI} standard solution. The pH was re-adjusted to 11.5 and volume increased to 195 ml. The pH was periodically measured and adjusted throughout the experiment with 1 M NaOH and 1 M HCl to maintain the correct pH (10.5, 11.5, and 12.5). The pH was measured on collection of a sample and was adjusted if the pH changed more than ± 0.05 pH units of the target value. The solutions were briefly shaken by hand immediately before sample collection to ensure the precipitates were suspended. 5 ml samples were filtered through 0.2, 0.45, 0.8 and 1 µm nylon filter membranes (Whatman) and analysed for U^{VI} using ICP-MS. To check the U^{VI} precipitation was repeatable, the experiment was repeated and U^{VI} samples were filtered through 0.2 µm nylon filter membranes.

3.3.2. Stirred Batch Experiments

Stirred batch reactor experiments were conducted for up to three days to test the short term effect of DFOB on U^{VI} particle formation. All batch experiments were repeated at least twice. The experiments were conducted in 250 ml amber bottles to prevent photo-oxidation of DFOB. 250 ml solutions containing 0.1 M NaCl and various DFOB concentrations (4.2, 42, 130 and 420 µM) were created. DFOB was added in a powder form to create the 130 and 420 µM DFOB solutions. A 4.2 mM DFOB stock solution was created and diluted to produce the 4.2 and 42 µM DFOB solutions. The 4.2 mM DFOB stock solution was freshly prepared before each experiment to minimise ligand

degradation. The solutions were prepared in the same way as the static batch experiments, except that the DFOB was added and collected as part of the representative blank. The pH was regularly adjusted throughout the experiment. 5 ml samples were collected and filtered through Whatman nylon membranes (0.2, 0.45, and 1 µm pore diameter), diluted 10 times in 2% nitric acid and analysed using ICP-MS. During two of the three repeats of the 420 µM DFOB experiment, samples were only filtered with a 0.2 µm nylon filter membrane.

To test the long term effects of DFOB on U^{VI} precipitate formation and ligand promoted dissolution/disaggregation, 250 ml solutions containing 42 µM U^{VI}, 130 µM DFOB and 0.1 M NaCl adjusted to pH 11.5 were placed in a shaking tray for two months (T=25˚C, 130 rpm). Three types of experiments were conducted; a control experiment; a precipitation inhibition experiment (see short term batch experiments method); and a dissolution experiment. At the start of the dissolution experiment, 42 µM U^{VI} was allowed to precipitate for 48 hours, and then 130 µM DFOB was added to solution. 5 ml samples were collected and filtered through 0.2, 0.45 and 1 µm Whatman nylon filter membranes, diluted 10 times in 2% nitric acid and analysed using ICP-MS.

3.3.3. Column Experiments

Column experiments were conducted at pH 10.5, 11.5 and 12.5 with 0.1 M NaCl and 42 µM U^{VI} in duplicate. For the pH 12.5 experiment, two glass chromatography columns (Chemglass CG-119-01) with 1.3 cm internal diameter (ID), and a 40-60 µm porous glass frit at the base of the column, were packed with approximately 40 g of quartz sand (sand column length = 19 cm). A glass frit and approximately 0.04 g of glass wool were placed at the top of the columns and sealed with a rubber stopper modified to contain an outlet tube. Water was pumped upwards through the column at 0.5 ± 0.1 ml/min using a Cole-Palmer L/S Masterflex peristaltic pump (model 77240-00) until the column was saturated.

The pH 10.5 and 11.5 experiments were conducted at a later date with a more appropriate design for particle transport. The results and issues with the initial column design are presented in Appendix A. In brief U^{VI} precipitate was removed by the inert glass frit used to prevent the quartz sand falling from the column, therefore the experiments did not represent U^{VI} transport through quartz sand. During the second run of column experiments, the glass chromatography columns were wet packed to minimise air was entrapment. The water height was kept at least 1 cm above the sand level and the column was tapped gently to prevent layering. The glass frit at the column inlet was replaced with a steel mesh which does not interfere with the transport of the U^{VI} precipitates. Pictures of the column setup is provided in Figure 3.3.

The pore volume (PV) of the columns were determined gravimetrically using Equation 3.1 where m_p, m_s and m_e are the mass of the saturated packed column, dry quartz sand, and empty column respectively. This assumes that 1 g of water is equal to 1 ml.

$$PV = m_p - m_s - m_e \quad (3.1)$$

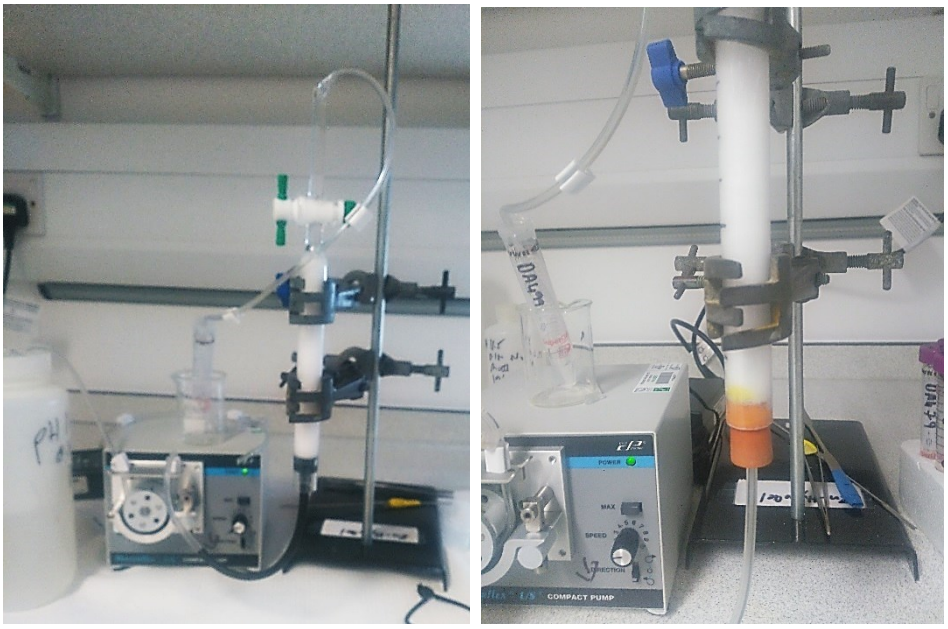

Figure 3.3. Photographs of the column experiment setup.

The porosity (ϕ) of the columns were calculated by dividing the PV by the total volume of the packed columns. The total volume of the columns were calculated geometrically using $h\pi r^2$ where h and r is the height and radius of the column respectively. The dry bulk density (ρ_b) was calculated by dividing the mass of the dry sand by the total volume of the sand column. The darcy velocity (q) and average linear velocity v, were calculated using equations 3.2 and 3.3. Q is the flow rate (cm^3/min), A is the cross sectional area (cm^2), and ϕ is the porosity. q is the velocity through a cylinder with cross sectional area A, assuming the cylinder contains no porous media. v takes into account that the actual average velocity will be greater than the darcy velocity for a given flow rate due to the presence of porous media which reduces the volume the solution can be transported through.[253]

$$q = \frac{Q}{A} \tag{3.2}$$

$$v = \frac{Q}{A\phi} = \frac{q}{\phi} \tag{3.3}$$

The columns were equilibrated with a U^{VI} free solution at the desired pH overnight. The U^{VI} containing inlet solution was prepared approximately 1 hour in advance of the pH 12.5 experiments, and 48 hours in advance of the pH 10.5 and 11.5 experiments. The pH 10.5 and 11.5 column experiments were conducted after 48 hours as this is the amount of time it takes for U^{VI} precipitation to reach equilibrium during the static batch experiments. No precipitation was observed during the pH 12.5 batch experiments therefore the solution was only left for approximately 1 hour before being injected through the columns. Approximately twelve pore volumes of the U^{VI} solution was injected into the columns during the pH 12.5 experiments, and six pore volumes of U^{VI} were injected during the pH 10.5 and pH 11.5 experiments. The solution was then switched to one which does not include U^{VI}. The solution was pumped upwards through the columns to minimise air entrapment, prevent flow due to gravity, and to ensure an even spread of the solution across the cross sectional area of the column.

During the pH 10.5 and 11.5 column experiments, three samples were collected from the U^{VI} containing inlet solution and filtered with a 0.2, 0.45 and 1 µm Whatman nylon filter membrane at the start and end of U^{VI} injection to determine the amount of U^{VI} which had precipitated before injection into the column. Several outlet samples were filtered with 0.2 µm Whatman nylon filter membranes to determine whether any precipitates were leaving the column. Several samples were collected from the column outlet during initial column equilibrium and during U^{VI} injection. These samples were analysed for Si using ICP-AES at the Natural History Museum. A separate column experiment was conducted at pH 12.5 to constrain the dissolved [Si].

At the end of the second set of column experiments, the sand was carefully removed using a spatula in 1.5 cm increments and placed in 10 ml of 4.5 M HNO_3 to dissolve the U^{VI}. These were placed on a rotary device for at least 48 hours. 1 ml of the solution was diluted with de-ionised water to reduce the [HNO_3] to 2% and then analysed with ICPMS for U^{VI}. The quartz sand was then dried at 60 ˚C in an oven so that the mass of U^{VI} could be normalised against the mass of the quartz sand. The U^{VI} mass balance was typically ca. 90% when considering the mass of U^{VI} injected into the column, the mass of U^{VI} retained in column and the mass of U^{VI} eluted from column. Propagation of the analytical error leads to ±c5-9% of the mass balance. Some U^{VI} could also be lost when the sand was manually removed with a spatula when measuring the retention profile of the column experiments.

3.3.4. Quality Control

The bottles, used test tubes, chromatography columns, filter membrane holders and magnetic stirrers were cleaned with 2% v/v HNO_3 for 24 hours and then transferred to a 15 MΩ.cm de-ionised water bath. The equipment was removed from the water bath after 24 hours, rinsed with 15 MΩ.cm de-ionised water and left to dry. The tygon tubing used for the column experiments were cleaned by injected 15 MΩ.cm de-ionised water into the tubes, followed by air and left to dry.

Procedural blanks were collected to check there was no U^{VI} present in U^{VI} free solutions, filter membranes and quartz sand columns. Cleaned test tubes had U^{VI} concentrations lower than the detection limit. The average U^{VI} concentration in the U^{VI} free solutions was 13 ± 8 nM. The average U^{VI} concentrations in the filter membrane procedural blanks is 2.1 ± 0.3 nM. The average U^{VI} concentration in the procedural blanks for the column experiments is 40 ± 30 nM. The error reported in the above values is 1 S.D. This is insignificant compared to the 42 µM initial U^{VI} concentration.

Sorption onto glass and plastics such as polypropylene and nalgene are insignificant at relatively high U^{VI} concentrations (21-420 µM).[254-256] There was no evidence for sorption during the batch experiments. 100% U^{VI} was recovered during the batch filtration experiments when no U^{VI} solids were observed (e.g. pH 11.5 with 420 µM DFOB, and pH 12.5 with 0 M DFOB) after considering the analytical error. Retardation of the breakthrough of the mobile fraction of U^{VI} during the column experiments was minimal with respect to the non-reactive tracer, hence no sorption occurred onto the glass columns at the pH range of interest.

3.4. Density Functional Theory Details

3.4.1. Computational Details

Electronic structure calculations were carried out with Gaussian 16-Rev. A.03[257] using GaussView version 6[258] for pre- and post-processing. All structures were geometrically optimized and the frequencies were calculated to confirm local minima and determine thermodynamic properties including Gibbs free energy (G). The PW91,[193] TPSS,[190] and M06[192] DFAs were utilized in addition to B3LYP[191] to provide comparisons to a GGA, meta-GGA and recent hybrid functional, respectively. Pople's polarised double zeta basis set, 6-31G(d,p),[203, 204] and Dunning's correlation-consistent, polarized valence n zeta basis sets augmented with polarization functions (aug-cc-pV*n*Z) were employed where *n* = double (D), triple (T), and quadruple (Q)[199, 200, 205] were used for ligand atoms.

Dolg's MWB60-RECP[195] and MDF60-RECP[215] along with Peterson's cc-pV*n*Z basis sets for pseudo potentials (cc-pV*n*Z-PP)[259] were employed for U^{VI}. Implicit solvation was accounted for with the integral equation formalism polarizable continuum model (IEFPCM)[220] and the universal solvation model built upon the integral equation formalism (SMD).[221] Mixed models were tested by using the $[UO_2(H_2O)_5(H_2O)_{10}]^{2+}$ structure from Gutowski and Dixon.[38] A sketch of $[UO_2(H_2O)_5(H_2O)_{10}]^{2+}$ is provided in Figure 3.4. This models aqua ligands as two water molecules hydrogen bonded to the aqua ligand interacting directly with the U^{VI} metal center. Symmetry was not constrained and all calculations utilized a pruned grid with 99 radial shells and 590 angular points per shell. The self-consistent Field (SCF) procedure convergence criteria used during the optimization and frequency calculations were the standard Gaussian values: Maximum force = 4.5×10^{-4} Hartrees/Bohr, root mean square (RMS) force = 3×10^{-4} Hartrees/Radians, maximum displacement = 1.8×10^{-3} Å, RMS displacement = 1.2×10^{-3} Å.

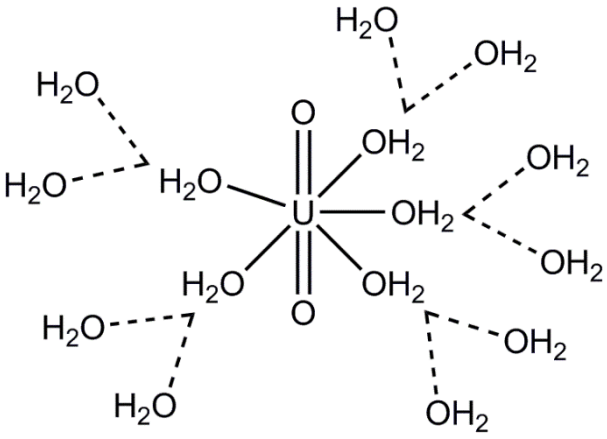

Figure 3.4. A sketch of the $[UO_2(H_2O)_5(H_2O)_{10}]^{2+}$ complex. The co-ordination bonds of water to U^{VI} are given as solid lines. Hydrogen bonds between occurring between water ligands is given by dashed lines.

3.4.2. Reactions used for selection of DFT components

The formation of 1:1, 1:2 and 1:3 U^{VI} acetate complexes was used to investigate the different model chemistry components (ECP, basis set, functional, solvation method). Acetate is similar to the α-hydroxycarboxylate siderophore functional group, and the geometries of the species, along with $\Delta_r G$

have been comprehensively studied experimentally.[31-34, 135, 260-262] The reactions for uranyl with one to three acetate ligands are given in equations 3.4 to 3.6 respectively.

$$UO_2(H_2O)_5^{2+} + CH_3COO^- = UO_2(CH_3COO)(H_2O)_3^+ + 2H_2O \quad (3.4)$$

$$UO_2(H_2O)_5^{2+} + 2CH_3COO^- = UO_2(CH_3COO)_2(H_2O)^0 + 4H_2O \quad (3.5)$$

$$UO_2(H_2O)_5^{2+} + 3CH_3COO^- = UO_2(CH_3COO)_3^- + 5H_2O \quad (3.6)$$

Reactants and products were optimized and vibrational frequencies were calculated to confirm that structures were at energy minima. All calculations were conducted in aqueous phase and free energies were calculated using $\Delta G_{gas} + \Delta G_{solvent} = \Delta G_{solvation}$. The G of explicit water molecules in the bulk solution were concentration corrected to 55.5 M by adding -17.88 or +17.88 kJ/mol (4.27 kcal/mol) depending if water is a reactant or product side respectively.[243, 263] Gibbs free energy (G) for each product and reactant was computed using the harmonic oscillator and rigid rotor approximations, without accounting for hindered rotation. No entropy values for low lying frequency modes were removed.

3.4.3. Organic molecule training set used for fitting calculated stability constants

Seven organic molecules were used for the 1:1 fitting are shown in Figure 3.5. They were chosen because they are, or are similar to, siderophore chelating groups. The reaction used to calculate $\Delta_r G$ is given in Equation 2.6, except for L-glycine which is given in Equation 3.7 where $G(H_3O)^+$ is the Gibbs energy of the hydronium ion. This equation was used based on the reaction used in the experimental literature.[56] In Equation 3.7 the G of the reactant proton is calculated by assuming hydrogen is present as a hydronium ion $(H_3O)^+$, and one of its protons dissociates during the reaction to generate the protonated L-glycine and a water molecule. The log β_{110} values were calculated using Equation 2.5.

$$\Delta_r G = G(ML(Sol)_{m-n}) + nG(Sol) - G(M(Sol)_m) - G(L) - G(H_3O^+) \quad (3.7)$$

For testing the fitting approach for multiple bound ligands, the formation of different 1:1, 1:2 and 1:3 U^{VI}-carboxylate complexes were calculated. The ligands were glycolate, acetate and oxalate. These were chosen to include changes in denticity, and difference in charge.

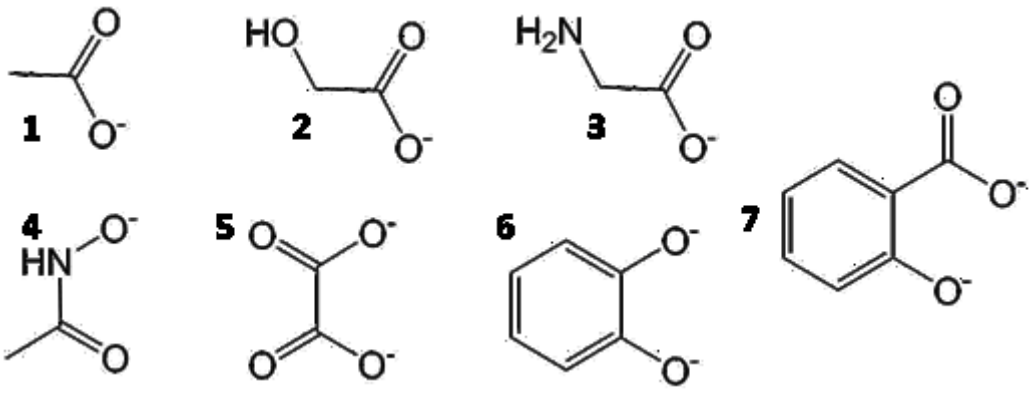

Figure 3.5. The ligand training set used for computational fitting. These are 1 acetate, 2 glycolate (protonated α-OH), 3 L-glycine, 4 aceto-hydroxamate, 5 oxalate, 6 catecholate, 7 salicycate.

The experimental log $\beta_{110/111}$ (and resulting $\Delta_r G$) used for all comparisons were adjusted to zero ionic strength by using the Specific Ion Theory and Davies equation[245, 246] depending on the ionic strength the experiments. The ion exchange parameters are provided in Table 3.1.

3.5. PHREEQC Modelling

Uranium speciation and saturation indices were predicted between pH 9-13 using PHREEQC[42] in conjunction with the SIT database.[43] The constant input conditions used for all pH values was 42 µM U^{VI}, 0.1 M NaCl. The solution was equilibrated with O_2 assuming its atmospheric partial pressure is 0.2, (log(0.2) = -0.7). The total CO_2 concentration ($\Sigma[CO_2]$) was added as CO_3^{2-} and the software automatically splits the CO_2 into $CO_{2(aq)}$, HCO_3^- and CO_3^{2-} depending on pH. The average $\Sigma[CO_2]$ (220 µM) from the column experiments was used in chapter 4, while in chapter 7 the average $\Sigma[CO_2]$ (380 µM) measured during the long term control batch experiment was used. The Si concentration included in the speciation modelling was obtained from the column experimental data in chapter 4. The Si

concentration used was 50, 90 and 30 µM at pH 10.5, 11.5 and 12.5 respectively. The solution was charge balanced by adding Na^+, representing the addition of NaOH to the experiments.

The stability data for two U^{VI} and Si containing minerals, sodium boltwoodite and sodium weeksite, are absent from the SIT database. These have been added into the database using the values given by the NEA database.[264] They have been included as they could potentially precipitate from solution under the chemical conditions of interest.

Table 3.1. Specific Ion interaction coefficient (ε) in kg/mol used to extrapolate the experimental data to zero ionic strength.

Interacting Ions	ε	±	Real/estimated
ε(UO_2^{2+},ClO_4^-)	0.46	0.03	Real
ε(Ox^{2-},Na^+)	-0.08	0.01	Real
ε(ClO_4^-,Na^+)	0.01	0.01	Real
ε(UO_2Ox^0, Na^+ + ClO_4^-)	-0.05	0.06	Real
ε($UO_2Ox_2^{2-}$, Na^+)	-0.18	0.07	Real
ε($UO_2Ox_3^{4-}$, Na^+)	-0.01	0.11	Real
ε($Acet^-$,Na^+)	0.08	0.01	Real
ε(UO_2Acet^+, ClO_4^-)	0.33		Estimate
ε(Gly^-,Na+)	0.08		Estimate
ε(UO_2Gly^+, ClO_4^-)	0.33		Estimate
ε(AHA^-,Na^+)	0.08		Estimate
ε(UO_2AHA^+, ClO_4^-)	0.33		Estimate

Chapter 4 - U^{VI} particle formation, characterisation and transport through quartz sand between pH 10.5 and 12.5 in 0.1 M sodium chloride solutions

Abstract

Understanding aqueous U^{VI} chemistry in alkaline solutions is imperative for radioactive waste disposal. The aim of the research carried out in this chapter was to characterise the precipitation kinetics of 42 µM U^{VI} in 0.1 M NaCl between pH 10.5-12.5, their physico-chemical properties, and their transport through quartz sand. Batch filtration experiments were conducted for 42 µM U^{VI}, 0.1 M NaCl solutions at pH 10.5, 11.5 and 12.5 to characterise U^{VI} precipitate formation. The physico-chemical properties of the precipitates were determined using Dynamic Light Scattering, Transmission Electron Microscopy and X-ray Diffraction. The mobility of U^{VI} was tested by injecting 42 µM U^{VI}, 0.1 M NaCl solutions at pH 10.5, 11.5 and 12.5 through quartz sand. The results show U^{VI} precipitates from solution at pH 10.5 and pH 11.5, approaching equilibrium after 48 hours. These precipitates were sodium diuranate ($Na_6U_7O_{24}$) with hydrodynamic diameters of 640 ± 111 nm and 837 ± 142 nm at pH 10.5 and 11.5 respectively. At pH 11.5 the U^{VI} particles were immobilised in the first 1.5 cm of the quartz sand column. The charge of the U^{VI} precipitates (-20.9 ± 0.19 mV) and quartz sand (-42.0 ± 2.16 mV) suggests the particles were not immobilised by electrostatic forces, therefore limiting immobilisation to physical mechanisms. At pH 10.5, the U^{VI} precipitates were also immobilised in the quartz sand, however 16-19% of U^{VI} was transported through the columns as ≥0.2 µm diameter precipitates. At pH 12.5, ≥0.2 µm diameter precipitates did not form and 100% U^{VI} eluted from the columns.

4.1. Introduction

In alkaline solutions, the formation of U precipitates can significantly influence U removal by mineral and rock surfaces. At low concentrations (0.8 µM), U^{VI} was observed to precipitate from Hanford groundwater when the solution pH was above 10.5.[17] Precipitation only occurred when the solutions contained sediments collected from the Hanford site. The sediments acted as nucleation points (heterogeneous precipitation) for the formation of a U^{VI}-calcium carbonate co-precipitate. U^{VI} was observed to precipitate at pH >9 to pH 11 in 0.01 M NaCl solutions containing 28 µM U^{VI} which increased U^{VI} removal by the surface of granite by adsorption.[151] Uranium may also have precipitated in 0.05 M $NaClO_4$ solutions with a similar initial U^{VI} concentration (28 µM) at pH > 9 to pH 11, leading to enhanced U^{VI} removal by a Ca-calcareous soil via sorption or heterogeneous precipitation.[152] A recent study by Kenney *et al*. [254] explored U^{VI} sorption onto quartz, sandstone and a volcanic rock between pH 2-12 in solutions containing 4.2 nM to 42 µM U^{VI}, 0.1 M NaCl, and 0 or 2 mM $NaHCO_3$. When the concentration of U^{VI} was 42 µM, U^{VI} precipitated from solution as a Na containing mineral composed of 20 nm crystals. These crystals aggregated to form particles with diameter ≥0.45 µm at pH ≥10. These precipitates were not immobilised on the quartz sand surface when no $NaHCO_3$ was added solution and the authors hypothesised that U^{VI} could be mobile. The ≥0.45 µm diameter U^{VI} aggregates no longer formed above pH 12. Although Kenney *et al*. [254] observed U^{VI} precipitation in solutions which do not contain mineral assemblages, the precipitation kinetics were not explored in detail. U^{VI} precipitation kinetics have been explored previously. However, these are typically solubility studies with pre-formed minerals such as meta-scheopite ($UO_3 \bullet 2H_2O$) and sodium diuranate hydrate ($Na_2U_2O_7 \bullet xH_2O$) in solutions containing high NaCl concentrations (> 0.5 mol/kg), or alternatively explore precipitation at high U^{VI} (10^{-2} M) and $NaClO_4$ (≥0.5 M) concentrations.[265, 266]

Batch sorption studies seldom explore the physico-chemical properties of the U^{VI} precipitates such as the precipitate diameter and surface charge. These properties, however, are key to understanding potential removal mechanisms such as adsorption processes and physical immobilisation in porous

media. The size of the U^{VI} precipitates were characterised in a synthetic cement leachate at pH 13.1.[149] The U^{VI} precipitates were 2 nm diameter crystals consisting of a clarkeite-type phase containing Ca, K and Na. These crystals aggregated to form 10 to 60 nm diameter colloids when 4.2-42 µM U^{VI} was present, and ≥ 0.22 µm diameter particulates when 252 µM U^{VI} was present in the cement leachate. Other studies have explored the surface charge of U^{VI} minerals which have been added to solution by measuring the zeta potential (Z_p). The zeta potential of a calcium uranate ($Ca[U_2O_7]$) precipitate disaggregated with a mortar and pestle was -22.2 mV in 0.01 M NaCl solutions. The size distributions measured in 0.1 M calcium nitrate solutions was 144-193 nm, 1.75-3.16 µm and 5.68-10.24 µm.[267] The Z_p of Na-boltwoodite ($Na[(UO_2)(SiO_3OH)]\bullet H_2O$) was measured as -46 mV in 0.1 M $NaClO_4$ solutions above pH 10.[268] However, to the best of my knowledge, the physico-chemical properties of the U^{VI} precipitates which have formed directly in solutions containing trace concentrations of U^{VI}, and the Na background cation often used in batch sorption studies, has not been explored in detail.

An important limitation of batch experiments is the high volume of solution relative to the solid. The mobility of U^{VI} can be characterised using column experiments where the solution/solid ratio is more realistic of geological environments. These type of studies are limited for trace U^{VI} concentrations in alkaline (>pH 10) solutions. These studies focus on exploring the overall mobility of U^{VI}, or focus on U^{VI} precipitation within the column, rather than injecting solutions containing U^{VI} precipitates. For example the mobility of 2.1 µM U^{VI} through unsaturated quartz sand in pH 11, 1 mM $NaClO_4$ solutions was explored. [269] Between 72-82% of the U^{VI} was eluted from the column during U^{VI} injection and a precipitate was observed in the samples collected at the column outlet. Uyusur et al.[269] proposed U^{VI} precipitated from solution and that these precipitates were subsequently immobilised in the column. However, Uyusur et al.[269] were unsure if the 18-28% of U^{VI} not measured at the column outlet was removed in the column, or whether the U^{VI} was not quantified because the U^{VI} precipitate had settled at the bottom of the test tubes before chemical analysis. The mobility of U^{VI} in pH 13 solutions (0.1 M NaOH, 1.0 M $NaNO_3$) was tested in Hanford sediment packed columns where were equilibrated with

pH 8 groundwater. A total mass of 0.35 mg U^{VI} were injected into the columns, followed by an injection of U^{VI} free groundwater.[16] U^{VI} was observed to precipitate near the column inlet and the authors attributed this to the formation of Na-boltwoodite ($Na[(UO_2)(SiO_3OH)]\bullet 2H_2O$). When the pH decreased below 9.5, the U^{VI} mineral dissolved, and further uranium from the pre-contaminated Hanford sediment was mobilised.

The aim of the research presented in this chapter is to increase our current understanding of the precipitation of U^{VI} from a static source, and the subsequent transport of U^{VI} through porous media. There are three objectives to achieve this. The first objective was to characterise U^{VI} precipitation in a static U^{VI} source. The second objective was to characterise the physico-chemical properties of the U^{VI} precipitates and quartz sand. This includes the zeta potential, diameter and mineralogy of the U^{VI} precipitates, and the zeta potential, grain, pore and pore throat diameter of the quartz sand. The final objective was to characterise the mobility of U^{VI} through the quartz sand porous media from the static U^{VI} source. The experiments were conducted using solutions containing 42 µM U^{VI} and 0.1 M NaCl at pH 10.5, 11.5 and 12.5, similar to the conditions employed by Kenney *et al.*[254] The background electrolyte (NaCl) was employed so that the results are not scenario specific, from which a component additive approach can be used to explore the effect of other dissolved ions (multivalent ions, organic ligands etc.) in future research. Quartz sand was employed as it is a common rock forming and fracture fill mineral [270] and U^{VI} could be highly mobile as a precipitate as evidenced by previous batch experiments.[254]

4.2. U^{VI} precipitate formation

To explore U^{VI} precipitation in a static system, batch experiments were conducted in the absence of stirring and quartz sand at pH 10.5, 11.5 and 12.5 in 42 µM U^{VI}, 0.1 M NaCl solutions (Figure 4.1). The data plotted in Figure 4.1a-Figure 4.1c are provided in Table B1-B3. During the first repeat, 5 ml samples were filtered through 0.2, 0.45, 0.8 and 1 µm diameter filter membranes across 7 days (168

hours). During the second repeat the solutions were only filtered through the 0.2 µm filter membranes to confirm U^{VI} precipitated from solution. The solutions were briefly shaken by hand to ensure the U^{VI} particles were suspended before sample filtration.

The results of the pH 10.5 (Figure 4.1a) batch experiments shows U^{VI} initially precipitated rapidly from solution. 45% of U^{VI} remained in the filtrate after 4 hours in the first batch experiment, and 57% of U^{VI} remained in the filtrate after 8 hours during the repeat experiment. Approximately 15% and 27% of the $[U^{VI}]$ remained in the filtrate after 48 hours for the two batch experiments. After 168 hours, 25% and 11% of U^{VI} remained in the filtrate in the first and second batch experiments respectively. Similar amounts of U^{VI} are removed for all filter membrane sizes providing an initial indication that the size fraction of the precipitates was ≥ 1 µm diameter. These results support previous observations that U^{VI} precipitates from solution above pH 9 to the highest experimental pH employed (pH 11) during batch sorption experiments on granite and Ca-calcareous soils.[152, 271]

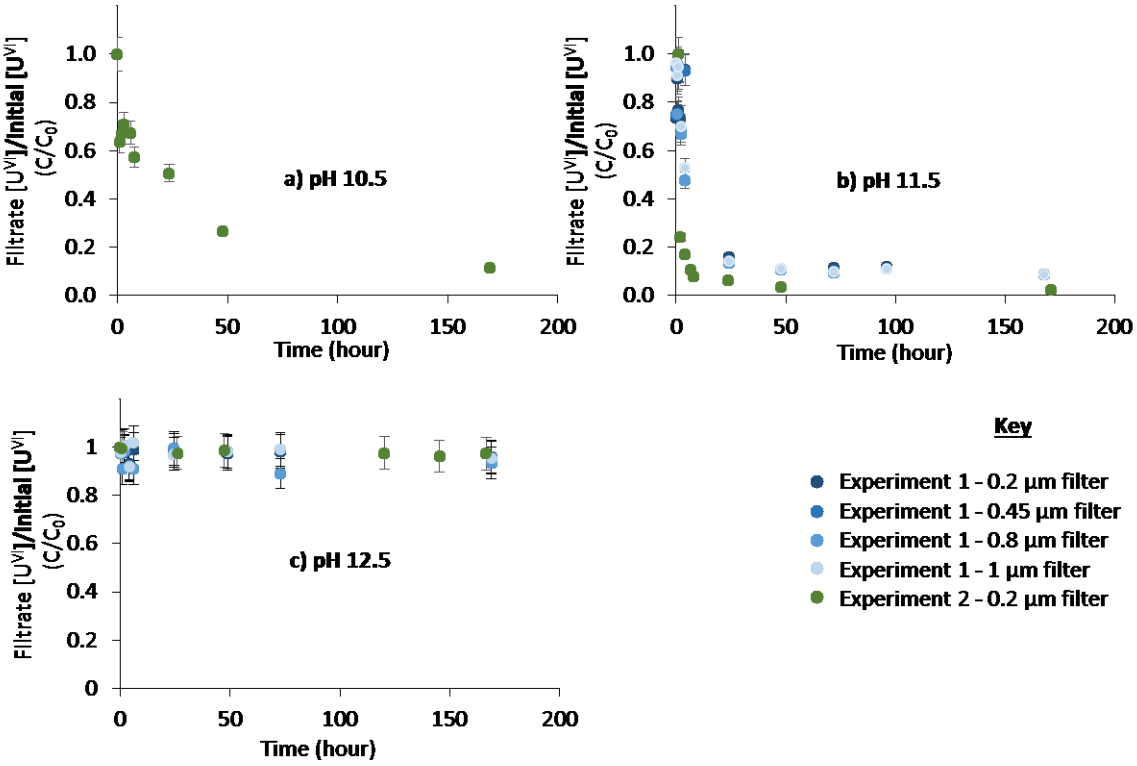

Figure 4.1. Batch filtration experiments at a) pH 10.5, b) pH 11.5 and c) pH 12.5 for 42 µM U^{VI}, 0.1 M NaCl solutions. The blue data points and green data points represent the two separate repeat experiments. The data plotted in a), b) and c) are given in Table B1, B2 and B3 respectively.

During the batch experiment conducted initially at pH 11.5 (Figure 4.1b), the reaction approached equilibrium after 48 hours with 11% and 4% of U^{VI} remaining in solution after filtration through 0.2-1 µm diameter filter membranes in the first and second experiment respectively. U^{VI} precipitated from solution more rapidly in the second batch experiment. The results show similar amounts of U^{VI} removal using four filter membrane sizes providing an initial indication that the size fraction of the precipitates formed at pH 11.5 is ≥ 1 µm diameter.

Speciation modelling can provide insights into potential U^{VI} minerals which are precipitating from the solution at pH 10.5 and pH 11.5. During these calculations, the average $\Sigma[CO_2]$ measured from the inlet solutions of the pH 10.5 and 11.5 column experiments was used (220 µM). The saturation indices from the speciation modelling are provided in Figure 4.2b. The saturation indices for soddyite, Na-boltwoodite and Na-weeksite can be ignored as they correspond to quartz dissolution during the column experiments. Several different U^{VI} minerals have positive saturation indices indicating these phases can be precipitating from solution. These are sodium diuranate (saturation index = 6.40), clarkeite (saturation index 5.10) and sodium compreignacite (saturation index = 5.93 to 10.00).

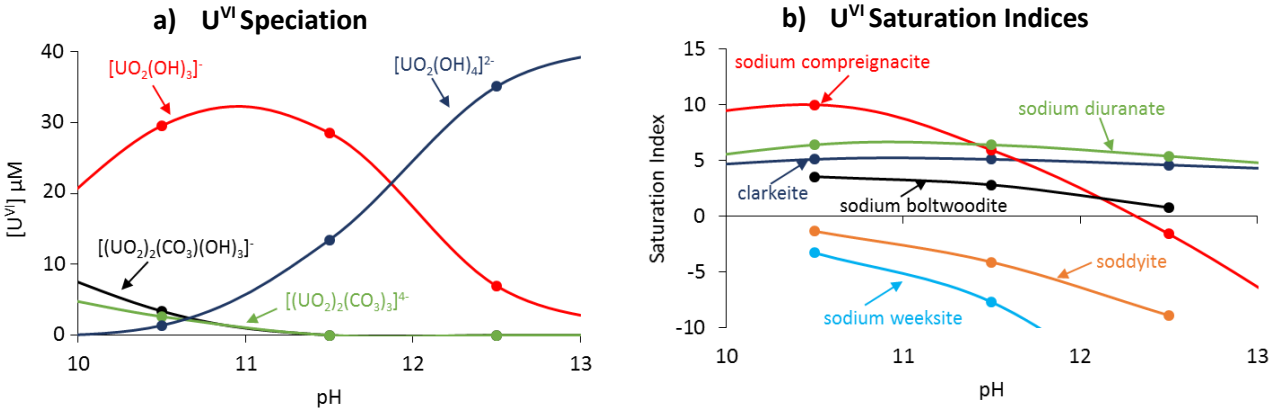

Figure 4.2. a) provides U^{VI} speciation while b) provides U^{VI} mineral saturation indices. The chemical conditions are $[U^{VI}]$ = 42 µM, [NaCl] = 0.1 M, $\Sigma[CO_2]$ = 220 µM, $[O_2]$ in equilibrium with pO_2 (pO_2 = -0.7). The [Si] is 50, 90 and 30 µM at pH 10.5, 11.5 and 12.5 respectively. The [Si] represent the concentration eluting from the column experiments. The minerals presented in b) are sodium compreignacite ($Na_2[(UO_2)_6O_4(OH)_6]•7H_2O$), sodium diuranate ($Na_2[U_2O_7]$), clarkeite ($Na[UO_2O(OH)]$), sodium boltwoodite ($Na[(H_3O)(UO_2)(SiO_4)]•H_2O$), sodium weeksite ($Na_2[(UO_2)_2(Si_2O_5)_3]•4H_2O$) and soddyite ($[(UO_2)_2SiO_4]•2H_2O$).

During the pH 12.5 batch experiments, typically 97 to 98% of U^{VI} passed through the filter membranes during the experiments for the entire timeframe studied (Figure 4.1c). This means U^{VI} does not form ≥ 0.2 µm diameter particles. This supports previous observations that U^{VI} precipitation as ≥0.45 µm diameter particles stops above pH 12.[254] The U^{VI} could be present as the dissolved species $[UO_2(OH)_4]^{2-}$ (Figure 4.2a), however the saturation indices at pH 12.5 are 4.59 and 5.38 for clarkeite and sodium diuranate indicate U^{VI} should have precipitated from solution. Therefore, U^{VI} could have been present as colloids with diameter <0.2 µm. This is supported by earlier work exploring 42 µM U^{VI} chemistry in pH 13.1 cement leachates which found 60 nm colloids of a clarkeite type mineral containing K Ca and Na was precipitating from solution.[149]

4.3. Physicochemical properties of the U^{VI} precipitates

4.3.1. DLS Size and Zeta Potential (Z_p) measurements

The batch experiments provides evidence of the quantity of U^{VI} which precipitated. However, smaller particles can be removed by larger diameter pores in filter membranes, as smaller particles can attach to larger ones during filtration.[55] To obtain greater insight into the size fraction of the U^{VI} precipitates in an in-situ environment, triplicate samples containing 42 µM U^{VI} and 0.1 M NaCl were created at pH 10.5 and pH 11.5 and duplicate samples were created at pH 12.5. These samples were analysed after 48 hours using DLS to determine the approximate diameter of the U^{VI} precipitates. The Z_p of the U^{VI} precipitates were also measured. The results from the size and Z_p measurements are provided in Table 4.1.

The U^{VI} precipitate size distributions are polydisperse (PDI = 1). The Z-average only provides one value for the entire sample, and decreases in accuracy for polydisperse samples. Therefore the size distribution by intensity is used for discussion rather than the Z-average. Histograms of size distribution by intensity for one of the samples at pH 10.5 and pH 11.5 is presented in Figure 4.3. The DLS measurements indicate that at approximately pH 10.34, the U^{VI} precipitates diameter are typically

between 459 to 955 nm, with average diameter 600 ± 100 nm. The Z_p of the particles at pH 10.34 are -22 ± 1 mV. The U^{VI} particles detected at pH 11.42 had a greater average diameter of 800 ± 100 nm with the particle diameter ranging between 530 to 1300 nm. The Z_p at pH 11.5 is -20.9 ± 0.2 mV, less negative than at pH 10.5. No particles were detected in the 42 µM U^{VI} solutions at pH 12.43, however, the size detection limit at 10 ppm (ca. 42 µM U mineral) is 100 nm therefore colloids with diameter <100 nm could be present in solution.[272]

Table 4.1. The particle diameter (nm) and zeta potential (Z_p) measurements of the U^{VI} precipitates at 25˚C. The size at the maximum peak height is provided along with the cumulative frequency size (Z-average) and corresponding polydispersity index (PDI). pH measured in a different laboratory at 17-18˚C. The error is one S.D. of the three measurement points. The pH error is typically 0.06 pH units.

Experiment	pH	Size– peak height (nm)	Size- Z average (nm)	PDI	Zp (mV)
pH 10.5 – 1	10.34	700 ± 100	780 ± 90	1	-23.5 ± 0.7
pH 10.5 – 2	10.34	700 ± 100	800 ± 100	1	-23.0 ± 0.7
pH 10.5 – 3	10.35	600 ± 100	710 ± 40	1	-21 ± 2
pH 10.5 – Average	**10.34**	**600 ± 100**	**760 ± 80**	**1**	**-22 ± 1**
pH 11.5 – 1	11.40	900 ± 200	1100 ± 100	1	-20 ± 1
pH 11.5 – 2	11.43	800 ± 100	1000 ± 100	1	-22 ± 1
pH 11.5 – 3	11.43	900 ± 100	1400 ± 300	1	-20.5 ± 0.8
pH 11.5 – Average	**11.42**	**800 ± 100**	**1200 ± 200**	**1**	**-20.9 ± 0.2**
pH 12.5 – 1	12.43	No particles	-	-	-
pH 12.5 – 2	12.47	No particles	-	-	-

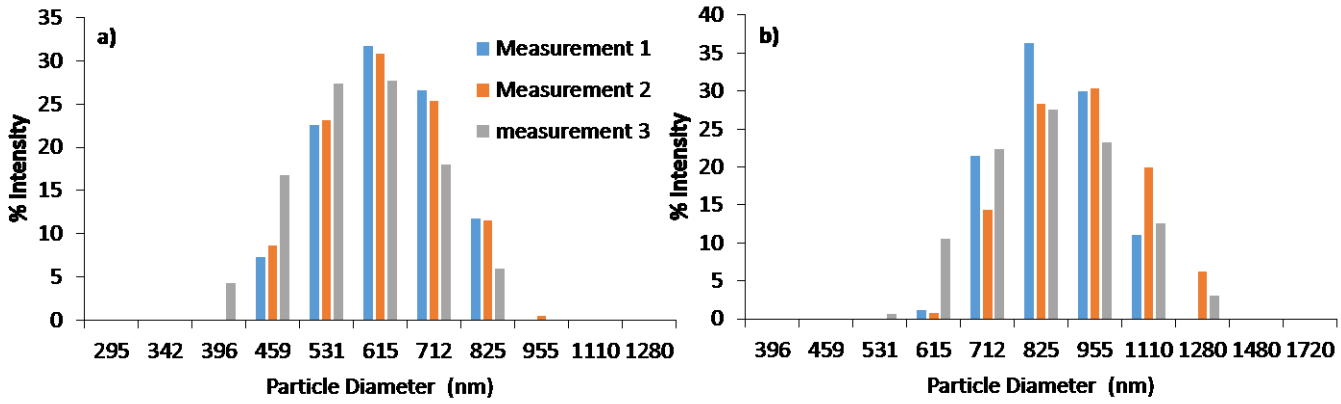

Figure 4.3. Size distribution of the U^{VI} precipitates by intensity for a a) pH 10.5 and b) pH 11.5 sample. The blue, orange and grey bars represent the first, second and third measurement for the samples.

4.3.2. TEM Imaging of the U^{VI} precipitates

Transmission electron microscopy (TEM) was used to gain further insight into the morphology of the U^{VI} precipitates. Energy dispersive spectroscopy (EDS) was used to confirm the precipitate contained U^{VI}. Images of only one or two precipitates were measured with TEM, therefore the DLS measurements provide more accurate information on the U^{VI} precipitate size distribution.

Figure 4.4 shows the U^{VI} precipitate in a solution initially prepared at pH 10.50. Locations A-E presented on Figure 4.4a were analysed with EDS (Figure 4.5). Location D (Figure 4.4a and 4.5a) allowed for the background pattern for the Cu sample holders to be characterised. Na and U dominates the EDS pattern (Figure 4.5b) of areas A-C on Figure 4.4a indicating the cloudy mineral is the U^{VI} precipitate with a sodium uranate type composition. This agrees with the U^{VI} saturation indices which predicted a sodium uranate type mineral to precipitate from solution (Figure 4.2b). The EDS spectra for location E (Figure 4.5c) on Figure 4.4a indicates the black mineral is NaCl. The total counts normalised against time collected for the U peak at 3.18 KeV in area E (26 counts/sec) are similar to that of areas A to C (14-29 counts/sec). This is also the case for the U peak at 3.35 KeV (E = 15 counts/sec, A-C = 8-18 counts/sec). This similar number of counts could indicate the sodium uranate precipitate overlies the NaCl crystal, however, U^{VI} could be sorbing to the NaCl mineral. The increased number of counts for Si observed in areas A-C and E with respect to the background spectra presented in area D is likely due to an increased sensitivity of the instrument as the Cu, C and O background peaks increase for areas A-C and E with respect to the background measurement (D). Therefore it is unlikely that the Si is due to solution contamination.

The image in Figure 4.4a shows the U^{VI} precipitate has a highly complex shape, and determining the diameters of the U^{VI} precipitates is challenging. The diameter of the U^{VI} precipitate along the y-axis of the figure is ≥1.125 µm while along the x-axis the diameter can be anything from 0.375 µm to ≥1.125 µm. Parts b, c and d of Figure 4.4 are images at a greater magnification of locations A, B and C

highlighted by the red circles on Figure 4.4a. These images show that the U^{VI} precipitate is comprised of an aggregation of 10's nm diameter crystals. The Fast Fourier Transform image highlights the crystals are oriented in many directions.

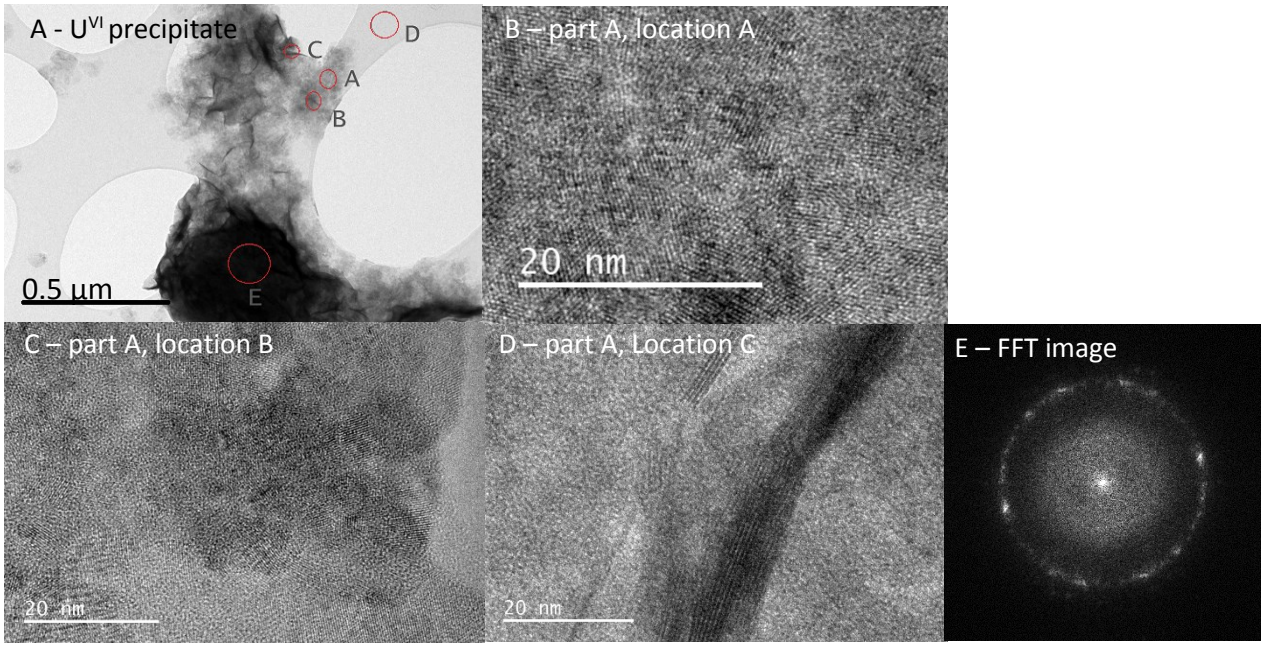

Figure 4.4. TEM images of the U^{VI} precipitates from an initially 42 µM U^{VI}, 0.1M NaCl pH 10.5 solution. Part A is at 8k magnification. Parts B, C and D were imaged at 400k magnification and represents Location A, B and C circled on part A. Part E is a Fast Fourier Transform image of the precipitate. A and D in this figure has been reproduced from Figure 6 in Kenney *et al.*[254]

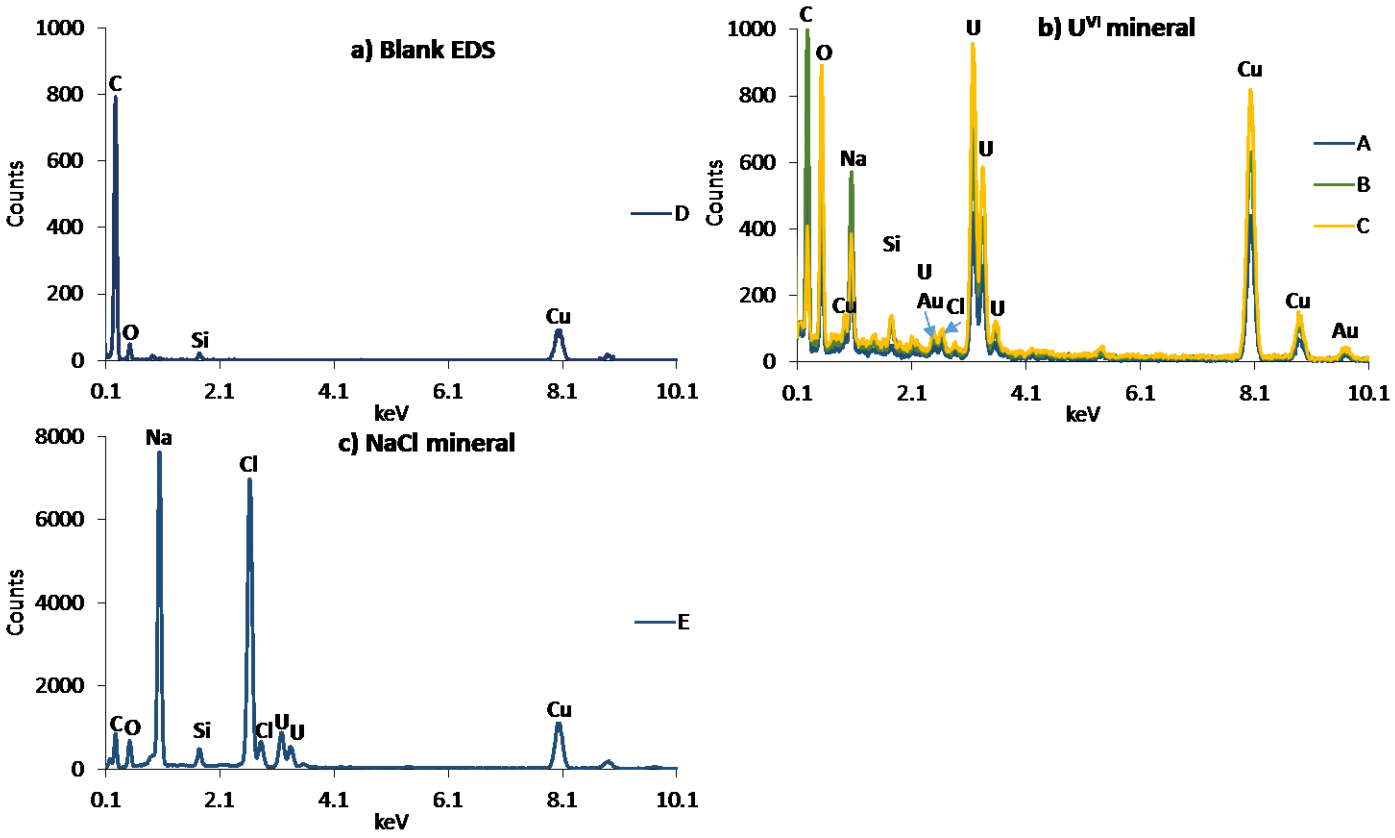

Figure 4.5. EDS patterns collected from locations D (A- Blank EDS), A-C (B – U^{VI} mineral) and E (C- NaCl) circled in red on Figure 4.3a. This figure has been reproduced from Figure 6 in Kenney *et al.*[254]

TEM images were also taken of a U^{VI} sample initially prepared at pH 11.50. Images of two particles were taken and are presented in Figure 4.6. The precipitate in Figure 4.6a has a diameter of ≥1.2µm in x direction and ≥ 0.8µm in the y direction. The U^{VI} precipitate in Figure 4.6b has a square shape with diameter of approximately 0.5 µm.

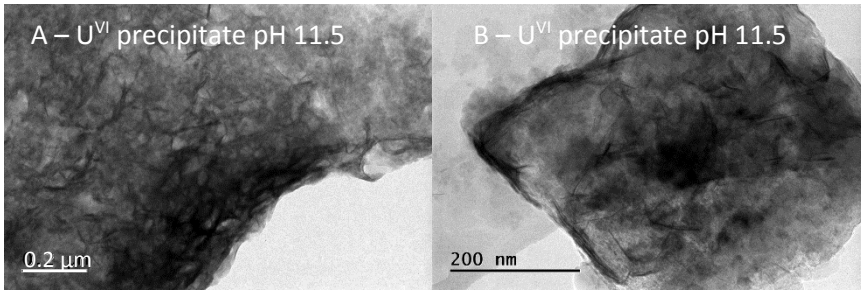

Figure 4.6. TEM images taken of the U^{VI} precipitates from an initially 42 µM U^{VI}, 0.1 M NaCl, and pH 11.5 solution.

The hydrodynamic particle diameter calculated by DLS (Table 4.1) for the U^{VI} particles at pH 10.5 (peak height = 600 ± 100 nm) and pH 11.5 (peak height = 800 ± 100 nm) is within the diameters observed in the TEM images (Figures 4.4 and 4.6) at pH 10.5 (375 to ≥1250 nm) and pH 11.5 (500 to ≥1200 nm). It is important to note that the DLS measures the particle diameter from the translation diffusion coefficient assuming the particles are spheroidal. When measuring non-spheroidal particles, the diameter measured by DLS is the diameter of a sphere which has the same translation diffusion coefficient as the non-spheroidal particle rather than the actual particle size.[249, 273]

Overall the TEM images show the U^{VI} precipitates were non-spheroidal, therefore the U^{VI} particles can be removed by the filter membranes which are larger than the pores average spheroidal diameter. The hydrodynamic diameter of the U^{VI} precipitates leads to an under predicted particle diameter due to the non-spheroidal nature of the U^{VI} precipitates. These results highlight the complex structure of the precipitates and the need for using several different measurement techniques.

4.3.3. U^{VI} mineral Identification using XRD

The saturation indices suggest multiple different sodium uranate type minerals could be precipitating from solution (Figure 4.2b). To determine the mineralogy the U^{VI} precipitates from 42 µM U^{VI}, 0.1 M NaCl at pH 10.5 and 11.5 were dried, washed with water to remove NaCl, and analysed using X-ray diffraction (XRD). The XRD patterns of the solid phase formed in solutions initially at pH 10.5 and 11.5 are presented in Figure 4.7.

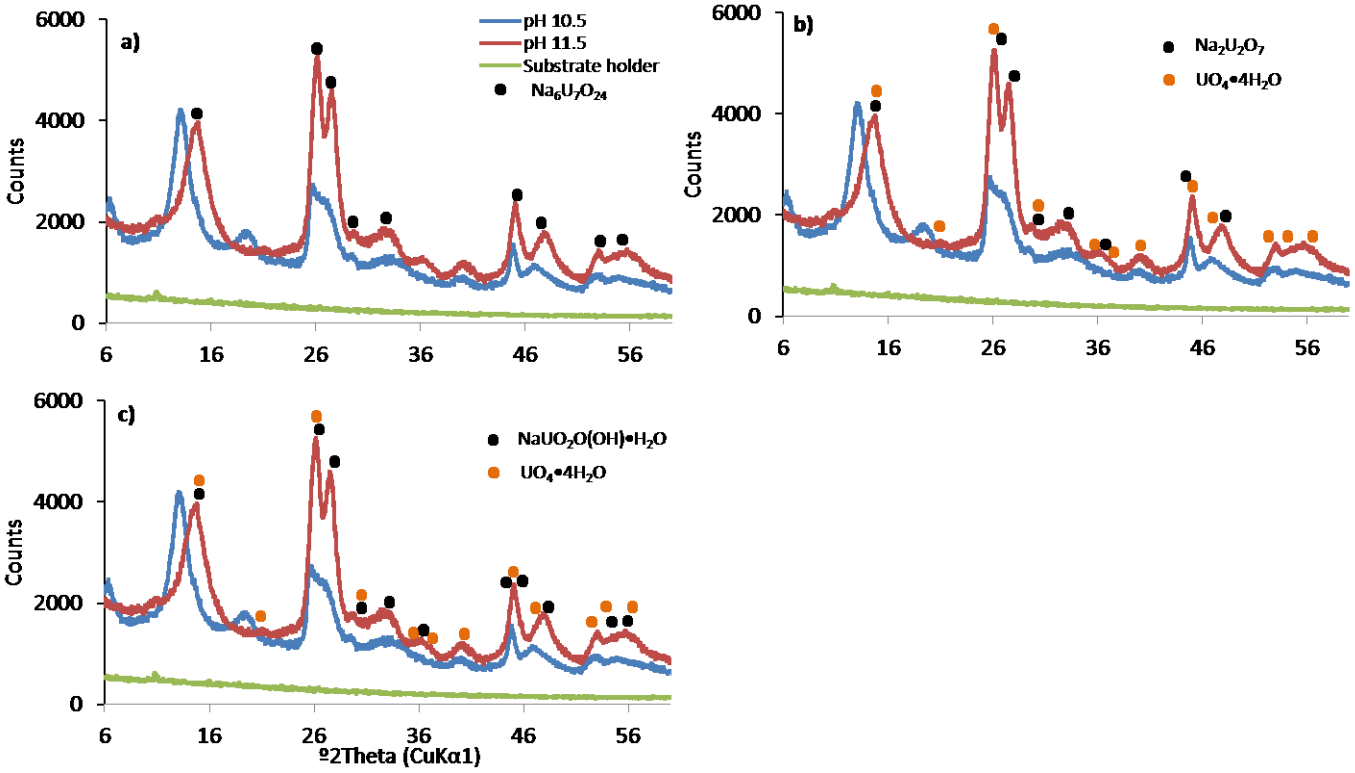

Figure 4.7. X-ray diffractograms of the U^{VI} containing solids obtained from solutions of 42 µM U^{VI}, 0.1 M NaCl originally prepared at pH 10.5 (blue) and pH 11.5 (red). The green diffractogram represents the sapphire substrate holder. Part a) contains the reference pattern for sodium diuranate $Na_6U_7O_{24}$ (black circles). Part b) contains the reference pattern for sodium diuranate ($Na_2U_2O_7$) and studtite ($UO_4•4H_2O$) as black and orange circles respectively. Part c) contains the reference pattern for clarkeite ($Na(UO_2)O(OH)•H_2O$) and studtite as black and orange circles respectively.

At pH 11.5, the standard with the greatest match is sodium diuranate ($Na_2U_2O_7$) with a slight deficiency of Na ($Na_6U_7O_{24,}$ (i.e. $Na_{1.72}U_2O_{6.86}$) PDF4 ICDD reference pattern [5-446]) [274] as shown in Figure 4.7a. However, several low intensity peaks in the experimental patterns are missing from the reference pattern (36.5° and 40.5° 2θ) which could suggest multiple mineral phases were present. These minerals could have been sodium diuranate ($Na_2U_2O_7$, PDF4 ICDD reference pattern [43-347])[275] combined with studtite ($UO_4•4H_2O$, PDF4 ICDD reference pattern [49-1821])[276] whose standard patterns are shown as black and orange circles in Figure 4.7b respectively. Alternatively it could have been clarkeite ($Na(UO_2)O(OH)]•H_2O$, reference pattern [50-1586])[277] combined with studtite, shown by the black and orange circles in Figure 4.7c, respectively. A combination of sodium diuranate and

studtite, or clarkeite and studtite could account for the unidentified peaks at 36.5° and 40.5° 2θ. Identifying whether the mineral is clarkeite or sodium diuranate is challenging by XRD as the diffractograms are almost identical.[265, 277] The diffraction pattern does not match any uranium mineral containing silicon or sodium chloride when compared to the standard patterns catalogued in the PDF4 ICDD database.

The peaks at pH 10.5 shifted to a lower angle compared to the pH 11.5 sample, a new peak was observed at 19°, and another disappeared at 36.5°. No sodium uranate reference patterns in the PDF4 ICDD 2014 database matched the pH 10.5 experimental pattern, but due to its similarity to the pH 11.5 experimental pattern, and the $Na_6U_7O_{24}$ standard pattern, the U^{VI} precipitated at pH 10.5 was likely a similar mineral phase. The differences in the patterns at pH 10.5 and pH 11.5 could be due to differences in the state of hydration of the mineral as changing the hydration of a mineral can change the size of the d-spacings of the mineral and subsequently the angle at which the X-rays diffract.[278]

4.4. Quartz Sand Characterisation

The physicochemical properties of the quartz sand were characterised before exploring U^{VI} transport through quartz sand. To test the purity of the quartz sand, XRD measurements were conducted. The quartz sand was crushed to a powder with a mortar and pestle and subsequently analysed with XRD. The XRD pattern presented in Figure 4.8 was compared to reference pattern 00-046-1045[279] highlights that only the quartz mineral phase was detected.

The effective charge of the quartz sand was determined by measuring the Z_p using DLS. The sand was crushed with a mortar and pestle and the hydrodynamic diameter of the particles were measured using DLS (Table 4.2). The average hydrodynamic diameter of two independent samples of the crushed quartz sand was 700 ± 100 nm based on peak intensity. The Z-average value was 900 ± 100 nm and the corresponding PDI is 1 indicating a polydisperse sample. The average Z_p of triplicate

independent samples were -41 ± 1 mV, -42 ± 2 mV and -34 ± 2 for pH 10.5, 11.5 and 12.5 respectively. Z_p measurements of 1-5 µm diameter quartz sand particles at pH 9 in 0.1 M NaCl provide similar results of approximately -38 mV.[280] Previous research indicates that the Z_p reaches a steady state by pH 7 for quartz sand and colloidal silica in $1x10^{-1}$ to $1x10^{-3}$ M KCl background electrolyte.[281] The similar agreement between the Z_p of the samples at pH 10.5-12.5 with those at pH 9 provide independent validation of the Z_p measurements.

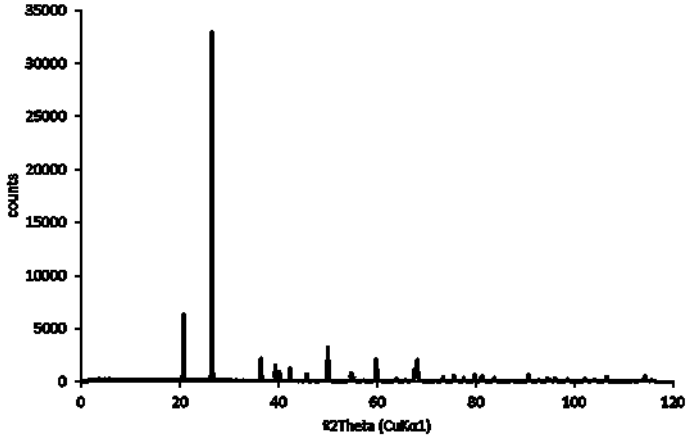

Figure 4.8. X-ray diffractogram of the quartz sand sample checked against the standard in Ref. 279. Peaks with %intensity >10% are at 20.9˚ and 26.6˚ 2θ.

Table 4.2. Zeta potential (Z_p) analysis of quartz sand in the pH range of interest at 25˚C. The pH was measured in a different laboratory at 20 ˚C. The errors are one standard deviation from three measurement points. 1 S.D. error of the pH measurements was typically ± 0.03 pH units.

Experiment	pH	Z_p (mV)
pH 10.5 – 1	10.45	-43.2 ± 0.4
pH 10.5 – 2	10.50	-43 ± 2
pH 10.5 – 3	10.44	-36 ± 2
pH 10.5 – Average	**10.46**	**-41 ± 1**
pH 11.5 – 1	11.53	-43 ± 2
pH 11.5 – 2	11.53	-41 ± 2
pH 11.5 – 3	11.52	-42 ± 2
pH 11.5 – Average	**11.53**	**-42 ± 2**
pH 12.5 – 1	12.54	-35 ± 2
pH 12.5 – 2	12.55	-37 ± 2
pH 12.5 – 3	12.55	-31 ± 2
pH 12.5 – Average	**12.55**	-34 ± 2

The grain, pore, and pore throat size distributions of a packed sand column were extracted from X-ray Computed Tomography (CT) images. These distributions are provided in Figure 4.9a to 4.9c. The quartz grains are angular with a bimodal grain size distribution. The two dominant grain diameters were 20 µm and between 60 to 240 µm. The sand had a median grain size (d_{50}) of 120 µm. The pore and pore throat diameters were usually between 10 to 34 µm and 4 to 20 µm respectively, in agreement with typical literature values for the diameter of sand grains observed in this system.[282]

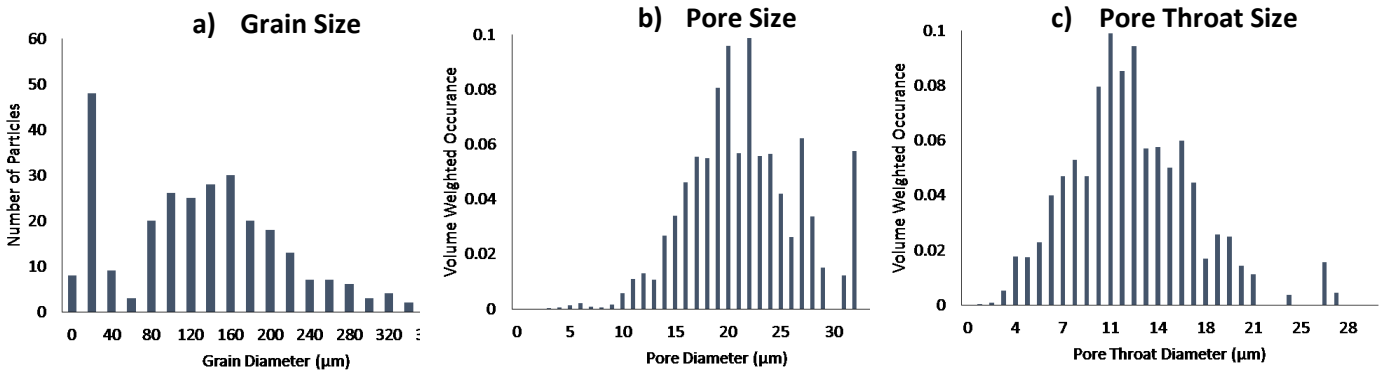

Figure 4.9. Physical properties of a representative sand column extracted from CT images. Figure 4.7a, b and c shows the distributions of the grain, pore and pore throat diameters.

4.5. U^{VI} transport through quartz sand in 0.1 M NaCl solutions between pH 10.5-12.5

To test the mobility of 42 µM U^{VI} in 0.1 M NaCl solutions at pH 10.5, 11.5 and 12.5, the U^{VI} solutions were injected into the quartz sand packed columns. The physical properties of the column experiments are provided in Table 4.3. The flow rate (Q) used in the column experiments were between 0.45-0.53 ml/min. The darcy velocity (q) calculated from the flow rate was between 0.34-0.40 cm/min, similar to the velocity used by Bradford *et al.*[156] (0.10 cm/min) and Xu *et al.*[173] (0.31 cm/min) during particle transport experiments.

Table 4.3. The physical properties of the quartz sand columns. The parameters provided are the dry bulk density (ρ_b), pore volume (PV), porosity (ϕ), flow rate (Q), darcy velocity (q) and average linear velocity (v). The error provided for Q, q and v is one standard deviation of greater than 10 measurements during U^{VI} injection.

Experiment	ρ_b (g/cm^3)	PV (ml)	ϕ	Q (cm^3/min)	q (cm/min)	v (cm/min)
pH 10.5-R1	1.60	11.09	0.45	0.45 ± 0.02	0.34 ± 0.02	0.76 ± 0.04
pH 10.5-R2	1.60	10.77	0.44	0.45 ± 0.03	0.34 ± 0.02	0.77 ± 0.05
pH 11.5-R1	1.68	11.10	0.45	0.53 ± 0.04	0.39 ± 0.03	0.88 ± 0.07
pH 11.5-R2	1.62	10.69	0.43	0.47 ± 0.02	0.36 ± 0.02	0.83 ± 0.04
pH 12.5-R1	1.59	7.86	0.31	0.52 ± 0.09	0.39 ± 0.06	1.25 ± 0.21
pH 12.5-R2	1.59	8.78	0.35	0.53 ± 0.12	0.40 ± 0.09	1.13 ± 0.25

The pH and Si concentration data are provided in Table 4.4. During the pH 12.5 experiment, the Si concentration of the inlet solution was less than the limit of quantification (LOQ). The limit of quantification (LOQ) of the ICP-AES was 2 µM during analysis of the pH 12.5 experiments. The samples were diluted six times during analysis of the pH 12.5 samples, leading to an overall LOQ of 10 µM. The pH 12.5 samples were below the LOQ, hence there could be < 10 µM Si present in solution. The LOQ during the pH 10.5 and pH 11.5 sample analysis was 0.3 µM. The samples were diluted 10 times leading to an overall LOQ of 3 µM. The results indicated there was minor contamination with Si during the pH 10.5 and pH 11.5 (10-20 µM) experiments. Glass was not used during the experiments which should minimise Si input due to dissolution, and analytical grade chemicals were used. The experiments were conducted in a trace metals laboratory and not a clean room laboratory with a controlled atmosphere, therefore minor amounts of Si could potentially enter the samples from the atmosphere.

Table 4.4. The pH and [Si] measured during the column experiments. The pH was measured in the column inlet solution (pH inlet) and samples collected at the outlet (pH outlet). The Si concentration was measured in the inlet solutions ([Si] inlet) and in samples collected at the outlet before U^{VI} injection and during U^{VI} injection. Si concentration errors are one S.D. of three samples. Si data without errors were obtained from one sample. The standard error for pH was typically ±0.05 pH units.

Experiment	Figure	pH inlet	pH outlet	[Si] inlet (µM)	[Si] outlet before U^{VI} injection (µM)	[Si] outlet during U^{VI} injection (µM)
pH 10.5 – R1	4.11A	10.32-10.55	10.07-10.37	10-20	40 ± 10	50 ± 10
pH 10.5 – R2	4.11A	10.26-10.54	10.04-10.36	10-20	30	40
pH 11.5 – R1	4.11B	11.43-11.47	11.39-11.40	10	90 ± 20	40 ± 10
pH 11.5 – R2	4.11B	11.37-11.49	11.26-11.40	20	40	80
pH 12.5 – R1	4.3A	12.40-12.47	12.30-12.45	<10	-	32.8 ± 0.7
pH 12.5 – R2	4.3A	12.40-12.47	12.33-12.46	<10	-	32.8 ± 0.7

The gravimetrically determined pore volume (PV) of the columns is 10.7-11.1 ml for the pH 10.5 and 11.5 column experiments, and 7.86-8.68 ml during the pH 12.5 column experiments. The porosity (ϕ) was calculated as 0.43-0.45 for the pH 10.5 and 11.5 experiments, and 0.31-0.35 for the pH 12.5 column experiments. The increased PV and ϕ at pH 10.5 and 11.5 was caused by changing to a wet packing method which reduce the amount of air entrapment. The Br non-reactive tracer tests for the experiments are provided on Figure 4.10 as black and orange circles for the first and second column experiments respectively. The Br data plotted on Figure 4.10a-c are provided in Tables B4-B6. The tailing during breakthrough of a Br free solution (after 3 PV) indicates non ideal behaviour. Ideal transport in this case assumes a homogenous porous media. [283] The grain size distribution extracted from the CT images (Figure 4.10) highlight the system was heterogeneous, and the non-ideal Br elution curves supports this. Trapped air in the pH 12.5 experiment does not appear to have effected transport as the behaviour of the Br tracer is similar for all the column experiments.

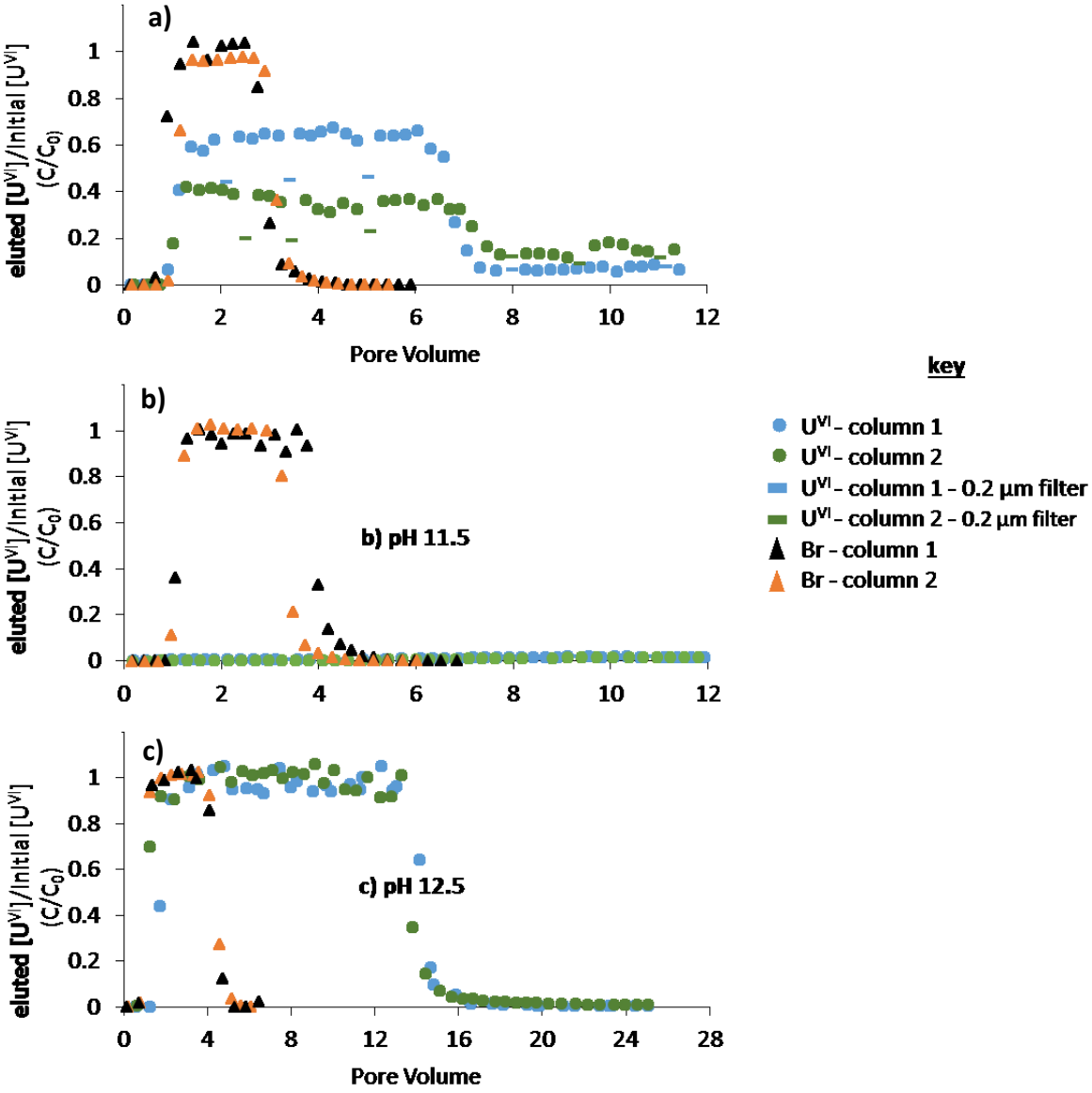

Figure 4.10. The U^{VI} and Br elution curves at a) pH 10.5, b) pH 11.5 and c) pH 12.5. The ICPMS error is ± 7% for U^{VI} measurements. The error bars for Br are typically ± 10% for measurements using both ion chromatography and ICP-MS. The U^{VI} data points are blue and green circles respectively for the first and second columns. The blue and green dashes on the elution curves is $[U]_{filtrate}/[U]_{initial}$ after the column outlet solution was filtered through 0.2 µm nylon filter membranes for column 1 and 2 respectively. The Br non-reactive tracer is included as black and orange triangles for the first and second column experiments and the Y axis becomes eluted Br/initial [Br]. The Br data plotted in a), b) and c) is presented in Table B4, B5 and B6 respectively. The U^{VI} data plotted in a), b) and c) is presented in Table B7, B8 and B9 respectively.

The concentration of U^{VI} in the filtrate at the start of U^{VI} injection at pH 10.5 was 22-24 µM (55-60%) and 13.9-18.5 µM (35-46%) for the two column experiments (Table 4.5). This is higher than that

observed in the batch experiments where the amount of U^{VI} remaining in the filtrate was 15-26% (Figure 4.1a). The concentration of U^{VI} in the filtrate at the start of U^{VI} injection at pH 11.5 was 0.92-1.00 µM (2%) and 0.92-1.01 µM (3%) for the two column experiments. This is less than the amount of U^{VI} remaining in the filtrate after 48 hours in the batch experiments (Figure 4.1b) where 5-10% remained in solution. The difference in amounts of precipitation occurring in the column inlet solutions, particularly at pH 10.5, is likely because stirred batch reactors were not used. When stirring is used, the amount of precipitation becomes more consistent. This is illustrated when comparing 42 µM U^{VI} precipitation in 0.1 M NaCl at pH 11.5 using stirred (Figure 4.11a) and static batch reactors (Figure 4.11b).

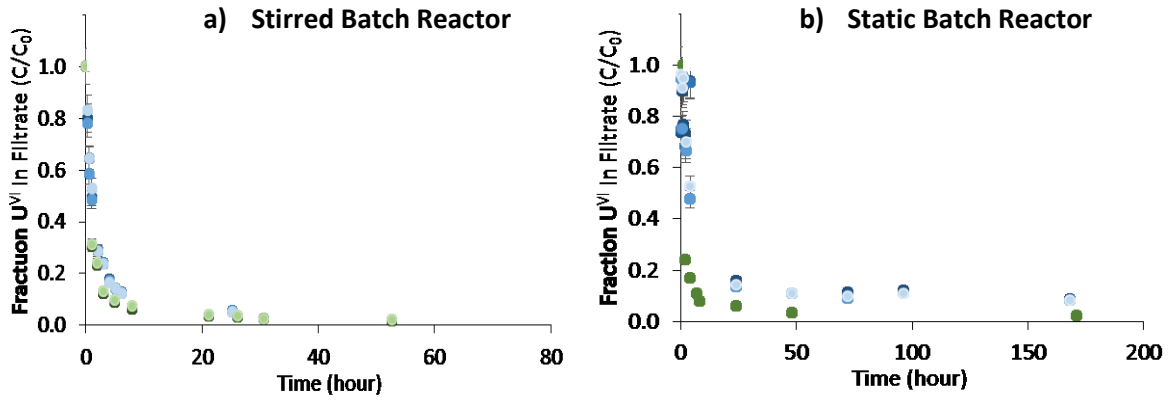

Figure 4.11. Comparison of U^{VI} precipitation in a 42 µM U^{VI}, 0.1 M NaCl and pH 11.5 solution using a) stirred batch reactors and b) static batch reactors. The blue and green data points represent the results of two repeat experiments, the shade of colour represent the filter membrane where the darkest shade is 0.2 µm pore diameter, and lightest shade is 1 µm diameter.

The U^{VI} elution curve data plotted in Figure 10a to 10c are given in Table B7 to B9. When the 42 µM U^{VI} suspension at pH 10.5 was injected into the quartz sand columns, approximately 26 µM (64%) and 15.1 µM (37%) of U^{VI} was eluted at the column outlet during the first and second column experiments respectively (Table 4.5, Figure 4.10a). This is similar to the concentration of U^{VI} which remained in the filtrate after samples of the U^{VI} column inlet solution were filtered through 0.2 µm, 0.45 µm and 1 µm membranes (Table 4.5, column 1 = 22 to 23 µM, column 2 = 14.7-15.1 µM). This indicates the U^{VI} particles contained within the 42 µM U^{VI} suspension were immobilised in the quartz sand columns when the U^{VI} suspension was injected into them.

Table 4.5. Details on the amounts of U^{VI} in solution during the column experiments. The results presented in column 2 and 3 of the table represent the concentration of U^{VI} in the filtrate after the U^{VI} input solution was filtered through 0.2, 0.45 and 1 µm filter membranes at the start and end of U^{VI} injection respectively. The average concentration of U^{VI} eluted at the column outlet during U^{VI} and U^{VI}-free solution injection is presented in columns 4 and 5 of the table respectively. The concentration of U^{VI} in filtrate after samples collected at the column outlet was filtered through a 0.2 µm filter membranes are given in columns 6 and 7 during U^{VI} and U^{VI}-free solution injection respectively. The total % U^{VI} recovered following sand cleaning is presented in the final column.

Experiment	**[U^{VI}] (µM) in filtrate of U inlet solution**		**Average [U] (µM) eluted from column**		**Average [U] (µM) of U^{VI} in filtrate of samples filtered at column outlet**		**%U recovery**
	at start of U^{VI} injection	***at end of U^{VI} injection***	***U^{VI} injection***	***U^{VI}-free injection***	***U^{VI} injection***	***U^{VI}-free injection***	
pH 10.5 - 1	24 ± 1 (0.2 µm) 22 ± 1 (0.45 µm) 22 ± 1 (1 µm)	22 ± 1 (0.2 µm) 23 ± 1 (0.45 µm) 22 ± 1 (1 µm)	26 ± 1	2.9 ± 0.1	18.5 ± 0.8	2.7 ± 0.1	86 ± 7
pH 10.5 - 2	13.9 ± 0.4 (0.2 µm) 13.9 ± 0.4 (0.45 µm) 18.5 ± 0.8 (1 µm)	15.1 ± 0.4 (0.2 µm) 14.7 ± 0.4 (0.45 µm) 17.6 ± 0.8 (1 µm)	15.1 ± 0.4	5.9 ± 0.4	8.3 ± 0.3	4.2 ± 0.01	90 ± 5
pH 11.5 - 1	0.92 ± 0.08 (0.2 µm) 0.97 ± 0.08 (0.45 µm) 1.0 ± 0.1 (1 µm)	0.84 ± 0.04 (0.2 µm) 0.88 ± 0.04 (0.45 µm) 0.92 ± 0.08 (1 µm)	0.29 ± 0.04	0.59 ± 0.04	0.29 ± 0.04	0.63 ± 0.04	91 ± 9
pH 11.5 – 2	0.97 ± 0.04 (0.2 µm) 1.01 ± 0.04 (0.45 µm) 0.92 ± 0.04 (1 µm)	1.05 ± 0.04 (0.2 µm) 1.05 ± 0.04 (0.45 µm) 1.01 ± 0.04 (1 µm)	0.101 ± 0.004	0.550 ± 0.002	0.126 ± 0.004	0.61 ± 0.02	74 ± 4

When samples collected at the outlet of the column were filtered through 0.2 µm nylon filter membranes, approximately 18.5 µM (45%) and 8.3 µM (21%) of U^{VI} was present in the filtrate for the first and second column experiments respectively (Table 4.5, green and blue dashes in Figure 4.10a). This is 7.5 µM (19%) and 6.8 µM (16%) less than the average concentration eluted from column 1 (26 µM) and column 2 (15.1 µM) respectively. This indicates that 7.5 µM and 6.8 µM of U^{VI} were eluted from column 1 and 2 as precipitates with diameter ≥0.2 µm while the remaining 18.5 µM (45%) and 8.5 µM (21%) of U^{VI} eluted from column 1 and 2 were transported as a dissolved phase or as precipitates with <0.2 µm diameter. This also means the amount of U^{VI} which precipitated from solution increased during transport through the quartz sand. This could be due to the formation of a U^{VI} silicate mineral in the solution phase or heterogeneous precipitation on the quartz mineral surface.[145] It could also be a kinetic effect due to enhance solution mixing during solution transport through the tubing.

The saturation indices (Figure 4.2b) indicate that the U and Si containing mineral, sodium boltwoodite, could have precipitated from solution. Table 4.4 shows that at pH 10.5 the concentration of Si at the outlet before injection of the 42 µM U^{VI} suspension were 40 ± 10 µM and 30 µM for column 1 and 2 respectively. When U^{VI} was injected into the column, the Si concentration changed to 50 ± 10 µM and 40 µM for column 1 and 2 respectively. Table 4.4 shows that the Si concentration at the column outlet was 90 ± 20 µM and 40 µM for column 1 and 2 before U^{VI} was injected into the quartz sand column. During U^{VI} injection, the Si concentration changed to 40 ± 10 µM and 80 µM for column 1 and 2 respectively. The differences in Si concentration are within the analytical error for the pH 10.5 data, and the change in Si concentration is opposite between the two columns before and during U^{VI} injection for the pH 11.5 experiments. Therefore any sodium boltwoodite precipitating from solution must be leaving the column. Kenney *et al.*[254] observed U^{VI} precipitates occurred in solution, not on the quartz mineral surface, in the same chemical conditions employed during this study. This indicates that heterogeneous precipitation on the surface of the

quartz sand grains was not occurring. Overall the enhanced U^{VI} precipitation is likely a combination of Na boltwoodite precipitation and enhanced mixing within the column.

When the solutions were switched to a pH 10.5, 0.1 M NaCl solution which does not contain U^{VI}, approximately 2.9 µM (7%) and 5.9 µM (15%) of U^{VI} was eluted from column 1 and 2 respectively (Table 4.5). Meanwhile, the concentration of U^{VI} remaining in solution after samples collected at the column outlet were filtered through 0.2 µm filter membranes were 2.7 µM (6%) and 4.2 µM (12%) for column 1 and 2 respectively. This is approximately the same concentration of U^{VI} measured in samples which were not filtered at the outlet, indicating U^{VI} was not being eluted as ≥0.2 µm diameter particles.

When the pH 11.5, 42 µM U^{VI} suspension was injected into the quartz sand columns, 0.29 µM (< 1%) and 0.101 µM (< 1%) were eluted at the outlet of column 1 and 2 respectively (Table 4.5, Figure 4.10b). Filtering samples collected at the column outlet through 0.2 µm filter membranes (column 1 = 0.29 µM, column 2 = 0.126 µM) showed similar concentrations of U^{VI} in the filtrate as the unfiltered outlet samples (Table 4.5), indicating the mobile fraction was not the ≥ 0.2 µm U^{VI} precipitates. These results indicate that virtually all U^{VI} had precipitated from solution, and the U^{VI} particles were immobilised within the column. When the injected solution was changed to one which does not contain U^{VI}, the concentration of U^{VI} eluted at the column outlet were 0.59 µM (1 %) and 0.55 µM (1 %) in column 1 and 2 respectively. This is similar to the concentration of U^{VI} eluted during injection of the U^{VI} suspension. Filtering samples collected at the column outlet with 0.2 µm filter membranes (column 1 = 0.63 µM, column 2 = 0.61 µM) led to similar concentrations compared to the unfiltered samples collected at the column outlet. This indicates U^{VI} was not leaving the column in a particulate form.

At pH 12.5 (Figure 4.10c) the elution curves shows 100% of U^{VI} breaks through at the column outlet within 3.09 and 3.13 PV for columns 1 and 2 respectively. This is retarded by a factor of 2.38 and 2.61 with respect to 100% breakthrough of the non-reactive tracer. This shows that U^{VI} was highly mobile when ≥0.2 µm precipitates were absent.

The retention profile data for the pH 10.5 and pH 11.5 column experiments are provided in Table B10 and B11 respectively. The retention profiles of the column experiments at pH 10.5 (Figure 4.12a) show that increased quantities of the U^{VI} particles were immobilised near the column outlet. 7.3 µg U^{VI}/g sand and 48.5 µg U^{VI}/g sand were immobilised in the first 1.5 cm for columns 1 and 2 respectively. Below an average depth of 6.75 cm, the quantity of U^{VI} immobilised decreases slowly through the remaining length of column from 2.81 to 1.69 µg U^{VI}/g sand in column 1 and 2.90 to 2.40 µg U^{VI}/g sand in column 2. The retention profiles for the pH 11.5 experiments (Figure 4.12b) show virtually all U^{VI} was immobilised within the first 1.5 cm of the column, near the solution inlet.

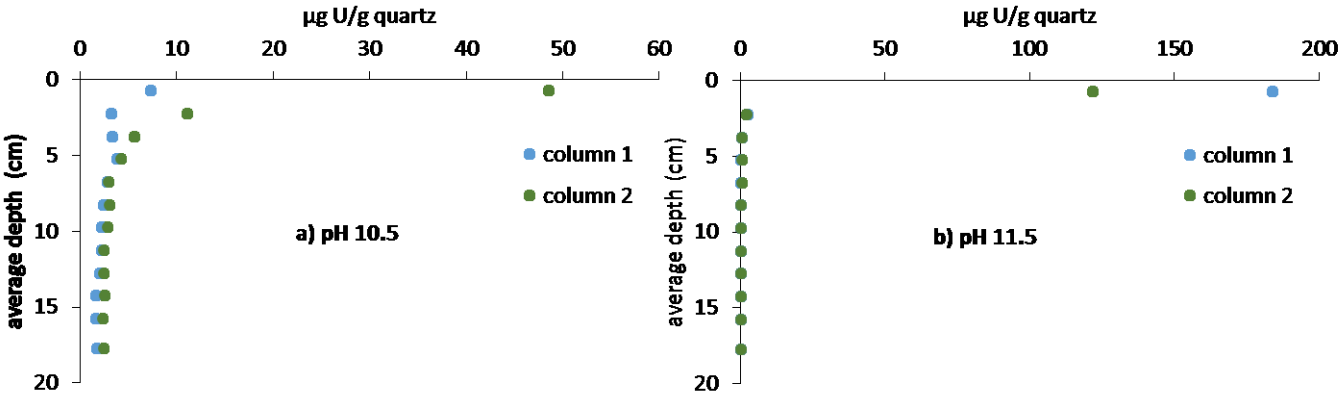

Figure 4.12. The retention profiles of U^{VI} at a) pH 10.5 and b) pH 11.5 for the first (blue) and second (green) column experiments respectively. The data plotted in a) and b) is provided in Table B10 and B11 respectively.

4.6. Possible mechanisms leading to U^{VI} immobilisation in quartz sand

The U^{VI} precipitates could have been immobilised by two main processes. The U^{VI} precipitates could have been immobilised due to attractive electrostatic and Van der Waals forces acting between the

U^{VI} precipitate and quartz sand. Alternatively the U^{VI} precipitates could have been physically immobilised due to the physical properties of the U^{VI} precipitates and quartz sand. The experimental results presented here suggest the latter processes.

The U^{VI} particles could have been immobilised physically in the column because of the physical properties of the porous media (pore size, pore throat size) and the U^{VI} precipitates (diameter). If the particles are bigger than the pores or pore throats then the particles will be trapped, a process known as particle straining.[156, 173] An empirical relationship of this straining process has been observed in glass beads and quartz sand columns, which relates the mean diameter of the travelling particles (d_p), and median grain size of the porous media (d_{50}). This relationship shows that significant immobilisation by straining occurs when d_p/d_{50} is >0.005-0.008.[156, 173] The median grain size (d_{50}) for the quartz sand was 120 µm while the average diameter of the U^{VI} particles is 600 nm and 800 nm at pH 10.5 and pH 11.5 respectively. The calculated d_p/d_{50} using these diameters is 0.005 and 0.007, within the range observed for significant straining.[156, 173] The d_p/d_{50} is further increased when considering the smaller size range observed in the bimodal distribution of the sand (Figure 4.9a). Assuming d_{50} is 20 µm, d_p/d_{50} increases to 0.032 and 0.042 for the precipitates formed at pH 10.5 and pH 11.5 respectively. The X-ray CT imaging indicates the pore and pore throat diameters were dominantly between 10 to 34 µm and 4 to 20 µm respectively (Figure 4.9b and 4.9c), in agreement with literature values for the diameter of sand grains observed here.[282] These pores and pore throats are larger than the U^{VI} precipitates diameter, however the resolution of the CT imaging was 3.5 µm which means pore throats with smaller diameters, which can be found within the quartz sand grain size distribution presented in Figure 4.9a,[282] cannot be observed.

The electrostatic and Van der Waals forces are described by the Derjaguin, Landau, Verwey and Overbeek (DLVO) theory, [159, 160] and have been studied extensively in laboratory experiments.[161-164] When the surfaces of the precipitates and mineral grains are oppositely charged, electrostatic and Van

der Waals forces strongly attach the particles to the mineral grain surface. [157, 158] When the surfaces of the precipitates and mineral grains have the same effective surface charge, short range electrostatic repulsion acts as a barrier to chemisorption and the travelling particles will only be weakly bound by van der Waals attraction.[157, 158] The effective surface charge is given by the Z_p of the precipitates (Z_p). The Z_p reported for the U^{VI} precipitates (Table 4.1) at pH 10.5 and 11.5 were -22 ± 1 mV and -20.9 ± 0.2 mV while the Z_p for the quartz sand (Table 4.2) at pH 10.5 and pH 11.5 were -41 ± 1 mV and -42 ± 2 mV. This means there is an energy barrier to chemical attachment of the U^{VI} precipitates to the quartz mineral surface. This is further evidenced by previous research[254] which observed that U^{VI} was not removed on the quartz surface during end over end rotating batch experiments, where the high solution to solid ratio prevents physical entrapment of U^{VI} precipitates. Therefore it seems unlikely that chemical attachment of U^{VI} to the quartz sand surface is occurring.

4.7. Conclusions

The aim of the research presented in this chapter was to increase current understanding of U^{VI} precipitation, the physicochemical properties of the precipitates, and characterise the subsequent transport of the U^{VI} precipitates through quartz sand. To do this a series of experiments were conducted in pH 10.5, 11.5 and 12.5 solutions containing 42 µM U^{VI} and 0.1 M NaCl. The batch experiments show that 73-85% and 89-96% formed ≥0.2 µm diameter precipitates after 48 hours. In situ size measurements made after 48 hours indicate the precipitates had a hydrodynamic diameter of 600 ± 100 nm and 800 ± 100 nm with Z_p -22 ± 1 and -20.9 ± 0.2 mV at pH 10.5 and pH 11.5 respectively. XRD indicate U^{VI} precipitated as sodium diuranate ($Na_6U_7O_{24}$), although a second phase may also be present.

All the particles at pH 11.5 were immobilised within 1.5 cm's of the column inlet. The effective surface charge for the U^{VI} particles and the quartz surface were both negative providing a first indication that there was a barrier to attachment. The d_p/d_{50} ratio indicate significant particle straining occurs in the

columns. Therefore immobilisation of the U^{VI} particles is attributed to the physical properties of the U^{VI} particles and quartz sand. Up to 19% of U^{VI} eluted from the columns in particulate form with diameter ≥0.2 µm. These are attributed to a mixture of mobile Na-Boltwoodite precipitates, and to further formation of sodium uranate minerals due to a mixing effect in the confined space of the tubing. The saturation indices of the silicate mineral Na-Boltwoodite was less than that of the sodium uranate, clarkeite and sodium-compreignacite minerals therefore the second mechanism is more likely to be occurring, limiting the impact of the Si contamination. The overall mobility of U^{VI} at pH 10.5 will likely remain the same in the absence and presence of the Si contamination. This is because in the absence of Si, the dissolved U^{VI} fraction was highly mobile as evidenced by the results from the pH 12.5 column experiments, and this had a similar mobility as the mobile fraction of U^{VI} precipitates which could be present as Na-Boltwoodite. The pH 11.5 experiments were not impacted by the Si contamination as virtually all U^{VI} had precipitated before injection into the quartz sand columns, and XRD measurements of samples representative of the U^{VI} inlet solution do not fit XRD standard patterns of uranium-silicate minerals.

These results show that in systems with high Na concentrations at pH 10.5 and 11.5, 42 µM U^{VI} will be immobilised in porous media, even though chemical interactions between the U^{VI} precipitates and quartz surface are unfavourable. Consequently, the conceptual model presented in Figure 9 in Kenney *et al.*[254] needs to be updated to reflect the reduced mobility of these precipitates between pH 10-12 in the quartz sand system. Cement based systems will be dominated by Ca containing U^{VI} minerals. The Z_p will likely be negative in 0.1 M ionic strength as the Z_p of calcium uranate precipitates is -22.2 mV in 0.01 M NaCl solutions.[267] The Z_p of U^{VI} and Si containing minerals will also likely be negative as Na-boltwoodite Z_p has been measured as approximately -45 mV above pH 10 in 0.1 M $NaClO_4$ solutions.[268] This suggests that chemical attachment of Ca and Si containing U^{VI} minerals to the quartz surface will be unfavourable. Therefore the transport of U^{VI} precipitates in these systems at 0.1 M ionic strength will be controlled by the physical properties of the U^{VI} precipitates and quartz sand,

analogous to the Na based system. The next steps are to conduct experiments which explore how the addition of multivalent (Ca^{2+} and Si^{4+}) effect aqueous U^{VI} precipitation to confirm this hypotheses.

Chapter 5 – Establishing a Cost Effective Density Functional Theory Protocol for Calculating log β Values of Geochemically Relevant Uranium Organic Ligand Complexes

Abstract

Uranium (U^{VI}) interacts with organic ligands, and subsequently controls the aqueous chemistry of U^{VI}. It is therefore imperative to assess the binding ability of natural organic molecules. In this chapter it is shown that density functional theory (DFT) can be used as a practical protocol for predicting the Gibbs free energy of reaction ($\Delta_r G$) and subsequently the stability constant (log β) of U^{VI} organic ligand complexes, allowing for the development of stability series for organic complexes with limited experimental data. Solvation methods and DFT settings were benchmarked to suggest a suitable off-the-shelf solution. The results indicate the IEFPCM solvation method should be employed. A mixed solvation approach improved the accuracy of the calculated $\Delta_r G$, however, the calculated $\Delta_r G$ were approximately four to six times more favorable than experimental data. Different basis sets, density functional approximations (DFAs) and effective core potentials were tested to check there are no major changes in molecular geometries and Gibbs free energy of reaction $\Delta_r G$. The recommended method employed is the B3LYP DFA, aug-cc-pVDZ basis set for ligands, MDF60 ECP and basis set for U^{VI}, and the IEFPCM solvation model. Using the fitting approach employed in the literature with these updated DFT settings allows fitting of 1:1 U^{VI} complexes with root mean square deviation of 1.18 log β units. Fitting multiple bound carboxylate ligands indicate a second, separate fitting for 1:2 and 1:3 complexes.

5.1. Introduction

Previous research found that siderophores can complex with uranium (log β 17.12-30.00)[1, 57, 116, 284] leading to the dissolution of uranium containing minerals[92, 115, 117] and desorption from mineral surfaces.[120, 285] This shows that siderophores have a significant impact on the aqueous chemistry and subsequent mobility of U^{VI} in simple laboratory experiments. Therefore the stability of U^{VI}-siderophore complexes need to be further understood.

The experimental determination of log β values often require multiple experimental techniques which is time consuming and labor intensive. It can be difficult to use certain experimental techniques such as potentiometric titrations in high pH and high ionic strength solutions due to the sodium error when using glass electrodes.[286] It can also be difficult to explore experimentally due to the formation of U^{VI} precipitates above circumneutral pH values at typical concentrations required for these experimental techniques (> mM U^{VI} concentration). Density functional theory (DFT) provides a cost-effective and radiation free way to estimate the log β of U^{VI} complexes as it computes the Gibbs energy (G) directly for each species in metal-ligand complexation reactions, allowing for the subsequent calculation of log β values.

The log β values for U^{VI} ligand reactions were calculated before using DFT.[125] The absolute values, however, were typically 10 log β (> -60 kJ/mol)[287, 288] or >30 log β units too positive.[125] Although absolute values differed from experiment, the relative values estimated chemical trends correctly. The accuracy and computational cost of log β calculations in aqueous conditions depends on four different model chemistry aspects in the DFT protocol suggested here. These are the solvation method employed, the effective core potential (ECP), basis set and density functional approximation (DFA). This is represented by Equation 6.1.

$$\log \beta = \mathrm{f}(\text{ solvation method}, \mathrm{ECP}, \text{basis set}, \mathrm{DFA}) \quad (6.1)$$

The reaction energy error associated with the DFA from benchmarking studies is between 10-64 kJ/mol (log β = 2-11) when optimized using the def2-QVZP basis set.[187] The error associated with reaction enthalpies is 10-53 kJ/mol (log β = 2-9) when comparing DFT calculations conduced with small-core ECPs to DFT calculations using all-electron relativistic calculations (excluding spin-orbit) when using the same DFA and basis set.[233] At the B3LYP level of theory, mean errors in atomization reaction energies for Pople's basis sets and Dunning's correlation consistent basis sets are between 2.5-22 kJ/mol (log β = 0.5-4).[289] Errors in water exchange reaction for UO_2^{2+} can be between 1 and 41 kJ/mol (log β = 1-7) when using B3LYP DFA, MWB60 ECP for U and aug-cc-pVTZ for ligands.[38]

Computational methods generally model water molecules that are not directly coordinated with U^{VI} implicitly to save on computational cost. The structure geometries and calculated log β, however, can be improved using a mixed solvation method as it more successfully incorporates solute-solvent cavity and dispersion terms.[176] This approach has to date only been explored for uranyl in detail for water exchange reactions.[36, 38, 211] A mixed approach was employed for 1:1 U^{VI} acetate, oxalate and catecholate complexes.[53]

To counter the absolute errors in log β, a fitting approach is often employed. In this case the computed log β of different complexes are plotted against experimental data, and the fitting curve is used to calculate fitted log β values. This was successfully applied for a variety of metal centres with ligands including siderophores.[110, 290, 291] Recently, this approach was also applied to 1:1 U^{VI} complexes for oxygen donor ligands allowing for prediction of log β value to within <1 unit (root mean square deviation).[125] This approach optimised the structures of interest in the gas phase using the B3LYP DFA, the 6-311++g(d,p) basis set for ligand atoms and the Stuttgart 1997 ECP (SSC) for U, (B3LYP/SSC/6-311++g(d,p) model chemistry). A frequency calculation was then conducted using the B3LYP/SSC/6-31g(d) model chemistry to calculate the gas phase Gibbs energy of the structures. Solvation was taken into account by doing single point energy calculations on the gas-phase optimized structures followed

by frequency calculations using the IEFPCM model with the solvation cavity being generated through UFF radii. The protocol developed in Vukovic *et al*.[125] was used in combination with the SMD implicit solvation model[221] in recent uranyl studies.[235, 236] However, the protocol used a model chemistry with prohibitive computational costs when investigating ligands containing tens of atoms and establishing a method for large ligands is key for modeling siderophore complexes. Furthermore, the solvation cavity used in the SMD model has not been parameterised for actinides.[221]

The aim of the research presented in this chapter is to establish a computationally cost-effective protocol which allows us to estimate the relative stability of functional groups that comprise the reactive components in siderophores. The protocol needs to be sufficiently cost-effective so that it can be applied to full siderophore structures in future research. Initially different solvation methods were tested as the greatest error in calculated stability is expected to be due to solvation. This was tested for 1:1, 1:2 and 1:3 U^{VI}-acetate complexes. Two implicit solvation methods were subsequently tested to examine whether a method which better calculates non-electrostatic contributions improved the calculated complex stability. A mixed solvation approach was employed where each aqua ligand was represented as one U^{VI} bound aqua ligand whose hydrogen atoms form one hydrogen bond to an explicit solvent molecule, $(H_2O)(H_2O)_2$. This was done to investigate if the approach proposed by Gutowski and Dixon[38] improves calculated log β, and whether this outweighs the difficulties associated with applying this method. After this, the effect of changing ECP, basis set size and functional was tested to establish the magnitude of differences in log β for the three U^{VI} acetate complexes (1:1, 1:2, and 1:3). A fitting equation was then established using the seven different ligands presented in Figure 3.5. These seven ligands were selected as they are similar, or the same as the functional groups which comprise the reactive components of siderophores, and have structural and stability data which the protocol can be validated against. Finally, the protocol was used to estimate the log β of 1:1, 1:2 and 1:3 uranyl carboxylate complexes and potential fitting trends were analyzed.

5.2. Implicit solvation models

For all calculations, the base model chemistry employed the B3LYP functional, aug-cc-pVDZ basis set for ligands and MDF60 ECP with the corresponding basis set for U^{VI}. The only exception to this rule applied when the U^{VI} ECP and basis set was explored. In this case the calculations used the cc-pVDZ ligand basis set to be consistent with the cc-pVDZ-PP basis set for U^{VI}. The effects of using two different implicit solvation methods, IEFPCM and SMD, on $\Delta_r G$ was studied and the results are shown in Table 5.1 and Figure 5.1. The thermodynamic parameters (H, TS, G) are provided in Table C1. Representative structures of the three U^{VI}-acetate complexes are provided in Figure 5.2. The experimental structural data for $[UO_2(H_2O)_5]^{2+}$, $[UO_2(H_2O)_3(Acet)]^{+}$, $[UO_2(H_2O)(Acet)_2]^{0}$ and $[UO_2(Acet)_3]^{-}$ were generated from EXAFS or high energy x-ray scattering (HEXS) conducted in aqueous solutions.[31-34]

Table 5.1. Average bond lengths (Å), angles (°) and $\Delta_r G$ (kJ/mol) for acetate (Acet) complexes calculated in the gas phase and using the IEFPCM and SMD implicit solvation models with the B3LYP/aug-cc-pVDZ/MDF60 model chemistry. The thermodynamic parameters (H, TS, G, $\Delta_r G$) are provided in Table C1.

Complex	Figure	Solvation	U=O (Å)	O=U=O (°)	U-O_{water} (Å)	U-$O_{acetate}$ (Å)	$\Delta_r G$ (kJ/mol)
$[UO_2(H_2O)_5]^{2+}$	5.2a	Experiment	1.764 – 1.790[a-d]		2.403 – 2.420[a-d]	-	-
		Gas phase	1.753	180	2.499	-	-
		IEFPCM	1.761	179	2.470	-	-
		SMD	1.775	179	2.566	-	-
$[UO_2(H_2O)_3(Acet)]^{+}$	5.2b	Experiment	1.771[a]		2.350[a]	2.465[a]	-19 ± 5[e]
		Gas phase	1.771	172	2.527	2.365	-863
		IEFPCM	1.774	176	2.480	2.410	-119
		SMD	1.785	178	2.535	2.479	-60
$[UO_2(H_2O)(Acet)_2]^{0}$	5.2c	Experiment	1.77[a,d]		2.350[a]	2.465[a]	-29 ± 5[e]
		Gas phase	1.777	180	2.539	2.432	-1361
		IEFPCM	1.784	173	2.520	2.457	-219
		SMD	1.791	180	2.568	2.494	-94
$[UO_2(Acet)_3]^{-}$	5.2d	Experiment	1.780[a]		-	2.47[a]	-43 ± 4[e]
		Gas phase	1.787	180	-	2.519	-1510
		IEFPCM	1.794	180	-	2.498	-271
		SMD	1.796	180	-	2.535	-115

[a]Ref. 31, [b]Ref. 32, [c]Ref. 33, [d]Ref. 34 [e]reaction energies from Ref. 135 corrected to zero ionic strength using the Specific Ion Theory outlined in Ref. 246.

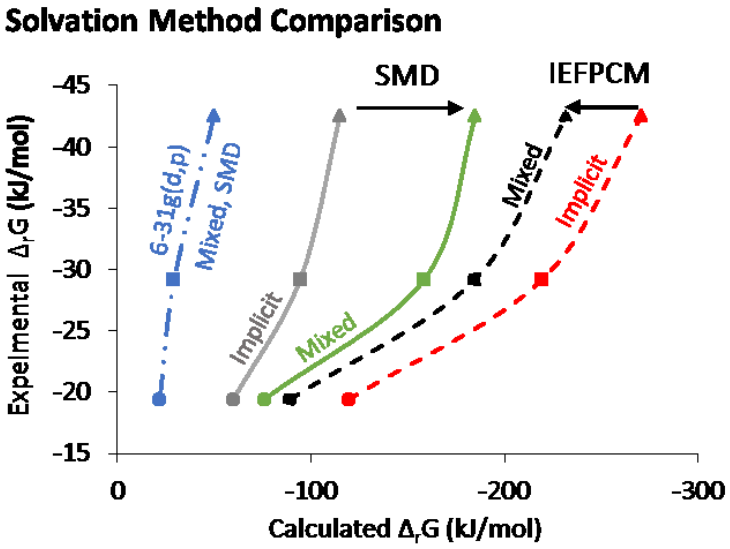

Figure 5.1. A comparison of calculated (x-axis) and experimental (y-axis) $\Delta_r G$ (kJ/mol) for the formation of 1:1 (circles), 1:2 (squares), and 1:3 (triangles) uranyl acetate complexes. The plot shows the effect of changing the solvation method. The ligand basis set is aug-cc-pVDZ unless otherwise stated. The experimental data is from Ref. 135 corrected to zero ionic strength using the Specific Ion Theory (Ref. 246). The $\Delta_r G$ presented in this figure is provided in Table 5.1 for implicit solvation and Table 5.2 for mixed solvation. The thermodynamic parameters (H, TS, G, $\Delta_r G$) are provided in Table C1 and C2 for the implicit and mixed solvation models.

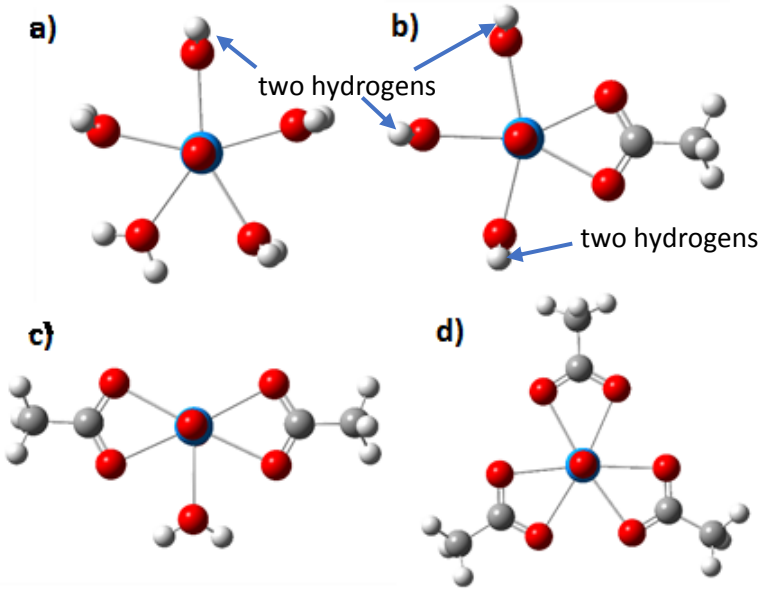

Figure 5.2. Representative structures of a) the aqueous uranyl complex $[UO_2(H_2O)_5]^{2+}$ and b) the 1:1 uranyl acetate c) 1:2 uranyl acetate and d) 1:3 uranyl acetate complexes optimised using B3LYP/ aug-cc-pVDZ/MDF60/IEFPCM model chemistry.

The structures were optimized with the standard Gaussian convergence criteria rather than opt = tight. Lengthening all bonds in the uranyl, uranyl-acetate, water and acetate structures when using the IEFPCM model changed $\Delta_r G$ by +2, +3 and +6 kJ/mol for the formation of 1:1, 1:2 and 1:3 uranyl acetate complexes respectively. This error is minor considering the larger differences to experimental $\Delta_r G$.

The SMD model should provide more accurate $\Delta_r G$ than IEFPCM. This is because the SMD model is a parameterised version of IEFPCM. It has been parameterised so that it better incorporates non-electrostatic contributions such as cavitation, dispersion and changes in local solvent structure.[221] Changing the implicit solvation model from IEFPCM to SMD changed $\Delta_r G$ by +59, +125 and 156 kJ/mol for U^{VI} complexation with one to three acetate ligands respectively, as shown in Table 5.1 and Figure 5.1. SMD was significantly more accurate for calculating $\Delta_r G$ when compared to the experimental data (-19,-29 and -43 kJ/mol)[135] highlighting the importance of non-electrostatic contributions.

Using the PCM solvation cavity option in the results toolbar of Gaussview 6 allows the solvation cavity to be visualised. The default cavity surface type generated during a Gaussian calculation is the Van der Waals surface and this surface is presented in Figure 5.3 for the SMD and IEFPCM solvation models. A downside of using the SMD method with metal containing systems is that the solvation cavity over-exposes metal density to the bulk solvent as seen in Figure 5.3a. This effect is the direct result of limited experimental data to calibrate SMD metallic radii for inorganic systems. This is an artifact of the way in which the non-electrostatic energy contributions were included into SMD. The solvation method was parameterised by adjusting the radii distance used to create the solvation cavity. This has only been applied to non-metallic elements typically found in organic ligands (e.g. H, C, N, O), and to date, the solvation method has not been parameterised for transition metals, lanthanides or actinides.[221] Therefore, the relative size of the cavity surrounding the U^{VI} metal center to the size of the cavity around the water molecules is much larger than it should be. The radii used to generate the

spheres were 1.860, 1.520 and 1.200 Å for the U, O and H atom respectively which resulted in a cavity surface area of 198.677 $Å^2$ and cavity volume of 131.501 $Å^3$. This is not the case for the IEFPCM model in Figure 5.3b. To generate the cavity spheres for each atom van der Waals radii generated using the universal force field (UFF) scaled by a factor of 1.1 was employed. The radii used for U, O and H atoms were 1.698, 1.750 and 1.443 Å leading to a cavity surface area 234.618 $Å^2$ of and cavity volume of 217.618 $Å^3$.

The modified method employed recently [235, 236] should be used cautiously due to the solvation cavity shortcomings of the SMD model, and ideally the IEFPCM model originally employed[125] should be used to predict the relative stabilities of U^{VI} complexes instead.

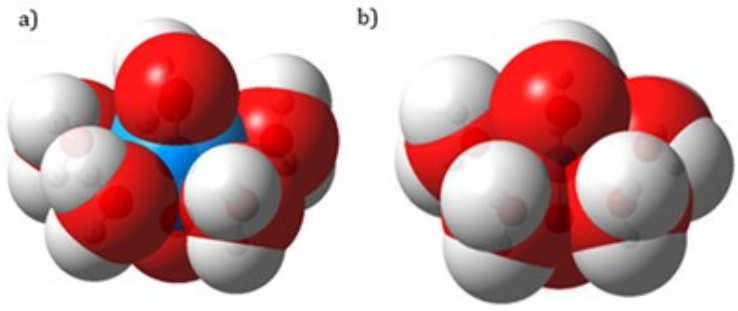

Figure 5.3. The solvation cavity $[UO_2(H_2O)_5]^{2+}$ which was generated as the van der Waals surface. Part a) is the SMD solvation cavity, and part b) is the IEFPCM solvation cavity. The cavity has been coloured to represent the contributions of the different elements to the cavity. Red represents oxygen, white represents hydrogen and blue represents uranium.

5.3. Mixed solvation model using IEFPCM as the implicit model

It has been observed that mixed solvation methods improve the accuracy of solvation energies.[38] This was explored for water exchange reactions between bulk water and U^{VI} bound aqua ligands.[38] Gutowski and Dixon[38] found that for accurate solvation energies, two water molecules were needed to solvate each U^{VI} bound aqua ligand, $[UO_2(H_2O)_5(H_2O)_{10}]^{2+}$. This approach was explored here for the U^{VI} complexation reactions with 1 to 3 acetate ligands, given in equations 5.1 to 5.3. The U^{VI} structures employed in equations 5.1 to 5.3 are shown in Figure 5.4 and the structural parameters and $\Delta_r G$ are

provided Table 5.2. The thermodynamic parameters (H, TS, G, $\Delta_r G$) are provided in Table C2. Sketches of Figure 5.4a-c are provided in Figure 5.5 to show that two water molecules are hydrogen-bonded to each U^{VI} bound aqua ligand.

$$[UO_2(H_2O)_5(H_2O)_{10}]^{2+} + CH_3OOH^- = [UO_2(CH_3OOH)(H_2O)_3(H_2O)_6]^+ + 6H_2O \quad (5.1)$$

$$[UO_2(H_2O)_5(H_2O)_{10}]^{2+} + 2CH_3OOH^- = [UO_2(CH_3OOH)_2(H_2O)(H_2O)_2]^0 + 12H_2O \quad (5.2)$$

$$[UO_2(H_2O)_5(H_2O)_{10}]^{2+} + 3CH_3OOH^- = [UO_2(CH_3OOH)_3]^0 + 15H_2O \quad (5.3)$$

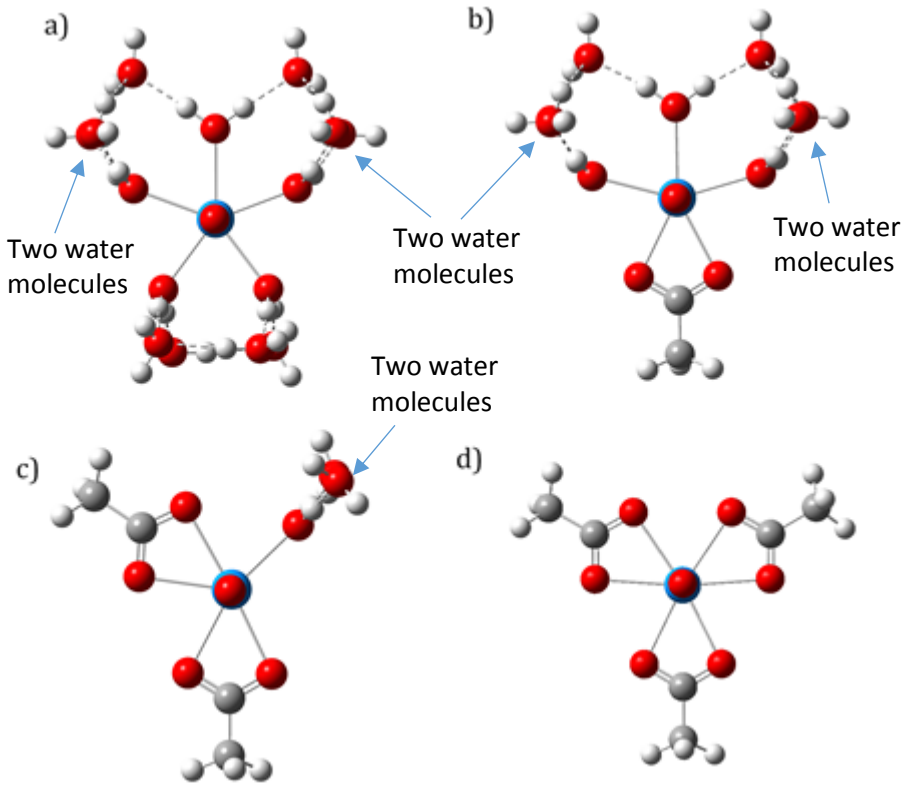

Figure 5.4. The a) uranyl water complex, and the b) 1:1, c) 1:2 and d) 1:3 uranyl acetate complexes used to work out $\Delta_r G$ in the mixed solvation methods. The uranyl complex was optimised from Ref. 38. The structures were optimised using the B3LYP/aug-cc-pVDZ/MDF60/IEFPCM model chemistry.

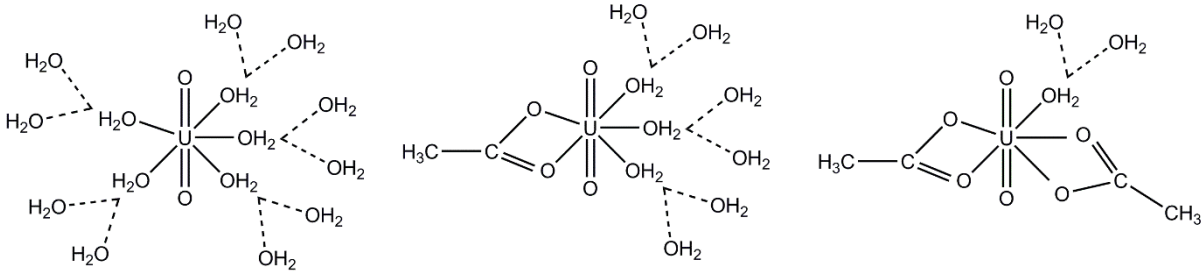

Figure 5.5. The sketches in a), b) and c) represent the structures in Figure 5.4a, Figure 5.4b and Figure 5.4c respectively.

Table 5.2. Average bond lengths (Å), angles (°) and $\Delta_r G$ (kJ/mol) for acetate (Acet) complexes using the mixed solvation approach where H_2O^* represents $(H_2O)(H_2O)_2$. The model chemistry is provided in the table. The thermodynamic parameters (H, TS, G, $\Delta_r G$) are provided in Table C2.

Complex	Figure	Model Chemistry	U=O (Å)	O=U=O (°)	U-O_{water} (Å)	U-$O_{acetate}$ (Å)	$\Delta_r G$ (kJ/mol)
$[UO_2(H_2O)_5]^{2+}$	5.4a	Experiment	1.764 – 1.790[a-d]		2.403 – 2.420[a-d]	-	-
$[UO_2(H_2O^*)_5]^{2+}$		aug-cc-pVDZ/ MDF60/IEFPCM	1.776	178	2.447	-	-
$[UO_2(H_2O^*)_5]^{2+}$		aug-cc-pVDZ/ MDF60/SMD	1.784	179	2.504	-	-
$[UO_2(H_2O^*)_5]^{2+}$		6-31g(d,p)/ MWB60/SMD	1.782	180	2.470	-	-
$[UO_2(Acet)(H_2O)_3]^{+}$	5.4b	Experiment	1.771[a]		2.350[a]	2.465[a]	-19 ± 5[e]
$[UO_2(Acet)(H_2O^*)_3]^{+}$		aug-cc-pVDZ/ MDF60/IEFPCM	1.781	179	2.449	2.436	-89
$[UO_2(Acet)(H_2O^*)_3]^{+}$		aug-cc-pVDZ/ MDF60/SMD	1.790	179	2.489	2.495	-76
$[UO_2(Acet)(H_2O^*)_3]^{+}$		6-31g(d,p)/ MWB60/SMD	1.782	179	2.462	2.474	-22
$[UO_2(Acet)_2(H_2O)]^{0}$	5.4c	Experiment	1.770[a,d]		2.350[a]	2.465[a]	-29 ± 5[e]
$[UO_2(Acet)_2(H_2O^*)]^{0}$		aug-cc-pVDZ/ MDF60/IEFPCM	1.786	178	2.425	2.461	-185
$[UO_2(Acet)_2(H_2O^*)]^{0}$		aug-cc-pVDZ/ MDF60/SMD	1.791	179	2.415	2.508	-159
$[UO_2(Acet)_2(H_2O^*)]^{0}$		6-31g(d,p)/ MWB60/SMD	1.787	179	2.421	2.471	-30
$[UO_2(Acet)_3]^{-}$	5.4d	Experiment	1.780[a]		-	2.470[a]	-43 ± 4[e]
$[UO_2(Acet)_3]^{-}$		aug-cc-pVDZ/ MDF60/IEFPCM	1.794	180	-	2.498	-232
$[UO_2(Acet)_3]^{-}$		aug-cc-pVDZ/ MDF60/SMD	1.796	180	-	2.535	-185
$[UO_2(Acet)_3]^{-}$		6-31g(d,p)/ MWB60/SMD	1.789	180	-	2.509	-50

[a]Ref. 31, [b]Ref. 32, [c]Ref. 33, [d]Ref. 34 [e]reaction energies from Ref. 135 corrected to zero ionic strength using method in Ref. 246.

The structures were chosen based on maintaining isodesmic reactions by preventing the formation of extra H bonds between water molecules which are not taking part directly in acetate complexation. If reactions are isodesmic, the number of bonds is preserved. If reactions are non-isodesmic and the resulting U^{VI}-L complex contains more or less bonds, then the stability of the complex will be higher or lower than it should be.[237] This can significantly affect $\Delta_r G$.

Using the mixed solvation method should reduce the errors compared to using the implicit method. This is because the explicit solvent molecules lead to an outward extension of the solvation cavity. This reduces the electrostatic interactions with the bulk solvent on the surface of the solvation cavity because it reduces the magnitude of the point charges on the solvation cavity surface caused by the positive charge of the U^{VI} atom. This subsequently reduces the $\Delta_r G$ dependence on the implicit model employed.[38, 211] As IEFPCM over-predicts solvation energies,[211] applying the mixed solvation approach should shift calculated $\Delta_r G$ to less negative values, and closer to the experimental data. When using the $[UO_2(H_2O)_5(H_2O)_{10}]^{2+}$ mixed solvation method $\Delta_r G$ changed by +30, +35 and +39 kJ/mol for one, two, and three acetate ligands respectively. However, this is still 70, 156 and 189 kJ/mol more negative than the experimental data for one, two and three acetate ligands, respectively. This is shown in Figure 5.1 and Table 5.2.

The calculated $\Delta_r G$ could be improved by releasing water as a cluster rather than as individual water molecules because it would keep the reaction isodesmic. The updated equations are presented in equation 5.4-5.6. For equations 5.4 and 5.5, the liberated water molecules were assumed to form a six-ring water structure. This was chosen rather than the three more energetically stable conformers[238] to maintain a consistent number of hydrogen bonds. In Equation 5.6, the final three water molecules were assumed to be released as a trimer. These two water clusters are presented in Figure 5.6. The standard state correction changes from -18 kJ/mol to -18/n kJ/mol for a cluster of $(H_2O)_n$ molecules.[243, 263] The reaction energies changed by +4, +9 and +4 kJ/mol to -85, -176 and -227 kJ/mol respectively. This suggests there is little improvement in releasing the water molecules as a cluster.

$$[UO_2(H_2O)_5(H_2O)_{10}]^{2+} + CH_3OOH^- = [UO_2(CH_3OOH)(H_2O)_3(H_2O)_6]^+ + (H_2O)_6 \quad (5.4)$$

$$[UO_2(H_2O)_5(H_2O)_{10}]^{2+} + 2CH_3OOH^- = [UO_2(CH_3OOH)_2(H_2O)(H_2O)_2]^0 + 2(H_2O)_6 \quad (5.5)$$

$$[UO_2(H_2O)_5(H_2O)_{10}]^{2+} + 3CH_3OOH^- = [UO_2(CH_3OOH)_3]^0 + 2(H_2O)_6 + (H_2O)_3 \quad (5.6)$$

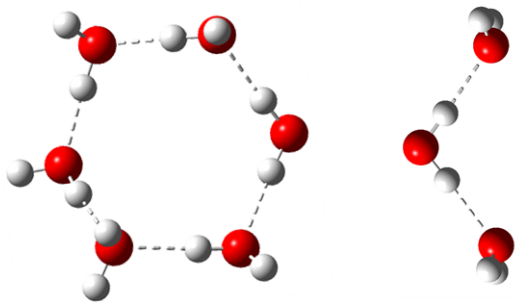

Figure 5.6 Part a) is a six water ring cluster and part b) is a three water cluster used during to calculate $\Delta_r G$. White and red atoms are H and O respectively. Hydrogen bonds (dashed lines) are between 1.76-1.89 Å for the six water cluster and approximately 1.90 Å for the three water cluster. The structures were optimised using B3LYP/ aug-cc-pVDZ/MDF60/IEFPCM model chemistry.

5.4. Mixed Solvation using SMD as the implicit component

One interesting idea is to combine the parameterised SMD model with the mixed, $(H_2O)(H_2O)_2$, method. The extra water molecules reduce the U^{VI} atom contribution to the solvation cavity by positioning the U^{VI} atom further into the structure, away from the bulk water. This leads to a better representation of the solvation cavity.

Using the mixed solvation method, $(H_2O)(H_2O)_2$, in combination with the SMD solvation model results in less accurate $\Delta_r G$ than modelling solvation implicitly by -16, -64 and -70 kJ/mol for the 1:1, 1:2 and 1:3 uranyl acetate complexes. This can be visualised in Figure 5.1. This is related to the different errors in solvation. The errors associated with adding increasing numbers of explicit water molecules has been explored.[211] The change in free energy of solvation in a reaction, ΔG_{solv}, is the sum of the change in the gas phase hydration energy, ΔG_{hyd}, and the change in the solvation correction for the reaction ΔG_{corr} ($\Delta G_{solv} = \Delta G_{hyd} + \Delta G_{corr}$). Parmar *et al.*[211] observed that when only aqua ligands are complexed around U^{III} and U^{IV}, a large solvation correction ΔG_{corr} is required to counter the errors associated with the gas phase hydration energy, ΔG_{hyd}. The ΔG_{corr} term is dominated by the change in electrostatic energy (ΔG_{elec}) which is sensitive to the volume and surface area of the solvation cavity. Parmar *et al.*[211] observed that the small cavity volume and large surface area of the SMD solvation model led to

an overestimated ΔG_{solv}. This means that the $\Delta_r G$ from adding aqua ligands to a U^{III} or U^{IV} ion is over predicted ($\Delta_r G$ too negative). In the U^{VI} acetate reactions, water molecules are released rather than added, therefore the predicted $\Delta_r G$ is too positive. Addition of the explicit water molecules leads to a reduction of the magnitude of ΔG_{corr} required as ΔG_{hyd} converges toward ΔG_{solv}.[211] The extra water molecules position the electron density of U^{VI} further into the solvation cavity, reducing G_{corr} at the edge of the solvation cavity, reducing the overestimation of solvation energies. This leads to a shift of SMD $\Delta_r G$ to more negative values as observed in Figure 5.1. Conversely, Parmar *et al*.[211] observed that the large surface area and volume of the UFF IEFPCM meant ΔG_{solv} is underestimated ($\Delta_r G$ of adding aqua ligands too positive), therefore in the U^{VI} acetate reactions where water molecules are released, $\Delta_r G$ will be too negative. Adding explicit molecules in this case reduces $\Delta_r G$, and so IEFPCM reaction energies shift towards more positive values, as observed in Figure 5.1a.

The addition of the extra water molecules in $[UO_2(H_2O)_5(H_2O)_{10}]^{2++}$ does not sufficiently shield the U^{VI} atom from the implicit solvation model as can be observed in Figure 5.7c-d which is depicted as the van der Waals surface. Only adding a significant quantity of water molecules buried the U^{VI} atom enough to prevent interactions with the implicit solvation model (e.g. $[UO_2(H_2O)_5(H_2O)_{25}]^{2+}$).[211] Keeping reactions isodesmic using such a structure is challenging, and computational cost increases significantly. This would not be a practical approach for exploring a relative stability series.

The results from combining the mixed solvation method with SMD and the 6-31g(d,p) basis set for ligands are worth noting due to the high accuracy of $\Delta_r G$ when comparing to the experimental data. The calculated $\Delta_r G$ for one, two, and three acetate molecules were -22, -29 and –50 kJ/mol, compared to the experimental values of -19 ± 5, -29 ± 5 and -43 ± 4 kJ/mol respectively, when treating uranium as $[UO_2(H_2O)_5]^{2+}$. This needs to be treated with caution, however, as there can be a large truncation error for smaller basis sets.[289, 292] The errors associated with the different model components could be

working in the favor of the reaction energetics, and the solvation cavity over-exposes the U atom to the bulk solvent when using the SMD model.

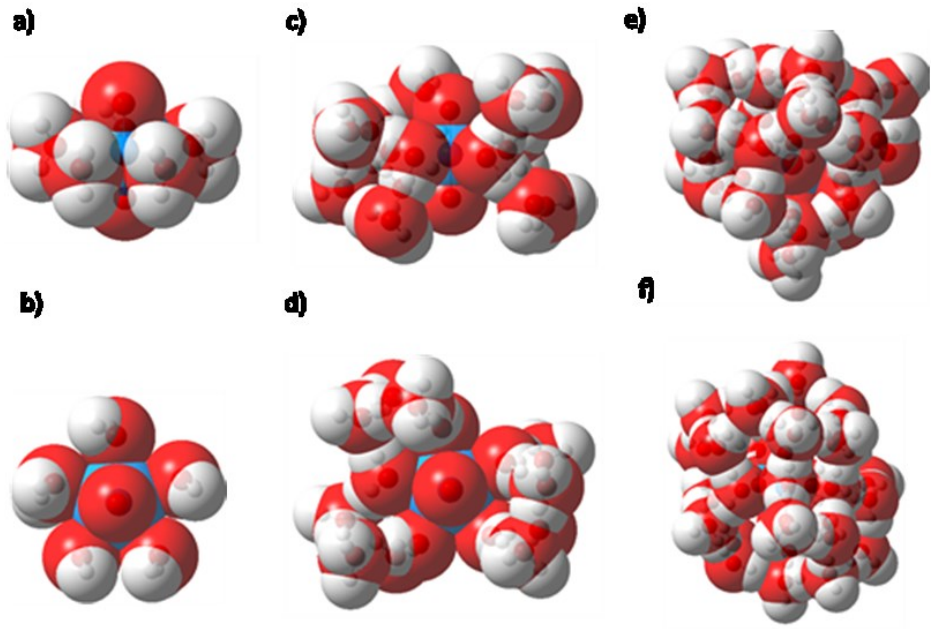

Figure 5.7. The solvation cavity of the uranyl dication with varying amounts explicitly drawn water molecules. Part a and b is side on and plan view of $[UO_2(H_2O)_5]^{2+}$, part c and d is side on and plan view of $[UO_2(H_2O)_5(H_2O)_{10}]^{2+}$. Part e and f is side on plan view of the $[UO_2(H_2O)_5(H_2O)_{25}]^{2+}$ complex (single point energy calculation on co-ordinates from Ref. 211).

5.5. U^{VI} ECP and Basis Set

Two small core ECP have been tested, i.e. the quasi-relativistic MWB60 ECP and the fully relativistic MDF60 ECP, to examine if changing U^{VI} ECP from quasi relativistic to fully relativistic improves Δ_rG and structure geometry. In these calculations the cc-pVDZ basis set was used for ligands while maintaining the use of B3LYP and IEFPCM. The calculated Δ_rG should improve when moving from the MWB60 to the MDF60 ECP. This is because the MWB60 was calibrated against reference data obtained through the quasi-relativistic Wood-Boring[216] approach which does not include the two small components of the four-component DHF Hamiltonian. The MDF60 ECP was calibrated against reference data calculated using the four-component MCDHF/DC+B Hamiltonian.[217] The results from these

calculations are presented in Table 5.3 and Figure 5.8. The thermodynamic parameters (H, TS, G, $\Delta_r G$) are provided in Table C3.

Table 5.3. Average bond lengths (Å), angles (°) and $\Delta_r G$ (kJ/mol) for acetate complexes with the MWB60 and MDF60 U^{VI} ECP's and the U^{VI} cc-pVDZ-PP basis set. The remaining DFT settings are B3LYP/cc-pVDZ/IEFPCM. The thermodynamic parameters (H, TS, G, $\Delta_r G$) are provided in Table C3.

Complex	**Figure**	**U ECP/basis set**	**U=O (Å)**	**O=U=O (°)**	**U-O_{water} (Å)**	**U-$O_{acetate}$ (Å)**	**$\Delta_r G$ (kJ/mol)**
$[UO_2(H_2O)_5]^{2+}$	5.2a	Experiment	1.764-1.79[a-d]		2.403-2.420[a-d]	-	-
		MWB60	1.752	175	2.459	-	-
		MDF60	1.767	172	2.471	-	-
		cc-pVDZ-PP	1.772	172	2.469	-	-
$[UO_2(H_2O)_3(Acet)]^{+}$	5.2b	Experiment	1.771[a]		2.350[a]	2.465[a]	-19 ± 5[e]
		MWB60	1.764	176	2.466	2.396	-130
		MDF60	1.779	176	2.470	2.398	-132
		cc-pVDZ-PP	1.782	176	2.472	2.398	-131
$[UO_2(H_2O)(Acet)_2]^{0}$	5.2c	Experiment	1.77[a,d]		2.350[a]	2.465[a]	-29 ± 5[e]
		MWB60	1.774	178	2.503	2.438	-228
		MDF60	1.791	178	2.507	2.439	-230
		cc-pVDZ-PP	1.794	178	2.508	2.439	-231
$[UO_2(Acet)_3]^{-}$	5.2d	Experiment	1.780[a]		-	2.47[a]	-43 ± 4[e]
		MWB60	1.785	180	-	2.485	-333
		MDF60	1.803	180	-	2.484	-330
		cc-pVDZ-PP	1.804	180	-	2.483	-338

[a]Ref. 31, [b]Ref. 32, [c]Ref. 33, [d]Ref. 34 [e]reaction energies from Ref. 135 corrected to zero ionic strength using method in Ref. 246.

Switching from the MWB60 ECP to the MDF60 ECP changed $\Delta_r G$ by -2, -2 and +3 kJ/mol for the reactions with one, two, and three acetate ligands respectively. These changes are small compared to the differences to the experimental data, and they all show the same stability trends. Changing the basis set for U^{VI} valence electrons from the MDF60 basis set to the cc-pVDZ-PP basis set should further improve U^{VI} valence energies and improve overall reaction energetics. The $\Delta_r G$ changed by +1, -1 and -8 kJ/mol for one, two and three acetate ligands respectively, indicating no significant difference. Using the MDF60 basis set is adequate in terms of $\Delta_r G$.

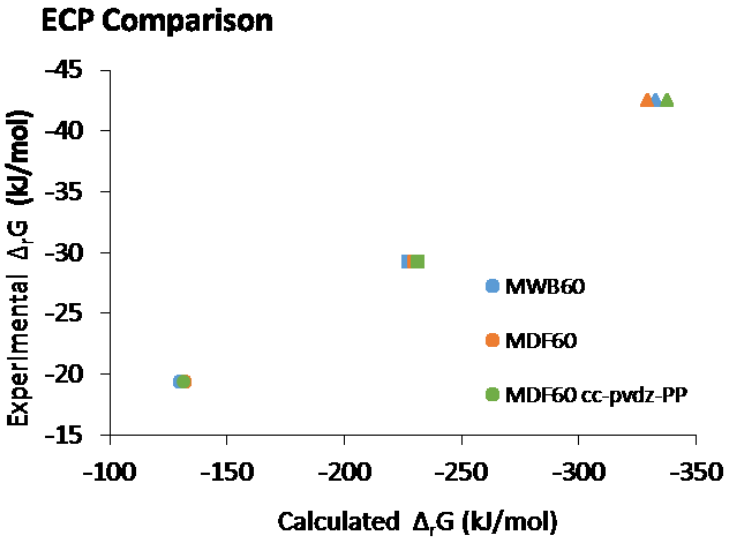

Figure 5.8. A comparison of calculated (x-axis) and experimental (y-axis) $\Delta_r G$ (kJ/mol) for the formation of 1:1 (circles), 1:2 (squares), and 1:3 (triangles) uranyl acetate complexes. The plot shows the effect of changing the ECP of uranium. The experimental data is from Ref. 135 corrected to zero ionic strength using the Specific Ion Theory (Ref. 246). $\Delta_r G$ is given in Table 5.3. The thermodynamic parameters (H, TS, G, $\Delta_r G$) are provided in Table C3.

Table 5.3 suggests that the geometries were very similar between the U^{VI} ECPs and basis sets, with average U=O, U-O_{water} and U-$O_{acetate}$ bond distances within 1%. The U=O bond distances were very close to the experimental data, typically within 2%.[31-34] The U-$O_{acetate}$ bond distances were also close to the experimental data,[31] typically within 3%.[31] The greatest difference to the experimental data occurred for the U-O_{water} bond distances which were lengthened by up to 7%. The O=U=O angle did not change between the different ECPs and basis sets except for $[UO_2(H_2O)_5]^{2+}$ where the angle was 3° lower when MWB60 was used compared to when MDF60 was used.

Overall, there is little change in the geometries and $\Delta_r G$ between the tested U^{VI} ECP and basis sets. Therefore, to reduce computational cost, it is best to use either the MWB60 or MDF60 basis set rather than the cc-pVDZ-PP basis set. The MDF60 ECP was used in subsequent calculations as it is fully relativistic.

5.6. Ligand Basis Set

Molecular geometries converge much faster than molecular energies when increasing basis set size, and typically geometries converge for double zeta basis sets.[176] To test this hypothesis the uranyl $[UO_2(H_2O)_5]^{2+}$ and uranyl acetate complexes ($[UO_2(H_2O)_3(Acet)]^+$, $[UO_2(H_2O)(Acet)_2]^0$, $[UO_2(Acet)_3]^-$) were optimized with Dunning's diffuse augmented correlation consistent split valence basis sets, aug-cc-pVnZ, where n= D (double), T (triple) and Q (quadruple). The results presented in Table 5.4 suggest that there is virtually no change in the geometries of the uranyl complexes as the basis size increase. Typically, the U=O, and U-O_{water} bond lengths and O=U=O angles vary by <1% between the different sized basis sets. Using the aug-cc-pVDZ basis set is adequate when wishing to predict the geometries of uranyl complexes.

The effect of changing the ligand basis set size on $\Delta_r G$ are presented in Table 5.4 and Figure 5.9. The thermodynamic parameters (H, TS, G, $\Delta_r G$) are provided in Table C4. Increasing basis set size from aug-cc-pVDZ to aug-cc-pVTZ changes $\Delta_r G$ by -4, -5 and -4 kJ/mol for the formation of 1:1, 1:2 and 1:3 uranyl acetate complexes respectively. Changing from aug-cc-pVTZ to aug-cc-pVQZ changes $\Delta_r G$ by a further -1, 0 and -4 kJ/mol for the three reactions. In future calculations, the aug-cc-pVDZ basis set is used, as the geometries have converged at this basis set size, and the calculated $\Delta_r G$ does not significantly change.

Table 5.4. Average bond lengths (Å), angles (°) and $\Delta_r G$ (kJ/mol) for acetate complexes with different ligand basis set and the B3LYP/MDF60/IEFPCM model chemistry. The thermodynamic parameters (H, TS, G, $\Delta_r G$) are provided in Table C4.

Complex	Figure	Ligand Basis Set	U=O (Å)	O=U=O (°)	U-O_{water} (Å)	U-$O_{acetate}$ (Å)	$\Delta_r G$ (kJ/mol)
$[UO_2(H_2O)_5]^{2+}$	5.2a	Experiment	1.764-1.79[a-d]		2.403-2.420[a-d]	-	-
		6-31g(d,p)	1.766	178	2.466	-	-
		aug-cc-pVDZ	1.761	179	2.470	-	-
		aug-cc-pVTZ	1.761	178	2.470	-	-
		aug-cc-pVQZ	1.761	178	2.481	-	-
$[UO_2(H_2O)_3(Acet)]^{+}$	5.2b	Experiment	1.771[a]		2.350[a]	2.465[a]	-19 ± 5[e]
		6-31g(d,p)	1.785	176	2.475	2.401	-134
		aug-cc-pVDZ	1.774	176	2.480	2.410	-119
		aug-cc-pVTZ	1.774	176	2.480	2.407	-123
		aug-cc-pVQZ	1.773	176	2.480	2.407	-124
$[UO_2(H_2O)(Acet)_2]^{0}$	5.2c	Experiment	1.77[a,d]		2.350[a]	2.465[a]	-29 ± 5[e]
		6-31g(d,p)	1.791	178	2.509	2.443	-244
		aug-cc-pVDZ	1.784	177	2.520	2.457	-219
		aug-cc-pVTZ	1.785	177	2.518	2.454	-224
		aug-cc-pVQZ	1.784	178	2.517	2.452	-224
$[UO_2(Acet)_3]^{-}$	5.2d	Experiment	1.780[a]		-	2.47[a]	-43 ± 4[e]
		6-31g(d,p)	1.802	180	-	2.487	-339
		aug-cc-pVDZ	1.794	180	-	2.498	-271
		aug-cc-pVTZ	1.795	180	-	2.495	-275
		aug-cc-pVQZ	1.794	180	-	2.495	-279

[a]Ref. 31, [b]Ref. 32, [c]Ref. 33, [d]Ref. 34 [e]reaction energies from Ref. 135 corrected to zero ionic strength using method in Ref. 246.

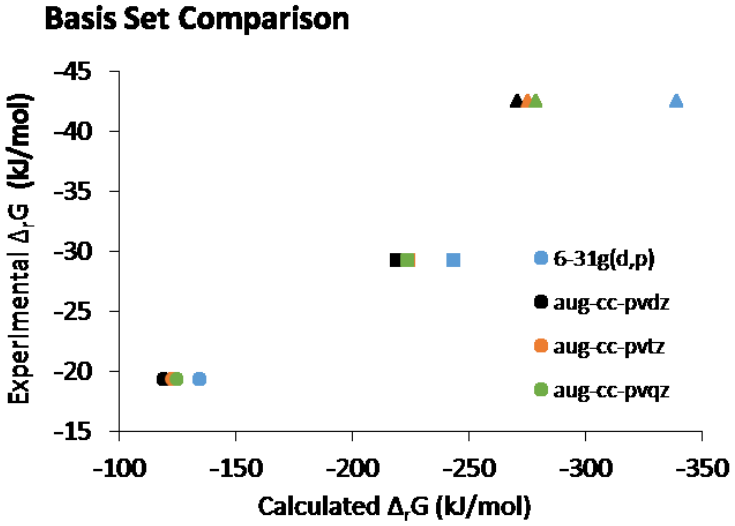

Figure 5.9. A comparison of calculated (x-axis) and experimental (y-axis) $\Delta_r G$ (kJ/mol) for the formation of 1:1 (circles), 1:2 (squares), and 1:3 (triangles) uranyl acetate complexes. The plot shows the effect of changing the ligand basis set. The experimental data is from Ref. 135 corrected to zero ionic strength using the Specific Ion Theory (Ref. 246). The $\Delta_r G$ is provided in Table 5.4. The thermodynamic parameters (H, TS, G, $\Delta_r G$) are provided in Table C4.

5.7. Density Functional Approximation

A comparison of $\Delta_r G$ between the PW91, TPSS, B3LYP and M06 DFAs is found in Table 5.5 and is illustrated in Figure 5.10. The thermodynamic parameters (H, TS, G, $\Delta_r G$) are provided in Table C5. The calculated $\Delta_r G$ typically improves with respect to experimental $\Delta_r G$ in the order TPSS, PW91, B3LYP and M06, with $\Delta_r G$ predicted by TPSS between 18 to 27 kJ/mol more negative than M06. This indicates that the hybrid DFAs are the most accurate at predicting $\Delta_r G$. The $\Delta_r G$ predicted by the M06 DFA differs from the B3LYP functional by +7, +5 and -13 kJ/mol for one, two and three acetate ligands respectively, indicating that M06 is more accurate for the formation of 1:1 and 1:2 U^{VI}-acetate complexes while B3LYP is more accurate for the formation of the 1:3 U^{VI}-acetate complex.

Table 5.5 Average bond lengths (Å), angles (°) and $\Delta_r G$ (kJ/mol) for acetate complexes with different DFAs and the aug-cc-pVDZ/MDF60/IEFPCM model chemistry. The thermodynamic parameters (H, TS, G, $\Delta_r G$) are provided in Table C5.

Complex	Figure	DFA	U=O (Å)	O=U=O (°)	U-O_{water} (Å)	U-$O_{acetate}$ (Å)	$\Delta_r G$ (kJ/mol)
$[UO_2(H_2O)_5]^{2+}$	5.2a	Experiment	1.764-1.79[a-d]		2.403-2.420[a-d]	-	-
		PW91PW91	1.787	168	2.460	-	-
		TPSSTPSS	1.784	168	2.457	-	-
		B3LYP	1.761	179	2.470	-	-
		M06	1.736	178	2.467	-	-
$[UO_2(H_2O)_3(Acet)]^{+}$	5.2b	Experiment	1.771[a]		2.350[a]	2.465[a]	-19 ± 5[e]
		PW91PW91	1.795	176	2.466	2.396	-127
		TPSSTPSS	1.793	176	2.464	2.391	-130
		B3LYP	1.774	176	2.480	2.410	-119
		M06	1.746	179	2.476	2.410	-112
$[UO_2(H_2O)(Acet)_2]^{0}$	5.2c	Experiment	1.77[a,d]		2.350[a]	2.465[a]	-29 ± 5[e]
		PW91PW91	1.807	177	2.519	2.440	-230
		TPSSTPSS	1.805	177	2.511	2.435	-241
		B3LYP	1.784	177	2.520	2.457	-219
		M06	1.754	177	2.518	2.479	-214
$[UO_2(Acet)_3]^{-}$	5.2d	Experiment	1.780[a]		-	2.47[a]	-43 ± 4[e]
		PW91PW91	1.818	180	-	2.486	-290
		TPSSTPSS	1.817	180	-	2.478	-303
		B3LYP	1.794	180	-	2.498	-271
		M06	1.764	180	-	2.498	-283

[a]Ref. 31, [b]Ref. 32, [c]Ref. 33, [d]Ref.34 [e]reaction energies from Ref. 135 corrected to zero ionic strength using method in Ref. 246.

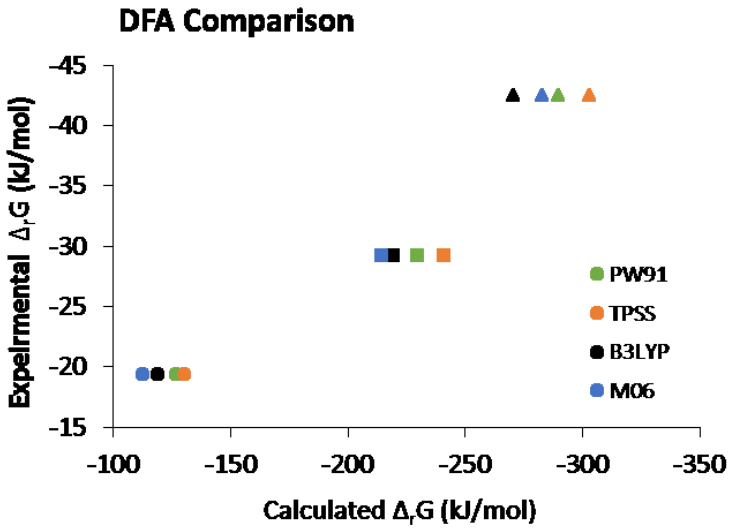

Figure 5.10. A comparison of calculated (x-axis) and experimental (y-axis) $\Delta_r G$ (kJ/mol) for the formation of 1:1 (circles), 1:2 (squares), and 1:3 (triangles) uranyl acetate complexes. The plot shows the effect of changing the DFA. The experimental data is from Ref. 135 corrected to zero ionic strength using the Specific Ion Theory (Ref. 246). The $\Delta_r G$ is provided in Table 5.5. The thermodynamic parameters (H, TS, G, $\Delta_r G$) are provided in Table C5.

The average U=O, U-O_{water} and U-$O_{acetate}$ bond distances presented in Table 5.5 for the uranyl and uranyl acetate complexes for the four different DFAs. These bond distances are similar between the four DFA's, varying by less than 3%. The average U=O and U-$O_{acetate}$ bond lengths were within 3% of the experimental data.[31] The difference between calculated and experimental U-O_{water} bond distances was up to 7%. The O=U=O bond angle was bent (167°) when employing the PW91 and TPSS DFAs, compared to the linear angle (178-179°) observed when the B3LYP and M06 DFAs were employed.

Overall a hybrid DFA is selected for the calculations because exact exchange needs to be included in DFT methods for thermochemical calculations. The B3LYP DFA is chosen over M06 to reduce computational cost.

5.8. Experimental Calibration

Finding isodesmic structures using a mixed solvation model is very challenging; the computational cost increases significantly, and there is no guarantee that the structures are at their global minima due to

the flexible nature of the hydrogen bonded water molecules. Using a fitting approach with $[UO_2(H_2O)_5]^{2+}$ as the starting structure, along with a DFT protocol such as the one proposed by Vukovic *et al*.[125] which is described in section 5.1, is currently the most practical method for scientists who are interested in exploring the relative stabilities of different U^{VI} complexes. The fitting approach presented by Vukovic *et al*.[125] was modified here so that it can be employed in future for ligands with many 10's atoms such as siderophores. This was done by employing Dunning's aug-cc-pVDZ basis set for the ligands, MDF60 ECP and corresponding basis set for U^{VI}. This protocol keeps B3LYP as the DFA and IEFPCM to model bulk solvation. The structures were optimised fully in the implicit solvation model rather than single point energy calculations employed in Vukovic *et al*.[125]

Vukovic *et al.*[125] calculated the relative stability of 1:1 U^{VI} complexes for monovalent and divalent ligands within 0.1-1.9 log β units with root mean square deviation (RMSD) <1 log β. This approach has been extended to organic molecules similar to the functional groups found in siderophores. The binding modes of the organic molecules tested have been selected based on previous experimental and computational work.[31, 125, 129, 136, 137, 293, 294] The ligands tested form bidentate complexes with the exception of glycolate which forms a monodentate complex. As there is no structural data for the 1:1 U^{VI}-AHA complexes, the possible bidentate and monodentate complexes were optimized as shown in Figure E1 in Appendix E. The most favourable reaction was for a bidentate complex. The reaction used for the log β_{110} is given in Equation 2.2. This is with the exception of L-glycine which uses Equation 5.7 in line with experimental derivation (log β_{111}).[56] The structures employed in the ligand training set are depicted in Figure 5.11. The structural parameters including bond length and angle are provided in Table D1 and the thermodynamic parameters (H, TS, G, $\Delta_r G$,) are provided in Table C6.

$$UO_2(H_2O)_5^{2+} + H_3O^+ + L^- = UO_2(HL)(H_2O)_3^{2+} + 3H_2O \quad (5.7)$$

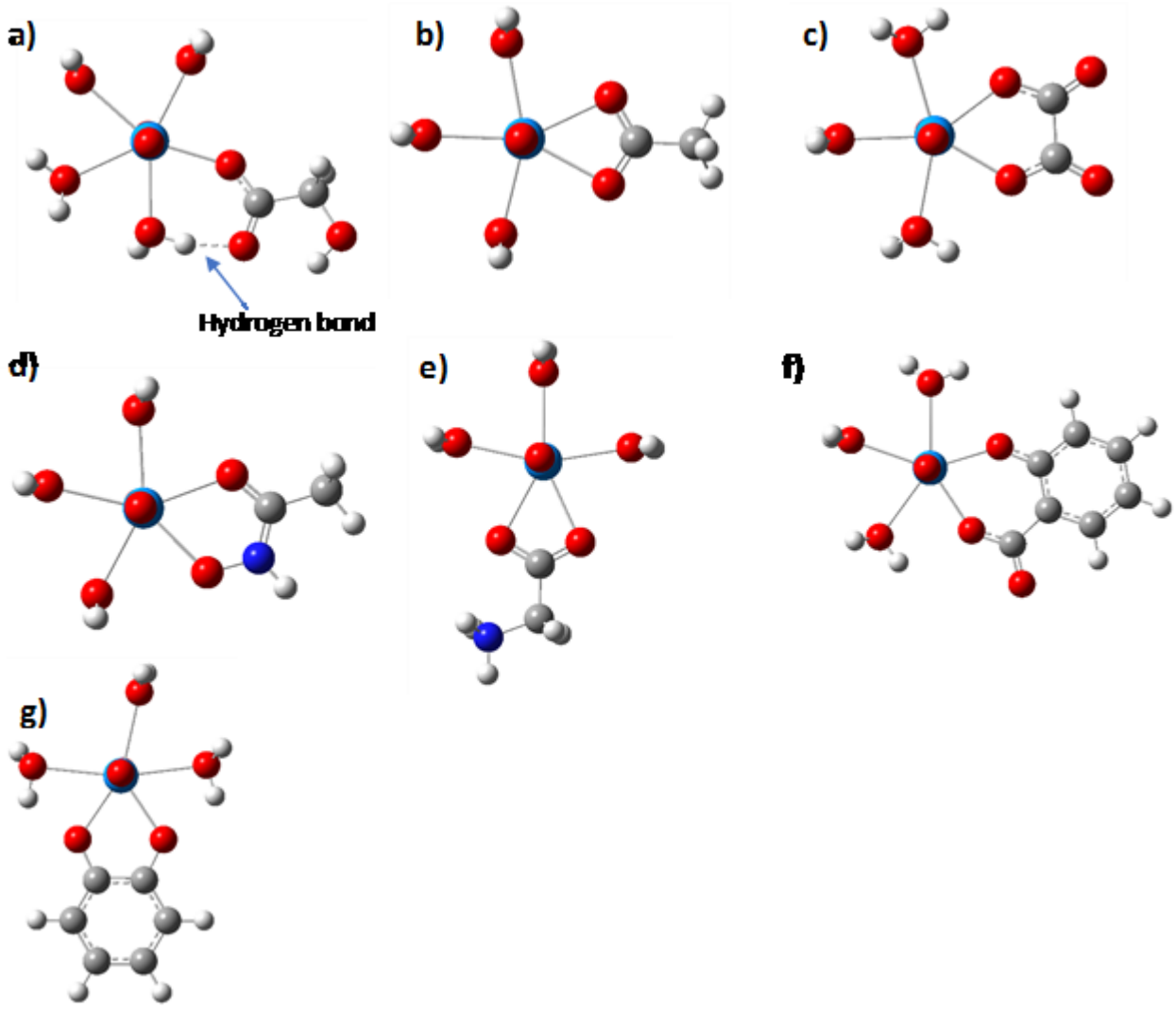

Figure 5.11. Optimised structures of the 1:1 U^{VI}-L complexes used to calibrate the calculated log β_{111} values. The white, dark blue, grey red and light blue atoms represent H, N, C, O and U respectively. The structures are: a) glycolate, b) acetate, c) oxalate, d) acetohydroxamate, e) L-glycine, f) salicyate g) catecholate. The structures were optimised using the B3LYP/aug-cc-pVDZ/MDF60/IEFPCM model chemistry. The structural parameters including bond length and angle are provided in Table D1.

Experimental and calculated log $\beta_{110/111}$ are presented in Table 5.6.[56, 123, 128, 134, 135, 295] The calculated versus experimental log β values presented in Figure 5.12 show a linear trend with a correlation coefficient (R^2) of 0.935, similar to the correlation found by Vukovi *et al.*[125] (R^2 = 0.926) once all data is included in the same plot. Equation 5.8 has been obtained from the data plotted in Figure 6.5 and is used to fit the calculated log $\beta_{110/111}$ of the 1:1 U^{VI} complexes. The standard error for the fitted log β obtained from linear regression analysis is 1.39 log β units. The RMSD calculated from the ligand training set after employing Equation 5.8 is 1.18 log β units. This is 0.21 log β less than the standard

error. Plotting the data for all 13 ligands published in Vukovic *et al.*[125] results in a similar RMSD (1.33 log β) supporting that the protocol presented here can calculate the relative stability of siderophore type functional groups. From herein the error is given as 1 significant figure (i.e. ±1 log β units).

$$\text{Fitted } \log \beta = (0.4053 * \text{calculated } \log \beta) - 4.2467 \quad (5.8)$$

Table 5.6. Experimental, calculated and fitted (Equation 6.5) log $\beta_{110/111}$ values for the different organic molecules used in the ligand training set. The difference between the experimental log β and the calculated, and fitted values are also reported. The thermodynamic parameters (H, TS, G, $\Delta_r G$) are provided in Table C6.

Ligand	Figure	Experiment	Calculated	Difference (Calculated – Experiment)	Fitted	Difference (Fitted – Experiment)
Glycolate[a]	5.11a	3[g]	15	12	2	-1
Acetate[b]	5.11b	3[g]	21	18	4	1
Oxalate[c]	5.11c	7[g]	32	25	9	2
Acetohydroxamate[d]	5.11d	8[g]	32	24	9	1
L-Glycine[e]	5.11e	11[h]	40	29	12	1
Salicylate[f]	5.11f	13[h]	37	24	11	-2
Catecholate[f]	5.11g	17[h]	51	34	16	-1

Experimental log $\beta_{110/111}$ data for the 1:1 U^{VI}-L complexes is from [a]Ref. 134, [b]Ref. 135, [c]Ref. 295, [d]Ref. 128, [e]Ref. 56, and [f]Ref. 123. These were corrected to zero ionic strength using the [g]Specific Ion Theory and [h]Davies equation outlined in Ref. 246 and Ref. 245 respectively.

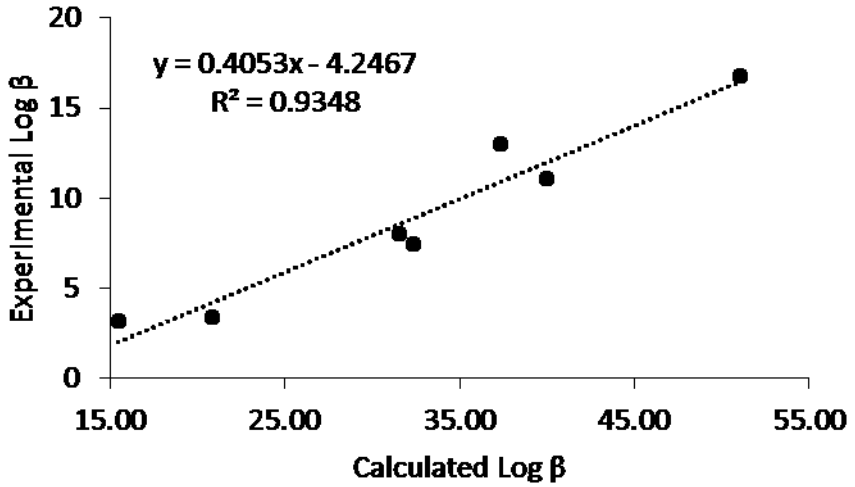

Figure 5. The correlation of experimental (y axis) to calculated (x axis) $1:1$ U^{VI}-L complexes. The ligands tested are given in Table 5.6. Experimental log β data for the 1:1 U^{VI}-L complexes is from [a]Ref. 134, [b]Ref. 135, [c]Ref. 295, [d]Ref. 128, [e]Ref. 56, and [f]Ref. 123. These were corrected to zero ionic strength using the [g]Specific Ion Theory and [h]Davies equation outlined in Ref. 246 and Ref. 245 respectively. The thermodynamic parameters (H, TS, G, $\Delta_r G$) are provided in Table C6.

The log $\beta_{110/111}$ of U^{VI} complex formation with formic and nicotinic acid were subsequently calculated to test the accuracy of the fitting curve for calculating the log $\beta_{110/111}$ of ligands beyond the training set. The optimised structures of these complexes are shown in Figure 5.13. These two ligands have been selected for the two different reactions shown in Equation 2.2 for formic acid and Equation 5.7 for nicotinic acid. Formic acid forms a monodentate complex[296] in 1 M $NaClO_4$ with log β_{110} of 3,[297] after correction to zero ionic strength using SIT theory. The calculated log β_{110} for the complex is 16 and applying the fitting equations reduces the log β_{110} to 2. This is within the error (1 log β unit) of the experimental error

Figure 5.13. Optimised structures of the 1:1 U^{VI}-L complexes used to independently validate the calibration curve. The white, dark blue, grey red and light blue atoms represent H, N, C, O and U respectively. The structures are: a) formate, b) bidentate nicotinate, c) monodentate nicotinate. The structures were optimised using the B3LYP/aug-cc-pVDZ/MDF60/IEFPCM model chemistry. The structural parameters including bond length and angle are provided in Table D1.

To my knowledge, no structural data is available for the U^{VI} nicotinic acid complex. Protonation data indicate the amine group is protonated and the ligand binds to U^{VI} via the carboxylate end of the molecule.[298] This could be in a bidentate fashion or a monodentate fashion, with one less water molecule released. The experimental log β_{111} collected in 0.1 M $NaClO_4$ [298] is 9 after correction to zero ionic strength using the Davies equation. The calculated log β_{111} for the monodentate and bidentate complexes are 38 log β units and applying the fitting equation reduces log β_{111} to 11. The difference in log β to the experimental data for the complexes is 2 log β units. These are higher than both the RMSD and standard error of the fitting equation (1 log β units). The experimental error is ± 0.2 log β

units calculated from the average of four independent measurements. [298] The error increases to ± 0.4 log β units after correcting to zero ionic strength. Applying the ionic strength corrected error decreases the difference to the fitted data, although the difference remains as 2 log β units after rounding to the error and fitted log β to one significant figure. These test ligands indicate that the fitting curve significantly improves the estimated stability constant for ligands outside the ligand training set.

5.9. Sequential Complexation

The fitting for 1:2 U^{VI}-L complexes was studied recently,[236] however this was conducted with the SMD solvation model rather than the IEFPCM solvation model that is employed here. To examine if a fitting can be used for 1:1 to 1:3 U^{VI}-L complexes on one fitting curve, the stability of U^{VI} glycolate, acetate and oxalate ligands were explored. All three glycolate ligands bind in a monodentate style via the carboxylate end (at pH <3.5), while all three acetate ligands bind in a bidentate fashion.[31, 136] Oxalate binds in a bidentate fashion in the 1:1 and 1:2 U^{VI}-L complex, while the third oxalate binds in a monodentate fashion.[293, 294] The optimised structures are shown in Figure 5.14. The structural parameters including bond length and angle are provided in Table D1 and the thermodynamic parameters (H, TS, G, $\Delta_r G$, calculated log β) are provided in Table C6.

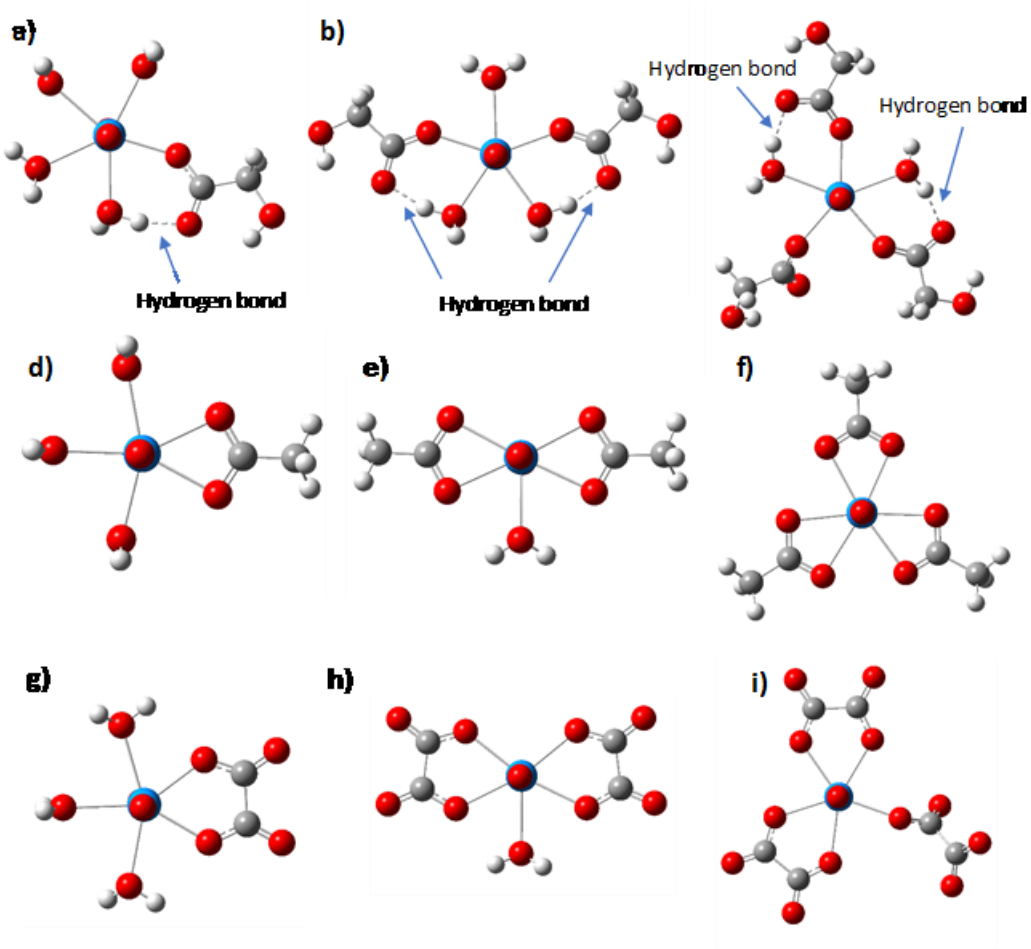

Figure 5.14. Optimised structures for 1:1, 1:2 and 1:3 U^{VI}-L complexes used to test whether a fitting approach can be employed to calibrate the calculated log β for multiple ligands coordinated around U^{VI}. The white, dark blue, grey red and light blue atoms represent H, N, C, O and U respectively. The structures are: a) glycolate (1:1 U^{VI}-L), b) glycolate (1:2 U^{VI}-L). c) glycolate (1:3 U^{VI}-L) d) acetate (1:1 U^{VI}-L), e) acetate (1:2 U^{VI}-L), f) acetate (1:3 U^{VI}-L), g) oxalate (1:1 U^{VI}-L), h) oxalate (1:2 U^{VI}-L), i) oxalate (1:3 U^{VI}-L). The structures were optimised using the B3LYP/aug-cc-pVDZ/MDF60/IEFPCM model chemistry. The structural parameters including bond length and angle are provided in Table D1.

Figure 5.15a shows that the experimental log β loosely increases exponentially with respect to calculated log β. The correlation is 0.889 for the nine complexes investigated during this study. Further inspection highlights the complexity of the fitting. In Figure 5.15b the data has been split by ligand charge, i.e. mono-anionic charged ligands, glycolate and acetate (green), and di-anionic charged oxalate (black). Both these curves are linearly correlated (R^2 = 0.9131 for -1 charge glycolate and acetate, and R^2 = 0.9918 for -2 charged oxalate). The trends, and the level of overestimation of the calculated log β are similar between glycolate and acetate. Oxalate under-predicts the calculated

stability compared to glycolate and acetate, and follows a steeper trend. Vukovic *et al.*[125] split the fitting of 1:1 U^{VI}-L complexes via ligand charge and improved accuracy in the fitted log β values. The results in Figure 5.15b support the evidence that splitting via ligand charge may be important, particularly when exploring multiple bound ligands on one fitting curve.

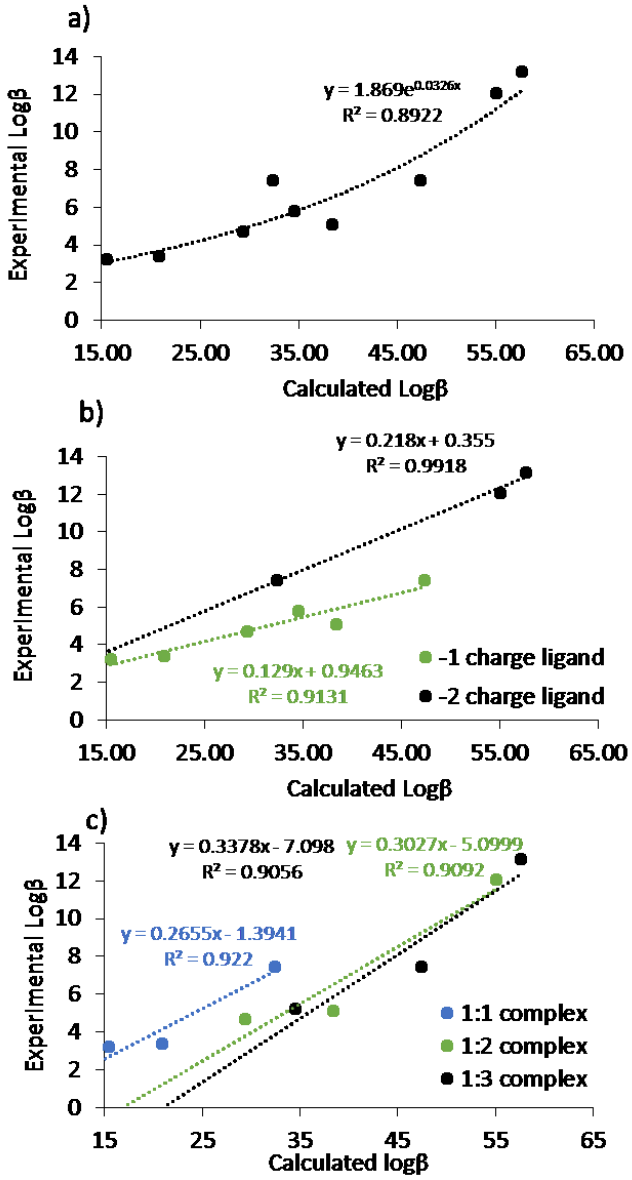

Figure 5.15. A comparison of 1:1, 1:2 and 1:3 U^{VI}-L complexes where L is glycolate, acetate and oxalate. The calculated log β is plotted on the x-axis and experimental log β is plotted on the y-axis. Part a shows an exponential fit of all nine complexes, part b shows that it is a linear fit when split by -1 (green) and -2 (black) ligand charge. Part c shows the linear fits when the complexes are split by the number of complexed ligands, where blue, green and black are one, two and three complexed ligands respectively. The experimental log β data are from [a]Ref. 134, [b]Ref. 135, [c]Ref. 295, and have been corrected to zero ionic strength using the Specific Ion Theory as outlined in Ref. 245. The thermodynamic parameters (H, TS, G, $\Delta_r G$, calculated log β) are provided in Table C6.

Figure 5.15c splits the complexes via the number of ligands complexed with U^{VI} where blue, green and black represent one, two and three ligands complexed around U^{VI} respectively. The results highlight that 1:2 and 1:3 complexes follow the same trend with similar correlations (R^2 = 0.9092 and 0.9056 for 1:2 and 1:3 complexes, respectively). This means that 1:2 and 1:3 complexes can be fitted on the same curve, regardless of ligand charge, indicating that if 1:2 or 1:3 experimental data is missing, it can be inferred from this plot. The trend for 1:1 complexes have similar correlation (R^2=0.922), however, the calculated log β are under predicted (shifted to the left) compared to 1:2 and 1:3 complexes. This indicates that the DFT calculations suggest it is more difficult to complex the first ligand, but once the first ligand is in, it becomes easier for the next two ligands to complex with U^{VI}.

5.10. Conclusions

The first objective of the research presented in this chapter was to modify the protocol for estimating the relative stability of U^{VI} complexes proposed by Vukovic *et al.*[125] This modified protocol allows us to estimate the relative stability of functional groups that comprise the reactive components in siderophores, while also providing a protocol whose computational cost will not prohibit future exploration of siderophores with 10's of atoms. This is important as siderophores complex with U^{VI}, significantly affecting U^{VI} aqueous chemistry and mobility in natural systems.

The second objective was to assess whether the difficulties associated with mixed solvation methods are outweighed by improvements in $\Delta_r G$. The third objective was to explore whether the fitting approach can be expanded to multiple bound ligands, focusing on carboxylate type ligands. The suggested protocol is the B3LYP functional, aug-cc-pVDZ ligand basis set, MDF60 ECP and basis set for U^{VI} and the IEFPCM solvation model. The complexes were optimised fully in the solvation model. Mixed solvation models based on previous research[38] were tested for U^{VI} acetate complexes. The research presented here demonstrates that applying the approach employed by Gutowski and Dixon[38] significantly improves calculated $\Delta_r G$. However, a fitting approach would still need to be employed to

determine accurate log β values. To save on computational cost and to prevent difficulties keeping reactions isodesmic, all water molecules outside of the uranyl complex $[UO_2(H_2O)_5]^{2+}$ should be modelled implicitly with the IEFPCM solvation model.

Using the protocol outlined above, in combination with a linear regression allows the user to obtained fitted log β for 1:1 U^{VI}-L complexes with RMSD of 1.19 log β units and a standard error of 1.39 log β units. This enables to develop relative stability series for organic ligands, and to aid future experiments by providing molecular level insight to macroscale experiments.

Chapter 6 - Determining the Relative Stability of U^{VI} Complexes with Siderophore Functional Groups in Acidic Solutions using Density Functional Theory

Abstract

In this chapter the stability series for six key siderophore functional groups was developed using the Density Functional Theory (DFT) protocol developed in chapter 5. This included calculating the stability of α-hydroxyimidazolate and hydroxy-phenyloxazolonate for the first time. The stability for the binding mode of the functional groups decreased in the order: bidentate, monodentate via ligand O atoms and monodentate via ligand N atoms. The siderophore functional groups stability decreased in the order: α-hydroxycarboxylate bound via the α-hydroxy and carboxylate groups (log β_{110} = 17), α-hydroxyimidazolate (log β_{110} = 17), catecholate (log β_{110} = 16), hydroxamate (log β_{110} = 9), hydroxy-phenyloxazolonate (log β_{110} = 8), α-hydroxycarboxylate bound via the carboxylate group (log β_{110} = 8) and α-aminocarboxylate (log β_{110} = 5). This stability series suggests that siderophores containing α-hydroxycarboxylate, α-hydroxyimidazolate and catecholate will have the greatest stability via functional group interactions and should be the focus of future research. To test whether, conceptually, the stability of the full siderophore complex can be calculating using the 1:1 U^{VI}-L stability series, the stability of the U^{VI}-desferrioxamine B complex was estimated by multiplying the hydroxamate β value by the number of hydroxamate functional groups which DFOB complexes U^{VI} with (i.e. 2). The model estimated a log β of 18 ± 2 accounting for 77 ± 7% of the experimental log β.

6.1. Introduction

Now that a cost effective DFT protocol has been developed, the stability series of U^{VI} complexes with siderophores can be established. However, most siderophores are not commercially available and need to be synthesised or isolated from bacteria, fungi or plants. This, along with the large number of siderophores, and possible siderophore conformers, makes characterising the stability of all U^{VI} siderophore complexes impractical. Therefore a method needs to be employed which can identify the types of siderophores which will likely have the greatest impact on the aqueous chemistry of U^{VI}. Siderophores bind to U^{VI} through chelating functional groups (Figure 2.3), and this is one of the major contributions to the stability of metal-siderophore complexes. Therefore predicting the stability series for these functional groups can provide an initial idea as to which siderophores will have the greatest effect on aqueous U^{VI} chemistry.

This chapter builds upon the DFT protocol developed in chapter 5 to create the stability series of U^{VI} complexes in acidic solutions which contain the six siderophore functional groups presented in Figure 2.3. The protocol was independently verified by comparing the fitted log β_{110} to the experimental log β_{110} for the hydroxamate functional group. The first step was to systematically characterise the log β_{110} of all possible U^{VI} complexes containing the siderophore functional groups. This assumed the ligands were initially deprotonated when complexing with $[UO_2(H_2O)_5]^{2+}$. This included calculating log β_{110} for U^{VI} complexes containing α-hydroxyimidazolate and hydroxy-phenyloxazolonate for the first time. The results for all six functional groups were then compared and physical insights are discussed. The most stable U^{VI} complex for each functional group was used to develop the stability series. Finally the stability series was used to test whether, conceptually, the stability of a full siderophore can be approximated using the log β of the 1:1 U^{VI}-L complexes. To do this, the log β of a U^{VI}-DFOB complex was estimated by multiplying the β value of the 1:1 complexes and the discrepancies between calculated and experimental log β are discussed.

6.2. The stability of U^{VI} complexes with the siderophore functional groups

The possible conformers were identified based on the possible interactions between the U^{VI} metal centre and typical donor atoms (O and N) found within the ligand of interest. The most stable conformer for a U^{VI}-L complex was chosen based on which conformer provided the most negative $\Delta_r G$ as this produces the most stable log β_{110}. For each monodentate complex, the ligands were placed in both the axial and equatorial conformations and the most stable complex resulting from the two optimisations is reported. The axial plane is defined as the plane in which the two oxo ligands in UO_2 are oriented. The most stable complex for each ligand is provided in Table 6.1.

Table 6.1. Average bond lengths (Å), angles (°) and fitted stability constants (log β_{110}) values for the most stable U^{VI} complexes containing α-hydroxyimidazolate (HI), hydroxyl-phenyloxazolonate (HPO), hydroxamate (HYD), α-hydroxycarboxylate (HC), α-aminocarboxylate (AC) and catecholate (CAT).

Complex	U=O	O=U=O	U-O_{water}	U-O(C)$_1$	U-O(C)$_2$	U-O(N)	U-N	log β_{110}	log β^a
$[UO_2(H_2O)_3(HYD)]^+$	1.784	173.4	2.513	2.394	-	2.296	-	9	8[b]
$[UO_2(H_2O)_3(AC)]^{2+}$	1.778	176.2	2.511	2.265	-	-	2.592	5	-
$[UO_2(H_2O)_3(CAT)]^0$	1.794	173.3	2.601	2.296	2.301	-	-	16	17[d]
$[UO_2(H_2O)_3(HI)]^+$	1.800	170.5	2.581	2.163	-	-	2.466	17	-
$[UO_2(H_2O)_3(HPO)]^+$	1.784	174.3	2.544		-	2.518	-	8	-
$[UO_2(H_2O)_3(HC)]^0$	1.798	171.8	2.569	2.179	2.364	-	-	17	-

[a] The experimental stability constants were corrected to zero ionic strength using the Davies equation.[245] Experimental stability constants are from [b]Ref. 130, [c]Ref. 56, [d]Ref. 123.

6.2.1. Catecholate ($C_6H_4(OH)_2$)

The thermodynamic (H, TS, G, $\Delta_r G$, calculated log β and fitted log β) and structural data of the catecholate complexes can be found in Table C7 and D2 respectively. The catecholate functional group contains two phenol groups which can deprotonate and potentially complex with U^{VI}. The pK_a's of the two phenol groups are 9.22 and 13.0.[299] Computational studies indicate the catecholate forms a bidentate complex with U^{VI} (Figure 6.1a).[53, 125] Extended x-ray absorption fine structure measurements in pH 5, 0.1 M $NaClO_4$ solutions were interpreted as bidentate complexation[126] supported by potentiometric and spectrophotometric data collected at pH 3.3-5.[124] A computational study also

indicates the fully deprotonated catecholate ligand forms a bidentate complex with U^{VI} however the formation of monodentate complexes were not studied.[125]

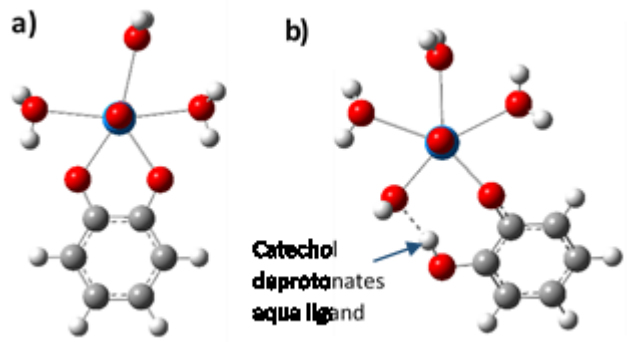

Figure 6.1. Structures of the U^{VI} catecholate complexes. The thermodynamic and structural data can be found in Table C7 and D2 respectively. The white, grey, red and light blue atoms are H, C, O and U respectively. Part a) is the bidentate complex. Part b) is the monodentate complex.

The experimental log β_{110} collected in 0.1 M ionic media[123] was corrected to zero ionic strength using the Davies equation.[245] The log β_{110} at zero ionic strength is 17. This is close to the fitted log β_{110} value for the complex which is 16 log β units. When catecholate was bound in a monodentate fashion, the ligand re-orientates into the equatorial plane of the U^{VI} atom. The free O atom carries a formal negative charge. This attracts one of the hydrogen atoms in a U^{VI} bound aqua ligand, deprotonating it to form $[UO_2(H_2O)_3(OH)(HL)]^0$ (Figure 6.1b). This led to a complex that is more stable (log β_{110} = 17) than the bidentate complex, closer to the experimental log β_{110} (17). However, spectrophotometry and EXAFS indicate catecholate binds to U^{VI} in a bidentate fashion.[124, 126] The difference between log β_{110} of the monodentate and bidentate complex is <1 log β units and within the rmsd of the fitting equation (1 log β units). Therefore the log β_{110} of the bidentate complex was employed in the relative stability series, so that it is in line with experimental data.

6.2.2. Hydroxamate (RC(O)N(OH)R' where R and R'= CH_3)

The thermodynamic (H, TS, G, Δ_rG, calculated log β and fitted log β) and structural data of the hydroxamate complexes can be found in Table C8 and D3 respectively. The formation of U^{VI}-L complexes with the hydroxamate functional group (N-methylacetohydroxamic acid, NMA) presented in Figure 2.3 was explored experimentally in 0.1 M KNO_3 solutions.[130] The pK_a of the hydroxyl group

in NMAH was calculated as 8.68 pK_a units. The log β_{110} was 7.76 and 7.81 when measured by glass electrode potentiometry and spectrophotometrically respectively. Crystals of $[UO_2(NMA)(NO_3)(H_2O)_2]$ were synthesised and structural analysis indicate hydroxamate binds to U^{VI} in a bidentate fashion.[131]

A previous experimental study[131] found that the free hydroxamate ligand was most energetically stable when the two oxygen (O) atoms are on the opposite side of the ligand (O atoms trans to each other). The trans and cis conformers were optimised, and support this conclusion. The trans conformer was used for future calculations. The optimised conformers are provided in Figure 6.2.

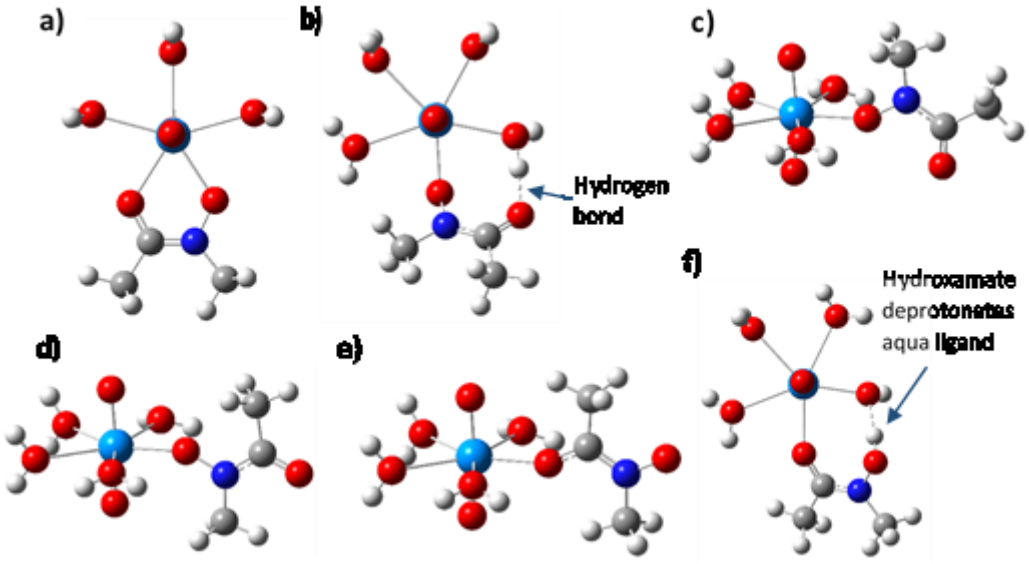

Figure 6.2. The structures of the possible U^{VI}-hydroxamate complexes. The thermodynamic and structural data can be found in Table C8 and D3 respectively. The white, dark blue, grey, red and light blue atoms are H, N, C, O and U respectively. The structures are: a) bidentate complex; b) and c) monodentate complex via the deprotonated O atom, where ligand O atoms are cis; d) monodentate complex via the deprotonated O atom, where ligand O atoms are trans; e) monodentate complex via carbonyl O, where ligand O atoms are trans; and f) monodentate complex via carbonyl O atom, where ligand O atoms are cis.

The results show hydroxamate forms the most stable complex with U^{VI} when binding in a bidentate fashion through the two O atoms of the ligand (Figure 6.2a, log β_{110} = 9). This agrees with crystal

data for the 1:1 U^{VI}-hydroxamate complex.[131] The experimental log β_{110} collected in 0.1 M KNO_3 [130] after correcting to zero ionic strength with the Davies equation[245] is 8 log β_{110} units. The fitted log β_{110} and experimental log β_{110} are within the rmsd of the fitting equation (1 log β units). This complex was not included within the initial training set employed for the fitting equation and provides additional external validation of the DFT and fitting protocol.

The possible monodentate complexes were explored. Hydroxamate can complex with U^{VI} through the deprotonated O atom when the hydroxamate O atoms are on the same (cis), or opposite (trans) side of the ligand. The ligand can complex with U^{VI} through the carbonyl O, when the hydroxamate O atoms are oriented cis and trans to each other within the ligand. The most stable monodentate complex formed when the ligand binds through the deprotonated O atom, when the hydroxamate O atoms are cis to each other. Optimising from an initially equatorial position led to the re-orientation of the ligand out of the equatorial plane of U^{VI}, causing the formation of a hydrogen bond between the carbonyl O atom and a U^{VI} aqua ligand (Figure 6.2b, log β_{110} = 7). The stability of the complex when the ligand was oriented within the axial plane (Figure 6.2c, log β_{110} = 5) is lower because it does not form a hydrogen bond between the carbonyl O atom in the hydroxamate and a U^{VI} bound aqua ligand. The next most stable conformer occured when hydroxamate complexes with U^{VI} through the O atom carrying a formal negative charge, when the O atoms of the ligand are trans to each other (Figure 6.2d, log β_{110} = 6). The ligand re-orientated itself into the axial plane of U^{VI} when the structure was initially optimised from an equatorial position.

The monodentate complexes formed by binding through the carbonyl O atom had a lower stability, reflecting the weaker interaction occurring through the O atom lone pair. When the O atoms were trans to each other within the free ligand, the hydroxamate orients itself within the axial plane of U^{VI} (Figure 6.2e, log β_{110} = 2). However, when the O atoms were cis to each other, the stability increased (Figure 6.2f, log β_{110} = 7). In this complex, the unbound O atom which carries a formal negative

charge deprotonated the adjacent aqua ligand to form $[UO_2(H_2O)_3(OH)(HL)]^+$. However, in aqueous solutions the bulk solvent will interact with the deprotonated O atom through the formation of hydrogen bonds. [231] This will decrease the electrostatic attraction between the free O atom of hydroxamate and the H atom of the U^{VI}-bound aqua ligand and likely prevent hydroxamate from stripping a proton from the aqua ligand.

6.2.3. α-hydroxycarboxylate ($OHCH_2C(O)OH$)

The thermodynamic (H, TS, G, Δ_rG, calculated log β and fitted log β) and structural data of the α-hydroxycarboxylate complexes can be found in Table C9 and D4 respectively. Experimentally, α-hydroxycarboxylate (glycolate) forms monodentate complexes with one to three ligands below pH 3.5. Above this pH the α-hydroxy group deprotonates, and the ligand binds in a bidentate fashion via the α-hydroxy O atom and one O atom from the carboxylate end of the ligand to form a 1:1 and 1:2 U^{VI}-L complex.[136] The possible bidentate and monodentate 1:1 U^{VI}-L complexes have been explored here assuming the ligand is fully deprotonated, which may be more relevant when the functional group is contained in a siderophore. Although the stability of this complex has been experimentally determined for a stepwise reaction where the α-hydoxy functional group protonates on reaction (log K = -1.25), uncertainties in the α-hydroxy pK_a limit the stability constant estimate (α-hydroxy $pK_a \geq 17$) to ≥ 15.75.[133]

There are two possible conformers for bidentate binding. The first is a bidentate complex via the O atoms in the carboxylate group, and the second is via the deprotonated α-hydroxy O atom and an O atom within the carboxylate group. The calculations indicate that the stability of the bidentate complex formed via the deprotonated α-hydroxy O atom (Figure 6.3a, log β_{110} = 17), is more than double the stability of the bidentate carboxylate complex (Figure 6.3b, log β_{110} = 8).

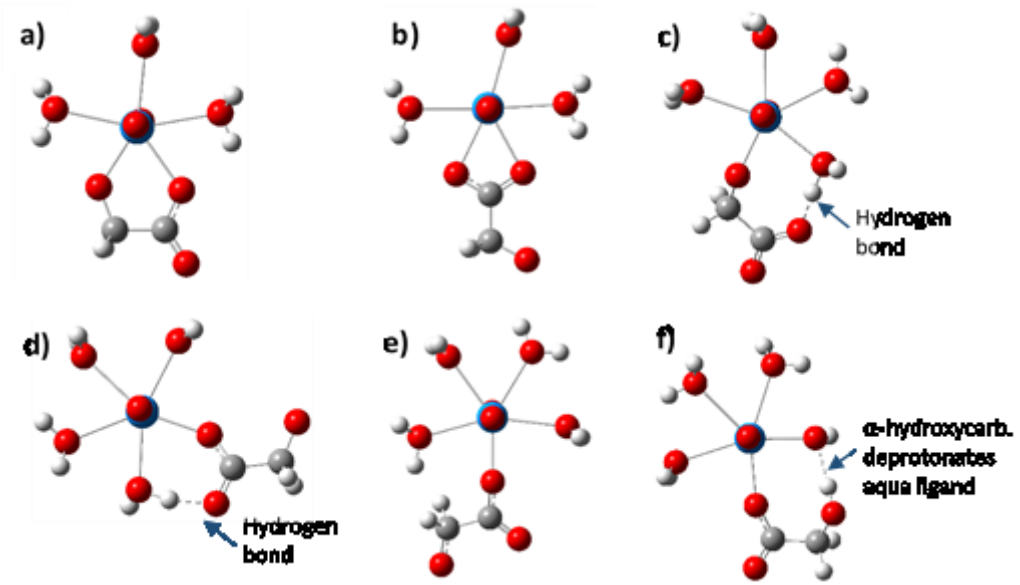

Figure 6.3. Structures of the U^{VI}- α-hydroxycarboxylate complexes. The thermodynamic and structural data can be found in Table C9 and D4 respectively. The white, grey, red and light blue atoms are H, C, O and U respectively. The structures are: a) bidentate complex via α-O atom; b) bidentate via carboxylate O atoms; c) monodentate via α-O atom, d) monodentate via carboxylate O atom, second carboxylate O atom oriented towards U^{VI}; e) monodentate via carboxylate O atom, second carboxylate O atom oriented away from U^{VI}; f) monodentate via carboxylate O atom, α-O cis to U^{VI} bound carboxylate O atom.

The ligand could form monodentate complexes by binding through the deprotonated α-hydroxy O atom, a carboxylate O atom that is on the same side of the ligand as the α-hydroxy group's O atom, and the carboxylate O atom which is on the opposite side of the α-hydroxy group's O atom. When the ligand was initially oriented in the axial plane of U^{VI}, the ligand rotates round into the equatorial plane of U^{VI}. From the possible conformers, the complex that binds via the negatively charged α-hydroxy O atom formed the most stable complex (Figure 6.3c, log β_{110} = 15). The complex where the carboxylate O atom was cis to O atom in the α-hydroxy group (Figure 6.3d, log β_{110} = 6), is more stable than when the bound carboxylate O atom was trans to α-hydroxy groups O atom (Figure 6.3e, log β_{110} = 4). This is because the second carboxylate O atom forms a hydrogen bond with a U^{VI} bound aqua ligand. However, when the deprotonated α-hydroxy group O atom was cis to the complexed carboxylate O atom, and pointing towards the aqua ligands, it can deprotonate a U^{VI} bound aqua ligand to form a highly stable complex, $[UO_2(H_2O)_3(OH)(HL)]^0$ (Figure 6.3f, log β_{110} = 16).

6.2.4. α-aminocarboxylate ($NH_3CH_2C(O)OH$)

The thermodynamic (H, TS, G, $\Delta_r G$, calculated log β and fitted log β) and structural data of the α-aminocarboxylate complexes can be found in Table C10 and D5 respectively. The α-aminocarboxylate functional group (glycine) is a zwitterion where the deprotonated O atom in the carboxylate group carries a formal negative charge, and the protonated amine group (NH_3) carries a formal positive charge. The pK_a's of the O atom and N atom are 2.38 and 9.58 respectively in 0.1 M ionic media.[56] The functional group can complex U^{VI} through the lone pair in the deprotonated N atom, lone pair in the carbonyl O atom, or through the deprotonated O atom. In acidic solutions, experimental and computational studies indicate glycine binds to U^{VI} in a bidentate fashion via the two carboxylate O atoms with the amine group protonating upon reaction.[56, 137] The experimental log β_{111} was calculated using Equation 5.7, where the amine group protonates upon reaction. [56]

The stability of the different U^{VI}-L complexes were calculated using Equation 5.7 when the ligand binds through the carboxylate O atom. The most stable complex for α-aminocarboxylate occured when the ligand formed a bidentate complex through the two carboxylate O atoms (Figure 6.4a, log β_{111} = 12). The experimental log β_{111} measured in 0.1 M $NaClO_4$[56] was corrected to zero ionic strength using the Davies equation.[245] The log β_{111} at zero ionic strength is 11 log β units. The difference between experimental and calculated log β_{111} (1 log β units) is within the rmsd of the fitting equation (1 log β units). There are two possible conformers when the ligand binds to U^{VI} in a monodentate fashion through the carboxylate group. These occur when the U^{VI} bound O atom is cis or trans to the amine group. In these conformers, the α-aminocarboxylate shifts orientation into the equatorial plane of the complex. The trans conformer (Figure 6.4b) and cis conformer (Figure 6.4c) have log β_{111} of 11.

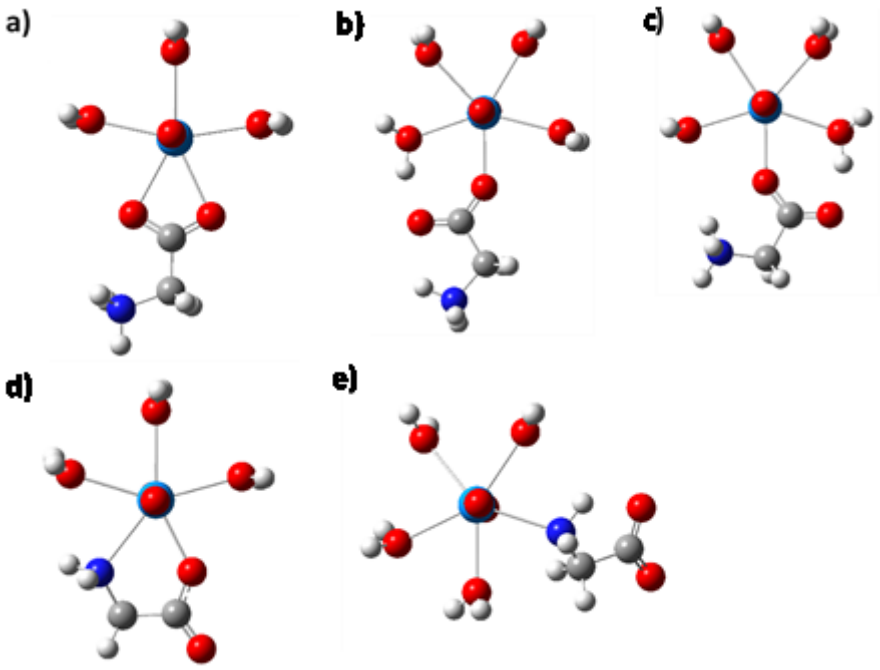

Figure 6.4. Structures of the U^{VI} α-aminocarboxylate complexes. The thermodynamic and structural data can be found in Table C10 and D5 respectively. The white, dark blue, grey, red and light blue atoms are H, N, C, O and U respectively. The structures are: a) bidentate complex via carboxylate O atoms;; b) monodentate via O atom, where the U^{VI} bound ligand O atom is trans to the amine group; c) monodentate via O atom, where the U^{VI} bound ligand O atom is cis to the amine group; d) bidentate complex via O and N atom; e) monodentate via the deprotonated N atom.

The overall stability of these reactions can be calculated by dividing the β_{111} value by the K_a of the amine group (pK_a = 10).[56] This correction assumes the amine group remains protonated through the reaction, rather than protonating upon reaction with U^{VI}. This reduces the stability of the bidentate complex to 2 log β_{111} units. The stability of the monodentate complexes is reduced to 2 and 1 log β_{111} units when the U^{VI} bound O atom is trans and cis to the amine group respectively.

The α-aminocarboxylate ligand could also complex to U^{VI} through the lone pair of the deprotonated N atom. This could be as part of a bidentate complex with a carboxylate O atom, or as a monodentate complex. These log β_{110} values were calculated using Equation 2.2. The log β_{110} is 5 when U^{VI} formed a bidentate complex (Figure 6.4d). The monodentate complex has a negative log β_{110} value after applying the fitting equation (Figure 6.4e, log β_{110} = -3), reflecting the weak interaction between U^{VI} (a hard Lewis acid) and the lone pair in the N atom (a soft Lewis base).

The bidentate complex involving the N atom is more stable than the bidentate complex via the two O atoms in the carboxylate group once the latter complex has been corrected so that the amine group remains protonated throughout the reaction (the pK_a correction). However, employing the pK_a correction means α-aminocarboxylate is treated as neutral ligand when binding only via the O atoms, compared to a -1 formal charge when binding through the deprotonated N atom. The charge may influence log β values, therefore to treat all the conformers consistently the structures presented in Figure 6.4a-c were re-optimised with the amine group deprotonated. This increased the stability of the bidentate complex presented in Figure 6.4a from 2 to 4 log β_{110} units, and the monodentate conformers presented in Figure 6.4b and 6.4c to 3 log β_{110} units. These results indicate that, thermodynamically, a bidentate complex through the N atom is more stable than through the two O atoms when treating the stability constants in a consistent manner (i.e. log β_{110}) and this is used in the relative stability series rather than the log β_{111} value.

6.2.5. Hydroxy-phenyloxazolonate ($C_6H_4(OH)C_3H_2NO$)

The thermodynamic (H, TS, G, $\Delta_r G$, calculated log β and fitted log β) and structural data of the hydroxy-phenyloxazolonate complexes can be found in Table C11 and D6 respectively. Hydroxy-phenyloxazolonate has one hydroxyl group with pK_a of 9, and complexes with metals in a bidentate fashion via the deprotonated O atom and the lone pair of the N in the oxazolone ring. [62] There are two possible conformers for the free hydroxy-phenyloxazolonate ligand. These arise when the O atom in the hydroxyl group and O atom in the oxazolone ring are oriented cis and trans to each other. The trans conformer was the most energetically stable conformer and was used for all log β_{110} calculations.

The most stable complex formed when hydroxy-phenyloxazolonate binds via the O atom in the hydroxyl group and the lone pair in the N atom (Figure 6.5a, log β_{110} = 8) in agreement with the

literature for other metal complexes.[62] The formation of a bidentate complex via the two O atoms was less favourable (Figure 6.5b, log β_{110} = 4). This is likely because of the energy cost associated with rotating the O atoms from the trans orientation in the free ligand, to the cis orientation in the U^{VI} complex.

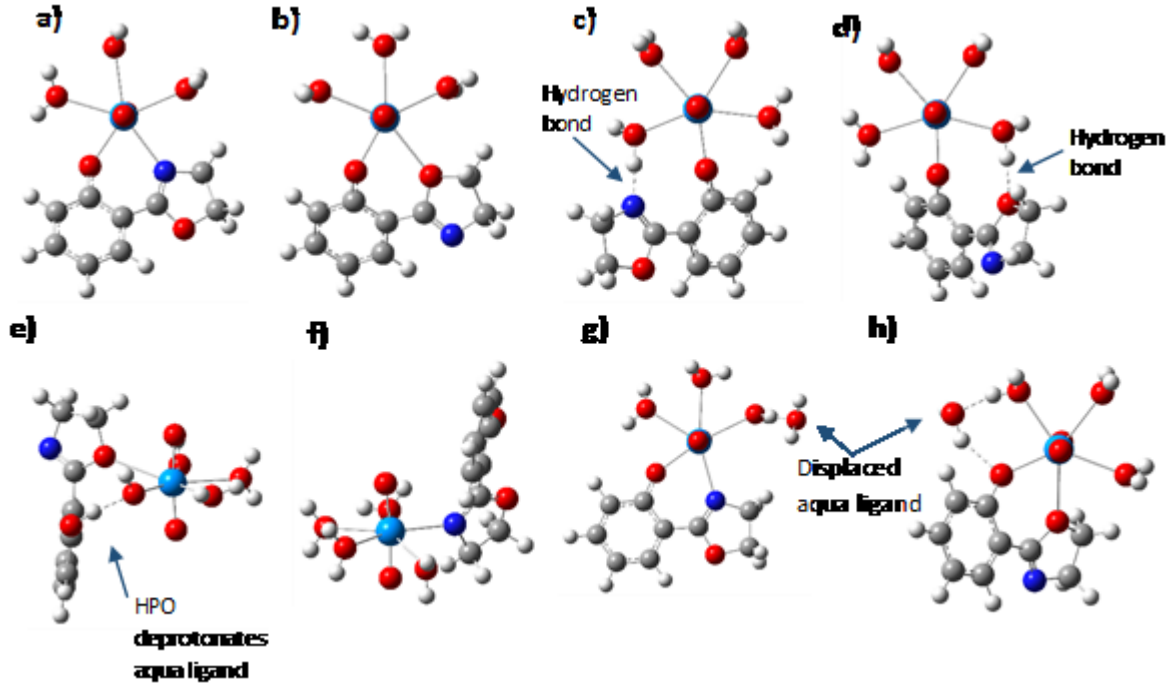

Figure 6.5. Structures of the U^{VI} hydroxy-phenyloxazolonate (HPO) complexes. The thermodynamic and structural data can be found in Table C11 and D6 respectively. The white, dark blue, grey, red and light blue atoms are H, N, C, O and U respectively. The structures are: a) bidentate complex via phenyl O atom and N atom; b) bidentate complex via two O atoms; c) monodentate via phenyl O atom, ligand O atoms trans; d) monodentate via phenyl O atom, ligand O atoms cis; e) monodentate via oxazolone O atom, ligand O atoms initially trans; f) monodentate via oxazolone N atom, ligand O atoms cis; g) structure resulting from optimisation of monodentate complex via oxazolone N atom, where O atoms were trans. h) structure resulting from optimisation of monodentate complex via oxazolone O atom, where O atoms were cis.

Hydroxy-phenyloxazolonate can form a monodentate complex with U^{VI} through its hydroxyl groups O atom, or the lone electron pairs of the O atom or the N atom in the oxazolone ring. The ligand re-orientated itself into the equatorial plane of the U^{VI} atom when bound via the deprotonated O atom. The stability was enhanced by the formation of a hydrogen bond between the lone pair from the N atom (Figure 6.5c, log β_{110} = 7) or the O atom (Figure 6.5d, log β_{110} = 5) in the oxazolone ring and a U^{VI} bound aqua ligand.

For monodentate complexes which form via the N and O atoms in the oxazolone ring, the complexes were only optimised when the ligand was initially orientated in the axial plane of U^{VI}. This is because the oxazolone and benzene rings of the ligand, in conjunction with the four remaining water molecules in the uranyl complex, sterically block the ligand donor atoms. When the binding donor atoms were on the opposite side of the ligand to the deprotonated hydroxyl groups O atom, a monodentate complex formed between the lone pairs of the oxazolone ring O (Figure 6.5e log β_{110} = 1) and N atoms (Figure 6.5f, log β_{110} = -3). When U^{VI} was bound by the oxazolone ring O, the second O atom within the ligand, which carries a formal negative charge, deprotonated one of the U^{VI} aqua bound ligands forming $[UO_2(H_2O)_3(OH)(HL)]^+$ (Figure 6.5e). When the binding donor atoms were cis to the deprotonated hydroxyl group O atom in hydroxy-phenyloxazolonate, the ligand rotated into the equatorial plane and formed a bidentate complex with the deprotonated hydroxyl groups O atom, forcing out a second water molecule (Figure 6.5g and 6.5h). The log β_{110} of these chelates are 9 and 4 when bound by the oxazolone ring N (Figure 6.5g) and O (Figure 6.5h) respectively.

6.2.6. α-hydroxyimidazolate (C_3N_2HCOH)

The thermodynamic (H, TS, G, $\Delta_r G$, calculated log β and fitted log β) and structural data of the α-hydroxyimidazolate complexes can be found in Table C12 and D7 respectively. α-hydroxyimidazolate contains two pK_a's corresponding to the hydroxyl group and deprotonation of the pyrrole-like-N atom within the imidazole ring (Figure 2.3), giving the ligand a -2 formal charge. The reported pK_a's are 6.00 and 14.52, where the latter pK_a represents that of the pyrrole-like-N atom.[62, 138] The ligand could complex to U^{VI} through the deprotonated O atom. Alternatively the ligand could complex to U^{VI} through the deprotonated pyrrole-like-N atom or through the lone pair in the pyridine-like-N atom. The formation of a direct U^{VI}-N co-ordination bond is supported by the formation of a U^{VI} complex directly through the N atoms of a similar ligand, 1-methylimidazole.[139]

α-hydroxyimidazolate can have a variety of conformers caused by the rotation of the α-hydroxy group. The two end members occur when the O atom is orientated cis to pyridine-type-N atom and cis to the pyrrole-type-N atom. The C-O bond rotated approximately 90˚ when the O atom was initially cis to the pyridine-type-N atom. The O atom remained orientated cis to the pyrrole-type-N atom in the second end member. The first conformer was 3 kJ/mol more favourable. This is less than chemical accuracy DFT (5 kJ/mol) suggesting either conformer could be present, however the most energetically favourable structure was used here to calculate $\Delta_r G$ for the U^{VI} complexes. The optimised conformers are presented in Figure 6.6.

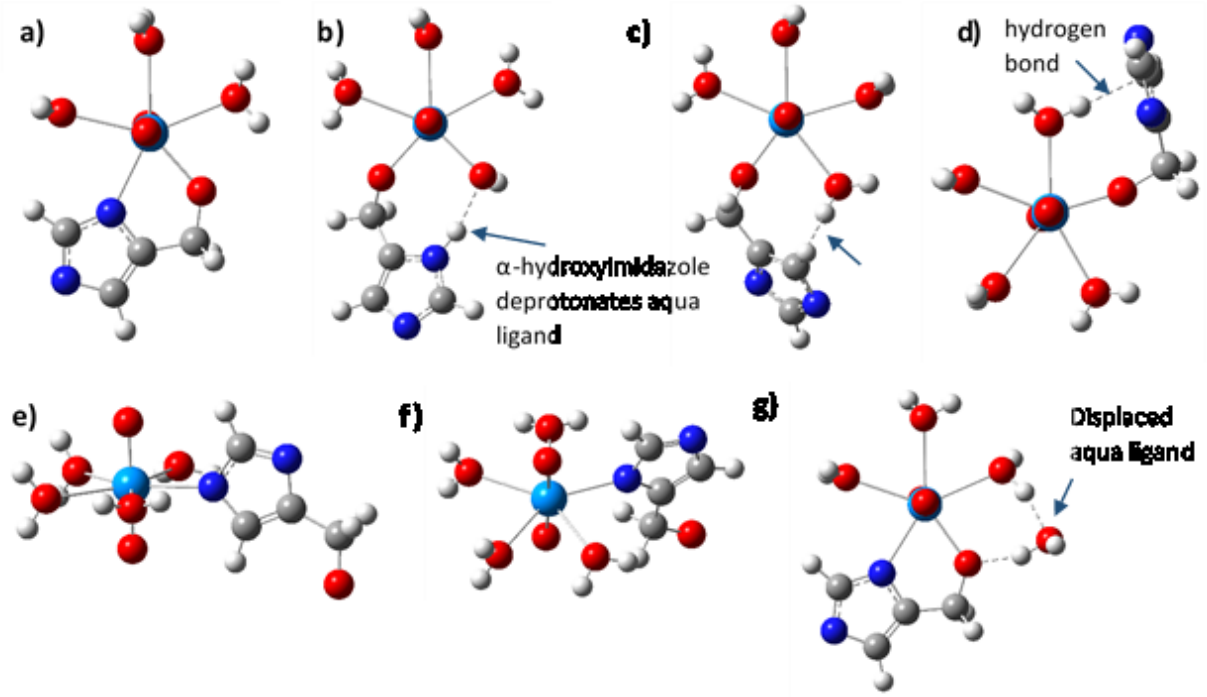

Figure 6.6 Structures of the U^{VI} α-hydroxyimidazolate complexes. The thermodynamic and structural data can be found in Table C12 and D7 respectively. The white, dark blue, grey, red and light blue atoms are H, N, C, O and U respectively. The structures are: a) bidentate complex, b) and c) monodentate via O atom, with ligand initially oriented in U^{VI} equatorial and plane respectively, O atom cis to pyridine-type-N atom. d) monodentate via O atom, O atom cis to pyrrole-type-N atom. e) monodentate via pyrrole-type-N atom. f) monodentate via pyridine-type-N atom, O atom trans to the N atom. g) initially monodentate via pyridine-type-N atom, with the O atom cis to the N atom

A bidentate complex could form between the deprotonated O atom and one of the N atoms in the imidazole ring. Steric hindrance caused by the protonated C atoms adjacent to the pyrrole-type-N atom prevent the formation of a bidentate complex, however a bidentate complex could form between the O atom and the pyridine-type-N atom. The stability of this was similar to that of the catecholate and α-hydroxycarboxylate complexes (Figure 6.6a, log β_{110} = 17).

There are four possible monodentate end member complexes when the α-hydroxyimidazolate complexes through the deprotonated O atom. It could form a complex when the deprotonated O is oriented on the same side of the pyrrole-type-N atom or the pyridine-type-N atom. The most stable complex formed when the deprotonated O was initially oriented cis to the pyridine-type-N atom and the ligand was initially orientated in the equatorial plane of U^{VI} (Figure 6.6b, log β_{110} = 17). In this complex, the pyridine N atom deprotonated a water molecule to form $[UO_2(OH)(H_2O)_3(HL)]^0$. When this complex was oriented initially in the axial plane of U^{VI}, the imidazole ring rotated out of the axial plane and interacted with a H atom in an adjacent water molecule through a C atom (Figure 6.6c, log β_{110} = 11). This also occured during the optimisation of the two end member complexes where the O atom was oriented cis to the pyrrole-type-N atom. The log β_{110} of this complex is 11 (Figure 6.6d) and has the same stability to the complex where the O atom was oriented on the same side of the ligand as the pyridine-type N atom complex (Figure 6.6c).

α-hydroxyimidazolate can complex with U^{VI} through the deprotonated pyrrole-type-N atom. The ligand re-orients itself into the axial plane and has a log β_{110} of 2 (Figure 6.6e). The orientation of the deprotonated O atom with respect to the imidazole ring will not affect the stability of the complexes as it is not possible for the deprotonated O atom to interact with the U^{VI} bound aqua ligands. The ligand can also complex with U^{VI} through the pyridine-type-N atom. There are potentially four different conformers for this complex, where the deprotonated O atom is oriented on the same and opposite sides of the ligand to the pyridine-type-N atom, with the ligand orientated in the axial and

equatorial plane of U^{VI}. When the deprotonated O atom was oriented trans to the pyridine-type-N atom, the ligand rotated into the axial plane of U^{VI} (log β_{110} = 2, Figure 6.6f). When the O atom was oriented cis to the pyridine-type-N atom, steric hindrance caused by the deprotonated O atom overlapping with an adjacent U^{VI} bound aqua ligand prevented the formation of a complex initially oriented in the equatorial plane. When the ligand was initially oriented in the axial plane, optimisation of the structure forced out an aqua ligand to form a bidentate complex (log β_{110} = 15, Figure 6.6g).

6.3. Physical insights obtained from comparing the log β_{110} data

Comparing the stability of all the 1:1 U^{VI}-L complexes provides physical insights into the importance of ligand charge and binding mode on the stability of U^{VI} complexes containing siderophore functional groups. The fitted versus calculated log β_{110} data have been plotted and separated according to ligand type, ligand charge and binding mode in Figure 6.7a to 6.7d. There are a total of 32 complexes (n = 32).

Figure 6.7a shows the data separated by ligand type. The results show that log β_{110} typically spans 6 to 16 orders of magnitude depending on the ligand. The results show that the siderophore functional group employed, and the binding mode is a major controlling factor on complex stability. The siderophore functional groups can be split into two stability bands. Catecholate (grey circles) and α-hydroxycarboxylate (green squares) form the most stable complexes, followed by hydroxamate (blue diamonds), α-aminocarboxylate (yellow triangles) and hydroxy-phenyloxazolonate (red squares). α-hydroxyimidazolate spans the entire stability range, reflecting on one hand the formation of highly stable bidentate complexes, and on the other hand the low stability of monodentate complexes via the N atoms.

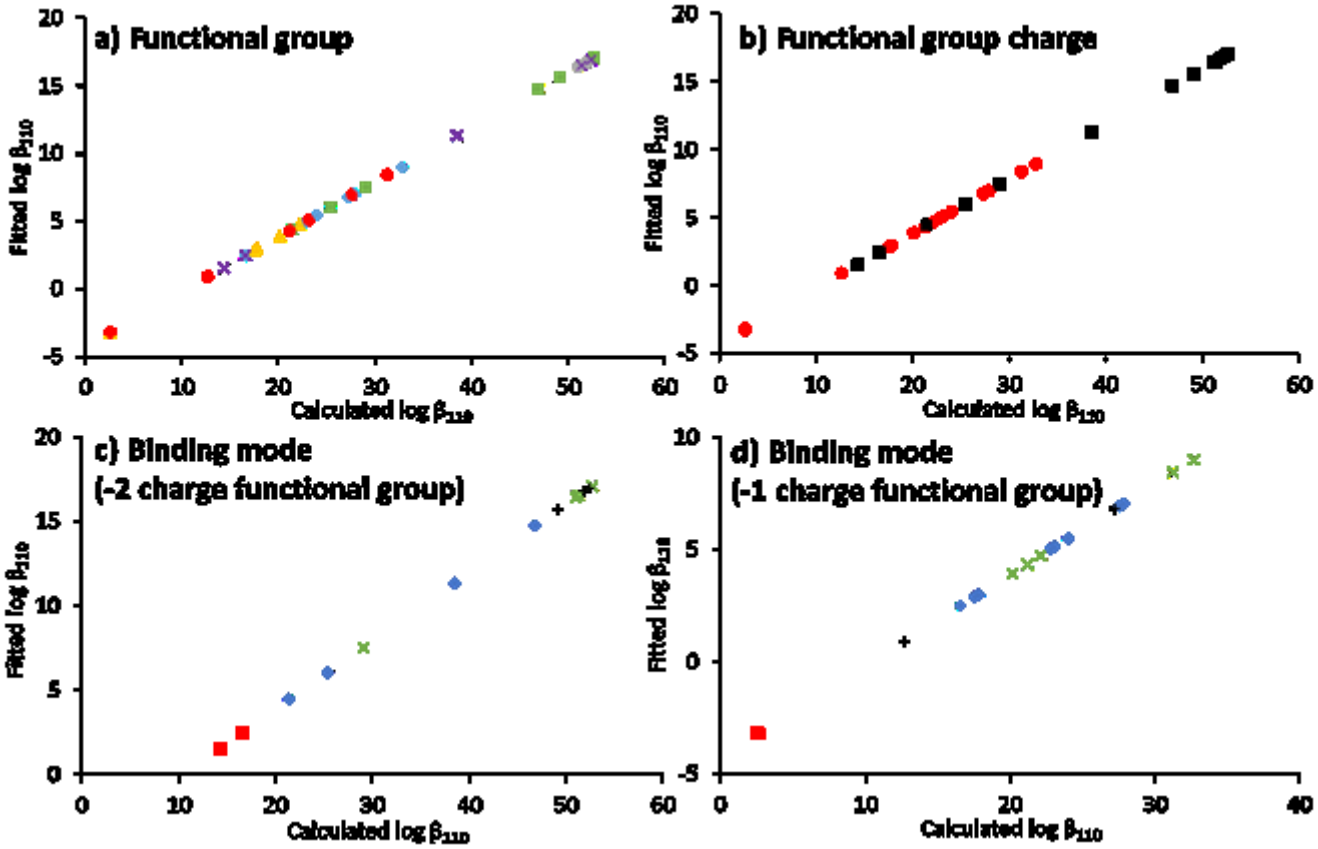

Figure 6.7. Plots of calculated versus fitted log β_{110} of all the U^{VI} complexes. In part a) the data is split into U^{VI} complexes containing catecholate (grey circle), hydroxamate (blue diamonds), α-hydroxycarboxylate (green squares), α-aminocarboxylate (yellow triangles), hydroxy-phenyloxazolonate (red circles), α-hydroxyimidazolate (purple X). In part b) the U^{VI} complexes are split into -1 (red circles) and -2 (black squares) charged ligands. Part c) and part d) are composed of U^{VI} complexes containing ligands with -1 and -2 charge respectively. In part c) and d) the complexes are further split into bidentate (green X), monodentate via O atom (blue diamonds), monodentate via N atom (red squares) and hydroxide complexes (black crosses).

In Figure 6.7b, the log β_{110} data are split by ligand charge. This shows that the stability of U^{VI} complexes containing -2 charge siderophore functional groups are offset to more stable values compared to -1 charge ligands by an average of 7 log β_{110} for all complexes (n= 17 and 15 for -1 and -2 charge ligands). The increased stability of the complexes containing -2 charge ligands reflects the increased electrodensity on the ligand donating atoms. The effect of ligand charge is responsible for the two bands of stabilities discussed for Figure 6.7a. The most stable band and least stable band are composed of U^{VI} complexes-containing siderophore functional groups with a -2 and -1 charge

respectively. This highlights the significant effect the ligand charge plays in the stability of U^{VI} complexes containing siderophore functional groups.

Note that increasing the charge of the structures leads to increased coulombic repulsion and decreased stability of the species when in the gas phase. For organic ligands, this can lead to the release of an electron, and cause multiply charged ligands to split into multiple monoanionic fragments.[300, 301] Therefore, treating a ligand with a negative charge rather as a neutral species is physically unrepresentative. This also means that the stability of the uranium-ligand complex may be over-represented when a -2 charge ligand complexes with uranium as it stabilises the ligand by forming a neutral species. Also, species with different charges require a different description (e.g. UFF, UA0) of the solvation cavity to correct the Gibbs energy for solvation effects. This may lead to errors when a reaction contains species with different charges. These issues could lead to errors in calculated $\Delta_r G$, and log β. However, calibrating the calculated data against experimental data, as done in chapter 5, counters these error. Future research could explore the reactions by ensuring all species are neutral by including counter-ions.[302] However, issues may arise in deciding where to place the counter-ion, and whether this counter-ion needs a solvation shell of its own.

The U^{VI} complexes are split by binding mode for -2 and -1 charge ligands in Figure 6.7c and 6.7d respectively. The results in Figure 6.7c shows the stability decreased in the order bidentate (green X's), monodentate via O atom (blue diamonds) and monodentate via N atom (red squares). The difference in stability between the bidentate and monodentate complexes primarily reflects increased entropic contributions associated with the chelate effect as shown in Table 6.2.[55] The increased stability of the monodentate complexes formed via the ligands O donor atom compared to the ligands N donor atom reflects the binding preferences of the ligand donor atom and the U^{VI} atom. U^{VI} is a hard acid which has low polarisation and prefers to form bonds of ionic nature. O has a higher electronegativity than N donor atom, and will therefore form co-ordination bonds of a more ionic nature. Therefore U^{VI}

interactions with O donor atoms tend to be stronger than with the N donor atom, forming greater stability complexes.[55]

Table 6.2. The change in entropy of the reaction at 298.15 Kelvin (-TΔS). This was calculated by subtracting the sum of TS of the reactants from that of the products to give TΔS and then multiplying it by -1 to give -TΔS. The thermodynamic data is provided in Table C7, C8, C9, C10, C11 and C12 for catecholate, hydroxamate, α-hydroxycarboxylate, α-aminocarboxylate, hydroxy-phenyloxazolonate and α-hydroxyimidazolate respectively.

	-TΔS (kJ/mol)	
Ligand	Bidentate	Monodentate
Catecholate	-24	13
Hydroxamate	-38	10
α-hydroxycarboxylate	-32	14
α-aminocarboxylate	-29	7
hydroxy-phenyloxazolonate	-23	18
α-hydroxyimidazolate	-24	13

The stability of the hydroxide complexes can be similar to that of the chelate. These hydroxides formed when a second ligand donor atom with high electrodensity deprotonates a U^{VI} bound aqua ligand. For example, the second deprotonated O atom in the catecholate functional group. However experimental data (e.g. EXAFS) for catecholate show the deprotonated O atoms bind directly to U^{VI}, and therefore the formation of these hydroxide complexes may be a forced interaction. As discussed in section 6.2.2, solvating the O atom of the ligands with explicit water molecules could possibly prevent the dissociation of the water molecule by decreasing the electrostatic attraction between the free O atom of the ligand and the H atom of the U^{VI}-bound aqua ligand.

The order of stability becomes less distinct when comparing the bi and monodentate complexes for monovalent ligands (Figure 6.7d). Stability differences between the ligands make the relationship harder to distinguish. Two of the three bidentate complexes occurring between 3.92-4.73 fitted log β units are due to the aminocarboxylate ligand, whose stability is lower than that of the hydroxamate and hydroxy-phenyloxazolonate complexes. The two monodentate complexes at ca. 3

fitted log β_{11} units are the a-aminocarboxylate complexes, showing the relationship holds for the ligand. The stability of monodentate complexes via O donor atoms remain more stable than monodentate complexes via the N donor atom, in agreement with the results of the divalent ligands (Figure 6.7c).

6.4. The relative stability series of U^{VI} complexes with siderophore functional groups

The relative stability series for six key functional groups found in siderophores and is presented in Figure 6.8. This includes the three most common functional groups in siderophores (catecholate, α-hydroxycarboxylate and hydroxamate) and three less common functional groups (α-aminocarboxylate, hydroxy-phenyloxazolonate and α-hydroxyimidazolate).

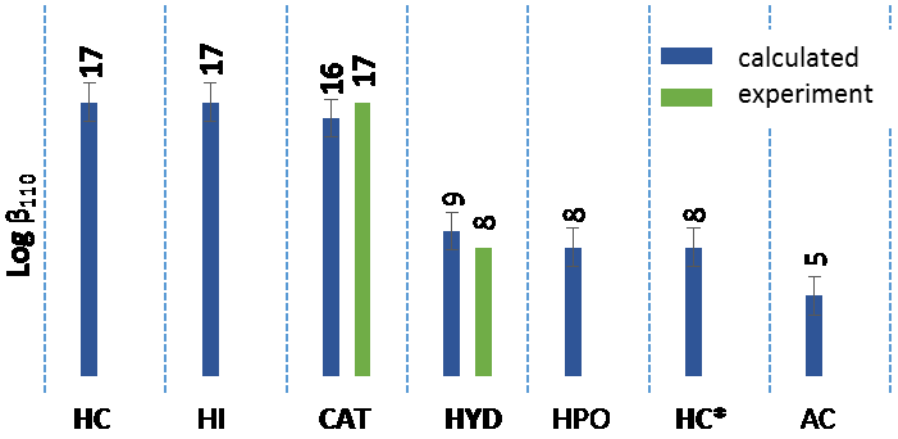

Figure 6.8. The stability series for six key siderophore functional groups. The most commonly found functional groups are highlighted in bold. The complexes are **α-hydroxycarboxylate chelated via carboxyl and hydroxyl groups (HC), α-hydroxycarboxylate chelated via carboxylate end (HC*), catecholate (CAT)**, α-hydroxyimidazolate (HI), α-aminocarboxylate (AC), hydroxy-phenyloxazolonate (HPO) and **hydroxamate (HYD)**. The log β calculated using the fitting equation and the available experimental log β values are represented by the blue and green bars respectively. The error bars on the fitted log β values are the rmsd of the fitting equation (1.19 log β units).

There are broadly two regions of stability. The most stable region is comprised of the U^{VI} α-hydroxycarboxylate complex, bound via the deprotonated α-hydroxy O atom and an O atom from

the carboxylate group (Figure 6.3a), α-hydroximidazole (Figure 6.6a) and the U^{VI} catecholate complex (Figure 6.1a). These make up two of the three most common siderophore types.[62] The second stability band is composed of hydroxamate (Figure 6.2a), hydroxy-phenyloxazolonate (Figure 6.5a), α-hydroxycarboxylate bound via the carboxyl end of the ligand (Figure 6.3b) and α-aminocarboxylate (Figure 6.4a). The second α-hydroxycarboxylate complex has been included in the stability series because not all carboxylate type siderophores contain the α-OH group, but is present as a carboxylate group. In general these two zones represent the divalent and monovalent ligands respectively.

Although hydroxamate make up the final most common class of siderophores,[62] the stability of the hydroxamate functional group (log β_{110} = 9) is in the lowest region of stability. The stability of hydroxamate is 7 and 8 log β_{110} units less than the catecholate and α-hydroxycarboxylate functional groups respectively. This observation is not specific to U^{VI}. For example, the stability of 1:1 Fe^{3+}-catecholate and Fe^{3+}-hydroxamate complexes are 20.01 and 11.37 log β units respectively.[299, 303] The pK_a of hydroxamate (pK_{a1} = 8.68)[130] is lower than the catecholate pK_a values (pK_{a1} = 9.22 pK_{a2} = 13.0)[299] and the α-OH group in α-hydroxycarboxylate (pKa_2 ≥17).[133] This may make it easier for hydroxamate to deprotonate and chelate with metal ions, including U^{VI}, in acidic conditions. However, the pK_a of the functional groups may significantly decrease on co-ordination of the ligand to the metal through the first deprotonated donor O atom. For example, the pK_a of the α-OH group in α-hydroxycarboxylate decreases from >17 to 3.64 upon co-ordination of a carboxylate O (pK_{a1} = 3.59), allowing the highly stable bidentate complex (Figure 6.4a) to form at pH >3.5.[133] Therefore the α-hydroxycarboxylate class of siderophores could form very stable complexes with U^{VI} in acidic solutions despite its high pK_{a2} value.

6.5. Estimating the stability of U^{VI} - DFOB complex

In this chapter the relative stability series for U^{VI} complexes containing six key functional groups found within siderophores has been developed. The next step is to predict the stability of mononuclear U^{VI} siderophore complexes in acidic conditions. However, it is computationally demanding to calculate the stability of all 500 siderophores.[62] One potential option is to use the relative stability series of the siderophore functional groups to gain a rough estimate of the stability of U^{VI} siderophore complexes. Assuming siderophores bind to metal ions in separate steps for each of its functional groups, the relative stability series can be used to provide an approximation of the U^{VI}-siderophore log β. This is achieved by multiplying the K values of the relevant bidentate or monodentate complexes as done to calculate the log β of 1:2 and 1:3 M-L complexes. The objective of this section is to assess how well such an approach can be used to predict the log β of U^{VI} siderophore complexes.

Currently experimental data for U^{VI}-siderophore structures and log β values is limited. One siderophore with experimental data is DFOB. This is a linear hydroxamate type siderophore (structure 1 in Figure 2.4) which contains three hydroxamate functional groups with average pKa values of 8.32, 8.97 and 9.52 and an amine group with an average pK_a of 10.84.[71] Complexation of U^{VI} with DFOB has been explored using spectrophotometric titrations.[1] A 1:1 U^{VI}-DFOB complex was dominant in the acidic region (pH 4-5.5) with a stability of 22.9 log β units collected in 0.1 M $NaClO_4$. The stability increases to 23 log β units following correction to zero ionic strength.[245] Mullen *et al.* [1] proposed the species was $[UO_2(DFOBH_2)]^0$ where two of the hydroxamate groups are deprotonated and are complexed with the U^{VI} metal centre. This speciation is supported by electrospray ionization mass spectrometry (ESI-MS).[304] Experimental data for acetohydroxamate (AHA) and N-methylacetohydroxamic acid (NMAH) indicate that two functional groups co-ordinate around the U^{VI} metal centre in a bidentate fashion.[128, 131, 305] Note that the 1:1 U^{VI}-DFOB complex is much more

stable than 1:1 U^{VI}-EDTA (log β_{11} = 7.40)[306] and 1:1 U^{VI}-citrate (log β_{11} = 6.69)[307] complexes. Therefore understanding how siderophores complex with U^{VI} can help us develop better synthetic chelating agents.

Based on this data the predicted stability for the U^{VI} DFOB complex is 18 ± 2 log β units by multiplication of the two hydroxamate β (log β = 9) values. The error was calculated via error propagation of the RMSD observed for the fitting equation (± 1 log β units). The predicted stability constant is 5 log β units less than the experimental stability. This indicates that the majority of stability (77 ± 7%) is associated with functional group interactions.

6.6. Exploring potential energy contributions to the U^{VI}-DFOB log β which are not included in the model

Other energy components contribute 23% to the stability of the U^{VI}-DFOB complex. I attempt to qualitatively discuss key potential energy contributions here for the U^{VI}-DFOB complex. These factors are illustrated informally in Equation 6.1.[308] Many of the terms will likely be linked together but they have been split into separate terms for discussion purposes. Key energy contributions are: complexation of the six functional groups calculated with the model (ΔG_F); complexation via nitrogen lone pair (ΔG_N) and sulphur lone pairs (ΔG_S) outside of those contained in the six functional groups presented in the stability series;[62] intramolecular hydrogen bonding (ΔG_H) outside those observed in the functional group complexes; contributions from the chelate effect and subsequent ligand atom re-organisation (ΔG_E); enhancements to the chelate effect due to pre-organisation of the ligands functional groups in macrocycles (the macrocycle effect, ΔG_M), and spacing between the functional groups in the siderophore to allow effective chelation (complementarity, ΔG_{comp}); solvation effects (ΔG_{sol});[308] and statistical decrease in stability due to reduction in co-ordination sites as complexation progresses (ΔG_σ):

$$\log\beta_{OI} = f(\Delta G_F, \Delta G_N, \Delta G_S, \Delta G_H, \Delta G_E, \Delta G_M, \Delta G_{Comp}, \Delta G_{Sol}, \Delta G_\sigma) \quad (6.1)$$

Equation 6.1 highlights the complexity of metal-siderophore interactions. However, chemically understanding the siderophore of interest allows us to narrow down which components will likely be contributing to the difference in stability between the log β values predicted by the model and the experiments. In the U^{VI} DFOB complex the amine group remains protonated and will likely interact with the U^{VI} dioxocation through hydrogen bonding (Figure 6.9a) rather than the lone pair in N (Figure 6.9b), so ΔG_N can be discounted. The ΔG_s term can be discounted as DFOB does not contain sulphur. DFOB is a linear molecule (Figure 6.9c) and will not have extra contributions to the chelate effect via pre-organisation of the reactive functional groups found in ring structures (Figure 6.9d) so ΔG_M can be ignored. ΔG_σ will decrease the siderophore log β rather than increase it.

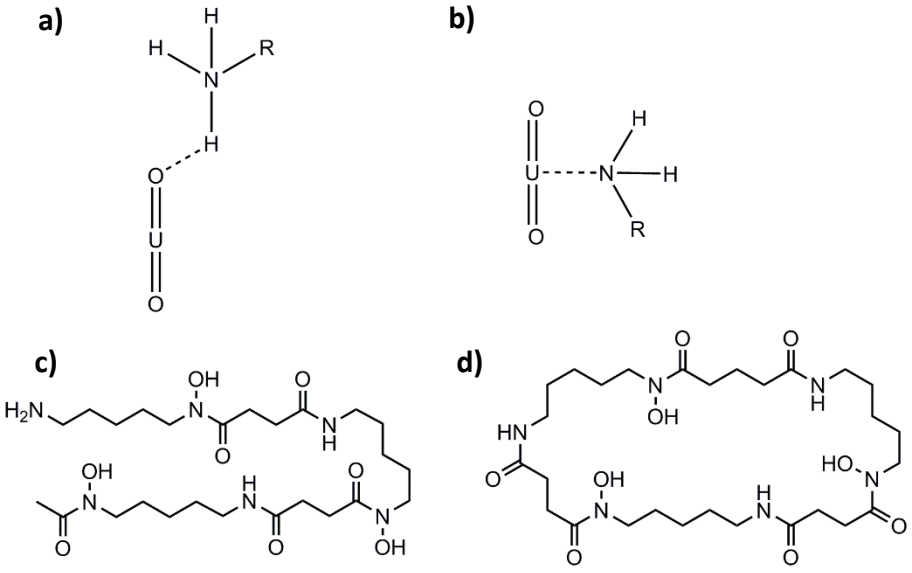

Figure 6.9. Part a) shows the protonated N atom of DFOB amine group forming an H bond with the axial oxygen of U^{VI}. Part b) shows the deprotonated N atom of DFOB forming a co-ordination bond with U^{VI}. Part c) shows the linear siderophore DFOB.[1] Part d) shows the cyclic siderophore desferrioxamine E.[2]

This leaves four potential key contributors to the stability of the DFOB complex compared to the stability predicted by the model, ΔG_H, ΔG_E, ΔG_{Comp} and ΔG_{Sol}. Hydrogen bonding may be possible between an axial oxygen and the protonated amine group. The key second contribution which could increase stability could be due to the chelate effect. This could be further enhanced by ΔG_{Comp} as the chain between the hydroxamate functional groups is long (9 atoms),[71] allowing for effective chelation of two hydroxamate groups around the large radius of the U^{VI} atom (Figure 6.10). The final key contribution is due to solvation effects, including stabilisation of water molecules released during the reaction by interactions in the bulk solution, and van der Waal interactions between the solvent and siderophore complex.[308] Van der Waal interactions could also be occurring between different atoms within the complex.

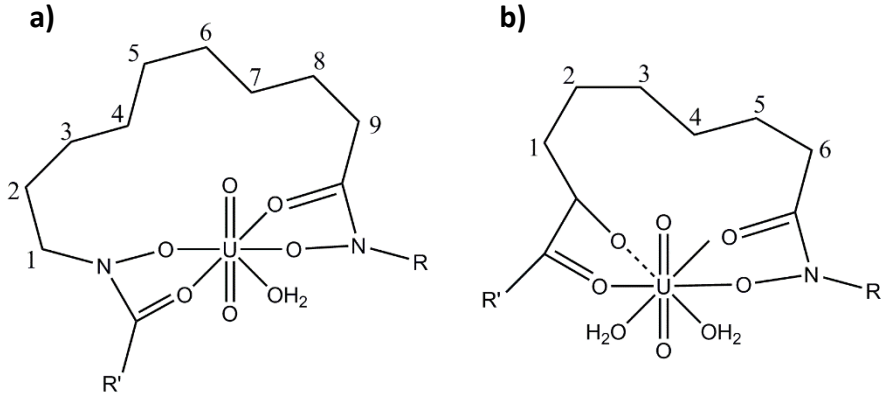

Figure 6.10. A comparison of two hydroxamate functional groups separated by different numbers of chain atoms. In part a) there are 9 atoms, while in part b) there are 6 atoms. The chain of 9 atoms allows the ligand to wrap around the uranyl dication and replace two U^{VI} bound aqua ligands, while the 6 chain of atoms is too short only allowing for the replacement of one U^{VI} bound aqua ligand.

6.7. Conclusions

The aim of the research presented here was to develop the relative stability series for 1:1 U^{VI}-L complexes where L is six key siderophore functional group complexes. In order to do this, the log β of all possible complexes were first calculated using DFT and fitted to a calibration curve of known experimental data. This included calculating the stability of U^{VI} complexes containing the α-

hydroxyimidazolate and hydroxyl-phenyloxazolonate functional groups for the first time. Comparison of all log β_{110} data highlight the stability of the binding modes for all ligands decreased in the order: bidentate, monodentate via ligand O donor atoms, and monodentate via ligand N donor atoms. The analysis highlights ligand charge also plays a significant role in the stability of the complex, with divalent ligands forming more stable complexes with U^{VI} than monovalent ligands.

The relative stability series was developed using the most stable complex where the ligand doesn't cause the formation of a hydroxide complex (a forced interaction). This is provided in Figure 6.8 and proceeds in the order:

HC via α-OH > HI > CAT > HYD > HPO > HC via carboxylate > AC

Based on these log β_{110} values, future U^{VI}-siderophore research should initially focus on the catecholate, α-hydroxycarboxylate and α-hydroxyimidazolate functional groups. This should focus on common siderophores first, such as enterobactin, mugineic acid and rhizobactin.[63] The results suggest that these three functional groups should be a priority when designing synthetic molecules to selectively complex with U^{VI} for removal from the human body, and applications such as seawater extraction, environmental remediation and nuclear fuel reprocessing.

The final objective was to test whether the stability series could be used to predict the stability of a U^{VI} complex containing a full siderophore (DFOB). By multiplying the β of the U^{VI} complex containing the hydroxamate functional group predicts 77 ± 5% of the stability of the U^{VI}-DFOB complex. The results from this highlight the significance, and complexity, of other binding aspects which may be lost when discussing macroscale experimental log β values without considering molecular level information. The results also highlights that simple computational models which explore reactions at the molecular scale can potentially be used to quantify the majority of the macro-scale experimental log β values. This is a fundamental parameter used in environmental and geochemical applications.

It is also a key consideration when developing molecules which selectively bind U^{VI} for a variety of purposes. However, this has only been tested for one siderophore.

Chapter 7 - Inhibition of U^{VI} Precipitation by the Siderophore Desferrioxamine B in pH 11.5, 0.1 M NaCl Solutions: A combined experimental and computational study

Abstract

Multidentate organic ligands from the degradation of cellulose in radioactive waste, (α-isosaccharinic acid) and additives in concrete (D-gluconate) solubilise uranium (U) minerals in high pH solutions. Multidentate siderophores could have a similar effect. The aim of the research presented here is to test whether the siderophore desferrioxamine B (DFOB) could prevent U^{VI} precipitation at pH 11.5 using a combined experimental and computational approach. To explore the effect of DFOB on U^{VI} precipitation, stirred batch experiments containing 0-420 µM DFOB, 42 µM U^{VI} and 0.1 M NaCl were conducted at pH 11.5. DFT was employed to explore whether $[UO_2(OH)_3]^-$ could complex with the hydroxamate functional groups within DFOB. The Δ_rG was calculated using an implicit and mixed solation method. During the stirred batch experiments, 5%, 11-12%, 41-53%, 95-96% and 100% of U^{VI} passes through the filter membranes (0.2-1 µm pore diameter) after 24 hours when 0, 4.2, 42, 130 and 420 µM DFOB was added to solution. DFOB desorbs from mineral surfaces, including uraninite, above pH 8, indicating the mechanism responsible is the formation of aqueous U^{VI}-DFOB complexes. The DFT results show that for both solvation models, the majority of possible complexes remained highly unfavourable, with $\Delta_rG \geq 64$ kJ/mol and ≥37 kJ/mol. The mixed solvation model predicted the $[UO_2(OH)_3(HYD\text{-}mono)]^{2-}$ had a Δ_rG β of 3 kJ/mol and corresponding log -0.5 log β units. This is similar to the experimentally derived log β of -1.2 ± 0.3, indicating this could be the potential binding mode. The results show that DFOB can significantly affect U^{VI} precipitation at DFOB concentrations often found in near surface environments.

7.1. Introduction

In chapter 4, the physico-chemical properties of U^{VI} precipitates in pH 11.5, 0.1 M NaCl solutions were characterised. The results showed that U^{VI} precipitates from solution as particles with hydrodynamic diameter of 800 ± 100 nm at pH 11.5. These precipitates were immobilised in quartz sand columns, however, U^{VI} was highly mobile when this size fraction was absent at pH 12.5.

One aspect which has not been explored in detail is the effect of low molecular weight organic molecules on the formation of U^{VI} precipitates.[148] Organic molecules with multiple functional groups produced from cellulose degradation (α-isosaccharinic) and cement degradation (D-gluconate) can complex with U^{IV} at pH 13.5 [309, 310] and with U^{VI} at pH 12-13.[82-84] Siderophores such as DFOB are also multidentate ligands which could have a similar effect on the aqueous chemistry of uranium as α-isosaccharinic and D-gluconate in highly alkaline conditions. Siderophores could affect U^{VI} precipitation by forming an aqueous U^{VI}-siderophore complex, preventing the formation of the uranium mineral phase.[1] Alternatively, siderophores could coat the surface of individual uranium crystals, modifying the surface charge of the uranium crystals, preventing aggregation of the U^{VI} precipitates.[311]

The aim of the research presented here is to determine whether the siderophore, desferrioxamine B can influence U^{VI} precipitation in alkaline solutions by forming an aqueous complex with U^{VI}. To explore the macroscale effect of DFOB on U^{VI} solutions, stirred batch experiments were conducted with 0, 4.2, 42, 130 and 420 µM DFOB in solutions containing 42 µM U^{VI} and 0.1 M NaCl at pH 11.5. Samples were filtered through 0.2, 0.45 and 1 µm filter membranes over three days (short term) or two months (long term). DFT was used to explore whether the functional groups of DFOB could complex with U^{VI} preventing the formation of the U^{VI} precipitate.

7.2. Experimental study: The effect of desferrioxamine B on U^{VI} precipitation

7.2.1. Three day batch experiments

The experimental data plotted for these batch experiments are provided in Table B12-B16. The filtered samples from the control experiments found that 4-5% of U^{VI} passed through the nylon filter membranes (0.2, 0.45 and 1 µm diameter pores) once the reaction had reached equilibrium (Figure 7.1, Table 7.1). This indicates that 95-96% of U^{VI} formed precipitates with diameter ≥1 µm, in agreement with the results from chapter 4, and Kenney *et al*.[254] The reaction occured rapidly with >90% U^{VI} precipitating from solution in approximately 8 hours.

When 4.2 µM DFOB is added to solution approximately 11-12% of U^{VI} passed through the filter membrane after the reaction reaches equilibrium, suppressing precipitate formation by 6% (Figure 7.1, Table 7.1). This indicates that within the concentration range expected in rocks (<10 µM),[89] siderophores will only have a small effect on aqueous U^{VI} chemistry. [90, 92, 312]

Increasing DFOB concentration into the range found for siderophores in soils leads to significant short term suppression of U^{VI} precipitate formation. When the DFOB concentration was increased to 42 µM (1:1 ratio with U^{VI}), 41-53% of U^{VI} passed through the filter membranes. When 130 µM DFOB was present, 94-95% of U^{VI} passed through the filter membranes indicating only 4-6% of U^{VI} formed ≥1 µm diameter precipitates. Finally, 100% of U^{VI} passed through the filter membranes when the DFOB concentration was increased to 420 µM, in the upper range of soil concentrations representative of the rhizosphere. The results from chapter 4 showed that in the absence of ≥ 0.2 µm diameter precipitates, U^{VI} was highly mobile through quartz sand. This means DFOB could have a mobilising effect in this system. It also means that siderophores could potentially have a significant effect on the mobility of U^{VI} in soil systems, although competition effects with other metal ions, in particular Fe^{III}, and other minerals and organic matter need to be explored.

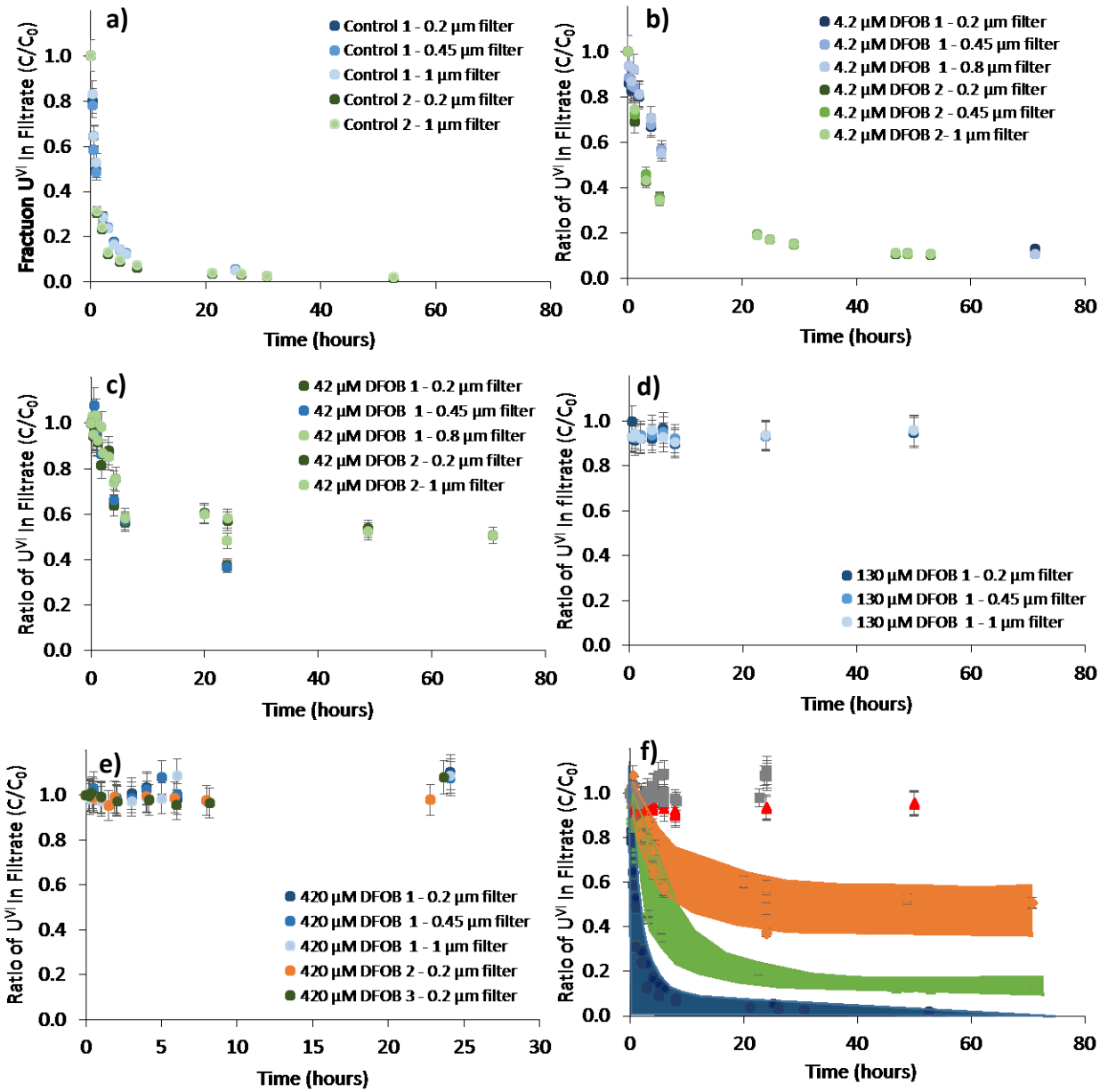

Figure 7.1. The effect of [DFOB] on U^{VI} precipitation over up to 3 days. a), b), c), d) and e) are the results from 0, 4.2, 42, 130, and 420 µM [DFOB] respectively. The first, second and third experiments are given as blue, green and orange circles respectively. The darkest shade of colour represents the smallest filter (0.45 µm) while the lightest shade represents the biggest filter (1 µm) The data is overlain in f) where the blue circles, green bars, orange diamonds, red triangles and grey squares represent the 0, 4.2, 42, 130 and 420 µM [DFOB] respectively. These are overlain with block colour as the second 4.2 µM DFOB data overlaps with that of the 42 µM DFOB data. The experimental data plotted in a), b), c), d) and e) are provided in Table B12, B13, B14, B15 and B16 respectively.

Table 7.1. The average percentage of U^{VI} remaining in the filtrate once the reaction has reached an approximate equilibrium during the short term batch experiments. The rate constant was estimated based on samples collected within the first 500 minutes (~8 hours) of the experiment. 1 S.D. of temperature and pH is typically 2˚C and 0.03 pH units respectively. The experimental data plotted are provided in Table B12- B16 and B18

Experiment	% U in filtrate after reaching equilibrium	Temperature (˚C)	pH
Control 1	5	26	11.44
Control 2	4	23	11.51
DFOB 4.2 µM 1	12	26	11.49
DFOB 4.2 µM 2	11	20	11.49
DFOB 42 µM 1	41	26	11.49
DFOB 42 µM 2	53	26	11.50
DFOB 130 µM 1	94	26	11.49
DFOB 130 µM 2[a]	95	23	11.40
DFOB 130 µM 3[a]	95	24	11.40
DFOB 420 µM 1	101	26	11.56
DFOB 420 µM 2	98	26	11.50
DFOB 420 µM 3	99	26	11.50

[a]Values taken from two month batch experiments after three days

7.2.2. Two month batch experiments

The experimental data plotted for these batch experiments are provided in Table B17-B19. The long term effects of DFOB on U^{VI} were explored using precipitation inhibition experiments. During these experiments 130 µM DFOB was added to the pH 11.5, 0.1 M NaCl solution before addition of U^{VI}. These 250 ml samples were placed on a shaker tray at 25 ˚C and 130 rpm and 5 ml samples were filtered through 0.2, 0.45 and 1 µm filter membranes typically once a week. Dissolution experiments were conducted where 250 ml solutions containing 42 µM U^{VI} and 0.1 M NaCl at pH 11.5 were placed on the shaker trays for 48 hours to allow U^{VI} to precipitate from solution. After 48 hours, 130 µM DFOB was added to the solution. Control experiments were conducted in the absence of 130 µM DFOB to determine whether U^{VI} precipitation remained stable over the 8 week timeframe.

The two control experiments show that 0-2% of U^{VI} passed through the filter members over the two month period, indicating virtually all U^{VI} had precipitated from solution (Figure 7.2a). This shows that

in the absence of DFOB, the U^{VI} precipitate remains stable in solution, and could be highly immobile in porous media, as observed in chapter 4.

During the inhibition experiments, approximately 6% of U^{VI} was removed by all filter membranes sizes in the first week, suggesting that precipitate formation was inhibited by 94% (Figure 7.2b). This means DFOB could potentially significantly enhance the mobility of U^{VI} in porous media such as quartz sand. However, as time progressed, the amount of U^{VI} removed by the filters increased. The change in U^{VI} concentration in the filtrate was greatest between week two and five, where the concentration of U^{VI} in the filtrate decreased linearly. In week two, 85-93% of U^{VI} passed through the filters while by week five 40-45% passed through the filter membranes. After seven weeks, equilibrium was reached and 28-34% U^{VI} passed through the filter membranes. One potential mechanism responsible for increased U^{VI} precipitation is the degradation of DFOB as indicated by the safety data sheet of the siderophore provided by Sigma-Aldrich. The degradation products are likely to be dihydroxamic and monohydroxamic acids as these have been observed to occur when DFOB is in the presence of bacteria.[313] These degradation products can still interact with U^{VI} but with reduced efficiency, leading to the continued inhibition of approximately 30% of U^{VI} precipitation after eight weeks. This mechanism needs to be tested in future research. This could be achieved by repeating the experiment and analysing the samples using high-performance liquid chromatography in combination with gas chromatography mass spectrometry (HPLC-GCMS) to identify DFOB and its degradation products. [313] Alternatively, pH 11.5 solutions containing 130 µM DFOB and 0.1 M NaCl at pH 11.5 could be prepared and left for eight weeks. Then the 42 µM U^{VI} solution could be added to see if 70% of the U^{VI} precipitates from solution.

The dissolution experiments indicate that 130 µM DFOB dissolved or disaggregated approximately 20% of the U^{VI} precipitates (Figure 7.2c). This was stable for approximately five weeks before the particles started to re-aggregate or re-precipitate. Only 12% of U^{VI} remained in solution after eight

weeks. This shows DFOB can dissolve U^{VI} after it has precipitated, although it is not as effective when compared to the experiments in which the siderophore is added before U^{VI} had precipitated from solution.

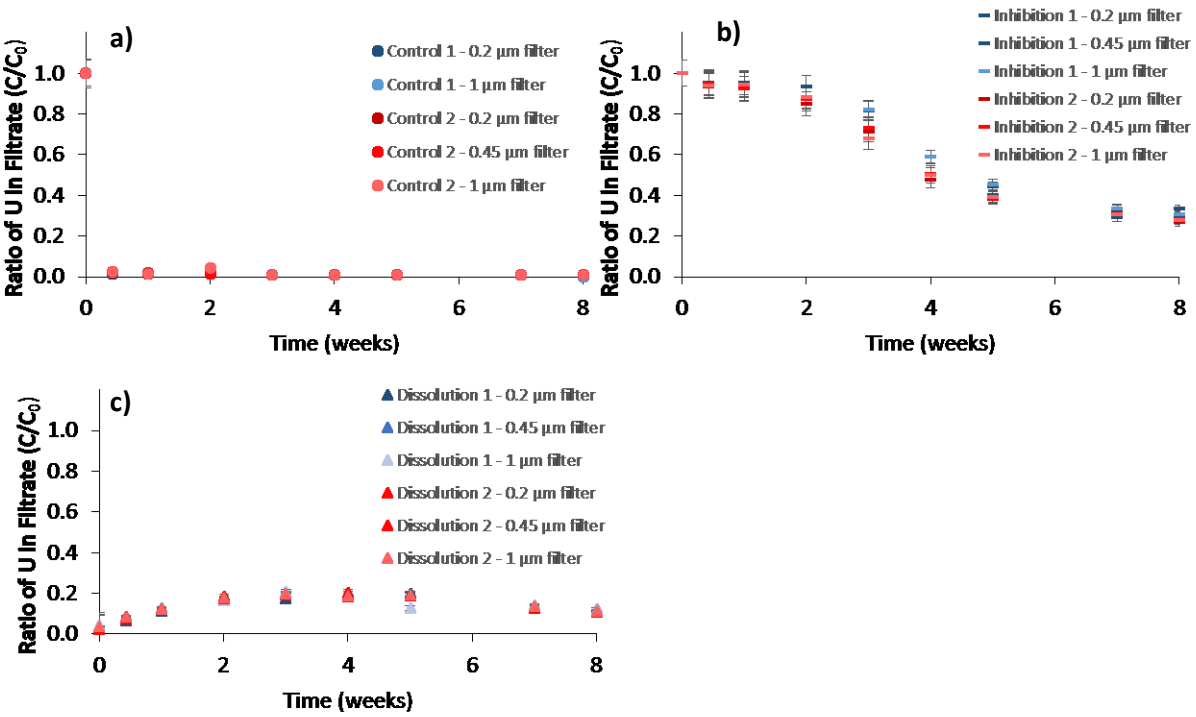

Figure 7.2. Results of batch experiments at pH 11.5 containing 42 µM U^{VI}, 130 µM DFOB and 0.1 M NaCl which were conducted over a two month time period. The results from the control experiment containing 42 µM U^{VI} and 0 µM DFOB are presented in part a), the results from the precipitation inhibition experiments are presented in part b) and the results from the dissolution experiments are presented in part c). The blue data points are the results from experiment 1 and the red points are results from experiment 2. Different shades represent the different filter sizes (0.2, 0.45 and 1 µm filter membrane pore size) where the darkest shade is 0.2 µm and lightest shade is 1 µm. The experimental data plotted in a), b) and c) are provided in Table B17, B18 and B19 respectively.

7.3. Possible mechanisms controlling U^{VI} precipitation

The experiments show that DFOB can significantly reduce the amount of U^{VI} which forms the 800 ± 100 nm diameter U^{VI} precipitates. There are two main mechanisms which could be causing this. DFOB could be sorbing to the U^{VI} crystals, modifying their surface charge and preventing aggregation.[311] Alternatively U^{VI} could complex with DFOB preventing precipitation.[1]

DFOB could potentially sorb to the uranium mineral surface through a variety of mechanism including electrostatic and van der Waals attraction, hydrophobic interactions via carbon atoms in DFOB and the mineral surface, cation bridging due to the background electrolyte and hydrogen bonding. [311] In chapter 4, the zeta potential (Z_p) of the U^{VI} mineral was measured as -20.9 ± 0.2 mV in pH 11.5, 0.1 M NaCl solutions. The average pK_a values of DFOB are 8.32, 8.97 and 9.52 for the hydroxamate groups and 10.84 for the amine group.[71] At pH 11.5, DFOB will be fully deprotonated with -3 formal charge. Therefore electrostatic repulsion will occur between the U^{VI} surface and the DFOB, minimising sorption and preventing hydrophobic interactions and hydrogen bonding. This agrees with experimental data which found that DFOB desorbs from mineral surfaces, including uraninite, once both the ligand and mineral surface have a negative surface charge.[121, 314, 315] Cation bridging between mineral surfaces and organic molecules tend to only occur with multivalent ions, such as Ca, and not for monovalent cations such as the Na employed here.[311] Therefore it is unlikely that DFOB will be sorbing to the U^{VI} crystal surface, modifying its surface charge and preventing aggregation.

The second mechanism is the formation of aqueous U^{VI}-L complexes. DFOB has been found to form a 1:1 complex with transition metals[110] and a 1:1 complex has been suggested to form for U^{VI}.[1] Other multidentate organic molecules such as α-isosaccharinic and D-gluconate do complex with U^{VI} at pH 12-13,[82-84] therefore it is possible for U^{VI} to complex with negatively charged multidentate organic ligands at such a high pH. The conditional log β, and subsequently $\Delta_r G$, were calculated assuming a 1:1 U^{VI}-L complex is forming as suggested by previous research. [1] The log β_{11} was calculated for each of the 4.2, 42 and 130 μM DFOB batch experiments. This employed the equilibrium concentrations presented in Figure 7.1 and Table 7.1 minus the control experiment equilibrium concentrations. The average log β_{11} calculated from the experiments is -1.2 ± 0.3 and subsequently $\Delta_r G$ was calculated as 7 ± 1 kJ/mol respectively. This indicates a slightly unfavourable reaction. This is illustrated by the 42

μM DFOB experiment where DFOB and U^{VI} are equimolar. If the reaction was favourable, virtually all U^{VI} should be complexed by the DFOB and no U^{VI} precipitates should have been observed.

7.4. Computational Study: U^{VI} complexes with hydroxamate

Hydroxamate is the reactive functional group found within DFOB[71] and the structures of 1:1 and 1:2 U^{VI}-hydroxamate complexes have been optimised. This number of hydroxamate ligands has been used because U^{VI} forms 1:1 and 1:2 U^{VI}-ligand complexes with the hydroxamate ligands acetohydroxamic acid[128] and N-methylacetohydroxamic acid.[130] The results presented in chapter 6 show that the most stable monodentate U^{VI}-hydroxamate conformers occur when the hydroxamate ligand was initially oriented in the axial plane, and bound via the deprotonated hydroxyl group of the ligand. The starting structures for the calculations were constrained to these monodentate conformers and a full geometry optimisation was conducted.

Speciation modelling indicates the dominant dissolved U^{VI} species is $[UO_2(OH)_3]^-$ (68%). The optimised DFT structures for this species indicates four ligands are bound directly to U^{VI} within the equatorial plane of UO_2, represented by $[UO_2(OH)_3(H_2O)]^-$ (Figure 8.1a) rather than five ligands $[UO_2(OH)_3(H_2O)_2]^-$. This is in agreement with a systematic density functional theory study exploring the geometry of mononuclear uranyl aqua and hydroxide complexes across the entire pH range.[44]

Based on this information, $\Delta_r G$ was calculated for the potential 1:1 and 1:2 U^{VI}-L complexes using equations 7.1 to 7.7 using the implicit solvation model and equations 7.8 to 7.14 using the mixed solvation model. L and L_{mono} represent hydroxamate bound in a bidentate and monodentate fashion respectively. In the mixed solvation model, OH^- is replaced with $OH(H_2O)^-$. H_2O is replaced with $(H_2O)(H_2O)_2$ when bound directly to U^{VI}, and L^- is replaced with $L(H_2O)_2^-$. The last group of water molecules in each reactant and product species in equations 7.8-7.14 represent the number of water molecules hydrogen bound to the hydroxyl, aqua, and hydroxamate groups. The U^{VI} complexes using

the implicit and mixed solvation models are provided are provided in Figure 7.3a and 7.4 respectively. The thermodynamic properties (H, TS, G, $\Delta_r G$) are provided in Table C13 and C14 for the implicit and mixed solvation methods respectively. The structural properties of these complexes are provided in Table D8 and D9 for the implicit and mixed solvation methods respectively.

Implicit solvation model

$$[UO_2(OH)_3(H_2O)]^- + L^- = [UO_2(L_{mono})(OH)_3]^{2-} + H_2O \quad (7.1)$$

$$[UO_2(OH)_3(H_2O)]^- + L^- = [UO_2(L_{mono})(H_2O)(OH)_2]^- + OH^- \quad (7.2)$$

$$[UO_2(OH)_3(H_2O)]^- + L^- = [UO_2(L)(OH)_2]^- + OH^- + H_2O \quad (7.3)$$

$$[UO_2(OH)_3(H_2O)]^- + L^- = [UO_2(L)(H_2O)(OH)]^0 + 2OH^- \quad (7.4)$$

$$[UO_2(OH)_3(H_2O)]^- + 2L^- = [UO_2(L)(L_{mono})(H_2O)]^0 + 3OH^- \quad (7.5)$$

$$[UO_2(OH)_3(H_2O)]^- + 2L^- = [UO_2(L)(L_{mono})(OH)]^- + 2OH^- + H_2O \quad (7.6)$$

$$[UO_2(OH)_3(H_2O)]^- + 2L^- = [UO_2(L)_2]^0 + 3OH^- + H_2O \quad (7.7)$$

Mixed solvation model

$$[UO_2(OH)_3(H_2O)(H_2O)_5)]^- + [L(H_2O)_2]^- = [UO_2(L_{mono})(OH)_3(H_2O)_4]^{2-} + 3H_2O \quad (7.8)$$

$$[UO_2(OH)_3(H_2O)(H_2O)_5)]^- + [L(H_2O)_2]^- = [UO_2(L_{mono})(OH)_2(H_2O)(H_2O)_5)]^- + OH^- + H_2O \quad (7.9)$$

$$[UO_2(OH)_3(H_2O)(H_2O)_5)]^- + [L(H_2O)_2]^- = [UO_2(L)(OH)(H_2O)_2]^- + OH^- + 4H_2O \quad (7.10)$$

$$[UO_2(OH)_3(H_2O)(H_2O)_5)]^- + [L(H_2O)_2]^- = [UO_2(L)(OH)(H_2O)(H_2O)_3)]^0 + 2OH^- + 2\,H_2O \quad (7.11)$$

$$[UO_2(OH)_3(H_2O)(H_2O)_5)]^- + 2[L(H_2O)_2]^- = [UO_2(L)(L_{mono})(H_2O)(H_2O)_3)]^0 + 3OH^- + 3H_2O \quad (7.12)$$

$$[UO_2(OH)_3(H_2O)(H_2O)_5)]^- + 2[L(H_2O)_2]^- = [UO_2(L)(L_{mono})(OH)(H_2O)_2]^- + 2OH^- + 5H_2O \quad (7.13)$$

$$[UO_2(OH)_3(H_2O)(H_2O)_5)]^- + 2[L(H_2O)_2]^- = [UO_2(L)_2]^0 + 3OH^- + 6H_2O \quad (7.14)$$

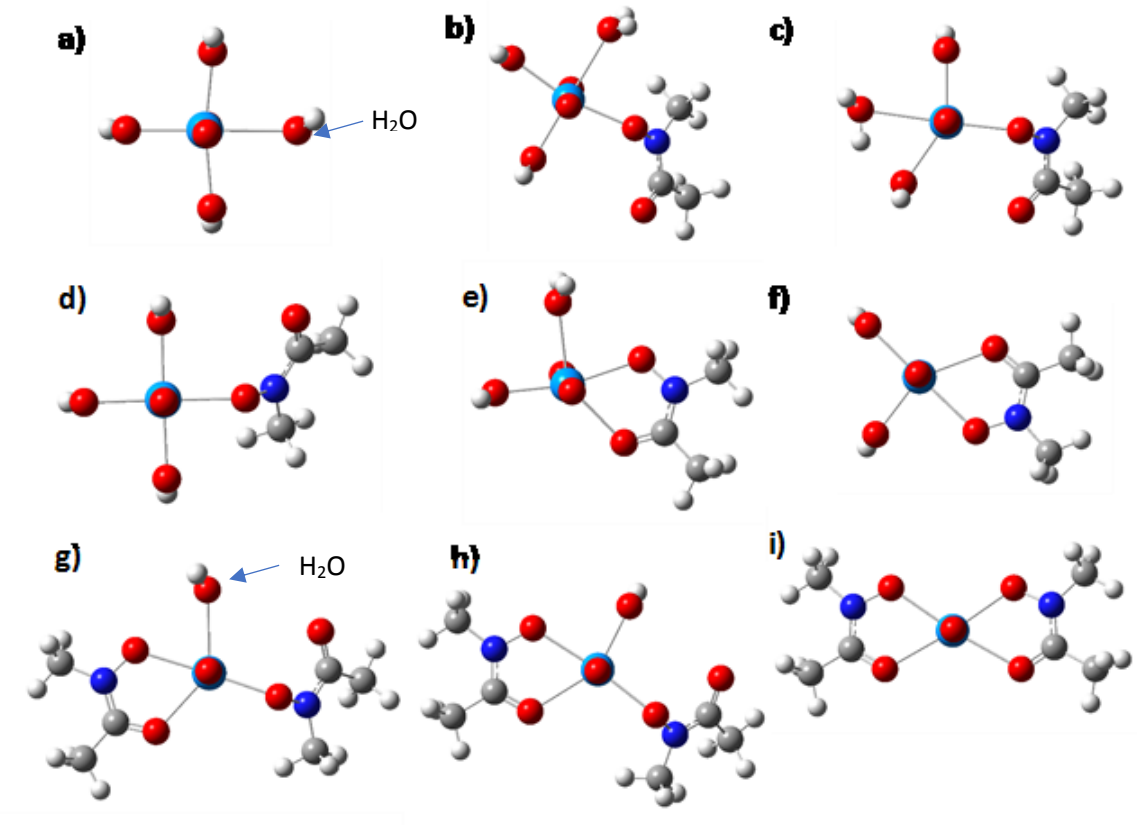

Figure 7.3. Structures of potential U^{VI} hydroxamate complexes using the implicit solvation model. a) is $[UO_2(OH)_3(H_2O)]^-$ b) and c) are the U^{VI}-L complex in Equation 7.1 where hydroxamate is cis and trans to the U^{VI} bound aqua ligand respectively. d) to i) are equations 7.2 to 7.7 respectively. The white, grey, dark blue, grey, red and light blue atoms represent H, C, N, O and U respectively. The thermodynamic properties (H, TS, G, $\Delta_r G$) are provided in Table C13 and the structural properties of these complexes are provided in Table D8.

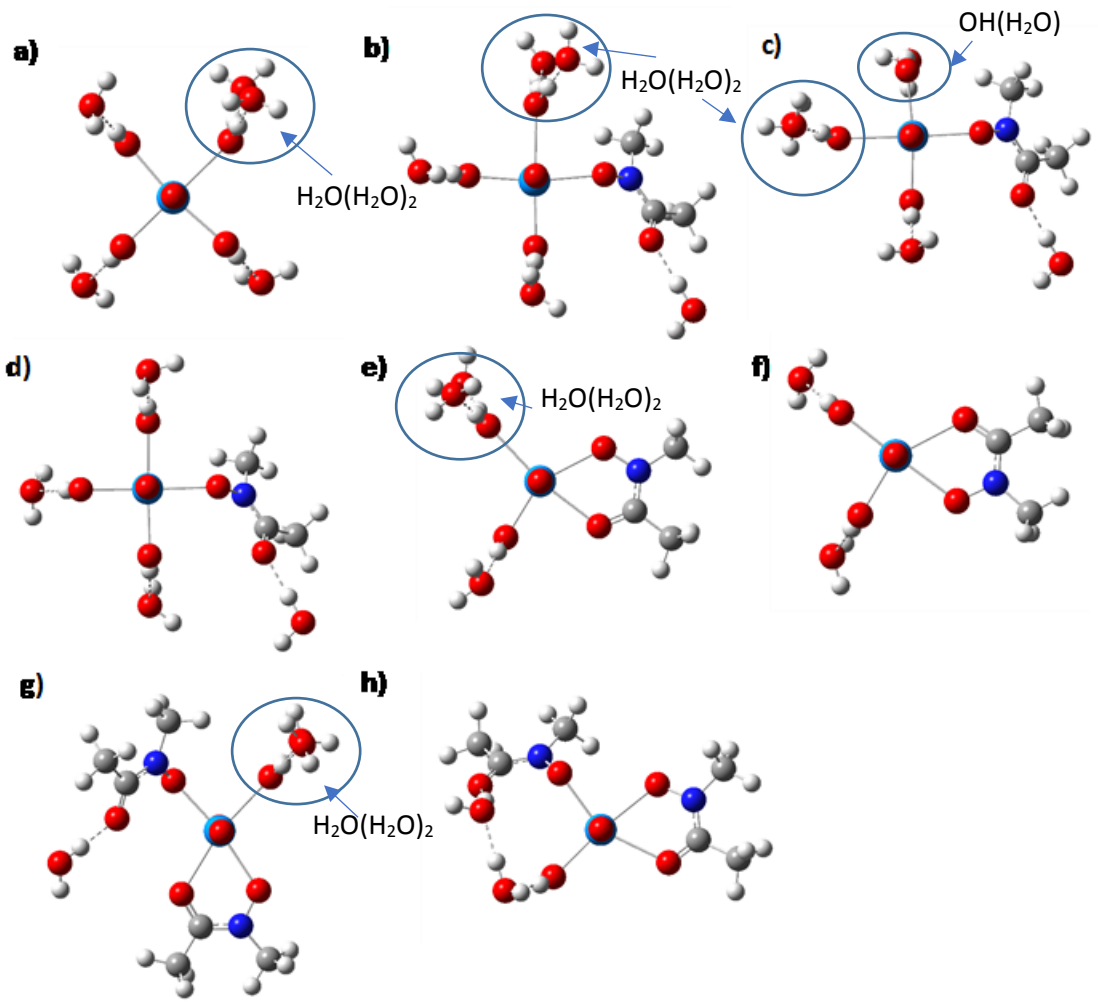

Figure 7.4. Structures of potential U^{VI} hydroxamate complexes using the mixed solvation model. a) is $[UO_2(OH)_3(H_2O)(H_2O)_5]^-$ b) and c) are the U^{VI}-L complex in Equation 7.8 where hydroxamate is cis and trans to the U^{VI} bound aqua ligand respectively. d) to h) are equations 7.9 to 7.14 respectively. The white, grey, dark blue, grey, red and light blue atoms represent H, C, N, O and U respectively. The thermodynamic properties (H, TS, G, $\Delta_r G$) are provided in Table C14 and the structural properties of these complexes are provided in Table D9.

The $\Delta_r G$ for the implicit (green circles) and mixed (blue triangles) solvation models are provided on Figure 7.5. $\Delta_r G$ was usually ≥64 kJ/mol and ≥37 kJ/mol when using the implicit and mixed solvation models respectively. The subsequent log β are ≥ -11 and ≥ -6 for the implicit and mixed solvation models respectively. This is significantly more unfavourable than the experimentally calculated log β (-1.2 ± 0.3) and these complexes unlikely represent the local binding mode of DFOB to U^{VI} through its functional groups.

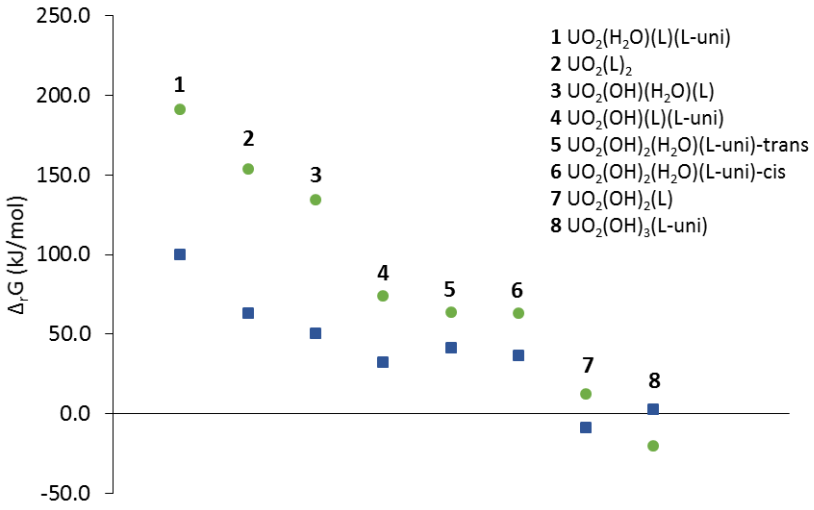

Figure 7.5. Calculated $\Delta_r G$ of the 1:1 and 1:2 U^{VI}-hydroxamate (L) complexes for the implicit (green circles) and mixed (blue squares) solvation models. The thermodynamic properties (H, TS, G, $\Delta_r G$) are provided in Table C13 and C14 for the implicit and mixed solvation methods respectively.

There are two complexes which both models predict could represent the local binding mode of U^{VI} to DFOB. These are $[UO_2(OH)_3(L\text{-mono})]^{2-}$ and $[UO_2(OH)_2(L)]^{-}$, whose structures are shown in part c and f on Figure 7.3 and 7.41. The two complexes $\Delta_r G$ are illustrated by structures 7 and 8 on Figure 7.5. The $\Delta_r G$ calculated using the implicit solvation model is -20 and +13 kJ/mol for $[UO_2(OH)_3(L\text{-mono})]^{2-}$ and $[UO_2(OH)_2(L)]^{-}$ respectively. This corresponds to 3.6 and -2.2 log β units respectively. When employing the mixed solvation model, the $\Delta_r G$ is +3 and -9 kJ/mol for $[UO_2(OH)_3(L\text{-mono})]^{2-}$ and $[UO_2(OH)_2(L)]^{-}$ respectively. This corresponds to -0.5 and 1.6 log β units. Both these complexes can be slightly unfavourable depending on the model used. Considering the mixed solvation model more accurately represents $\Delta_r G$, the local binding mode of U^{VI} to DFOB is represented by $[UO_2(OH)_3(L\text{-mono})]^{2-}$ (log β = -0.5).

7.5. Implications of pH changes on U^{VI} mobility in the presence of desferrioxamine B

The stability constant results determined in this chapter can be used to estimate how the stability of U^{VI}-DFOB complexes when a pH 11.5 U^{VI} waste plume mixes with pH 7 groundwater (Figure 7.6). The stability of U^{VI}-DFOB complex is very low at pH 11.5 as the experimental and DFT log β values are -

1.2 and -0.5 log β units respectively. Therefore U^{VI} will likely be present as a precipitate in a geological disposal facility and mobility will be fairly low. The pH of the U^{VI} plume will decrease as it travels away from the waste facility due to mixing with natural groundwater. As the pH approaches 7, experimental data indicates the log β of the U^{VI}-siderophore complex will increase to 17.1 log β units[1] increasing the quantity of U^{VI}-siderophore complexes. The spectrophotometrically predicted species[1] is $UO_2(HDFOB)^0$ which will have minimal interactions with charged mineral surfaces, enhancing U^{VI} mobility. Therefore as the plume pH progressively decreases the mobility of U^{VI} progressively increases as highlighted by time steps 1, 2 and 3 (T1-T3) in Figure 7.6.

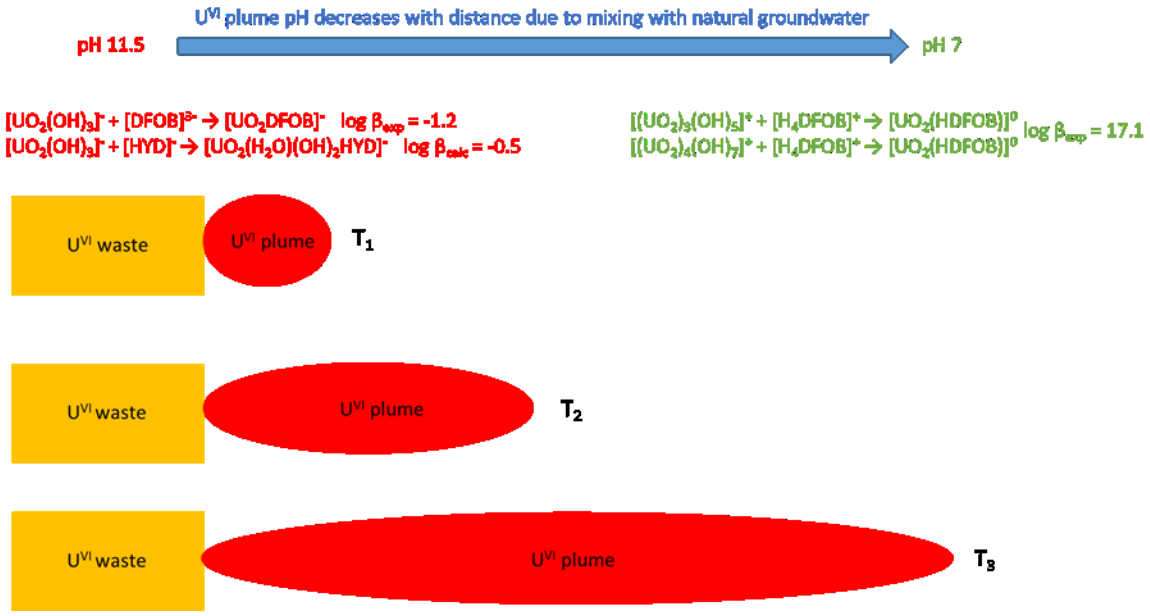

Figure 7.6. Conceptual model of the mobility of a U^{VI} contaminant plume with increasing time given by time steps T1, T2 and T3. The plume initially starts at pH 11.5 at the waste source and decreases to pH 7 with increasing distance away from the waste source. The log β determined experimentally ($\log \beta_{exp} = -1.21$) and computationally ($\log \beta_{calc} = -0.46$) at pH 11.5 for the U^{VI}-DFOB complex is provided in red. The experimental log β at pH 7 for the U^{VI}-DFOB complex ($\log \beta_{exp} = 17.1$) is given in green. The experimental log β for $[UO_2(HDFOB)]^0$ at pH 7 is from Mullen *et al.*[1]

The results from chapter five can be help estimate how the stability of U^{VI}-DFOB will change when U^{VI} is transported as part of an acidic waste (pH <5.5) plume (Figure 7.7). At pH ≤5.5 when U^{VI} is present as $[UO_2(H_2O)_5]^{2+}$ the calculated log β for DFOB estimated in section 6.5 from the DFT calculations is 18 log β units. The U^{VI}-DFOB complex is highly stable in aqueous solution. The species predicted spectrophotometrically[1] at pH 4 is $[UO_2(H_2DFOB)]^{+}$. If the rock surface is positively charged (e.g. ferrihydride pK_{a1}= 6.5, pK_{a2} = 9.1)[316] then U^{VI} will be highly mobile due to charge repulsion. If the mineral surface is negatively charged (e.g. quartz pK_a = 3.0)[317] then U^{VI} mobility will be reduced due to sorption. Mixing the plume with pH 7 groundwater will increase the plume pH with distance from the waste source. Increasing the pH is predicted to change the species to the neutral $UO_2(HDFOB)^0$ with similar log β (log β =17.1)[1] and U^{VI} will be highly mobile due to limited sorption to charged mineral surfaces.

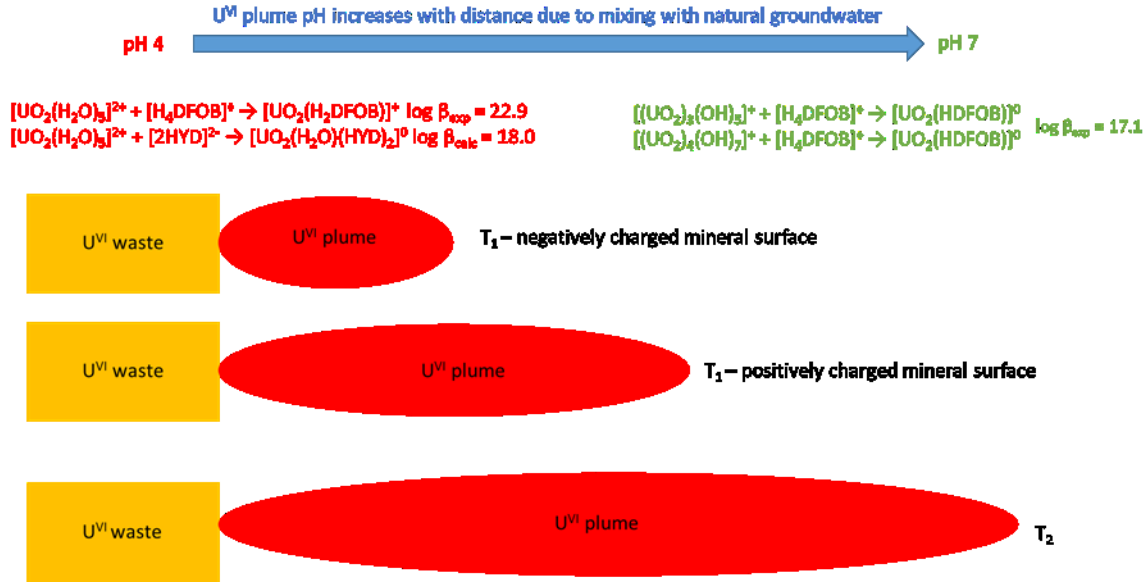

Figure 7.7. Conceptual model of the mobility of a U^{VI} contaminant plume with increasing time given by time steps T1, T2. The plume initially starts at pH 4 at the waste source and increases to pH 7 with increasing distance away from the waste source. T1-negatively mineral charged surface and T1-positively charged mineral surface highlight the differences in U^{VI} mobility at a given time step (T1) when the mineral surface is negatively and positively charged respectively. The log β determined experimentally (log β_{exp} = 22.9) and computationally (log β_{calc} = 18.0) for the U^{VI}-DFOB complex at pH 4 is provided in red. The experimental log β at pH 7 for the U^{VI}-DFOB complex (log β_{exp} = 17.1) is given in green. The experimental log β for $[UO_2(H_2DFOB)]^{+}$ and $[UO_2(HDFOB)]^0$ at pH 4 and 7 is from Mullen *et al*. [1]

7.6. Conclusions

The first objective of the research presented in this chapter was to investigate the effect of DFOB on U^{VI} precipitation by conducting a series of short term (3 days) and long term (2 months) batch filtration experiments. The experimental results show that DFOB can prevent almost 100% U^{VI} precipitation as ≥0.2 µm precipitates for two weeks, and dissolve up to 20% U^{VI} between two and five weeks, when 130 µM DFOB is initially present. The results presented in chapter 4 show that U^{VI} is highly mobile in quartz sand in the absence of ≥0.2 µm precipitates. This means DFOB could have a mobilising effect on U^{VI} at pH 11.5 in NaCl solutions. The results also suggests DFOB could have a significant impact on the mobility of U^{VI} in soil environments. However, further research is required to determine the effects of different mineralogies, organic matter and competitive cations on U^{VI} mobility in the presence of DFOB.

The second objective of the research presented in this chapter was to gain a first insight into the potential binding mode of U^{VI} to DFOB by calculating the $\Delta_r G$, and subsequently log β of 1:1 and 1:2 U^{VI}-hydroxamate complexes. This was done using both an implicit and mixed solvation model. Changing from the less accurate implicit solvation to more accurate mixed solvation model shifts $\Delta_r G$ towards 0. The proposed local binding mode is for one hydroxamate group to displace the U^{VI} bound water molecule, forming a monodentate bond, $[UO_2(OH)_3(\text{L-mono})]^{2-}$. Experimental work needs to be conducted to confirm this is the case. Note that the DFT calculations could cause the -2 uranium-ligand complexes to have a more positive $\Delta_r G$ than the -1 charge uranium-ligand complexes due to the increased instability of anions with increasingly negative charge in the gas phase, as discussed in chapter 6. Future research should also explore the effect of adding a counter-ion to all charged species in the reactions to remove potential errors to $\Delta_r G$ which could be caused because of the decreased stability of the anionic species in the gas phase, and to ensure the best description (e.g. UFF, UAO etc) of the solvation cavity can be applied to all species.

Chapter 8 – PhD Summary

The aim of the research presented in this thesis was to advance our understanding of the effect of the naturally occurring organic molecules, siderophores, on the aqueous chemistry of U^{VI} in alkaline and saline solutions. To address this, a multidisciplinary approach was used which combined macroscale experiments with molecular level calculations. Key conclusions from the research are outlined below:

1. The results show 42 µM U^{VI} precipitates from 0.1 M NaCl solutions at pH 10.5 and pH 11.5 as sodium diuranate ($Na_6U_7O_{24}$). The hydrodynamic diameters of the U^{VI} precipitates at pH 10.5 and 11.5 were 600 ± 100 and 800 ± 100 nm respectively. These precipitates were usually immobilised in quartz sand with median grain diameter 120 µm. The charge of the U^{VI} precipitates (-22 ± 1 and -20.9 ± 0.2 mV) and the quartz sand (-41 ± 1 and -42 ± 2 mV) were negative at pH 10.5 and 11.5, indicating the precipitates did not sorb to the mineral surface. The d_p/d_{50} ratio is 0.0053 and 0.0070, indicating significant immobilisation through particle straining. The Z_p of other U^{VI} minerals such as calcium uranate (-22.2 mV in 0.01 M NaCl) and sodium boltwoodite (-45 mV in 0.1 M $NaClO_4$) are also negative. Therefore their mobility in quartz sand will also be controlled by the physical properties of the U^{VI} precipitates and quartz sand under the chemical conditions employed here.
2. In the absence of detectable U^{VI} precipitates (≥0.2 µm diameter) at pH 10.5 and 12.5, U^{VI} was transported at approximately the same rate as the non-reactive tracer. At pH 10.5, 16% to 19% of U^{VI} was eluted from the quartz sand column as ≥0.2 µm diameter precipitates.
3. Addition of DFOB at environmentally relevant concentrations (130 and 420 µM DFOB) quantitatively prevents 42 µM U^{VI} from precipitating in pH 11.5, 0.1 M NaCl solutions. A review of the literature shows the adsorption of DFOB to negatively charged mineral surfaces, including uraninite, significantly decreased above pH 8 once DFOBs hydroxamate functional groups have deprotonated. Instead, U^{VI} is likely forming an aqueous U^{VI} complex

as observed for other multidentate organic molecules at pH 12-13. This complex will be negatively charged and therefore should not adsorb to the surface of quartz, implying U^{VI} will be highly mobile in this system.

4. A DFT protocol can be used to calculate the log β for unknown 1:1 U^{VI}-L complexes provided a fitting equation is used. Changing the U^{VI} small core ECPs, U^{VI} basis sets, ligand basis sets and DFAs used in the DFT protocol did not significantly affect calculated $\Delta_r G$ compared to the absolute difference between the calculated and experimental $\Delta_r G$. Modelling U^{VI} bound aqua ligands as $(H_2O)(H_2O)_2$ in combination with the IEFPCM solvation model improves the calculated $\Delta_r G$ with respect to the experimental $\Delta_r G$. However, the calculated $\Delta_r G$ were still four to six times too favourable and a fitting approach would still need to be employed. Therefore implicitly modelling all but the U^{VI} bound aqua ligands (i.e. $[UO_2(H_2O)_5]^{2+}$) remains the most practical approach for developing relative stability series.
5. The relative stability series for U^{VI} complexes with six key siderophore functional groups has been established using the DFT protocol: α-hydroxycarboxylate bound via the α-hydroxy and carboxylate groups (log β_{110} = 17), α-hydroxyimidazolate (log β_{110} = 17), catecholate (log β_{110} = 16), hydroxamate (log β_{110} = 9), hydroxy-phenyloxazolonate (log β_{110} = 8), α-hydroxycarboxylate bound via the carboxylate group (log β_{110} = 8) and α-aminocarboxylate (log β_{110} = 5). The advantage of using a computational over experimental method is that the log β of each possible conformer can be explored. Only the log β of the most stable conformer will be calculated experimentally which may not necessarily be the binding mode for full siderophores.
6. Although there is a wide variety of siderophores with complex structures, the numbers of functional groups that bind directly to U^{VI} atoms are relatively few. Conceptually, it would be very useful if the stability of U^{VI} complexes with whole siderophores could be approximately predicted based on the relative stability series of the functional groups. This concept was tested for DFOB, assuming it will bind via two functional groups as observed for AHA, NMAH

and suggested for DFOB. Multiplying the β of two hydroxamate groups estimated a stability constant (log β) of 18 ± 2 accounting for 77 ± 7% of the experimental log β. This highlights the potential of such an application once the log β and structures of a reasonable number of U^{VI} siderophores have been characterised.

7. The DFT protocol was adapted to include a mixed solvation model and the stability constants of possible 1:1 and 1:2 U^{VI}-hydroxamate complexes were calculated. This provided a first indication of the binding mode of DFOB to U^{VI} at pH 11.5. The most likely hydroxamate complex is $[UO_2(OH)_3(L\text{-mono})]^{2-}$. The calculated log β is -0.5, and compares well to the experimentally derived log β of -1.2 ± 0.3.

Chapter 9 - Future Research

Although the research presented here helps increase our understanding of U^{VI} aqueous chemistry in alkaline solutions and siderophore interactions with U^{VI}, there are a variety of areas that need further work.

1. The mobile fraction of U^{VI} between pH 10.5 and 12.5 needs further analysis to confirm whether U^{VI} is present as < 200 nm precipitates or whether it is present as a dissolved species. This could be achieved by using ultrafiltration or Small Angle X-Ray Scattering (SAXS) at a synchrotron. The advantage of SAXS is that it is an in situ measurement, however the drawback is that it is complex and time consuming (proposal for synchrotron, complex experimental method). The advantage of ultrafiltration is that it is much simpler and cheaper to do.
2. Although the experimental data points towards physical processes controlling U^{VI} mobility in quartz sand, it would be really useful to conduct one dimensional transport modelling to confirm this. To gain greater mechanistic insight, a variety of different quartz sand grain size distributions could be tested which are representative of typical sizes observed in nature (fine sandstone, medium sandstone, coarse sandstone etc.). This would allow us to move away from model systems (spherical latex particles), to more environmentally relevant systems (U^{VI} minerals). Although the Darcy velocity employed here is similar to mechanistic studies in the literature for particle straining, it would also be useful to assess the effect of particle straining at natural Darcy velocities.
3. The experiments reported here were conducted in a simple NaCl system. A component additive approach can now be taken to explore the effect of other chemical components. For example, the effect of adding multivalent cations such as Ca^{2+}, and Si^{4+} could be explored. Different inorganic and organic ligands present in radioactive waste or natural

groundwater could be included. This could be very useful as it provides a broad understanding across a variety of chemical conditions, which do not risk being site specific.

4. The results in chapter 5 highlight the significant effect the model siderophore, DFOB, can play in aqueous U^{VI} chemistry in alkaline solutions. However, there is very little experimental or computational data for any pH value for U^{VI}-siderophore interactions. This includes macroscale effects such as reported in chapter 5 of my thesis, structural data, or log β data. It would be worthwhile expanding this knowledge initially to common siderophores such as enterobactin, rhizoferrin, rhizobactin, ferriochrome and mugineic acid. This could initially be conducted in a simple system (e.g. $NaClO_4$ for log β) before adding different cations to solution which are relevant to radioactive waste disposal (K^+, Ca^{2+}, $Fe^{2/3+}$, Al^{3+}, Si^{4+} etc.).
5. The U^{VI} slowly precipitates from solution in the long term DFOB batch experiments and the mechanism for this needs to be explored. Conducting experiments over time which use HPLC-GCMS may be a good way to confirm whether DFOB is degrading over time in these alkaline solutions.
6. The next step from the macroscale perspective is to conduct column experiments in quartz sand to explore how DFOB effects U^{VI} mobility to confirm it is highly mobile as proposed here. It would be really interesting to add alkalophilic bacteria (e.g. *Bacillus*) to either batch or column experiments to explore whether U^{VI} can be taken up as a metal-siderophore complex, and subsequently immobilised if, for example, the bacteria is in a microbial mat on the surface of the quartz mineral.
7. Considering there are over 500 known siderophores, it will be impractical to calculate the log β for all siderophore complexes with any metal. However, as so few functional groups are used which bind with the metal, an approach where the stability of metal-siderophore complexes could be roughly estimated from multiplication of functional group β values could be really useful. It could provide us with trends in siderophore. However U^{VI} is not the best starting point for this because of the lack of available data to find any stability trends, and

increased complexity caused by being a dication. It could be tested initially for Fe^{III} where there is far more experimental data, and is a simpler cation.

8. Future work should extend the protocol to U^{VI} complexes with multiple bound functional groups to take into account changes in the geometry of the structures which are expected to occur for U^{VI}-whole siderophore complexes. Future work should also explore the change in $\Delta_r G$ for neutral species containing counter-ions to prevent energy contributions from instabilities caused by highly charged ions.
9. Although DFT can be very useful for predicting log β, it relies on using a fitting method which means its limited to areas in which experimental data available. It would be useful if improvements could be made to implicit solvation models to improve $\Delta_r G$ calculations. This would be really useful as it can be used for scenarios where it is very difficult to gain experimental data. The results in chapter 6 highlight that the SMD implicit model has good potential as it much more accurately calculates $\Delta_r G$ than IEFPCM. It would be good if the SMD model could be parameterised for transition metals, lanthanides and actinides.

Bibliography

1. Mullen, L.; Gong, C.; Czerwinski, K., Complexation of uranium(VI) with the siderophore desferrioxamine B. *Journal of Radioanalytical and Nuclear Chemistry* **2007,** *273*, (3), 683-688.
2. Yamanaka, K.; Oikawa, H.; Ogawa, H. O.; Hosono, K.; Shinmachi, F.; Takano, H.; Sakuda, S.; Beppu, T.; Ueda, K., Desferrioxamine E produced by Streptomyces griseus stimulates growth and development of Streptomyces tanashiensis. *Microbiology-Sgm* **2005,** *151*, 2899-2905.
3. NDA *Radioactive wastes in the UK: A summary of the 2016 Inventory*; Nuclear Decommissioning Authority: Cumbria, CA24 3HU, 2016; p 19.
4. BEIS *Industrial strategy: Nuclear sector deal*; The Department for Business, Energy and Industrial Strategy: London, UK, 2018; p 43.
5. NDA *Geological disposal: An overview of the generic disposal system safety case*; Oxfordshire OX11 0RH, 2010; p 50.
6. NDA *Geological disposal generic environmental safety case-main report*; Oxfordshire OX11 0RH, 2010; p 258.
7. DEFRA *Managing radioactive waste safely: Proposals for developing a policy for managing solid radioactive waste in the UK*; Department for Environment, Food and Rural Affairs: London, UK, 2001; p 91.
8. CoRWM *Managing our radioactive waste safely: CoRWM's recommendations to government*; Committee on Radioactive Waste Management: London, UK, 2006; p 192.
9. DECC *Implementing geological disposal: A framework for the long term management of higher activity radioactive waste*; Department of Energy and Climate Change: London, SW1A 2AW, 2014; p 55.
10. IAEA *Scientific and technical basis for geological disposal of radioactive wastes*; International Atomic Energy Agency: Vienna, 2003; p 80.
11. NDA *Geological Disposal Near-field Evolution Status Report*; Oxfordshire OX11 0RH, 2010; p 152.
12. SG *Implementation strategy for Scotland's policy on higher activity radioactive waste*; Scottish Government: Edinburgh, EH1 3DG, 2016; p 46.
13. Stockdale, A.; Bryan, N. D., The influence of natural organic matter on radionuclide mobility under conditions relevant to cementitious disposal of radioactive wastes: A review of direct evidence. *Earth-Science Reviews* **2013,** *121*, 1-17.
14. RWM *Geological disposal: Investigating the implications of managing DNLEU through geological disposal* Radioactive Waste Management Ltd.: Didcot, Oxfordshire OX11 0RH, 2015; p 83.
15. Gephart, R. E., A short history of waste management at the Hanford Site. *Physics and Chemistry of the Earth* **2010,** *35*, (6-8), 298-306.
16. Szecsody, J. E.; Truex, M. J.; Qafoku, N. P.; Wellman, D. M.; Resch, T.; Zhong, L. R., Influence of acidic and alkaline waste solution properties on uranium migration in subsurface sediments. *Journal of Contaminant Hydrology* **2013,** *151*, 155-175.
17. Kaplan, D. I.; Gervais, T. L.; Krupka, K. M., Uranium(VI) sorption to sediments under high pH and ionic strength conditions. *Radiochimica Acta* **1998,** *80*, (4), 201-211.
18. Parry, S. A.; O'Brien, L.; Fellerman, A. S.; Eaves, C. J.; Milestone, N. B.; Bryan, N. D.; Livens, F. R., Plutonium behaviour in nuclear fuel storage pond effluents. *Energy & Environmental Science* **2011,** *4*, (4), 1457-1464.
19. Bondici, V. F.; Lawrence, J. R.; Khan, N. H.; Hill, J. E.; Yergeau, E.; Wolfaardt, G. M.; Warner, J.; Korber, D. R., Microbial communities in low permeability, high pH uranium mine tailings: characterization and potential effects. *Journal of Applied Microbiology* **2013,** *114*, (6), 1671-1686.

20. Alexander, W. R.; Dayal, R.; Eagleson, K.; Eikenberg, J.; Hamilton, E.; Linklater, C. M.; McKinley, I. G.; Tweed, C. J., A natural analog of high pH cement pore waters from the Maqarin area of Northern Jordan .2. Results of predictive geochemical calculations. *Journal of Geochemical Exploration* **1992,** *46*, (1), 133-146.
21. Khoury, H. N.; Salameh, E.; Clark, I. D.; Fritz, P.; Bajjali, W.; Milodowski, A. E.; Cave, M. R.; Alexander, W. R., A natural analog of high pH cement pore waters from the Maqarin area of Northern Jordan .1. Introduction to the site. *Journal of Geochemical Exploration* **1992,** *46*, (1), 117-132.
22. Rizoulis, A.; Milodowski, A. E.; Morris, K.; Lloyd, J. R., Bacterial diversity in the hyperalkaline Allas Springs (Cyprus), a natural analogue for cementitious radioactive waste repository. *Geomicrobiology Journal* **2016,** *33*, (2), 73-84.
23. Maher, K.; Bargar, J. R.; Brown, G. E., Environmental speciation of actinides. *Inorganic Chemistry* **2013,** *52*, (7), 3510-3532.
24. Berglund, M.; Wieser, M. E., Isotopic compositions of the elements 2009 (IUPAC Technical Report). *Pure and Applied Chemistry* **2011,** *83*, (2), 397-410.
25. U.S.NRC Uranium Enrichment. https://www.nrc.gov/materials/fuel-cycle-fac/ur-enrichment.html (30/01/2019),
26. IAEA *Management of Reprocessed Uranium: Current status and future prospects*; Vienna, Austria, 2007; p 99.
27. NDA *2016 UK radioactive waste and materials inventory: UK radioactive waste inventory report*; Cumbria, UK, 2017; p 207.
28. Du, X.; Boonchayaanant, B.; Wu, W.-M.; Fendorf, S.; Bargar, J.; Criddle, C. S., Reduction of uranium(VI) by soluble iron(II) conforms with thermodynamic predictions. *Environmental Science & Technology* **2011,** *45*, (11), 4718-4725.
29. Newsome, L.; Morris, K.; Lloyd, J. R., The biogeochemistry and bioremediation of uranium and other priority radionuclides. *Chemical Geology* **2014,** *363*, 164-184.
30. Grenthe, I.; Fuger, J.; Konings, R. J. M.; Lemire, R. J.; Muller, A. B.; Nguyen-Trung-Cregu, C.; Wanner, H., *Chemical thermodynamics of uranium*. OECD Nuclear Energy Agency: 2004; p 735.
31. Lucks, C.; Rossberg, A.; Tsushima, S.; Foerstendorf, H.; Scheinost, A. C.; Bernhard, G., Aqueous uranium(VI) complexes with acetic and succinic acid: Speciation and structure revisited. *Inorganic Chemistry* **2012,** *51*, (22), 12288-12300.
32. Soderholm, L.; Skanthakumar, S.; Neuefeind, J., Determination of actinide speciation in solution using high-energy X-ray scattering. *Analytical and Bioanalytical Chemistry* **2005,** *383*, (1), 48-55.
33. Moll, H.; Reich, T.; Szabo, Z., The hydrolysis of dioxouranium(VI) investigated using EXAFS and O-17-NMR. *Radiochimica Acta* **2000,** *88*, (7), 411-415.
34. Thompson, H. A.; Brown, G. E.; Parks, G. A., XAFS spectroscopic study of uranyl coordination in solids and aqueous solution. *American Mineralogist* **1997,** *82*, (5-6), 483-496.
35. Denning, R. G., Electronic structure and bonding in actinyl ions and their analogs. *Journal of Physical Chemistry A* **2007,** *111*, (20), 4125-4143.
36. Shamov, G. A.; Schreckenbach, G., Density functional studies of actinyl aquo complexes studied using small-core effective core potentials and a scalar four-component relativistic method. *Journal of Physical Chemistry A* **2005,** *109*, (48), 10961-10974.
37. Tsushima, S.; Yang, T. X.; Suzuki, A., Theoretical Gibbs free energy study on $UO_2(H_2O)_n^{2+}$ and its hydrolysis products. *Chemical Physics Letters* **2001,** *334*, (4-6), 365-373.
38. Gutowski, K. E.; Dixon, D. A., Predicting the energy of the water exchange reaction and free energy of solvation for the uranyl ion in aqueous solution. *Journal of Physical Chemistry A* **2006,** *110*, (28), 8840-8856.

39. Spencer, S.; Gagliardi, L.; Handy, N. C.; Ioannou, A. G.; Skylaris, C. K.; Willetts, A.; Simper, A. M., Hydration of UO_2^{2+} and PuO_2^{2+}. *Journal of Physical Chemistry A* **1999,** *103*, (12), 1831-1837.
40. Nichols, P.; Bylaska, E. J.; Schenter, G. K.; de Jong, W., Equatorial and apical solvent shells of the UO_2^{2+} ion. *Journal of Chemical Physics* **2008,** *128*, (12), 8.
41. Berto, S.; Crea, F.; Daniele, P. G.; Gianguzza, A.; Pettignano, A.; Sammartano, S., Advances in the investigation of dioxouranium(VI) complexes of interest for natural fluids. *Coordination Chemistry Reviews* **2012,** *256*, (1-2), 63-81.
42. Parkhurst, D. L.; Appelo, C. A. J., Description of input and examples for PHREEQC version 3--A computer program for speciation, batch-reaction, one-dimensional transport, and inverse geochemical calculations. In *U.S. Geological Survey Techniques and Methods, Book 6*, U.S. Geological Survey: 2013; p 497.
43. Giffaut, E.; Grive, M.; Blanc, P.; Vieillard, P.; Colas, E.; Gailhanou, H.; Gaboreau, S.; Marty, N.; Made, B.; Duro, L., Andra thermodynamic database for performance assessment: ThermoChimie. *Applied Geochemistry* **2014,** *49*, 225-236.
44. Ingram, K. I. M.; Haller, L. J. L.; Kaltsoyannis, N., Density functional theory investigation of the geometric and electronic structures of $UO_2(H_2O)_m(OH)_n^{2-n}$ (n+m=5). *Dalton Transactions* **2006**, (20), 2403-2414.
45. Clark, D. L.; Conradson, S. D.; Donohoe, R. J.; Keogh, D. W.; Morris, D. E.; Palmer, P. D.; Rogers, R. D.; Tait, C. D., Chemical speciation of the uranyl ion under highly alkaline conditions. Synthesis, structures, and oxo ligand exchange dynamics. *Inorganic Chemistry* **1999,** *38*, (7), 1456-1466.
46. Eliet, V.; Bidoglio, G.; Omenetto, N.; Parma, L.; Grenthe, I., Characterization of hydroxide complexes by uranium(VI) by time-resolved fluorescence spectroscopy. *Journal of the Chemical Society-Faraday Transactions* **1995,** *91*, (15), 2275-2285.
47. Martinez-Torrents, A.; Meca, S.; Baumann, N.; Marti, V.; Gimenez, J.; de Pablo, J.; Casas, I., Uranium speciation studies at alkaline pH and in the presence of hydrogen peroxide using time-resolved laser-induced fluorescence spectroscopy (vol 55, pg 92, 2013). *Polyhedron* **2015,** *90*, 266-266.
48. Martinez-Torrents, A.; Meca, S.; Baumann, N.; Marti, V.; Gimenez, J.; de Pablo, J.; Casas, I., Uranium speciation studies at alkaline pH and in the presence of hydrogen peroxide using time-resolved laser-induced fluorescence spectroscopy. *Polyhedron* **2013,** *55*, 92-101.
49. Sandino, A.; Bruno, J., The solubility of $(UO_2)_3(PO_4)_2.4H_2O_{(S)}$ and the formation of U(VI) phosphate complexes. *Geochimica Et Cosmochimica Acta* **1992,** *56*, (12), 4135-4145.
50. Cheng, T.; Barnett, M. O.; Roden, E. E.; Zhuang, J. L., Effects of phosphate on uranium(VI) adsorption to goethite-coated sand. *Environmental Science & Technology* **2004,** *38*, (22), 6059-6065.
51. Clark, D. L.; Hobart, D. E.; Neu, M. P., Actinide carbonate complexes and their importance in environmental chemistry. *Chemical Reviews* **1995,** *95*, (1), 25-48.
52. de Jong, W. A.; Apra, E.; Windus, T. L.; Nichols, J. A.; Harrison, R. J.; Gutowski, K. E.; Dixon, D. A., Complexation of the carbonate, nitrate, and acetate anions with the uranyl dication: Density functional studies with relativistic effective core potentials. *Journal of Physical Chemistry A* **2005,** *109*, (50), 11568-11577.
53. Kubicki, J. D.; Halada, G. P.; Jha, P.; Phillips, B. L., Quantum mechanical calculation of aqueuous uranium complexes: carbonate, phosphate, organic and biomolecular species. *Chemistry Central Journal* **2009,** *3*, 29.
54. Burneau, A.; Tazi, M.; Bouzat, G., Raman spectroscopic determination of equilibrium constants of uranyl sulfate complexes in aquoeus solutions. *Talanta* **1992,** *39*, (7), 743-748.
55. Stumm, W., *Aquatic chemistry : chemical equilibria and rates in natural waters*. 3rd ed. ed.; New York ; Chichester : Wiley, 1996.

56. Gunther, A.; Geipel, G.; Bernhard, G., Complex formation of uranium(VI) with the amino acids L-glycine and L-cysteine: A fluorescence emission and UV-Vis absorption study. *Polyhedron* **2007,** *26*, (1), 59-65.
57. Moll, H.; Glorius, M.; Bernhard, G.; Johnsson, A.; Pedersen, K.; Schafer, M.; Budzikiewicz, H., Characterization of pyoverdins secreted by a subsurface strain of Pseudomonas fluorescens and their interactions with Uranium(VI). *Geomicrobiology Journal* **2008,** *25*, (3-4), 157-166.
58. White, W. M., *Geochemistry*. United Kingdom: Wiley-Blackwell: 2013.
59. Ikeda, A.; Hennig, C.; Tsushima, S.; Takao, K.; Ikeda, Y.; Scheinost, A. C.; Bernhard, G., Comparative study of uranyl(VI) and -(V) carbonato complexes in an aqueous solution. *Inorganic Chemistry* **2007,** *46*, (10), 4212-4219.
60. Guckel, K.; Tsushima, S.; Foerstendorf, H., Structural characterization of the aqueous dimeric uranium(VI) species: $(UO_2)_2CO_3(OH)_3^-$. *Dalton Transactions* **2013,** *42*, (28), 10172-10178.
61. Anderson, C.; Johnsson, A.; Moll, H.; Pedersen, K., Radionuclide geomicrobiology of the deep biosphere. *Geomicrobiology Journal* **2011,** *28*, (5-6), 540-561.
62. Hider, R. C.; Kong, X. L., Chemistry and biology of siderophores. *Natural Product Reports* **2010,** *27*, (5), 637-657.
63. Ahmed, E.; Holmstrom, S. J. M., Siderophores in environmental research: roles and applications. *Microbial Biotechnology* **2014,** *7*, (3), 196-208.
64. Saha, M.; Sarkar, S.; Sarkar, B.; Sharma, B. K.; Bhattacharjee, S.; Tribedi, P., Microbial siderophores and their potential applications: a review. *Environmental Science and Pollution Research* **2016,** *23*, (5), 3984-3999.
65. Boukhalfa, H.; Crumbliss, A. L., Chemical aspects of siderophore mediated iron transport. *Biometals* **2002,** *15*, (4), 325-339.
66. Renshaw, J. C.; Robson, G. D.; Trinci, A. P. J.; Wiebe, M. G.; Livens, F. R.; Collison, D.; Taylor, R. J., Fungal siderophores: structures, functions and applications. *Mycological Research* **2002,** *106*, 1123-1142.
67. Neilands, J. B., Siderophores - structure and function of microbial iron transport compounds. *Journal of Biological Chemistry* **1995,** *270*, (45), 26723-26726.
68. Harris, W. R.; Carrano, C. J.; Cooper, S. R.; Sofen, S. R.; Avdeef, A. E.; McArdle, J. V.; Raymond, K. N., Coordination chemistry of microbial iron transport compounds .19. stability constants and electrochemical behavior of ferric enterobactin and model complexes. *Journal of the American Chemical Society* **1979,** *101*, (20), 6097-6104.
69. Loomis, L. D.; Raymond, K. N., Solution equilibria of enterobactin and metal enterobactin complexes. *Inorganic Chemistry* **1991,** *30*, (5), 906-911.
70. Carrano, C. J.; Drechsel, H.; Kaiser, D.; Jung, G.; Matzanke, B.; Winkelmann, G.; Rochel, N.; AlbrechtGary, A. M., Coordination chemistry of the carboxylate type siderophore rhizoferrin: The iron(III) complex and its metal analogs. *Inorganic Chemistry* **1996,** *35*, (22), 6429-6436.
71. Kiss, T.; Farkas, E., Metal-binding ability of desferrioxamine B. *Journal of Inclusion Phenomena and Molecular Recognition in Chemistry* **1998,** *32*, (2-3), 385-403.
72. Trick, C. G., Hydroxamate-siderophore production and utilization by marine eubacteria. *Current Microbiology* **1989,** *18*, (6), 375-378.
73. Cabaj, A.; Kosakowska, A., Iron-dependent growth of and siderophore production by two heterotrophic bacteria isolated from brackish water of the southern Baltic Sea. *Microbiological Research* **2009,** *164*, (5), 570-577.
74. Garibaldi, J. A.; Neilands, J. B., Formation of iron-bindingcCompounds by micro-organisms. *Nature* **1956,** *177*, (4507), 526-527.
75. Kobayashi, T.; Nishizawa, N. K., Iron uptake, translocation, and regulation in higher plants. *Annual Review of Plant Biology, Vol 63* **2012,** *63*, 131-152.
76. Andrews, S. C.; Robinson, A. K.; Rodriguez-Quinones, F., Bacterial iron homeostasis. *Fems Microbiology Reviews* **2003,** *27*, (2-3), 215-237.

77. Emmenegger, L.; King, D. W.; Sigg, L.; Sulzberger, B., Oxidation kinetics of Fe(II) in a eutrophic Swiss lake. *Environmental Science & Technology* **1998,** *32*, (19), 2990-2996.
78. Rumble, J. R., Solubility product constants of inorganic salts. In *CRC Handbook of Chemistry and Physics*, 99th Edition (Internet Version 2018) ed.; CRC Press/Taylor & Francis: Boca Raton, FL, 2018.
79. Raymond, K. N.; Dertz, E. A.; Kim, S. S., Enterobactin: An archetype for microbial iron transport. *Proceedings of the National Academy of Sciences of the United States of America* **2003,** *100*, (7), 3584-3588.
80. Homann, V. V.; Sandy, M.; Tincu, J. A.; Templeton, A. S.; Tebo, B. M.; Butler, A., Loihichelins A-F, a suite of amphiphilic siderophores produced by the marine bacterium Halomonas LOB-5. *Journal of Natural Products* **2009,** *72*, (5), 884-888.
81. Smith, M. J.; Shoolery, J. N.; Schwyn, B.; Holden, I.; Neilands, J. B., Rhizobactin, a structurally novel siderophore from rhizobium meliloti. *Journal of the American Chemical Society* **1985,** *107*, (6), 1739-1743.
82. Colas, E.; Grive, M.; Rojo, I., Complexation of uranium(VI) by gluconate in alkaline solutions. *Journal of Solution Chemistry* **2013,** *42*, (7), 1545-1557.
83. Warwick, P.; Evans, N.; Vines, S., Studies on some divalent metal alpha-isosaccharinic acid complexes. *Radiochimica Acta* **2006,** *94*, (6-7), 363-368.
84. Sawyer, D. T.; Kula, R. J., Uranium(VI) gluconate complexes. *Inorganic Chemistry* **1962,** *1*, (2), 303-309.
85. Ratledge, C.; Dover, L. G., Iron metabolism in pathogenic bacteria. *Annual Review of Microbiology* **2000,** *54*, 881-941.
86. Gehring, A. M.; Bradley, K. A.; Walsh, C. T., Enterobactin biosynthesis in Escherichia coli: Isochorismate lyase (EntB) is a bifunctional enzyme that is phosphopantetheinylated by EntD and then acylated by EntE using ATP and 2,3-dihydroxybenzoate. *Biochemistry* **1997,** *36*, (28), 8495-8503.
87. Gehring, A. M.; Mori, I.; Walsh, C. T., Reconstitution and characterization of the Escherichia coli enterobactin synthetase from EntB, EntE, and EntF. *Biochemistry* **1998,** *37*, (8), 2648-2659.
88. Griffin, A. S.; West, S. A.; Buckling, A., Cooperation and competition in pathogenic bacteria. *Nature* **2004,** *430*, (7003), 1024-1027.
89. Kraemer, S. M., Iron oxide dissolution and solubility in the presence of siderophores. *Aquatic Sciences* **2004,** *66*, (1), 3-18.
90. Romheld, V., The role of phytosiderophores in acquisition of iron and other micronutrients in gramineous species - an ecological approach. *Plant and Soil* **1991,** *130*, (1-2), 127-134.
91. Bau, M.; Tepe, N.; Mohwinkel, D., Siderophore-promoted transfer of rare earth elements and iron from volcanic ash into glacial meltwater, river and ocean water. *Earth and Planetary Science Letters* **2013,** *364*, 30-36.
92. Kraemer, D.; Kopf, S.; Bau, M., Oxidative mobilization of cerium and uranium and enhanced release of "immobile" high field strength elements from igneous rocks in the presence of the biogenic siderophore desferrioxamine B. *Geochimica Et Cosmochimica Acta* **2015,** *165*, 263-279.
93. Butler, A., Marine siderophores and microbial iron mobilization. *Biometals* **2005,** *18*, (4), 369-374.
94. Sandy, M.; Butler, A., Microbial iron acquisition: Marine and terrestrial siderophores. *Chemical Reviews* **2009,** *109*, (10), 4580-4595.
95. Rajkumar, M.; Ae, N.; Prasad, M. N. V.; Freitas, H., Potential of siderophore-producing bacteria for improving heavy metal phytoextraction. *Trends in Biotechnology* **2010,** *28*, (3), 142-149.

96. Fiedler, H. P.; Krastel, P.; Muller, J.; Gebhardt, K.; Zeeck, A., Enterobactin: the characteristic catecholate siderophore of Enterobacteriaceae is produced by Streptomyces species. *Fems Microbiology Letters* **2001,** *196*, (2), 147-151.
97. Padan, E.; Bibi, E.; Ito, M.; Krulwich, T. A., Alkaline pH homeostasis in bacteria: New insights. *Biochimica Et Biophysica Acta-Biomembranes* **2005,** *1717*, (2), 67-88.
98. Padan, E.; Zilberstein, D.; Rottenberg, H., The proton electrochemical gradient in escherichia coli cells. *European Journal of Biochemistry* **1976,** *63*, (2), 533-541.
99. Slonczewski, J. L.; Rosen, B. P.; Alger, J. R.; Macnab, R. M., pH homeostasis in escherichia coli: Measurement by 31 P nuclear magnetic resonance of methylphosphonate and phosphate. *Proceedings of the National Academy of Sciences of the United States of America* **1981,** *78*, (10), 6271-6275.
100. Vasseur, C.; Baverel, L.; Hebraud, M.; Labadie, J., Effect of osmotic, alkaline, acid or thermal stresses on the growth and inhibition of Listeria monocytogenes. *Journal of Applied Microbiology* **1999,** *86*, (3), 469-476.
101. Rowbury, R. J.; Lazim, Z.; Goodson, M., Regulatory aspects of alkali tolerance induction in Escherichia coli. *Letters in Applied Microbiology* **1996,** *22*, (6), 429-432.
102. Wood, J. M., Bacterial responses to osmotic challenges. *Journal of General Physiology* **2015,** *145*, (5), 381-388.
103. Kramer, R., Bacterial stimulus perception and signal transduction: Response to osmotic stress. *Chemical Record* **2010,** *10*, (4), 217-229.
104. McMillan, D. G. G.; Velasquez, I.; Nunn, B. L.; Goodlett, D. R.; Hunter, K. A.; Lamont, I.; Sander, S. G.; Cook, G. M., Acquisition of iron by alkaliphilic bacillus species. *Applied and Environmental Microbiology* **2010,** *76*, (20), 6955-6961.
105. Gascoyne, D. J.; Connor, J. A.; Bull, A. T., Isolation of bacteria producing siderophores under alkaline conditions. *Applied Microbiology and Biotechnology* **1991,** *36*, (1), 130-135.
106. Figueroa, L. O. S.; Schwarz, B.; Richards, A. M., Structural characterization of amphiphilic siderophores produced by a soda lake isolate, Halomonas sp SL01, reveals cysteine-, phenylalanine- and proline-containing head groups. *Extremophiles* **2015,** *19*, (6), 1183-1192.
107. Huet, B.; L'Hostis, V.; Santarini, G.; Feron, D.; Idrissi, H., Steel corrosion in concrete: Determinist modeling of cathodic reaction as saturation a function of water degree. *Corrosion Science* **2007,** *49*, (4), 1918-1932.
108. King, D. W.; Lounsbury, H. A.; Millero, F. J., Rates and mechanism of Fe(II) oxidation at nanomolar total iron concentrations. *Environmental Science & Technology* **1995,** *29*, (3), 818-824.
109. Hansen, H. C. B.; Borggaard, O. K.; Sorensen, J., Evaluation of the free energy of formation of Fe(II)-Fe(III) hydroxide-sulfate (green rust) and its reduction of nitrite. *Geochimica Et Cosmochimica Acta* **1994,** *58*, (12), 2599-2608.
110. Kruft, B. I.; Harrington, J. M.; Duckworth, O. W.; Jarzecki, A. A., Quantum mechanical investigation of aqueous desferrioxamine B metal complexes: Trends in structure, binding, and infrared spectroscopy. *Journal of Inorganic Biochemistry* **2013,** *129*, 150-161.
111. Duckworth, O. W.; Bargar, J. R.; Sposito, G., Quantitative structure-activity relationships for aqueous metal-siderophore complexes. *Environmental Science & Technology* **2009,** *43*, (2), 343-349.
112. Hernlem, B. J.; Vane, L. M.; Sayles, G. D., Stability constants for complexes of the siderophore desferrioxamine B with selected heavy metal cations. *Inorganica Chimica Acta* **1996,** *244*, (2), 179-184.
113. Kato, M.; Izuka, S.; Fujihara, T.; Nagasawa, A.; Kawai, S.; Tanaka, T.; Takayanagi, T., Electronic structure calculation study of metal complexes with a phytosiderophore mugineic acid. *Inorganica Chimica Acta* **2011,** *370*, (1), 304-310.

114. Buglyo, P.; Culeddu, N.; Kiss, T.; Micera, G.; Sanna, D., Vanadium(IV) and vanadium(V) complexes of desferrioxamine B in aqueous solution. *Journal of Inorganic Biochemistry* **1995,** *60*, (1), 45-59.
115. Kalinowski, B. E.; Oskarsson, A.; Albinsson, Y.; Arlinger, J.; Odegaard-Jensen, A.; Andlid, T.; Pedersen, K., Microbial leaching of uranium and other trace elements from shale mine tailings at Ranstad. *Geoderma* **2004,** *122*, (2-4), 177-194.
116. Bouby, M.; Billard, I.; MacCordick, J.; Rossini, I., Complexation of uranium VI with the siderophore pyoverdine. *Radiochimica Acta* **1998,** *80*, (2), 95-100.
117. Kalinowski, B. E.; Johnsson, A.; Arlinger, J.; Pedersen, K.; Odeggrd-Jensen, A.; Edberg, F., Microbial mobilization of uranium from shale mine waste. *Geomicrobiology Journal* **2006,** *23*, (3-4), 157-164.
118. Ejje, N.; Soe, C. Z.; Gu, J. S.; Codd, R., The variable hydroxamic acid siderophore metabolome of the marine actinomycete Salinispora tropica CNB-440. *Metallomics* **2013,** *5*, (11), 1519-1528.
119. Wolff-Boenisch, D.; Traina, S. J., The effect of desferrioxamine B, enterobactin, oxalic acid, and Na-alginate on the dissolution of uranyl-treated goethite at pH 6 and 25 degrees C. *Chemical Geology* **2007,** *243*, (3-4), 357-368.
120. Wolff-Boenisch, D.; Traina, S. J., The effect of desferrioxamine B on the desorption of U(VI) from Georgia kaolinite KGa-1b and its ligand-promoted dissolution at pH 6 and 25 degrees C. *Chemical Geology* **2007,** *242*, (1-2), 278-287.
121. Frazier, S. W.; Kretzschmar, R.; Kraemer, S. M., Bacterial siderophores promote dissolution of UO2 under reducing conditions. *Environmental Science & Technology* **2005,** *39*, (15), 5709-5715.
122. Harrington, J. M.; Parker, D. L.; Bargar, J. R.; Jarzecki, A. A.; Tebo, B. M.; Sposito, G.; Duckworth, O. W., Structural dependence of Mn complexation by siderophores: Donor group dependence on complex stability and reactivity. *Geochimica Et Cosmochimica Acta* **2012,** *88*, 106-119.
123. Smith, R. M., *Critical stability constants / Vol.3, Other organic ligands*. New York ; London : Plenum.; 1977.: New York ; London, 1977.
124. Bartusek, M.; Sommer, L., On the complex forming tendency of phenolic hydroxyl with UO22+. *Journal of Inorganic and Nuclear Chemistry* **1965,** *27*, (11), 2397 - 2412.
125. Vukovic, S.; Hay, B. P.; Bryantsev, V. S., Predicting stability constants for uranyl complexes using density functional theory. *Inorganic Chemistry* **2015,** *54*, (8), 3995-4001.
126. Rossberg, A.; Baraniak, L.; Reich, T.; Hennig, C.; Bernhard, G.; Nitsche, H., EXAFS structural analysis of aqueous uranium(VI) complexes with lignin degradation products. *Radiochimica Acta* **2000,** *88*, (9-11), 593-597.
127. Edwards, D. C.; Nielsen, S. B.; Jarzecki, A. A.; Spiro, T. G.; Myneni, S. C. B., Experimental and theoretical vibrational spectroscopy studies of acetohydroxamic acid and desferrioxamine B in aqueous solution: Effects of pH and iron complexation. *Geochimica Et Cosmochimica Acta* **2005,** *69*, (13), 3237-3248.
128. Chung, D. Y.; Choi, E. K.; Lee, E. H.; Kim, K. W., Complexation of U(VI), Ce(III) and Nd(III) with acetohydroxamic acid in perchlorate aqueous solution. *Journal of Radioanalytical and Nuclear Chemistry* **2011,** *289*, (2), 315-319.
129. Taylor, R. J.; Denniss, I. R.; May, I. *Hydroxamic acids - novel reagents for Advanced Purex process*; BNFL: Sellafield, CA20 1PG UK, 2000.
130. Sornosa-Ten, A.; Jewula, P.; Fodor, T.; Brandes, S.; Sladkov, V.; Rousselin, Y.; Stern, C.; Chambron, J. C.; Meyer, M., Effects of preorganization in the chelation of UO22+ by hydroxamate ligands: cyclic PIPO- vs. linear NMA. *New Journal of Chemistry* **2018,** *42*, (10), 7765-7779.
131. Brandes, S.; Sornosa-Ten, A.; Rousselin, Y.; Lagrelette, M.; Stern, C.; Moncomble, A.; Cornard, J. P.; Meyer, M., Conformational and structural studies of N-

methylacetohydroxamic acid and of its mono- and bis-chelated uranium(VI) complexes. *Journal of Inorganic Biochemistry* **2015,** *151*, 164-175.
132. Terencio, T.; Roithova, J.; Brandes, S.; Rousselin, Y.; Penouilh, M. J.; Meyer, M., A Comparative IRMPD and DFT study of Fe^{3+} and UO_2^{2+} complexation with N-methylacetohydroxamic acid. *Inorganic Chemistry* **2018,** *57*, (3), 1125-1135.
133. Szabo, Z.; Grenthe, I., Potentiometric and multinuclear NMR study of the binary and ternary uranium(VI)-L-fluoride systems, where L is alpha-hydroxycarboxylate or glycine. *Inorganic Chemistry* **2000,** *39*, (22), 5036-5043.
134. Ahrland, S., The complex chemistry of the uranyl ion. VII. The complexity of uranyl glycolate. *Acta Chemica Scandinavica* **1953,** *7*, 485-494.
135. Jiang, J.; Rao, L. F.; Di Bernardo, P.; Zanonato, P.; Bismondo, A., Complexation of uranium(VI) with acetate at variable temperatures. *Journal of the Chemical Society-Dalton Transactions* **2002**, (8), 1832-1838.
136. Moll, H.; Geipel, G.; Reich, T.; Bernhard, G.; Fanghanel, T.; Grenthe, I., Uranyl(VI) complexes with alpha-substituted carboxylic acids in aqueous solution. *Radiochimica Acta* **2003,** *91*, (1), 11-20.
137. Su, J.; Zhang, K.; Schwarz, W. H. E.; Li, J., Uranyl-glycine-water complexes in solution: Comprehensive computational modeling of coordination geometries, stabilization energies, and luminescence properties. *Inorganic Chemistry* **2011,** *50*, (6), 2082-2093.
138. Bauman, J. E.; Wang, J. C., Imidazole complexes of nickel(II), copper(II), zinc(II), and silver(I). *Inorganic Chemistry* **1964,** *3*, (3), 368-373.
139. Gutowski, K. E.; Cocalia, V. A.; Griffin, S. T.; Bridges, N. J.; Dixon, D. A.; Rogers, R. D., Interactions of 1-methylimidazole with $UO_2(CH_3CO_2)_2$ and $UO_2(NO_3)_2$: Structural, spectroscopic, and theoretical evidence for imidazole binding to the uranyl ion. *Journal of the American Chemical Society* **2007,** *129*, (3), 526-536.
140. Kenney, J. P. L.; Ellis, T.; Nicol, F. S.; Porter, A. E.; Weiss, D. J., The effect of bacterial growth phase and culture concentration on U(VI) removal from aqueous solution. *Chemical Geology* **2018,** *482*, 61-71.
141. Li, X. L.; Ding, C. C.; Liao, J. L.; Du, L.; Sun, Q.; Yang, J. J.; Yang, Y. Y.; Zhang, D.; Tang, J.; Liu, N., Bioaccumulation characterization of uranium by a novel Streptomyces sporoverrucosus dwc-3. *Journal of Environmental Sciences* **2016,** *41*, 162-171.
142. Theodorakopoulos, N.; Chapon, V.; Coppin, F.; Floriani, M.; Vercouter, T.; Sergeant, C.; Camilleri, V.; Berthomieu, C.; Fevrier, L., Use of combined microscopic and spectroscopic techniques to reveal interactions between uranium and Microbacterium sp A9, a strain isolated from the Chernobyl exclusion zone. *Journal of Hazardous Materials* **2015,** *285*, 285-293.
143. Borch, T.; Kretzschmar, R.; Kappler, A.; Van Cappellen, P.; Ginder-Vogel, M.; Voegelin, A.; Campbell, K., Biogeochemical redox processes and their impact on contaminant dynamics. *Environmental Science & Technology* **2010,** *44*, (1), 15-23.
144. Lovley, D. R.; Phillips, E. J. P.; Gorby, Y. A.; Landa, E. R., Microbial reduction of uranium. *Nature* **1991,** *350*, (6317), 413-416.
145. De Yoreo, J. J.; Vekilov, P. G., Principles of crystal nucleation and growth. *Biomineralization* **2003,** *54*, 57-93.
146. Burns, P. C., U^{6+} minerals and inorganic compounds: Insights into an expanded structural hierarchy of crystal structures. *Canadian Mineralogist* **2005,** *43*, 1839-1894.
147. Shvareva, T. Y.; Fein, J. B.; Navrotsky, A., Thermodynamic properties of uranyl minerals: Constraints from calorimetry and solubility measurements. *Industrial & Engineering Chemistry Research* **2012,** *51*, (2), 607-613.
148. Swanton, S. W.; Alexander, W. R.; Berry, J. A. *Review of the behaviour of colloids in the near field of a cementitious repository*; Serco: Oxfordshire, OX11 0RA, 2009; p 193.

149. Bots, P.; Morris, K.; Hibberd, R.; Law, G. T. W.; Mosselmans, J. F. W.; Brown, A. P.; Doutch, J.; Smith, A. J.; Shaw, S., Formation of stable uranium(VI) colloidal nanoparticles in conditions relevant to radioactive waste disposal. *Langmuir* **2014,** *30*, (48), 14396-14405.
150. Smith, K. F.; Bryan, N. D.; Swinburne, A. N.; Bots, P.; Shaw, S.; Natrajan, L. S.; Mosselmans, J. F. W.; Livens, F. R.; Morris, K., U(VI) behaviour in hyperalkaline calcite systems. *Geochimica Et Cosmochimica Acta* **2015,** *148*, 343-359.
151. Fan, Q. H.; Hao, L. M.; Wang, C. L.; Zheng, Z.; Liu, C. L.; Wu, W. S., The adsorption behavior of U(VI) on granite. *Environmental Science-Processes & Impacts* **2014,** *16*, (3), 534-541.
152. Zhang, Y. Y.; Zhao, H. G.; Fan, Q. H.; Zheng, X. B.; Li, P.; Liu, S. P.; Wu, W. S., Sorption of U(VI) onto a decarbonated calcareous soil. *Journal of Radioanalytical and Nuclear Chemistry* **2011,** *288*, (2), 395-404.
153. RWM *Generic disposal system specification part A: High level requirements*; Didcot, OX11 0RH, UK, 2016; p 53.
154. Yao, K. M.; Habibian, M. M.; Omelia, C. R., Water and waste water filtration - concepts and applications. *Environmental Science & Technology* **1971,** *5*, (11), 1105-&.
155. McDowellboyer, L. M.; Hunt, J. R.; Sitar, N., Particle transport through porous media. *Water Resources Research* **1986,** *22*, (13), 1901-1921.
156. Bradford, S. A.; Simunek, J.; Bettahar, M.; Van Genuchten, M. T.; Yates, S. R., Modeling colloid attachment, straining, and exclusion in saturated porous media. *Environmental Science & Technology* **2003,** *37*, (10), 2242-2250.
157. Ryan, J. N.; Elimelech, M., Colloid mobilization and transport in groundwater. *Colloids and Surfaces a-Physicochemical and Engineering Aspects* **1996,** *107*, 1-56.
158. Molnar, I. L.; Johnson, W. P.; Gerhard, J. I.; Willson, C. S.; O'Carroll, D. M., Predicting colloid transport through saturated porous media: A critical review. *Water Resources Research* **2015,** *51*, (9), 6804-6845.
159. Derjaguin, B.; Landau, L., Theory of the stability of strongly charged lyophobic sols and of the adhesion of strongly charged particles in solutions of electrolytes. *Acta Physicochimica U. S. S. R* **1941,** *14*, 733 –762.
160. Verwey, E. J. W.; TH.G., O., *Theory of the stability of lyophobic colloids*. Elsevier: Amsterdam, 1948.
161. Li, X. Q.; Zhang, P. F.; Lin, C. L.; Johnson, W. P., Role of hydrodynamic drag on microsphere deposition and re-entrainment in porous media under unfavorable conditions. *Environmental Science & Technology* **2005,** *39*, (11), 4012-4020.
162. Elimelech, M.; Nagai, M.; Ko, C. H.; Ryan, J. N., Relative insignificance of mineral grain zeta potential to colloid transport in geochemically heterogeneous porous media. *Environmental Science & Technology* **2000,** *34*, (11), 2143-2148.
163. Li, X. Q.; Scheibe, T. D.; Johnson, W. P., Apparent decreases in colloid deposition rate coefficients with distance of transport under unfavorable deposition conditions: A general phenomenon. *Environmental Science & Technology* **2004,** *38*, (21), 5616-5625.
164. Elimelech, M.; Omelia, C. R., Kinetics of deposition of colloidal particles in porous media. *Environmental Science & Technology* **1990,** *24*, (10), 1528-1536.
165. Hoek, E. M. V.; Agarwal, G. K., Extended DLVO interactions between spherical particles and rough surfaces. *Journal of Colloid and Interface Science* **2006,** *298*, (1), 50-58.
166. Tufenkji, N.; Elimelech, M., Breakdown of colloid filtration theory: Role of the secondary energy minimum and surface charge heterogeneities. *Langmuir* **2005,** *21*, (3), 841-852.
167. Liang, Y.; Bradford, S. A.; Simunek, J.; Vereecken, H.; Klumpp, E., Sensitivity of the transport and retention of stabilized silver nanoparticles to physicochemical factors. *Water Research* **2013,** *47*, (7), 2572-2582.
168. Shen, C. Y.; Li, B. G.; Wang, C.; Huang, Y. F.; Jin, Y., Surface roughness effect on deposition of nano- and micro-sized colloids in saturated columns at different solution ionic strengths. *Vadose Zone Journal* **2011,** *10*, (3), 1071-1081.

169. Shen, C. Y.; Jin, Y.; Li, B. G.; Zheng, W. J.; Huang, Y. F., Facilitated attachment of nanoparticles at primary minima by nanoscale roughness is susceptible to hydrodynamic drag under unfavorable chemical conditions. *Science of the Total Environment* **2014,** *466*, 1094-1102.
170. Bradford, S. A.; Yates, S. R.; Bettahar, M.; Simunek, J., Physical factors affecting the transport and fate of colloids in saturated porous media. *Water Resources Research* **2002,** *38*, (12).
171. Shen, C. Y.; Huang, Y. F.; Li, B. G.; Jin, Y., Effects of solution chemistry on straining of colloids in porous media under unfavorable conditions. *Water Resources Research* **2008,** *44*, (5), 12.
172. Li, X. Q.; Lin, C. L.; Miller, J. D.; Johnson, W. P., Role of grain-to-grain contacts on profiles of retained colloids in porous media in the presence of an energy barrier to deposition. *Environmental Science & Technology* **2006,** *40,* (12), 3769-3774.
173. Xu, S. P.; Gao, B.; Saiers, J. E., Straining of colloidal particles in saturated porous media. *Water Resources Research* **2006,** *42*, (12).
174. Raychoudhury, T.; Tufenkji, N.; Ghoshal, S., Straining of polyelectrolyte-stabilized nanoscale zero valent iron particles during transport through granular porous media. *Water Research* **2014,** *50*, 80-89.
175. Auset, M.; Keller, A. A., Pore-scale processes that control dispersion of colloids in saturated porous media. *Water Resources Research* **2004,** *40*, (3).
176. Jensen, F., *Introduction to Computational Chemistry*. 2nd ed. ed.; Hoboken Chichester, England, 2007.
177. Ochterski, J. W. *Thermochemistry in Gaussian*; Gaussian, Inc.: Wallingford, CT 06492 USA, 2000.
178. Perdew, J. P.; Schmidt, K. In *Jacob's ladder of density functional approximations for the exchange-correlation energy*, International Conference on Density Functional Theory and its Applications to Materials, Antwerp, Belgium, Jun 08-10, 2000; Antwerp, Belgium, 2000; pp 1-20.
179. Foresman, J. B.; Frisch, A., *Exploring chemistry with electronic structure methods*. 3rd Edition ed.; Gaussian: Wallingford, CT USA, 2015; p 531.
180. Sullivan, D. M., The harmonic oscillator. **2012**, 227-244.
181. Pitzer, K. S.; Gwinn, W. D., Energy levels and thermodynamic functions for molecules with internal rotation I. Rigid frame with attached tops. *The Journal of Chemical Physics* **1942,** *10*, (7), 428-440.
182. Ayala, P. Y.; Schlegel, H. B., Identification and treatment of internal rotation in normal mode vibrational analysis. *Journal of Chemical Physics* **1998,** *108*, (6), 2314-2325.
183. Bootsma, A. N.; Wheeler, S., Popular integration grids can result in karge errors in DFT-computed free energies. *ChemRxiv* **2019**.
184. Ryu, H.; Park, J.; Kim, H. K.; Park, J. Y.; Kim, S. T.; Baik, M. H., Pitfalls in computational modeling of chemical reactions and how to avoid them. *Organometallics* **2018,** *37*, (19), 3228-3239.
185. Ribeiro, R. F.; Marenich, A. V.; Cramer, C. J.; Truhlar, D. G., Use of solution-phase vibrational frequencies in continuum models for the free Energy of solvation. *Journal of Physical Chemistry B* **2011,** *115*, (49), 14556-14562.
186. Harrison, N. M., An introduction to density functional theory. Imperial College London: 2006.
187. Zhao, Y.; Truhlar, D. G., Density functional theory for reaction energies: Test of meta and hybrid meta functionals, range-separated functionals, and other high-performance functionals. *Journal of Chemical Theory and Computation* **2011,** *7*, (3), 669-676.
188. Weigend, F.; Ahlrichs, R., Balanced basis sets of split valence, triple zeta valence and quadruple zeta valence quality for H to Rn: Design and assessment of accuracy. *Physical Chemistry Chemical Physics* **2005,** *7*, (18), 3297-3305.
189. Weigend, F.; Furche, F.; Ahlrichs, R., Gaussian basis sets of quadruple zeta valence quality for atoms H-Kr. *Journal of Chemical Physics* **2003,** *119*, (24), 12753-12762.

190. Tao, J. M.; Perdew, J. P.; Staroverov, V. N.; Scuseria, G. E., Climbing the density functional ladder: Nonempirical meta-generalized gradient approximation designed for molecules and solids. *Physical Review Letters* **2003,** *91*, (14).
191. Stephens, P. J.; Devlin, F. J.; Chabalowski, C. F.; Frisch, M. J., Ab-initio calculation of vibrational absorption and circular-dichroism spectra using density functional force fields. *Journal of Physical Chemistry* **1994,** *98*, (45), 11623-11627.
192. Zhao, Y.; Truhlar, D. G., The M06 suite of density functionals for main group thermochemistry, thermochemical kinetics, noncovalent interactions, excited states, and transition elements: two new functionals and systematic testing of four M06-class functionals and 12 other functionals. *Theoretical Chemistry Accounts* **2008,** *120*, (1-3), 215-241.
193. Perdew, J. P.; Burke, K.; Wang, Y., Generalized gradient approximation for the exchange-correlation hole of a many-electron system. *Physical Review B* **1996,** *54*, (23), 16533-16539.
194. Iche-Tarrat, N.; Marsden, C. J., Examining the performance of DFT methods in uranium chemistry: Does core size matter for a pseudopotential? *Journal of Physical Chemistry A* **2008,** *112*, (33), 7632-7642.
195. Cao, X. Y.; Dolg, M., Segmented contraction scheme for small-core actinide pseudopotential basis sets. *Journal of Molecular Structure-Theochem* **2004,** *673*, (1-3), 203-209.
196. Bouteiller, Y.; Mijoule, C.; Nizam, M.; Barthelat, J. C.; Daudey, J. P.; Pelissier, M.; Silvi, B., Extended Gaussian-type valence basis-sets for calculations involving non-empirical core pseudopotentials. *Molecular Physics* **1988,** *65*, (2), 295-312.
197. Han, Y. K.; Hirao, K., Density functional studies of UO_2^{2+} and AnF_6 (An=U, Np, and Pu) using scalar-relativistic effective core potentials. *Journal of Chemical Physics* **2000,** *113*, (17), 7345-7350.
198. Kuchle, W.; Dolg, M.; Stoll, H.; Preuss, H., Energy-adjusted pseudopotentials for the actinides - parameter sets and test calculations for thorium and thorium monoxide. *Journal of Chemical Physics* **1994,** *100*, (10), 7535-7542.
199. Kendall, R. A.; Dunning, T. H.; Harrison, R. J., Electron-affinities of the 1st-row atoms revisited - systematic basis-sets and wave-functions. *Journal of Chemical Physics* **1992,** *96*, (9), 6796-6806.
200. Dunning, T. H., Gaussian-basis sets for use in corrected molecular calculations .1. The atoms boron through neon and hydrogen. *Journal of Chemical Physics* **1989,** *90*, (2), 1007-1023.
201. Shamov, G. A.; Schreckenbach, G.; Vo, T. N., A comparative relativistic DFT and ab initio study on the structure and thermodynamics of the oxofluorides of uranium(IV), (V) and (VI). *Chemistry-a European Journal* **2007,** *13*, (17), 4932-4947.
202. Goerigk, L.; Kruse, H.; Grimme, S., Benchmarking density functional fethods against the S66 and S66x8 datasets for non-covalent interactions. *Chemphyschem* **2011,** *12*, (17), 3421-3433.
203. Hehre, W. J.; Ditchfield, K.; Pople, J. A., Self- consistent molecular orbital methods. XII. Further extensions of gaussian-type basis sets for use in molecular orbital studies of organic molecules. *The Journal of Chemical Physics* **1972,** *56*, (5), 2257-2261.
204. Hariharan, P.; Pople, J., The influence of polarization functions on molecular orbital hydrogenation energies. *Theoret. Chim. Acta* **1973,** *28*, (3), 213-222.
205. Woon, D. E.; Dunning, T. H., Gaussian-Basis sets for use in correlated molecular calculations .3. The atoms aluminium through argon. *Journal of Chemical Physics* **1993,** *98*, (2), 1358-1371.
206. Peterson, K. A.; Dunning, T. H., Intrinsic errors in several ab-initio methods - The dissociation energy of N_2 . *Journal of Physical Chemistry* **1995,** *99*, (12), 3898-3901.
207. Pyykko, P., Relativistic effects in chemistry: More common than you thought. *Annual Review of Physical Chemistry, Vol 63* **2012,** *63*, 45-64.
208. Pyykko, P., Relativistic effects in structural chemistry. *Chemical Reviews* **1988,** *88*, (3), 563-594.

209. Saue, T., Relativistic Hamiltonians for chemistry: A primer. *Chemphyschem* **2011,** *12*, (17), 3077-3094.
210. Garcia-Hernandez, M.; Lauterbach, C.; Kruger, S.; Matveev, A.; Rosch, N., Comparative study of relativistic density functional methods applied to actinide species AcO_2^{2+} and AcF_6 for Ac=U, Np. *Journal of Computational Chemistry* **2002,** *23*, (8), 834-846.
211. Parmar, P.; Samuels, A.; Clark, A. E., Applications of polarizable continuum models to determine accurate solution-phase thermochemical values across a broad range of cation charge - the case of U(III-VI). *Journal of Chemical Theory and Computation* **2015,** *11*, (1), 55-63.
212. Dirac, P. A. M., The quantum theory of the electron. *Procedures of the Royal Society A* **1928,** *177*, 610-624.
213. Dolg, M.; Cao, X. Y., Relativistic pseudopotentials: Their development and scope of applications. *Chemical Reviews* **2012,** *112*, (1), 403-480.
214. Breit, G., Dirac's equation and the spin-spin interactions of two electrons. *Physical Review* **1932,** *39*, (4), 616-624.
215. Dolg, M.; Cao, X. Y., Accurate relativistic small-core pseudopotentials for actinides. Energy adjustment for uranium and first applications to uranium hydride. *Journal of Physical Chemistry A* **2009,** *113*, (45), 12573-12581.
216. Wood, J. H.; Boring, A. M., Improved Pauli Hamiltonian for local-potential problems. *Physical Review B* **1978,** *18*, (6), 2701-2711.
217. Dyall, K. G.; Grant, I. P.; Johnson, C. T.; Parpia, F. A.; Plummer, E. P., GRASP - A general-purpose relativistic atomic-structure program. *Computer Physics Communications* **1989,** *55*, (3), 425-456.
218. Miertuš, S.; Scrocco, E.; Tomasi, J., Electrostatic interaction of a solute with a continuum. A direct utilizaion of AB initio molecular potentials for the prevision of solvent effects. *Chemical Physics* **1981,** *55*, (1), 117-129.
219. Barone, V.; Cossi, M., Quantum calculation of molecular energies and energy gradients in solution by a conductor solvent model. *J. Phys. Chem. A* **1998,** *102*, (11), 1995-2001.
220. Tomasi, J.; Mennucci, B.; Cances, E., The IEF version of the PCM solvation method: an overview of a new method addressed to study molecular solutes at the QM ab initio level. *Journal of Molecular Structure-Theochem* **1999,** *464*, (1-3), 211-226.
221. Marenich, A. V.; Cramer, C. J.; Truhlar, D. G., Universal solvation model based on solute electron density and on a continuum model of the solvent defined by the bulk dielectric constant and atomic surface tensions. *Journal of Physical Chemistry B* **2009,** *113*, (18), 6378-6396.
222. Frisch, M. J.; Trucks, G. W.; Schlegel, H. B.; Scuseria, G. E.; Robb, M. A.; Cheeseman, J. R.; Scalmani, G.; Barone, V.; Petersson, G. A.; Nakatsuji, H.; Li, X.; Caricato, M.; Marenich, A. V.; Bloino, J.; Janesko, B. G.; Gomperts, R.; Mennucci, B.; Hratchian, H. P.; Ortiz, J. V.; Izmaylov, A. F.; Sonnenberg, J. L.; Williams; Ding, F.; Lipparini, F.; Egidi, F.; Goings, J.; Peng, B.; Petrone, A.; Henderson, T.; Ranasinghe, D.; Zakrzewski, V. G.; Gao, J.; Rega, N.; Zheng, G.; Liang, W.; Hada, M.; Ehara, M.; Toyota, K.; Fukuda, R.; Hasegawa, J.; Ishida, M.; Nakajima, T.; Honda, Y.; Kitao, O.; Nakai, H.; Vreven, T.; Throssell, K.; Montgomery Jr., J. A.; Peralta, J. E.; Ogliaro, F.; Bearpark, M. J.; Heyd, J. J.; Brothers, E. N.; Kudin, K. N.; Staroverov, V. N.; Keith, T. A.; Kobayashi, R.; Normand, J.; Raghavachari, K.; Rendell, A. P.; Burant, J. C.; Iyengar, S. S.; Tomasi, J.; Cossi, M.; Millam, J. M.; Klene, M.; Adamo, C.; Cammi, R.; Ochterski, J. W.; Martin, R. L.; Morokuma, K.; Farkas, O.; Foresman, J. B.; Fox, D. J. *Gaussian 16 Rev. B.01*, Wallingford, CT, 2016.
223. Rappe, A. K.; Casewit, C. J.; Colwell, K. S.; Goddard, W. A.; Skiff, W. M., UFF, A full periodic-table force-field for molecular mechanics and molecular dynamics simulations. *Journal of the American Chemical Society* **1992,** *114*, (25), 10024-10035.
224. Pauling, L., The Nature of the Chemical Bond. **1960**.

225. Bondi, A., Van der waals volumes and radii. *Journal of Physical Chemistry* **1964,** *68*, (3), 441-451.
226. Barone, V.; Cossi, M.; Tomasi, J., A new definition of cavities for the computation of solvation free energies by the polarizable continuum model. *Journal of Chemical Physics* **1997,** *107*, (8), 3210-3221.
227. Takano, Y.; Houk, K. N., Benchmarking the conductor-like polarizable continuum model (CPCM) for aqueous solvation free energies of neutral and ionic organic molecules. *Journal of Chemical Theory and Computation* **2005,** *1*, (1), 70-77.
228. Afaneh, A. T.; Schreckenbach, G.; Wang, F. Y., Theoretical study of the formation of mercury (Hg^{2+}) complexes in solution using an explicit solvation shell in implicit solvent calculations. *Journal of Physical Chemistry B* **2014,** *118*, (38), 11271-11283.
229. Martin, R. L.; Hay, P. J.; Pratt, L. R., Hydrolysis of ferric ion in water and conformational equilibrium. *Journal of Physical Chemistry A* **1998,** *102*, (20), 3565-3573.
230. Asthagiri, D.; Pratt, L. R.; Paulaitis, M. E.; Rempe, S. B., Hydration structure and free energy of biomolecularly specific aqueous dications, including Zn^{2+} and first transition row metals. *Journal of the American Chemical Society* **2004,** *126*, (4), 1285-1289.
231. Kelly, C. P.; Cramer, C. J.; Truhlar, D. G., Adding explicit solvent molecules to continuum solvent calculations for the calculation of aqueous acid dissociation constants. *Journal of Physical Chemistry A* **2006,** *110*, (7), 2493-2499.
232. Pliego, J. R.; Riveros, J. M., Theoretical calculation of pK(a) using the cluster-continuum model. *Journal of Physical Chemistry A* **2002,** *106*, (32), 7434-7439.
233. Schreckenbach, G.; Shamov, G. A., Theoretical actinide molecular science. *Accounts of Chemical Research* **2010,** *43*, (1), 19-29.
234. Dinescu, A.; Clark, A. E., Thermodynamic and structural features of aqueous Ce(III). *Journal of Physical Chemistry A* **2008,** *112*, (44), 11198-11206.
235. Mehio, N.; Ivanov, A. S.; Williams, N. J.; Mayes, R. T.; Bryantsev, V. S.; Hancock, R. D.; Dai, S., Quantifying the binding strength of salicylaldoxime-uranyl complexes relative to competing salicylaldoxime-transition metal ion complexes in aqueous solution: a combined experimental and computational study. *Dalton Transactions* **2016,** *45*, (22), 9051-9064.
236. Ladshaw, A. P.; Ivanov, A. S.; Das, S.; Bryantsev, V. S.; Tsouris, C.; Yiacoumi, S., First-principles integrated adsorption modeling for selective capture of uranium from seawater by polyamidoxime sorbent materials. *Acs Applied Materials & Interfaces* **2018,** *10*, (15), 12580-12593.
237. McNaught, A. D., *Compendium of chemical terminology : IUPAC recommendations*. 2nd ed / compiled by Alan D. McNaught and Andrew Wilkinson. ed.; Oxford : Blackwell Science: Oxford, 1997.
238. Gillan, M. J.; Alfe, D.; Michaelides, A., Perspective: How good is DFT for water? *Journal of Chemical Physics* **2016,** *144*, (13).
239. Bates, D. M.; Tschumper, G. S., CCSD(T) complete basis set limit relative energies for low-lying water hexamer structures. *Journal of Physical Chemistry A* **2009,** *113*, (15), 3555-3559.
240. Olson, R. M.; Bentz, J. L.; Kendall, R. A.; Schmidt, M. W.; Gordon, M. S., A novel approach to parallel coupled cluster calculations: Combining distributed and shared memory techniques for modern cluster based systems. *Journal of Chemical Theory and Computation* **2007,** *3*, (4), 1312-1328.
241. Merrill, G. N.; Gordon, M. S., Study of small water clusters using the effective fragment potential model. *Journal of Physical Chemistry A* **1998,** *102*, (16), 2650-2657.
242. Bryantsev, V. S.; Diallo, M. S.; Goddard, W. A., Calculation of solvation free energies of charged solutes using mixed cluster/continuum models. *Journal of Physical Chemistry B* **2008,** *112*, (32), 9709-9719.
243. Asthagiri, D.; Pratt, L. R.; Ashbaugh, H. S., Absolute hydration free energies of ions, ion-water clusters, and quasichemical theory. *Journal of Chemical Physics* **2003,** *119*, (5), 2702-2708.

244. Grabowski, P.; Riccardi, D.; Gomez, M. A.; Asthagiri, D.; Pratt, L. R., Quasi-chemical theory and the standard free energy of H+(aq). *Journal of Physical Chemistry A* **2002,** *106*, (40), 9145-9148.
245. Sun, M. S.; Harriss, D. K.; Magnuson, V. R., Activity corrections for ionic equilibria in aqueous-solutions. *Canadian Journal of Chemistry-Revue Canadienne De Chimie* **1980,** *58*, (12), 1253-1257.
246. Hummel, W.; Anderegg, G.; Puigdomenech, I.; Rao, L.; Tochiyama, O., *Chemical thermodynamics of compounds and complexes of U, Np, Pu, Am, Tc, Se, Ni and Zr with selected organic ligands*. 1 ed.; OECD Nuclear Energy Agency (NEA): Issy-les-Moulineaux, France, 2005; Vol. 9, p 1130.
247. Sipos, P., Application of the specific ion interaction theory (SIT) for the ionic products of aqueous electrolyte solutions of very high concentrations. *Journal of Molecular Liquids* **2008,** *143*, (1), 13-16.
248. Scatchard, G., Concentrated solutions of strong electrolytes. *Chemical Reviews* **1936,** *19*, (3), 309-327.
249. Stetefeld, J.; McKenna, S.; Patel, T., Dynamic light scattering: a practical guide and applications in biomedical sciences. *Biophysical Reviews* **2016,** *8*, (4), 409-427.
250. Delgado, A. V.; Gonzalez-Caballero, F.; Hunter, R. J.; Koopal, L. K.; Lyklema, J., Measurement and interpretation of electrokinetic phenomena. *Journal of Colloid and Interface Science* **2007,** *309*, (2), 194-224.
251. Avizo *Avizo*, 9.3; https://www.fei.com/software/amira-avizo/: 2016.
252. Dong, H.; Blunt, M. J., Pore-network extraction from micro-computerized-tomography images. *Physical Review E* **2009,** *80*, (3).
253. Fetter, *Contaminant Hydrogeology*. 2 ed.; Prentice Hall: Upper Saddle River, NJ, 1999; p 500.
254. Kenney, J. P. L.; M.E., K.; Cuadros, J.; Weiss, D. J., A conceptual model to predict uranium removal from aqueous solutions in water–rock systems associated with low- and intermediate-level radioactive waste disposal. *RSC Advances* **2017,** *7*, 7876-7884.
255. Hu, M. Z. C.; Norman, J. M.; Faison, B. D.; Reeves, M. E., Biosorption of uranium by Pseudomonas aeruginosa strain CSU: Characterization and comparison studies. *Biotechnology and Bioengineering* **1996,** *51*, (2), 237-247.
256. Fasfous, II; Dawoud, J. N., Uranium (VI) sorption by multiwalled carbon nanotubes from aqueous solution. *Applied Surface Science* **2012,** *259*, 433-440.
257. Frisch, M. J.; Trucks, G. W.; Schlegel, H. B.; Scuseria, G. E.; Robb, M. A.; Cheeseman, J. R.; Scalmani, G.; Barone, V.; Petersson, G. A.; Nakatsuji, H.; al., e. *Gaussian 16 Rev. a.01*, Wallingford, CT, 2016.
258. Dennington, R.; Keith, T. A.; Millam, J. M. *GaussView, Version 6*, Semichem Inc.: Shawnee Mission, KS, 2016.
259. Peterson, K. A., Correlation consistent basis sets for actinides. I. The Th and U atoms. *Journal of Chemical Physics* **2015,** *142*, (7).
260. Kirishima, A.; Onishi, Y.; Sato, N.; Tochiyama, O., Determination of the thermodynamic quantities of uranium(VI)-carboxylate complexes by microcalorimetry. *Journal of Chemical Thermodynamics* **2007,** *39*, (11), 1432-1438.
261. Groenewold, G. S.; de Jong, W. A.; Oomens, J.; Van Stipdonk, M. J., Variable denticity in carboxylate binding to the uranyl coordination complexes. *Journal of the American Society for Mass Spectrometry* **2010,** *21*, (5), 719-727.
262. Crea, F.; De Robertis, A.; Sammartano, S., Dioxouranium-carboxylate complexes. Part 1. Formation and stability of acetate species at different ionic strengths in NaClaq. *Annali Di Chimica* **2003,** *93*, (12), 1027-1035.
263. Bennaim, A.; Marcus, Y., Solvation thermodynamics of nonionic solutes. *Journal of Chemical Physics* **1984,** *81*, (4), 2016-2027.

264. Guillaumont, R.; Fanghänel T; Fuger, J.; Grenthe, I.; V., N.; Palmer, D. A.; Rand, M. H., *Update on the chemical thermodynamics of uranium, neptunium, plutonium, americium and technetium*. NEA OECD: North-Holland, Amsterdam, 2003; p 918.
265. Altmaier, M.; Yalcintas, E.; Gaona, X.; Neck, V.; Muller, R.; Schlieker, M.; Fanghanel, T., Solubility of U(VI) in chloride solutions. I. The stable oxides/hydroxides in NaCl systems, solubility products, hydrolysis constants and SIT coefficients. *Journal of Chemical Thermodynamics* **2017,** *114*, 2-13.
266. Yamamura, T.; Kitamura, A.; Fukui, A.; Nishikawa, S.; Yamamoto, T.; Moriyama, H., Solubility of U(VI) in highly basic solutions. *Radiochimica Acta* **1998,** *83*, (3), 139-146.
267. Ding, W. X.; Botha, J. A.; Hanson, B. C.; Burke, I. T., Aqueous hydroxylation mediated synthesis of crystalline calcium uranate particles. *Journal of Alloys and Compounds* **2016,** *688*, 260-269.
268. Wall, N. A.; Clark, S. B.; McHale, J. L., Synthesis and characterization of 1:1 layered uranyl silicate mineral phases. *Chemical Geology* **2010,** *274*, (3-4), 149-157.
269. Uyusur, B.; Li, C. Y.; Baveye, P. C.; Darnault, C. J. G., pH-dependent reactive transport of uranium(VI) in unsaturated sand. *Journal of Soils and Sediments* **2015,** *15*, (3), 634-647.
270. Huber, F.; Kunze, P.; Geckeis, H.; Schafer, T., Sorption reversibility kinetics in the ternary system radionuclide-bentonite colloids/nanoparticles-granite fracture filling material. *Applied Geochemistry* **2011,** *26*, (12), 2226-2237.
271. Tran, E. L.; Klein-BenDavid, O.; Teutsch, N.; Weisbrod, N., Influence of intrinsic colloid formation on migration of Cerium through fractured carbonate rock. *Environmental Science & Technology* **2015,** *49*, (22), 13275-13282.
272. Malvern, Zetasizer nano series: user manual. In Malvern: WR14 1XZ, 2013.
273. Tomaszewska, E.; Soliwoda, K.; Kadziola, K.; Tkacz-Szczesna, B.; Celichowski, G.; Cichomski, M.; Szmaja, W.; Grobelny, J., Detection limits of DLS and UV-Vis spectroscopy in characterization of polydisperse nanoparticles colloids. *Journal of Nanomaterials* **2013**.
274. Wamser, C. A.; Belle, J.; Bernsohn, E.; Williamson, B., The constitution of the uranates of sodium .1. *Journal of the American Chemical Society* **1952,** *74*, (4), 1020-1022.
275. Kovba, L. M., Sodium diuranate crystal structure. *Soviet Radiochemistry* **1972,** *14*, 727-730.
276. Cejka, J.; Sejkora, J.; Deliens, M., New data on studtite, $UO_4 \bullet 4H_2O$, from Shinkolobwe, Shaba, Zaire. *Neues Jahrbuch Fur Mineralogie-Monatshefte* **1996**, (3), 125-134.
277. Finch, R. J.; Ewing, R. C., Clarkeite: New chemical and structural data. *American Mineralogist* **1997,** *82*, (5-6), 607-619.
278. Oueslati, W.; Ammar, M.; Chorfi, N., Quantitative XRD analysis of the structural changes of Ba-exchanged montmorillonite: Effect of an in situ hydrous perturbation. *Minerals* **2015,** *5*, (3), 507-526.
279. Kern, A.; Eysel, W., Mineralogisch-Petrograph. Inst., Univ. Heidelberg, Germany ICDD Grant-in-Aid. In 1993.
280. Romero, C. P.; Jeldres, R. I.; Quezada, G. R.; Concha, F.; Toledo, P. G., Zeta potential and viscosity of colloidal silica suspensions: Effect of seawater salts, pH, flocculant, and shear rate. *Colloids and Surfaces a-Physicochemical and Engineering Aspects* **2018,** *538*, 210-218.
281. Johnson, P. R.; Sun, N.; Elimelech, M., Colloid transport in geochemically heterogeneous porous media: Modeling and measurements. *Environmental Science & Technology* **1996,** *30*, (11), 3284-3293.
282. Nelson, P. H., Pore-throat sizes in sandstones, tight sandstones, and shales. *Aapg Bulletin* **2009,** *93*, (3), 329-340.
283. Brusseau, M. L., Transport of reactive contaminants in heterogenous porous media. *Reviews of Geophysics* **1994,** *32*, (3), 285-313.
284. Mo, K. F.; Dai, Z. Y.; Wunschel, D. S., Production and characterization of desmalonichrome relative binding affinity for uranyl ions in relation to other siderophores. *Journal of Natural Products* **2016,** *79*, (6), 1492-1499.

285. Wolff-Boenisch, D.; Trama, S. J., A comparative study of the effect of desferrioxamine B, oxalic acid, and Na-alginate on the desorption of U(VI) from goethite at pH 6 and 5 degrees C. *Geochimica Et Cosmochimica Acta* **2006,** *70*, (17), 4356-4366.
286. Harris, D. C., *Quantitative chemical analysis*. 8th ed., International ed. ed.; New York : W. H. Freeman: New York, 2010.
287. Gutten, O.; Rulisek, L., Predicting the stability constants of metal-ion complexes from first principles. *Inorganic Chemistry* **2013,** *52*, (18), 10347-10355.
288. Gutten, O.; Besseova, I.; Rulisek, L., Interaction of metal ions with biomolecular ligands: How accurate are calculated free energies associated with metal ion complexation? *Journal of Physical Chemistry A* **2011,** *115*, (41), 11394-11402.
289. Bauschlicher, C. W.; Partridge, H., The senstivity of B3LYP atomization energies to the basis-set and a comparison of basis-set requirements for CCSD(T) and B3LYP. *Chemical Physics Letters* **1995,** *240*, (5-6), 533-540.
290. Chen, Y. L.; Barlow, D. J.; Kong, X. L.; Ma, Y. M.; Hider, R. C., Prediction of 3-hydroxypyridin-4-one (HPO) log K-1 values for Fe(III). *Dalton Transactions* **2012,** *41*, (35), 10784-10791.
291. Zhang, S. M., A reliable and efficient first principles-based method for predicting pK_a values. III. Adding explicit water molecules: Can the theoretical slope be reproduced and pK_a values predicted more accurately? *Journal of Computational Chemistry* **2012,** *33*, (5), 517-526.
292. Wang, N. X.; Wilson, A. K., Effects of basis set choice upon the atomization energy of the second-row compounds SO2, CCl, and ClO2 for B3LYP and B3PW91. *Journal of Physical Chemistry A* **2003,** *107*, (34), 6720-6724.
293. Vallet, V.; Moll, H.; Wahlgren, U.; Szabo, Z.; Grenthe, I., Structure and bonding in solution of dioxouranium(VI) oxalate complexes: Isomers and intramolecular ligand exchange. *Inorganic Chemistry* **2003,** *42*, (6), 1982-1993.
294. Tsushima, S.; Brendler, V.; Fahmy, K., Aqueous coordination chemistry and photochemistry of uranyl(VI) oxalate revisited: a density functional theory study. *Dalton Transactions* **2010,** *39*, (45), 10953-10958.
295. Di Bernardo, P.; Zanonato, P. L.; Tian, G.; Tolazzi, M.; Rao, L., Thermodynamics of the complexation of uranium(VI) with oxalate in aqueous solution at 10-70 degrees C. *Dalton Transactions* **2009**, (23), 4450-4457.
296. Lucks, C.; Rossberg, A.; Tsushima, S.; Foerstendorf, H.; Fahmy, K.; Bernhard, G., Formic acid interaction with the uranyl(VI) ion: structural and photochemical characterization. *Dalton Transactions* **2013,** *42*, (37), 13584-13589.
297. Miyake, C.; Nürnberg, H. W., Co-ordination compounds of actinides—I: The determination of the stability constants of uranyl complexes with anions of carboxylic acids. *Journal of Inorganic and Nuclear Chemistry* **1967,** *29*, (9), 2411-2429.
298. Raditzky, B.; Schmeide, K.; Sachs, S.; Geipel, G.; Bernhard, G., Interaction of uranium(VI) with nitrogen containing model ligands studied by laser-induced fluorescence spectroscopy. *Polyhedron* **2010,** *29*, (1), 620-626.
299. Avdeef, A.; Sofen, S. R.; Bregante, T. L.; Raymond, K. N., Coordination chemistry of microbial iron transport compounds .9. Stability constants for catechol models of enterobactin. *Journal of the American Chemical Society* **1978,** *100*, (17), 5362-5370.
300. Pluharova, E.; Oncak, M.; Seidel, R.; Schroeder, C.; Schroeder, W.; Winter, B.; Bradforth, S. E.; Jungwirth, P.; Slavicek, P., Transforming anion instability into stability: Contrasting photoionization of three protonation forms of the phosphate ion upon moving into water. *Journal of Physical Chemistry B* **2012,** *116*, (44), 13254-13264.
301. Dreuw, A.; Cederbaum, L. S., Multiply charged anions in the gas phase. *Chemical Reviews* **2002,** *102*, (1), 181-200.
302. Sure, R.; Grimme, S., Comprehensive benchmark of association (free) energies of realistic host-guest Complexes. *Journal of Chemical Theory and Computation* **2015,** *11*, (8), 3785-3801.

303. Brink, C. P.; Crumbliss, A. L., Kinetics, mechanism and thermodynamics of aqueous iron(III) chelation and dissociation - influence of carbon and nitrogen substituents in hydroxamic acid ligands. *Inorganic Chemistry* **1984,** *23*, (26), 4708-4718.
304. Groenewold, G. S.; Van Stipdonk, M. J.; Gresham, G. L.; Chien, W.; Bulleigh, K.; Howard, A., Collision-induced dissociation tandem mass spectrometry of desferrioxamine siderophore complexes from electrospray ionization of UO_2^{2+}, Fe^{3+} and Ca^{2+} solutions. *Journal of Mass Spectrometry* **2004,** *39*, (7), 752-761.
305. Gong, C. M. S.; Poineau, F.; Czerwinski, K. R., Synthesis and characterization of the solid uranium(VI) dioxo-diacetohydroxamate complex. *Radiochimica Acta* **2007,** *95*, (8), 439-450.
306. Da Silva, J. J. R. F.; Simoes, M. L. S., Studies on uranyl complexes—III: Uranyl complexes of edta 1 1 Part II: Communication to the Academy of Sciences of Lisbon, May 1967. *Talanta* **1968,** *15*, (7), 609-622.
307. Lenhart, J. J.; Cabaniss, S. E.; MacCarthy, P.; Honeyman, B. D., Uranium(VI) complexation with citric, humic and fulvic acids. *Radiochimica Acta* **2000,** *88*, (6), 345-353.
308. Steed, J. W., Supramolecular chemistry. In 2nd ed. ed.; Atwood, J. L.; Atwood, J. L., Eds. Hoboken : John Wiley & Sons, Ltd.: Hoboken Chichester, UK, 2009.
309. Warwick, P.; Evans, N.; Hall, T.; Vines, S., Stability constants of uranium(IV)-alpha-isosaccharinic acid and gluconic acid complexes. *Radiochimica Acta* **2004,** *92*, (12), 897-902.
310. Gaona, X.; Montoya, V.; Colas, E.; Grive, M.; Duro, L., Review of the complexation of tetravalent actinides by ISA and gluconate under alkaline to hyperalkaline conditions. *Journal of Contaminant Hydrology* **2008,** *102*, (3-4), 217-227.
311. Philippe, A.; Schaumann, G. E., Interactions of dissolved organic matter with natural and engineered inorganic colloids: A review. *Environmental Science & Technology* **2014,** *48*, (16), 8946-8962.
312. Powell, P. E.; Cline, G. R.; Reid, C. P. P.; Szaniszlo, P. J., Occurrence of hydroxamate siderophore iron chelators in soils. *Nature* **1980,** *287*, (5785), 833-834.
313. Pierwola, A.; Krupinski, T.; Zalupski, P.; Chiarelli, M.; Castignetti, D., Degradation pathway and generation of monohydroxamic acids from the trihydroxamate siderophore deferrioxamine B. *Applied and Environmental Microbiology* **2004,** *70*, (2), 831-836.
314. Neubauer, U.; Nowack, B.; Furrer, G.; Schulin, R., Heavy metal sorption on clay minerals affected by the siderophore desferrioxamine B. *Environmental Science & Technology* **2000,** *34*, (13), 2749-2755.
315. Borer, P.; Hug, S. J.; Sulzberger, B.; Kraemer, S. M.; Kretzschmar, R., ATR-FTIR spectroscopic study of the adsorption of desferrioxamine B and aerobactin to the surface of lepidocrocite (gamma-FeOOH). *Geochimica Et Cosmochimica Acta* **2009,** *73*, (16), 4661-4672.
316. Waite, T. D.; Davis, J. A.; Payne, T. E.; Waychunas, G. A.; Xu, N., Uranium(VI) adosrption to ferrihydrite - application of a surface complexation model. *Geochimica Et Cosmochimica Acta* **1994,** *58*, (24), 5465-5478.
317. Sverjensky, D. A.; Sahai, N., Theoretical prediction of single-site surface-protonation equilibrium constants for oxides and silicates in water. *Geochimica Et Cosmochimica Acta* **1996,** *60*, (20), 3773-3797.

Appendix A – Column Experiment Design

The mobility of U^{VI} was initially characterised through a series of column experiments. During these initial scoping experiments, the U^{VI} solution was injected into the columns approximately 1 to 2 hours after preparation. The pore volumes (PV) for the two columns are 7.86 and 8.68 ml. These column experiments provided the initial indication that U^{VI} was precipitating and being physically removed in the columns. This is highlighted in Figure A.1. If sorption were occurring, C/C_0 would reach 1, not remain at 0.1.

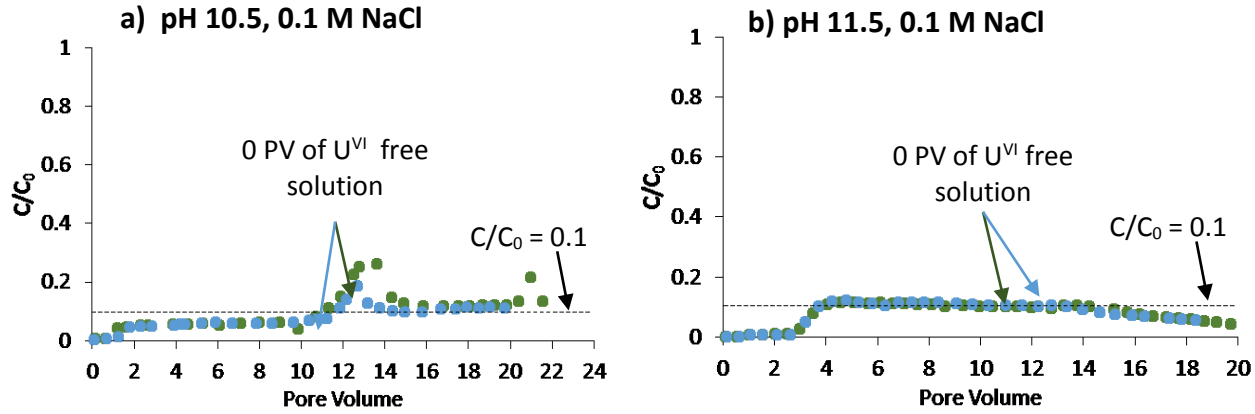

Figure A.1. Elution curves of the scoping column experiments. Part a, are the UVI elution curves at pH 10.5 and 11.5 respectively. The blue (•) and green (•) circles are [U] for columns 1 and 2 respectively. The error for the measurements are ± 0.07 C/C_0 units following propagation of 5% error from the ICPMS measurements.

However, upon visual inspection, the U^{VI} was immobilised in the inert glass frit which was holding the quartz sand in the column. This is highlighted in Figure A.2. A second column experiment was conducted where the glass frit and wool from the top of the column was removed, and the U^{VI} solution was injected downward, directly onto the quartz surface. Visually U^{VI} was removed within approximately 5 mm of the inlet, similar to when the U^{VI} was injected through the glass frit. However, in this column design the flow rate will be effected by gravity. To gain quantitative information on U^{VI} mobility in quartz sand the column experiments need to be designed with an inert material holding in the sand. For these types of studies, a steel mesh is commonly used.[156, 173] The results from these improved column experiments are provided in Chapter 4.

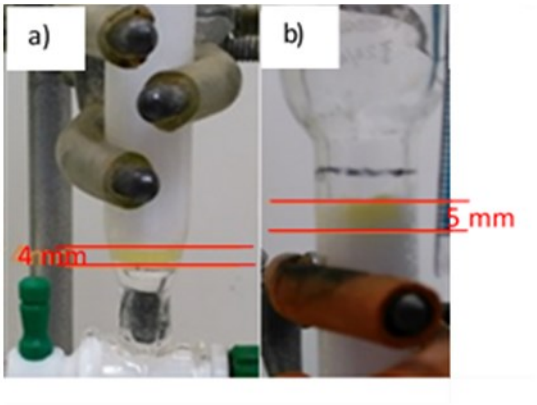

Figure A.2. Photographs showing a) the glass frit, and b) quartz sand turning yellow due to U^{VI} particulate immobilisation. The flow direction was upwards in a) and downwards in b). The schematic in part c) explains the photographs in greater detail.

Appendix B – Experimental Data

B.1. Chapter 4 - U^{VI} particle formation, characterisation and transport through quartz sand between pH 10.5 and 12.5 in 0.1 M sodium chloride solutions

Table B1. The time and ratio of sample concentration over initial concentration (C/C_0) for the batch experiments conducted at pH 10.5 which contain 42 µM U^{VI} and 0.1 M NaCl.

	Sample U^{VI} concentration / Initial U^{VI} concentration (C/C_0)			
Time	0.2 µm filter membrane	0.45 µm filter membrane	0.8 µm filter membrane	1 µm filter membrane
		Experiment 1		
0.2	1.0 ± 0.2		0.9 ± 0.1	0.57 ± 0.09
0.5	1.0 ± 0.2		0.51 ± 0.08	0.54 ± 0.08
1	0.48 ± 0.07	0.48 ± 0.07	0.49 ± 0.08	0.49 ± 0.08
2	0.46 ± 0.07		0.49 ± 0.08	0.55 ± 0.09
4	0.47 ± 0.07	0.45 ± 0.07	0.46 ± 0.07	0.64 ± 0.1
24	0.37 ± 0.06		0.39 ± 0.06	0.47 ± 0.07
48	0.18 ± 0.03		0.15 ± 0.02	0.60 ± 0.09
72	0.19 ± 0.03		0.21 ± 0.03	0.25 ± 0.04
168	0.27 ± 0.04		0.25 ± 0.04	0.33 ± 0.05
		Experiment 2		
1.1	0.64 ± 0.04			
1.8	0.67 ± 0.04			
2.9	0.71 ± 0.04			
6.0	0.67 ± 0.04			
7.7	0.57 ± 0.03			
23.6	0.51 ± 0.03			
48	0.27 ± 0.02			
169	0.114 ± 0.006			

Table B2. The time and ratio of sample concentration over initial concentration (C/C_0) for the batch experiments conducted at pH 11.5 which contain 42 µM U^{VI} and 0.1 M NaCl.

	Sample U^{VI} concentration / Initial U^{VI} concentration (C/C_0)			
Time	0.2 µm filter membrane	0.45 µm filter membrane	0.8 µm filter membrane	1 µm filter membrane
		Experiment 1		
0.2	0.7 ± 0.1	0.8 ± 0.1	1.0 ± 0.1	1.0 ± 0.1
0.6	0.9 ± 0.1	1.0 ± 0.1	0.8 ± 0.1	0.9 ± 0.1
1	0.8 ± 0.1	0.9 ± 0.1	1.0 ± 0.1	1.0 ± 0.1
2	0.7 ± 0.1	0.7 ± 0.1	0.7 ± 0.1	0.7 ± 0.1
4	0.9 ± 0.1	0.9 ± 0.1	0.48 ± 0.07	0.53 ± 0.08
24	0.16 ± 0.02		0.14 ± 0.02	0.14 ± 0.02
48			0.11 ± 0.02	0.11 ± 0.02
72	0.11 ± 0.02	0.10 ± 0.02	0.09 ±0.01	0.10 ± 0.02
96	0.12 ± 0.02			0.11 ± 0.02
168	0.09 ± 0.01		0.09 ± 0.01	0.09 ± 0.01
		Experiment 2		
1.1	0.241 ± 0.01			
2.0	0.171 ± 0.009			
4.1	0.109 ± 0.006			
6.8	0.080 ± 0.005			
8.1	0.062 ± 0.004			
24	0.036 ± 0.002			
48	0.023 ± 0.002			
171	0.019 ± 0.001			

Table B3. The time and ratio of sample concentration over initial concentration (C/C_0) for the batch experiment conducted at pH 12.5 which contain 42 µM U^{VI} and 0.1 M NaCl.

	Sample U^{VI} concentration / Initial U^{VI} concentration (C/C_0)			
Time	0.2 µm filter membrane	0.45 µm filter membrane	0.8 µm filter membrane	1 µm filter membrane
		Experiment 1		
0.2	0.99 ± 0.06	0.97 ± 0.06	0.99 ± 0.06	0.98 ± 0.06
1.2	1.00 ± 0.06	0.91 ± 0.05	0.99 ± 0.06	1.00 ± 0.06
2.0	0.98 ± 0.06	0.98 ± 0.06	0.99 ± 0.06	1.01 ± 0.06
4.2	0.93 ± 0.05	0.92 ± 0.05	0.99 ± 0.06	0.92 ± 0.05
6.2	0.99 ± 0.06	0.91 ± 0.05	0.92 ± 0.05	1.02 ± 0.06
25	0.99 ± 0.06	1.00 ± 0.06	0.97 ± 0.05	0.97 ± 0.05
49	0.98 ± 0.06	0.98 ± 0.06	0.98 ± 0.06	0.98 ± 0.06
73	0.98 ± 0.06	0.89 ± 0.05	0.88 ± 0.05	0.99 ± 0.06
169	0.96 ± 0.05	0.94 ± 0.05	0.95 ± 0.05	0.96 ± 0.05
		Experiment 2		
0.95	0.99 ± 0.06			
26	0.98 ± 0.06			
48	0.99 ± 0.06			
120	0.98 ± 0.06			
145	0.96 ± 0.05			
167	0.97 ± 0.06			

Table B4. The pore volume and ratio of sample concentration over initial concentration (C/C_0) for the bromide non-reactive tracer column experiment collected at the start of the pH 10.5 column experiments.

Experiment 1		**Experiment 2**	
Pore volume	C/C_0	Pore volume	C/C_0
0.13	0.00	0.17	0.00
0.38	0.00	0.42	0.00
0.64	0.03	0.67	0.00
0.88	0.72	0.92	0.02
1.16	0.95	1.15	0.66
1.43	1.04	1.40	0.96
1.72	0.96	1.64	0.96
2.00	1.03	1.92	0.97
2.24	1.04	2.20	0.98
2.49	1.04	2.44	0.98
2.74	0.85	2.66	0.97
3.00	0.26	2.91	0.92
3.26	0.09	3.15	0.37
3.52	0.06	3.39	0.09
3.81	0.03	3.66	0.04
4.08	0.01	3.92	0.02
4.35	0.01	4.15	0.01
4.60	0.00	4.40	0.01
4.85	0.00	4.68	0.00
5.13	0.00	4.95	0.00
5.40	0.00	5.20	0.00
5.65	0.00	5.45	0.00
5.90	0.00		

Table B5. The pore volume and ratio of sample concentration over initial concentration (C/C_0) for the bromide non-reactive tracer column experiment collected at the start of the pH 11.5 column experiments.

Experiment 1		**Experiment 2**	
Pore volume	C/C_0	Pore volume	C/C_0
0.17	0.00	0.16	0.00
0.40	0.00	0.42	0.00
0.63	0.00	0.68	0.00
0.84	0.00	0.95	0.11
1.05	0.36	1.24	0.89
1.30	0.97	1.51	1.01
1.55	1.00	1.78	1.03
1.78	0.98	2.04	1.01
2.00	0.94	2.33	1.01
2.25	0.99	2.62	1.01
2.50	0.99	2.93	1.00
2.80	0.94	3.23	0.80
3.09	0.99	3.47	0.21
3.32	0.91	3.71	0.07
3.54	1.00	3.98	0.03
3.76	0.94	4.26	0.02
3.97	0.33	4.55	0.01
4.20	0.14	4.83	0.00
4.43	0.07	5.11	0.00
4.66	0.04	5.41	0.00
4.89	0.02	5.73	0.00
5.13	0.01	6.01	0.00
5.41	0.01		
5.70	0.00		
5.96	0.00		
6.23	0.00		
6.50	0.00		
6.84	0.00		

Table B6. The pore volume and ratio of sample concentration over initial concentration (C/C_0) for the bromide non-reactive tracer column experiment collected at the start of the pH 12.5 column experiments.

Experiment 1		Experiment 2	
Pore volume	C/C_0	Pore volume	C/C_0
0.12	0.00	0.18	0.00
0.73	0.02	0.75	0.02
1.35	0.97	1.24	0.94
1.92	0.99	1.78	1.00
2.58	1.03	2.26	1.01
3.20	1.03	2.74	1.01
3.46	1.00	3.30	1.01
4.09	0.86	3.54	1.03
4.72	0.12	4.06	0.92
5.28	0.00	4.58	0.28
5.80	0.00	5.13	0.03
6.43	0.02	5.59	0.00
		6.06	0.00

Table B7. The pore volume and ratio of sample concentration over initial concentration (C/C_0) for the U^{VI} column experiment. The solutions containing 42 µM U^{VI}, 0.1 M NaCl at pH 10.5.

Experiment 1		Experiment 2	
Pore Volume	C/C_0	Pore Volume	C/C_0
0.15	0.00	0.20	0.00
0.41	0.00	0.49	0.00
0.67	0.00	0.75	0.00
0.91	0.07	1.01	0.18
1.14	0.41	1.29	0.42
1.39	0.59	1.56	0.41
1.63	0.58	1.80	0.42
1.87	0.62	2.04	0.41
2.39	0.64	2.26	0.39
2.64	0.63	2.77	0.39
2.90	0.65	3.00	0.38
3.18	0.64	3.22	0.36
3.62	0.65	3.74	0.36
3.84	0.64	3.99	0.33
4.06	0.66	4.24	0.31
4.31	0.68	4.51	0.35
4.58	0.65	4.79	0.33

Experiment 1		Experiment 2	
Pore Volume	C/C_0	Pore Volume	C/C_0
4.80	0.62	5.35	0.36
5.28	0.64	5.59	0.36
5.55	0.64	5.87	0.37
5.80	0.65	6.17	0.34
6.05	0.66	6.46	0.37
6.32	0.59	6.71	0.33
6.59	0.55	6.91	0.33
6.82	0.27	7.17	0.25
7.06	0.15	7.47	0.17
7.33	0.07	7.74	0.13
7.65	0.06	8.27	0.14
8.26	0.07	8.54	0.14
8.51	0.06	8.84	0.13
8.78	0.07	9.38	0.09
9.05	0.07	9.68	0.17
9.31	0.07	9.97	0.18
9.58	0.08	10.26	0.17
9.85	0.08	10.54	0.15
10.13	0.06	10.79	0.14
10.41	0.08	11.04	0.12
10.65	0.08	11.31	0.15
10.90	0.09		
11.16	0.08		
11.68	0.08		
Max Error	**± 0.05**	**Max Error**	**± 0.02**

Table B8. The pore volume and ratio of sample concentration over initial concentration (C/C_0) for the U^{VI} column experiment. The solutions containing 42 µM U^{VI}, 0.1 M NaCl at pH 11.5.

Experiment 1		Experiment 2	
Pore volume	C/C_0	Pore Volume	C/C_0
0.19	0.00	0.18	0.00
0.44	0.00	0.48	0.00
0.70	0.00	0.76	0.00
0.97	0.01	1.01	0.00
1.22	0.01	1.29	0.00
1.45	0.01	1.57	0.00
1.66	0.01	1.85	0.00
2.11	0.01	2.42	0.00
2.11	0.01	2.42	0.00

Experiment 1		**Experiment 2**	
Pore volume	C/C_0	Pore Volume	C/C_0
2.39	0.01	2.70	0.00
2.66	0.01	2.97	0.00
2.91	0.01	3.24	0.00
3.12	0.01	3.52	0.00
3.35	0.01	3.79	0.00
3.57	0.01	4.08	0.00
3.82	0.01	4.34	0.00
4.38	0.01	4.61	0.00
4.91	0.01	4.90	0.00
5.15	0.01	5.18	0.00
5.37	0.01	5.44	0.01
5.70	0.01	5.71	0.01
6.08	0.01	6.00	0.01
6.33	0.01	6.27	0.01
6.58	0.01	6.55	0.01
6.89	0.01	6.82	0.01
7.17	0.02	7.09	0.01
7.42	0.02	7.36	0.01
7.67	0.02	7.63	0.01
7.90	0.02	7.91	0.01
8.16	0.02	8.19	0.01
8.41	0.02	8.80	0.01
8.65	0.02	9.11	0.01
8.89	0.02	9.41	0.02
9.11	0.02	9.72	0.02
9.30	0.02	10.05	0.02
9.54	0.02	10.37	0.02
9.82	0.02	10.67	0.02
10.08	0.02	10.96	0.02
10.33	0.02	11.23	0.02
10.60	0.02	11.50	0.01
10.86	0.02	11.81	0.02
11.10	0.02		
11.37	0.02		
11.66	0.02		
11.92	0.02		
12.15	0.02		
12.39	0.01		
12.63	0.01		
12.87	0.02		
13.10	0.01		
Max Error	**± 0.003**	**Max error**	**± 0.001**

Table B9. The pore volume and ratio of sample concentration over initial concentration (C/C_0) for the U^{VI} column experiment. The solutions containing 42 µM U^{VI}, 0.1 M NaCl at pH 12.5.

Experiment 1		**Experiment 2**	
Pore volume	C/C_0	Pore volume	C/C_0
0.56	0.00	0.63	0.01
1.24	0.44	1.24	0.70
1.71	0.91	1.79	0.92
2.25	0.96	2.40	0.91
3.09	1.02	3.13	1.01
3.52	1.03	3.62	0.99
4.25	1.05	4.62	1.05
4.79	0.95	5.15	0.98
5.17	0.96	5.67	1.03
5.86	0.95	6.14	1.01
6.37	0.93	6.66	1.02
6.69	1.04	7.12	1.03
7.43	0.96	7.59	1.00
7.96	0.99	8.07	1.03
8.25	0.94	8.61	1.02
9.05	0.97	9.11	1.06
9.65	0.94	9.58	0.98
9.90	0.97	10.06	1.03
10.82	1.01	10.59	0.95
11.39	0.95	11.12	0.95
11.31	1.05	11.61	1.00
12.30	0.95	12.23	0.92
12.84	0.96	12.77	0.92
13.02	0.64	13.26	1.01
14.11	0.17	13.79	0.35
14.65	0.10	14.43	0.15
14.79	0.05	15.09	0.07
15.87	0.02	15.67	0.05
16.53	0.02	16.18	0.04
16.56	0.01	16.67	0.03
17.60	0.01	17.19	0.03
18.11	0.01	17.72	0.02
18.14	0.01	18.21	0.02
19.26	0.01	18.74	0.02
19.78	0.01	19.23	0.02
19.85	0.01	19.70	0.02
21.00	0.01	20.30	0.02
21.56	0.00	20.91	0.01
21.52	0.00	21.58	0.01

Experiment 1		Experiment 2	
Pore volume	C/C_0	Pore volume	C/C_0
22.74	0.00	22.19	0.01
23.34	0.00	22.75	0.01
23.19	0.00	23.43	0.01
24.42	0.00	23.97	0.01
25.03	0.00	24.55	0.01
		25.06	0.01
Max Error	**± 0.06**	**Max error**	**± 0.06**

Table B10. The average depth, U^{VI} mass, and ratio of U^{VI} mass over quartz sand mass for the retention profiles for the U^{VI} column experiments which contained 42 µM U^{VI}, 0.1 M NaCl at pH 10.5.

Experiment 1			**Experiment 2**		
Average Depth (cm)	mass U (µg)	µg U/g quartz	Average Depth (cm)	mass U (µg)	µg U/g quartz
0.75	22 ± 1	7.3 ± 0.4	0.75	142± 6	49 ± 2
2.25	7.0 ± 0.4	3.2 ± 0.2	2.25	20.6 ± 0.8	11.1 ± 0.6
3.75	7.0 ± 0.4	3.3 ± 0.2	3.75	14.8 ± 0.6	5.6 ± 0.3
5.25	8.2 ± 0.4	3.8 ± 0.2	5.25	11.6 ± 0.5	4.2 ± 0.2
6.75	5.7 ± 0.3	2.8 ± 0.1	6.75	7.4 ± 0.3	2.9 ± 0.1
8.25	4.2 ± 0.2	2.4 ± 0.1	8.25	7.5 ± 0.3	3.0 ± 0.1
9.75	4.8 ± 0.2	2.3 ± 0.1	9.75	7.1 ± 0.3	2.8 ± 0.1
11.25	2.9 ± 0.1	2.2 ± 0.1	11.25	4.0 ± 0.2	2.5 ± 0.1
12.75	2.8 ± 0.1	2.0 ± 0.1	12.75	6.9 ± 0.3	2.5 ± 0.1
14.25	2.1 ± 0.1	1.7 ± 0.1	14.25	3.4 ± 0.1	2.5 ± 0.1
15.75	2.1 ± 0.1	1.6 ± 0.1	15.75	6.0 ± 0.2	2.3 ± 0.1
17.75	4.6 ± 0.2	1.7 ± 0.1	17.75	8.5 ± 0.3	2.4 ± 0.1

Table B11. The average depth, U^{VI} mass, and ratio of U^{VI} mass over quartz sand mass for the retention profiles for the U^{VI} column experiments which contained 42 µM U^{VI}, 0.1 M NaCl at pH 11.5.

Experiment 1			Experiment 2		
Average Depth (cm)	mass U (µg)	µg U/g quartz	Average Depth (cm)	mass U (µg)	µg U/g quartz
0.75	590 ± 40	180 ± 10	0.75	372 ± 10	122 ± 4
2.25	8.72 ± 0.6	2.66 ± 0.2	2.25	5.32 ± 0.2	2.35 ± 0.07
3.75	1.45 ± 0.1	0.60 ± 0.04	3.75	1.96 ± 0.06	0.69 ± 0.02
5.25	0.98 ± 0.07	0.40 ± 0.03	5.25	1.59 ± 0.05	0.55 ± 0.02
6.75	0.84 ± 0.06	0.35 ± 0.02	6.75	1.34 ± 0.04	0.66 ± 0.02
8.25	0.80 ± 0.06	0.28 ± 0.02	8.25	0.60 ± 0.02	0.35 ± 0.01
9.75	0.49 ± 0.03	0.30 ± 0.02	9.75	0.79 ± 0.02	0.30 ± 0.01
11.25	0.85 ± 0.06	0.29 ± 0.02	11.25	0.62 ± 0.02	0.36 ± 0.01
12.75	0.49 ± 0.03	0.30 ± 0.02	12.75	0.66 ± 0.02	0.32 ± 0.01
14.25	0.50 ± 0.03	0.28 ± 0.02	14.25	0.72 ± 0.02	0.29 ± 0.01
15.75	0.54 ± 0.03	0.27 ± 0.02	15.75	0.46 ± 0.01	0.25 ± 0.01
17.75	0.89 ± 0.06	0.23 ± 0.02	17.75	0.65 ± 0.02	0.22 ± 0.01

B.2. Chapter 7 - Inhibition of U^{VI} Precipitation by the Siderophore Desferrioxamine B in pH 11.5, 0.1 M NaCl Solutions: A combined experimental and computational study

Table B12. The time and ratio of sample concentration over initial concentration (C/C_0) for the stirred batch reactor experiments at pH 11.5 which contain 42 µM U^{VI} and 0.1 M NaCl.

	Sample U^{VI} concentration / Initial U^{VI} concentration (C/C_0)		
Time (h)	0.2 µm filter membrane	0.45 µm filter membrane	1 µm filter membrane
	Experiment 1		
0.27	0.80 ± 0.05	0.78 ± 0.04	0.83 ± 0.05
0.55	0.65 ± 0.04	0.59 ± 0.03	0.65 ± 0.04
1	0.50 ± 0.03	0.49 ± 0.03	0.53 ± 0.03
2.05	0.29 ± 0.02	0.29 ± 0.02	0.29 ± 0.02
3.02	0.24 ± 0.01	0.24 ± 0.01	0.24 ± 0.01
4.07	0.18 ± 0.01	0.17 ± 0.01	0.17 ± 0.01
5.1	0.14 ± 0.01	0.14 ± 0.01	0.14 ± 0.01
6.1	0.13 ± 0.01	0.13 ±0.01	0.12 ±0.01
25.18	0.050 ± 0.003	0.050 ± 0.003	0.050 ± 0.003
	Experiment 2		
1.03	0.31 ± 0.02		0.31 ± 0.03
2.017	0.24 ± 0.02		0.24 ± 0.02
3	0.12 ± 0.01		0.13 ± 0.01
5.017	0.089 ± 0.008		0.096 ± 0.008
8.017	0.065 ±0.006		0.076 ± 0.006
21.13	0.037 ± 0.003		0.040 ± 0.003
26.18	0.032 ± 0.002		0.038 ± 0.003
30.67	0.025 ± 0.002		0.027 ± 0.002
52.67	0.019 ± 0.001		0.020 ± 0.002

Table B13. The time and ratio of sample concentration over initial concentration (C/C_0) for the first stirred batch reactor experiment containing 4.2. µM DFOB, 42 µM U^{VI}, 0.1 M NaCl at pH 11.5

	Sample U^{VI} concentration / Initial U^{VI} concentration (C/C_0)		
Time (h)	0.2 µm filter membrane	0.45 µm filter membrane	0.8 µm filter membrane
	Experiment 1		
0.22	0.86 ± 0.04	0.88 ± 0.04	0.94 ± 0.04
0.55	0.83 ± 0.04	0.85 ± 0.04	0.87 ± 0.04
1	0.84 ± 0.04	0.84 ± 0.04	0.92 ± 0.04
1.97	0.80 ± 0.03	0.81 ± 0.03	0.81 ± 0.03
4.03	0.67 ± 0.03	0.68 ± 0.03	0.71 ± 0.02
5.92	0.57 ± 0.02	0.57 ± 0.02	0.55 ± 0.02
71.22	0.132 ± 0.006	0.109 ± 0.005	0.108 ± 0.005
	Experiment 2		
1.2	0.69 ± 0.03	0.72 ± 0.03	0.74 ± 0.03
3.2	0.43 ± 0.02	0.46 ± 0.02	0.43 ± 0.02
5.57	0.35 ± 0.01	0.36 ± 0.02	0.35 ± 0.01
22.61	0.196 ± 0.008	0.193 ± 0.008	0.191 ± 0.008
24.88	0.174 ± 0.007	0.173 ± 0.007	0.173 ± 0.007
29.12	0.152 ± 0.006	0.150 ± 0.006	0.152 ± 0.006
46.88	0.107 ± 0.005	0.113 ± 0.005	0.112 ± 0.005
48.97	0.112 ± 0.005	0.110 ± 0.005	0.111 ± 0.005
52.97	0.103 ± 0.004	0.108 ± 0.005	0.108 ± 0.005

Table B14. The time and ratio of sample concentration over initial concentration (C/C_0) for the stirred batch reactor experiment containing 42 µM DFOB, 42 µM U^{VI}, 0.1 M NaCl at pH 11.5.

	Sample U^{VI} concentration / Initial U^{VI} concentration (C/C_0)		
Time (h)	0.2 µm filter membrane	0.45 µm filter membrane	0.8 µm filter membrane
Experiment 1			
0.28	1.01 ± 0.04	1.02 ± 0.04	1.03 ± 0.04
0.55	0.97 ± 0.04	1.08 ± 0.05	1.00 ± 0.04
0.9	0.94 ± 0.04	0.95 ± 0.04	1.03 ± 0.04
1.87	0.81 ± 0.03	0.86 ± 0.04	0.98 ± 0.04
4.05	0.64 ± 0.03	0.66 ± 0.03	0.74 ± 0.03
6	0.56 ± 0.02	0.57 ± 0.02	0.58 ± 0.02
23.97	0.38 ± 0.02	0.37 ± 0.02	0.48 ± 0.02
Experiment 2			
0.42	0.95 ± 0.04		0.95 ± 0.04
1.13	0.92 ± 0.04		0.92 ± 0.04
2.08	0.87 ± 0.04		0.87 ± 0.04
3.15	0.88 ± 0.04		0.85 ± 0.04
4.4	0.75 ± 0.03		0.75 ± 0.03
19.93	0.61 ± 0.03		0.60 ± 0.03
24	0.57 ± 0.02		0.58 ± 0.02
48.78	0.54 ± 0.02		0.52 ± 0.02
70.75	0.51 ± 0.02		0.51 ± 0.02

Table B15. The time and ratio of sample concentration over initial concentration (C/C_0) for the stirred batch reactor experiment containing 130 µM DFOB, 42 µM U^{VI}, 0.1 M NaCl at pH 11.5.

	Sample U^{VI} concentration / Initial U^{VI} concentration (C/C_0)		
Time (h)	0.2 µm filter membrane	0.45 µm filter membrane	1 µm filter membrane
0.5	1.0 ± 0.1	0.93 ± 0.09	0.93 ± 0.09
1	0.91 ± 0.09	0.92 ± 0.09	0.94 ± 0.09
2	0.92 ± 0.09	0.93 ± 0.09	0.92 ± 0.09
4	0.92 ± 0.09	0.94 ± 0.09	0.96 ± 0.09
6	1.0 ± 0.1	0.95 ± 0.09	0.93 ± 0.09
8	0.90 ± 0.09	0.92 ± 0.09	0.91 ± 0.09
24	0.93 ± 0.09	0.93 ± 0.09	0.94 ± 0.09
50	0.95 ± 0.09	0.95 ± 0.09	0.96 ± 0.09

Table B16. The time and ratio of sample concentration over initial concentration (C/C_0) for the stirred batch reactor experiments containing 420 µM DFOB, 42 µM U^{VI}, 0.1 M NaCl at pH 11.5.

	Sample U^{VI} concentration / Initial U^{VI} concentration (C/C_0)		
Time (h)	0.2 µm filter membrane	0.45 µm filter membrane	1 µm filter membrane
	Experiment 1		
0.27	0.99 ± 0.06	1.00 ± 0.06	0.98 ± 0.06
0.52	1.00 ± 0.06	1.03 ± 0.06	0.99 ± 0.06
1.03	0.99 ± 0.06	0.99 ± 0.06	0.97 ± 0.06
2.03	0.98 ± 0.06	0.99 ± 0.06	0.97 ± 0.06
3.03	1.01 ± 0.06	0.99 ± 0.06	0.97 ± 0.05
4.03	1.03 ± 0.06	1.03 ± 0.06	0.99 ± 0.06
5.02	1.08 ± 0.06	1.08 ± 0.06	0.98 ± 0.06
6.03	0.98 ± 0.06	1.00 ± 0.06	1.09 ± 0.06
24.1	1.10 ± 0.06	1.07 ± 0.06	1.09 ± 0.06
	Experiment 2		
0.25	1.00 ± 0.04		
0.5	0.99 ± 0.04		
1	0.99 ± 0.04		
1.5	0.95 ± 0.04		
1.9	0.99 ± 0.04		
4	0.99 ± 0.04		
5.87	0.99 ± 0.04		
7.98	0.98 ± 0.04		
22.77	0.98 ± 0.04		
	Experiment 3		
0.22	1.00 ± 0.04		
0.42	1.01 ± 0.04		
1	0.99 ± 0.04		
2.08	0.97 ± 0.04		
4.17	0.98 ± 0.04		
6	0.96 ± 0.04		
8.17	0.96 ±0.04		
23.67	1.08 ± 0.05		

Table B17. The time and ratio of sample concentration over initial concentration (C/C_0) for the long term (2 month) batch reactor experiment containing 42 µM U^{VI}, 0.1 M NaCl at pH 11.5.

	Sample U^{VI} concentration / Initial U^{VI} concentration (C/C_0)		
Time (week)	0.2 µm filter membrane	0.45 µm filter membrane	1 µm filter membrane
Experiment 1			
0.43	0		0
1	0		0
2	0		0
3	0		0
4	0		0
5	0		0
7	0		0
8	0		0
Experiment 2			
0.43	0.02	0.02	0.02
1	0.02	0.02	0.02
2	0.01	0.01	0.04
3	0.88	0.01	0.01
4	0.01	0.01	0.01
5	0.01	0.01	0.01
7	0.01	0.01	0.01
8	0.01	0.01	0.01

Table B18. The time, and ratio of sample concentration over initial concentration (C/C_0) for the long term (2 month) U^{VI} precipitation inhibition batch reactor experiment which contain 130 µM DFOB, 42 µM U^{VI}, 0.1 M NaCl at pH 11.5.

	Sample U^{VI} concentration / Initial U^{VI} concentration (C/C_0)		
Time (week)	0.2 µm filter membrane	0.45 µm filter membrane	1 µm filter membrane
Experiment 1			
0.43	0.95 ± 0.05	0.96 ± 0.05	0.94 ± 0.05
1	0.94 ± 0.05	0.96 ± 0.05	0.95 ± 0.05
2	0.93 ± 0.05	0.93 ± 0.05	0.88 ± 0.05
3	0.82 ± 0.05	0.82 ± 0.05	0.82 ± 0.05
4	0.59 ± 0.03	0.59 ± 0.03	0.59 ± 0.03
5	0.40 ± 0.02	0.44 ± 0.03	0.45 ± 0.03
7	0.33 ± 0.02	0.29 ± 0.02	0.34 ± 0.02
8	0.34 ± 0.02	0.30 ± 0.02	0.31 ± 0.02
Experiment 2			
0.43	0.94 ± 0.05	0.95 ± 0.05	0.94 ± 0.05
1	0.92 ± 0.05	0.92 ± 0.05	0.94 ± 0.05
2	0.85 ± 0.05	0.87 ± 0.05	0.88 ± 0.05
3	0.72 ± 0.04	0.73 ± 0.04	0.68 ± 0.04
4	0.48 ± 0.03	0.51 ± 0.03	0.50 ± 0.03
5	0.38 ± 0.02	0.39 ± 0.02	0.39 ± 0.02
7	0.31 ± 0.02	0.31 ± 0.02	0.31 ± 0.02
8	0.27 ± 0.02	0.28 ± 0.02	0.28 ± 0.02

Table B19. The time and ratio of sample concentration over initial concentration (C/C_0) for the long term (2 month) U^{VI} dissolution batch reactor experiments which contain 130 µM DFOB, 42 µM U^{VI}, 0.1 M NaCl at pH 11.5.

	Sample U^{VI} concentration / Initial U^{VI} concentration (C/C_0)		
Time (week)	0.2 µm filter membrane	0.45 µm filter membrane	1 µm filter membrane
	Experiment 1		
0	0.030 ± 0.002	0.034 ± 0.002	0.044 ± 0.002
0.43	0.066 ± 0.004	0.082 ± 0.005	0.082 ± 0.005
1	0.11 ± 0.01	0.126 ± 0.007	0.128 ± 0.007
2	0.18 ± 0.01	0.163 ± 0.009	0.164 ± 0.009
3	0.17 ± 0.01	0.19 ±0.01	0.21 ± 0.01
4	0.19 ± 0.01	0.20 ± 0.01	0.19 ± 0.01
5	0.20 ± 0.01	0.19 ± 0.01	0.128 ± 0.007
7	0.128 ± 0.007	0.138 ± 0.008	0.140 ± 0.008
8	0.109 ± 0.006	0.121 ± 0.007	0.120 ± 0.007
	Experiment 2		
0	0.025 ± 0.001	0.025 ± 0.001	0.040 ± 0.002
0.43	0.077 ± 0.004	0.085 ± 0.005	0.083 ± 0.005
1	0.123 ± 0.007	0.120 ± 0.007	0.122 ± 0.007
2	0.17 ± 0.01	0.19 ± 0.01	0.18 ± 0.01
3	0.20 ± 0.01	0.20 ± 0.01	0.20 ± 0.01
4	0.18 ± 0.01	0.20 ± 0.01	0.19 ± 0.01
5	0.19 ± 0.01	0.19 ± 0.01	0.19 ± 0.01
7	0.130 ± 0.007	0.134 ± 0.008	0.135 ± 0.008
8	0.109 ± 0.006	0.113 ± 0.006	0.113 ± 0.006

Appendix C – Thermodynamic data calculated using DFT

C.1. - Chapter 5 - Establishing a Cost Effective Density Functional Theory Protocol for Calculating log β Values of Geochemically Relevant Uranium Organic Ligand Complexes

Table C1. Thermodynamic properties of U^{VI} acetate complexes for the tested implicit solvation methods. The thermodynamic properties are: Electronic energy (E_e), enthalpy (H), entropy (TS_{total}), Gibbs energy (G). The latter three properties are provided at 298.15 K.

Complex	**Thermodynamics**				
	TS_{total} (kJ/mol)	**E_e (Ha)**	**H (Ha)**	**G (Ha)**	**ΔG (kJ/mol)**
Model Chemistry: B3LYP/aug-cc-pVDZ /MDF60/IEFPCM					
H_2O	58.001	-76.451061	-76.426145	-76.448237	-
$[CH_3OOH]^-$	89.307	-228.665848	-228.612571	-228.646586	-
$[UO_2(H_2O)_5]^{2+}$	169.782	-1007.492584	-1007.345290	-1007.409956	-
$[UO_2(H_2O)_3(CH_3OOH)]^+$	175.071	-1083.300235	-1083.152360	-1083.219041	-120
$[UO_2(H_2O)(CH_3OOH)_2]^0$	174.007	-1159.103556	-1158.954704	-1159.020980	-219
$UO_2(CH_3OOH)_3^-$	191.671	-1311.349860	-1311.172613	-1311.245617	-271
Model Chemistry: B3LYP/aug-cc-pVDZ/MDF60/SMD					
H_2O	58.017	-76.455668	-76.430938	-76.453035	-
$[CH_3OOH]^-$	85.676	-228.674746	-228.621494	-228.654126	-
$[UO_2(H_2O)_5]^{2+}$	161.651	-1007.574251	-1007.427375	-1007.488945	-
$[UO_2(H_2O)_3(CH_3OOH)]^+$	167.206	-1083.356862	-1083.209685	-1083.273370	-60
$[UO_2(H_2O)(CH_3OOH)_2]^0$	169.676	-1159.131800	-1158.983635	-1159.048261	-94
$[UO_2(CH_3OOH)_3]^-$	190.860	-1311.367760	-1311.191257	-1311.263952	-115

Table C2. Thermodynamic properties of U^{VI} acetate complexes for the tested mixed solvation methods. The thermodynamic properties are: Electronic energy (E_e), enthalpy (H), entropy (TS_{total}), Gibbs energy (G). The latter three properties are provided at 298.15 K.

Complex	Thermodynamics				
	TS_{total} (kJ/mol)	E_e (Ha)	H (Ha)	G (Ha)	ΔG (kJ/mol)
Mixed Solvation, Model Chemistry: B3LYP/aug-cc-pVDZ /MDF60/IEFPCM					
H_2O	58.001	-76.451061	-76.426145	-76.448237	-
$(H_2O)_3$	113.525	-229.364523	-229.284879	-229.328118	-
$(H_2O)_6$	170.287	-458.745619	-458.583209	-458.648068	-
$[CH_3OOH]^-$	89.307	-228.665848	-228.612571	-228.646586	-
$[UO_2(H_2O)_5*]^{2+}$	323.196	-1772.139573	-1771.715870	-1771.838968	-
$[UO_2(H_2O)_3*(CH_3OOH)]$	262.535	-1542.084695	-1541.770863	-1541.870857	-89
$[UO_2(H_2O)*(CH_3OOH)_2]$	219.202	-1312.025403	-1311.821889	-1311.905378	-185
$[UO_2(CH_3OOH)_3]^-$	191.671	-1311.349860	-1311.172613	-1311.245617	-232
Mixed Solvation, Model Chemistry: B3LYP/aug-cc-pVDZ /MDF60/SMD					
H_2O	58.017	-76.455668	-76.430938	-76.453035	-
$[CH_3OOH]^-$	85.676	-228.674746	-228.621494	-228.654126	-
$[UO_2(H_2O)_5*]^{2+}$	333.400	-1772.21557218	-1771.797542	-1771.924527	-
$[UO_2(H_2O)_3*(CH_3OOH)]$	261.136	-1542.14097952	-1541.830627	-1541.930089	-76
$[UO_2(H_2O)*(CH_3OOH)_2]$	214.557	-1312.05889235	-1311.856724	-1311.938444	-158
$[UO_2(CH_3OOH)_3]^-$	190.860	-1311.367760	-1311.191257	-1311.263952	-185
Mixed Solvation, Model Chemistry: B3LYP/6-31g(d,p) /MWB60/SMD					
H_2O	58.026	-76.43223806	-76.407281	-76.429382	
$[CH_3OOH]^-$	85.623	-228.61992169	-228.565984	-228.598597	
$[UO_2(H_2O)_5*]^{2+}$	311.325	-1774.13785243	-1773.715078	-1773.833656	
$[UO_2(H_2O)_3*(CH_3OOH)]$	256.284	-1544.12146809	-1543.807429	-1543.905042	-22
$[UO_2(H_2O)*(CH_3OOH)_2]$	209.739	-1314.09566401	-1313.891217	-1313.971103	-29
$[UO_2(CH_3OOH)_3]^-$	187.027	-1313.41690541	-1313.238685	-1313.309919	-50

Table C3. Thermodynamic properties for different U^{VI} ECP and basis sets. The thermodynamic properties are: Electronic energy (E_e), enthalpy (H), entropy (TS_{total}), Gibbs energy (G). The latter three properties are provided at 298.15 K.

Complex	**Thermodynamics**				
	TS_{total} (kJ/mol)	**E_e (Ha)**	**H (Ha)**	**G (Ha)**	**ΔG (kJ/mol))**
Model Chemistry: B3LYP/cc-pVDZ/MWB60/IEFPCM					
H_2O	58.034	-76.42686138	-76.395743	-76.417847	-
$[CH_3OOH]^-$	86.791	-228.61588415	-228.460373	-228.493429	-
$[UO_2(H_2O)_5]^{2+}$	169.033	-1009.61736592	-1009.470453	-1009.534835	-
$[UO_2(H_2O)_3(CH_3OOH)]$	174.940	-1085.42578748	-1085.278061	-1085.344692	-130
$[UO_2(H_2O)(CH_3OOH)_2]$	169.073	-1161.22697875	-1161.077871	-1161.142268	-228
$UO_2(CH_3OOH)_3^-$	192.321	-1313.46080652	-1313.283294	-1313.356545	-333
Model Chemistry: B3LYP/cc-pVDZ/MDF60/IEFPCM					
H_2O	58.034	-76.42686138	-76.395743	-76.417847	-
$[CH_3OOH]^-$	86.791	-228.61588415	-228.460373	-228.493429	-
$[UO_2(H_2O)_5]^{2+}$	166.623	-1007.43905089	-1007.292456	-1007.355919	-
$[UO_2(H_2O)_3(CH_3OOH)]$	176.242	-1083.246861	-1083.099387	-1083.166514	-132
$[UO_2(H_2O)(CH_3OOH)_2]$	168.628	-1159.049065	-1158.900052	-1158.964279	-230
$[UO_2(CH_3OOH)_3]^-$	191.612	-1311.284289	-1311.106795	-1311.179777	-330
Model Chemistry: B3LYP/cc-pVDZ/MDF60 ECP, cc-pVDZ-PP/IEFPCM					
H_2O	58.034	-76.42686138	-76.395743	-76.417847	-
$[CH_3OOH]^-$	86.791	-228.61588415	-228.460373	-228.493429	-
$[UO_2(H_2O)_5]^{2+}$	171.047	-1007.43588094	-1007.289277	-1007.354425	-
$[UO_2(H_2O)_3(CH_3OOH)]$	177.092	-1083.24488779	-1083.097376	-1083.164826	-131
$[UO_2(H_2O)(CH_3OOH)_2]$	168.338	-1159.04815033	-1158.899137	-1158.963253	-231
$[UO_2(CH_3OOH)_3]^-$	190.865	-1311.28614968	-1311.108678	-1311.181374	-338

Table C4. Thermodynamic properties for different ligand basis sets. The thermodynamic properties are: Electronic energy (E_e), enthalpy (H), entropy (TS_{total}), Gibbs energy (G). The latter three properties are provided at 298.15 K.

Complex	Thermodynamics				
	TS_{total} (kJ/mol))	E_e (Ha)	H (Ha)	G (Ha)	ΔG (kJ/mol)
Model Chemistry: B3LYP/6-31g(d,p)/MDF60/IEFPCM					
H_2O	58.009	-76.42673971	-76.401619	-76.423714	-
$[CH_3OOH]^-$	85.271	-228.60620056	-228.552326	-228.584804	-
$[UO_2(H_2O)_5]^{2+}$	170.245	-1007.40017216	-1007.252205	-1007.317048	-
$[UO_2(H_2O)_3(CH_3OOH)]$	175.282	-1083.20123394	-1083.052430	-1083.119192	-134
$[UO_2(H_2O)(CH_3OOH)_2]$	168.962	-1158.99763800	1158.847447	-1158.911801	-244
$UO_2(CH_3OOH)_3^-$	191.486	-1311.22193684	-1311.043072	-1311.116005	-339
Model Chemistry: B3LYP/aug-cc-pVDZ/MDF60/IEFPCM					
H_2O	58.001	-76.451061	-76.426145	-76.448237	-
$[CH_3OOH]^-$	89.307	-228.665848	-228.612571	-228.646586	-
$[UO_2(H_2O)_5]^{2+}$	169.782	-1007.492584	-1007.345290	-1007.409956	-
$[UO_2(H_2O)_3(CH_3OOH)]$	175.071	-1083.300235	-1083.152360	-1083.219041	-119
$[UO_2(H_2O)(CH_3OOH)_2]$	174.007	-1159.103556	-1158.954704	-1159.020980	-219
$UO_2(CH_3OOH)_3^-$	191.671	-1311.349860	-1311.172613	-1311.245617	-271
Model Chemistry: B3LYP/aug-cc-pVTZ/MDF60/IEFPCM					
H_2O	57.979	-76.47269058	-76.447793	-76.469876	-
$[CH_3OOH]^-$	88.632	-228.72540194	-228.671874	-228.705632	-
$[UO_2(H_2O)_5]^{2+}$	170.973	-1007.63250831	-1007.485269	-1007.550389	-
$[UO_2(H_2O)_3(CH_3OOH)]$	177.622	-1083.45686499	-1083.308882	-1083.376535	-122
$[UO_2(H_2O)(CH_3OOH)_2]$	176.022	-1159.27703855	-1159.127755	-1159.194798	-224
$[UO_2(CH_3OOH)_3]^-$	193.263	-1311.56094726	-1311.383108	-1311.456718	-275
Model Chemistry: B3LYP/aug-cc-pVQZ/MDF60/IEFPCM					
H_2O	57.968	-76.47871928	-76.453776	-76.475855	-
$[CH_3OOH]^-$	86.968	-228.74188923	-228.688349	-228.721473	-
$[UO_2(H_2O)_5]^{2+}$	171.250	-1007.67437672	-1007.526992	-1007.592218	-
$[UO_2(H_2O)_3(CH_3OOH)]$	177.834	-1083.50332474	-1083.355240	-1083.422974	-124
$[UO_2(H_2O)(CH_3OOH)_2]$	172.357	-1159.32801318	-1159.178637	-1159.244284	-224
$[UO_2(CH_3OOH)_3]^-$	191.688	-1311.62240959	-1311.444523	-1311.517533	-279

Table C5. Thermodynamic properties for different DFAs. The thermodynamic properties are: Electronic energy (E_e), enthalpy (H), entropy (TS_{total}), Gibbs energy (G). The latter three properties are provided at 298.15 K.

Complex	Thermodynamics				
	TS_{total} (kJ/mol)	E_e (Ha)	H (Ha)	G (Ha)	ΔG (kJ/mol)
Model Chemistry: PW91PW91/aug-cc-pVDZ/MDF60/IEFPCM					
H_2O	58.066	-76.42311072	76.398723	76.420839	-
$[CH_3OOH]^-$	89.183	-228.59079164	-228.538725	-228.572693	-
$[UO_2(H_2O)_5]^{2+}$	171.690	-1007.46217991	-1007.317845	-1007.383239	-
$[UO_2(H_2O)_3(CH_3OOH)]^+$	178.660	-1083.25284448	-1083.108148	-1083.176196	-127
$[UO_2(H_2O)(CH_3OOH)_2]^0$	174.465	-1159.03917040	-1158.893542	-1158.959992	-230
$UO_2(CH_3OOH)_3^-$	192.896	-1311.24144314	-1311.068103	-1311.141573	-290
Model Chemistry: TPSSTPSS/aug-cc-pVDZ/MDF60/IEFPCM					
H_2O	58.066	-76.45258019	-76.428144	-76.450260	-
$[CH_3OOH]^-$	89.410	-228.69371394	-228.641149	-228.675204	-
$[UO_2(H_2O)_5]^{2+}$	172.517	-1007.34104216	-1007.196222	-1007.261930	-
$[UO_2(H_2O)_3(CH_3OOH)]^+$	177.612	-1083.17784538	-1083.032224	-1083.099873	-130
$[UO_2(H_2O)(CH_3OOH)_2]^0$	172.757	-1159.01139065	-1158.864499	-1158.930299	-241
$UO_2(CH_3OOH)_3^-$	192.633	-1311.28741116	-1311.112425	-1311.185795	-303
Model Chemistry: B3LYP/aug-cc-pVDZ/MDF60/IEFPCM					
H_2O	58.009	-76.42673971	-76.401619	-76.423714	-
$[CH_3OOH]^-$	85.271	-228.60620056	-228.552326	-228.584804	-
$[UO_2(H_2O)_5]^{2+}$	170.245	-1007.40017216	-1007.252205	-1007.317048	-
$[UO_2(H_2O)_3(CH_3OOH)]^+$	175.282	-1083.20123394	-1083.052430	-1083.119192	-119
$[UO_2(H_2O)(CH_3OOH)_2]^0$	168.962	-1158.99763800	1158.847447	-1158.911801	-219
$[UO_2(CH_3OOH)_3]^-$	191.486	-1311.22193684	-1311.043072	-1311.116005	-271
Model Chemistry: M06/aug-cc-pVDZ/MDF60/IEFPCM					
H_2O	57.977	-76.41339865	-76.388198	-76.410280	-
$[CH_3OOH]^-$	86.629	-228.53462938	-228.377316	-228.410311	-
$[UO_2(H_2O)_5]^{2+}$	172.707	-1007.14564054	-1006.997719	-1007.063500	-
$[UO_2(H_2O)_3(CH_3OOH)]^+$	174.216	-1082.89514025	-1082.746567	-1082.812923	-112
$[UO_2(H_2O)(CH_3OOH)_2]^0$	171.774	-1158.64263601	-1158.493095	-1158.558520	-214
$[UO_2(CH_3OOH)_3]^-$	191.334	-1310.79973570	-1310.621979	-1310.694855	-283

Table C6. Thermodynamic properties for ligand training set. The thermodynamic properties are: Electronic energy, enthalpy (H), entropy (TS_{total}), Gibbs energy (G). The latter three properties are provided at 298.15 K. Bold data are the conformers used in the training set. AHA, Sal and Cat are acetohydroxamate, salicylate and catecholate respectively.

Complex	Thermodynamics					
	TS_{total} (kJ/mol)	E_e (Ha)	H (Ha)	G (Ha)	$\Delta_r G$ (kJ/mol)	Log β_{calc}
Model Chemistry: B3LYP/aug-cc-pVDZ/MDF60/IEFPCM						
H_3O^+	60.282	-76.838515	-76.800023	-76.822983	-	
$Glycolate^-$	88.542	-303.90532439	-303.845757	-303.879481	-	
$Oxalate^{2-}$	93.104	-377.489329	-377.460147	-377.495609	-	
AHA^-	90.402	-283.956061	-283.884992	-283.919424	-	
$L\text{-}glycine^-$	94.920	-284.027817	-283.955252	-283.991406	-	
$Salicylate^{2-}$	111.545	-495.178981	-495.077736	-495.120221	-	
$Catecholate^{2-}$	97.352	-381.775994	-381.687439	-381.724518	-	
$Formate^-$	72.874	-189.344113	-189.320008	-189.347764	-	
$Nicotinate^-$	105.082	-436.471810	-436.373781	-436.413804	-	
$[UO_2(H_2O)_3(glycolate)]^+$	190.470	-1234.990518	-1234.809119	-1234.881664	-88	15.48
$[UO_2(H_2O)(glycolate)_2]^0$ (ligands trans)	**214.538**	**-1462.483398**	**-1462.268155**	**-1462.349869**	**-168**	**29.34**
$[UO_2(H_2O)(glycolate)_2]^0$ (ligands cis)	209.510	-1462.482556	-1462.26689	-1462.346688	-159	27.88
$[UO_2(glycolate)_3]^-$ (water trans)	**238.509**	**-1689.958168**	**-1689.708297**	**-1689.799140**	**-197**	**34.50**
$[UO_2(glycolate)_3]^-$ (water cis)	238.509	-1689.958168	-1689.708297	-1689.79914	-193	33.78
$[UO_2(H_2O)_3(oxalate)]^0$	174.780	-1232.149931	-1232.026551	-1232.093121	-185	32.38
$[UO_2(H_2O)(oxalate)_2]^{2-}$	177.875	-1456.787404	-1456.687466	-1456.755215	-314	55.07
$[UO_2(oxalate)_3]^{4-}$	208.670	-1757.839129	-1757.735481	-1757.814959	-329	57.63
$[UO_2(H_2O)_3(AHA)]^+$	**184.493**	**-1138.610457**	**-1138.444879**	**-1138.515148**	**-180**	**31.56**

Complex	Thermodynamics					
	TS_{total} (kJ/mol)	E_e (Ha)	H (Ha)	G (Ha)	$\Delta_r G$ (kJ/mol)	Log β_{calc}
$[UO_2(H_2O)_4(AHA)]^+$ (Fig 6.5b)	191.181	-1215.068206	-1214.875473	-1214.948289	-158	27.75
$[UO_2(H_2O)_4(AHA)]^+$ (Fig 6.5c)	199.310	-1215.056362	-1214.863307	-1214.939221	-135	23.58
$[UO_2(H_2O)_4(AHA)]^+$ (Fig 6.5d)	190.718	-1215.066236	-1214.873075	-1214.945715	-152	26.56
$[UO_2(H_2O)_3(L\text{-glycine})]^+$	180.653	-1139.100786	-1138.918137	-1138.986944	-228	43.09
$[UO_2(H_2O)_3(Sal)]^0$ (catecholate O atoms)	**193.054**	**-1349.865030**	**-1349.668639**	**-1349.742169**	**-213**	**37.35**
$[UO_2(H_2O)_3(Sal)]^0$ (catecholate + carbonyl O	189.969	-1349.834062	-1349.637945	-1349.710300	-165	28.96
$[UO_2(H_2O)_3(Cat)]^0$	174.868	-1236.480178	-1236.295962	-1236.362566	-291	51.02
$[UO_2(H_2O)_4(Formate)]^+$	171.035	-1120.431904	-1120.285532	-1120.350676	-90	15.81
$[UO_2(H_2O)_3(Nicotinate)]^{2+}$	192.075	-1291.539066	-1291.332203	-1291.405360	-218	38.12
$[UO_2(H_2O)_4(Nicotinate)]^{2+}$	202.575	-1368.002259	-1367.768028	-1367.845185	-213	37.38

C.2. - Chapter 6 - Determining the Relative Stability of U^{VI} Complexes with Siderophore Functional Groups in Acidic Solutions using Density Functional Theory

Table C7. Thermodynamic properties of the catecholate (CAT) complexes, H_2O, H_3O^+ and $[UO_2(H_2O)_5]^{2+}$. The thermodynamic properties are: Electronic energy (E_e), enthalpy (H), entropy (TS_{total}), Gibbs energy (G). The latter three properties are provided at T = 298.15 K. The Δ_rG for the U^{VI}-L complex and the log β values calculated from Δ_rG (log β_{calc}), and after applying the fitting equation (log β_{fit}) are also provided.

Complex	Figure	E_e (Ha)	H (Ha)	TS_{total} (kJ/mol)	G (Ha)	ΔG (kJ/mol)	Log β_{calc}	Log β_{fit}
H_2O		-76.451061	-76.426145	58.001	-76.448237	-	-	-
H_3O^+		-76.838515	-76.800023	60.282	-76.822983	-	-	-
$[UO_2(H_2O)_5]^{2+}$		-1007.492584	-1007.345290	169.782	-1007.409956	-	-	-
$[L]^{2-}$	-	-381.775994	-381.687439	97.352	-381.724518	-	-	-
$[UO_2(H_2O)_3(L)]^0$	6.1a	-1236.480178	-1236.295962	174.868	-1236.362566	-291	51.02	16.43
$[UO_2(H_2O)_3(OH)(HL)]^0$	6.1b	-1312.942602	-1312.731095	196.043	-1312.805764	-296	51.84	16.68

Table C8. Thermodynamic properties of the hydroxamate (HYD) complexes. The thermodynamic properties are: Electronic energy (E_e), enthalpy (H), entropy (TS_{total}), Gibbs energy (G). The latter three properties are provided at T = 298.15 K. The $\Delta_r G$ for the U^{VI}-L complex and the log β values calculated from $\Delta_r G$ (log β_{calc}), and after applying the fitting equation (log β_{fit}) are also provided.

Complex	Figure	E_e (Ha)	H (Ha)	TS_{total} (kJ/mol)	G (Ha)	ΔG (kJ/mol)	Log β_{calc}	Log β_{fit}
$[L\ (cis)]^-$		-323.261628	-323.161559	100.273	-323.199751	-	-	-
$[L\ (trans)]^-$		-323.264562	-323.164929	100.655	-323.203267	-	-	-
$[UO_2(H_2O)_3(L)]^+$	6.2a	-1177.922903	-1177.728046	192.760	-1177.801464	-187	32.69	9.00
$[UO_2(H_2O)_4(L)]^+$	6.2b	-1254.3772	-1254.155333	202.122	-1254.232317	-159	27.83	7.03
$[UO_2(H_2O)_4(L)]^+$	6.2c	-1254.364666	-1254.142331	207.595	-1254.2214	-130	22.81	5.00
$[UO_2(H_2O)_4(L)]^+$	6.2d	-1254.367957	-1254.145958	206.503	-1254.22461	-139	24.29	5.60
$[UO_2(H_2O)_4(L)]^+$	6.2e	-1254.351507	-1254.129384	206.058	-1254.207867	-95	16.59	2.48
$[UO_2(H_2O)_3(OH)(HL)]^+$	6.2f	-1254.375912	-1254.15394	205.630	-1254.232261	-159	27.81	7.02

Table C9. Thermodynamic properties of the α-hydroxycarboxylate (HC) complexes. The thermodynamic properties are: Electronic energy (E_e), enthalpy (H), entropy (S_{total}), Gibbs energy (G). The latter three properties are provided at T = 298.15 K. The $\Delta_r G$ for the U^{VI}-L complex and the log β values calculated from $\Delta_r G$ (log β_{calc}), and after applying the fitting equation (log β_{fit}) are also provided.

Complex	Figure	E_e (Ha)	H (Ha)	TS_{total} (kJ/mol)	G (Ha)	ΔG (kJ/mol)	Log β_{calc}	Log β_{fit}
$[L]^{2-}$		-303.383119	-303.337775	88.606	-303.371523	-	-	-
$[UO_2(H_2O)_3(L)]^0$	6.3a	-1158.087398	-1157.946593	174.502	-1158.013057	-300	52.62	17.08
$[UO_2(H_2O)_3(L)]^0$	6.3b	-1158.034985	-1157.895548	173.631	-1157.96168	-166	29.00	7.51
$[UO_2(H_2O)_4(L)]^0$	6.3c	-1234.537934	-1234.370956	186.338	-1234.441929	-267	46.85	14.74
$[UO_2(H_2O)_4(L)]^0$	6.3d	-1234.489902	-1234.323519	188.167	-1234.395188	-145	25.36	6.03
$[UO_2(H_2O)_4(L)]^0$	6.3e	-1234.48056	-1234.313832	191.113	-1234.386624	-122	21.42	4.43
$[UO_2(H_2O)_3(OH)(L)]^0$	6.3f	-1234.545223	-1234.376358	188.198	-1234.448039	-284	49.66	15.88

Table C10. Thermodynamic properties of the α-aminocarboxylate (AC) complexes. The thermodynamic properties are: Electronic energy (E_e), enthalpy (H), entropy (S_{total}), Gibbs energy (G). The latter three properties are provided at T = 298.15 K. The $\Delta_r G$ for the U^{VI}-L complex and the log β values calculated from $\Delta_r G$ (log β_{calc}), and after applying the fitting equation (log β_{fit}) are also provided.

Complex	Figure	E_e (Ha)	H (Ha)	TS_{total} (kJ/mol)	G (Ha)	ΔG (kJ/mol)	Log β_{calc}	Log β_{fit}
$[L]^-$		-284.027817	-283.955252	94.920	-283.991406	-	-	-
$[UO_2(H_2O)_3(HL)]^{2+}$	6.4a	-1139.100786	-1138.918137	180.653	-1138.986944	-228	39.95	11.95
$[UO_2(H_2O)_4(HL)]^{2+}$	6.4b	-1215.565381	-1215.355734	198.718	-1215.431422	-218	38.22	11.25
$[UO_2(H_2O)_4(HL)]^{2+}$	6.4c	-1215.565406	-1215.355808	199.834	-1215.43192	-220	38.45	11.34
$[UO_2(H_2O)_3(L)]^+$	6.4d	-1138.667001	-1138.49904	177.600	-1138.566684	-126	22.15	4.73
$[UO_2(H_2O)_4(L)]^+$	6.4e	-1215.090097	-1214.89446	186.528	-1214.965505	-15	2.56	-3.21

Table C11. Thermodynamic properties of the hydroxy-phenyloxazolonate (HPO) complexes. The thermodynamic properties are: Electronic energy (E_e), enthalpy (H), entropy (TS_{total}), Gibbs energy (G). The latter three properties are provided at T = 298.15 K. The $\Delta_r G$ for the U^{VI}-L complex and the log β values calculated from $\Delta_r G$ (log β_{calc}), and after applying the fitting equation (log β_{fit}) are also provided.

Complex	Figure	E_e (Ha)	H (Ha)	TS_{total} (kJ/mol)	G (Ha)	ΔG (kJ/mol)	Log β_{calc}	Log β_{fit}
$[L\ (cis)]^-$		-553.167391	-553.004249	122.116	-553.050760	-	-	-
$[L\ (trans)]^-$		-553.167652	-553.004414	123.182	-553.051331	-	-	-
$[UO_2(H_2O)_3(L)]^+$	6.5a	-1407.829242	-1407.570126	200.386	-1407.646449	-179	31.28	8.43
$[UO_2(H_2O)_3(L)]^+$	6.5b	-1407.806911	-1407.548445	199.726	-1407.624516	-121	21.19	4.34
$[UO_2(H_2O)_4(L)]^+$	6.5c	-1484.28195	-1483.997008	217.253	-1484.079754	-157	27.54	6.92
$[UO_2(H_2O)_4(L)]^+$	6.5d	-1484.270672	-1483.984846	223.877	-1484.070116	-132	23.11	5.12
$[UO_2(H_2O)_4(L)]^+$	6.5e	-1484.251924	-1483.966214	213.279	-1484.047448	-72	12.69	0.89
$[UO_2(H_2O)_4(L)]^+$	6.5f	-1484.230962	-1483.944112	213.835	-1484.025557	-15	2.62	-3.19
$[UO_2(H_2O)_3(L)\bullet H_2O]^+$	6.5g	-1484.269723	-1483.983764	216.746	-1484.066318	-122	21.36	4.41
$[UO_2(H_2O)_3(L)\bullet H_2O]^+$	6.5h	-1484.290835	-1484.003896	221.485	-1484.088255	-180	31.45	8.50

Table C12. Thermodynamic parameters of the α-hydroxyimidazolate (HI) complexes. The thermodynamic properties are: Electronic energy (E_e), enthalpy (H), entropy (TS_{total}), Gibbs energy (G). The latter three properties are provided at T = 298.15 K. The $\Delta_r G$ for the U^{VI}-L complex and the log β values calculated from $\Delta_r G$ (log β_{calc}), and after applying the fitting equation (log β_{fit}) are also provided. The two ligand conformers are where the O atom was initially cis and trans to the pyrrole-type N atom.

Complex	Figure	E_e (Ha)	H (Ha)	TS_{total} (kJ/mol)	G (Ha)	ΔG (kJ/mol)	Log β_{calc}	Log β_{fit}
$[L]^{2-}$ (cis)	-	-339.812131	-339.729147	95.689	-339.765593	-	-	-
$[L]^{2-}$ (trans)	-	-339.813548	-339.730443	95.620	-339.766863	-	-	-
$[UO_2(H_2O)_3(L)]^0$	7.6a	-1194.514267	-1194.335491	183.902	-1194.405535	-293	51.31	16.55
$[UO_2(H_2O)_3(OH)(HL)]^0$	7.6b	-1270.989953	-1270.783062	191.743	-1270.856093	-299	52.38	16.98
$[UO_2(H_2O)_4(L)]^0$	7.6c	-1270.856093	-1270.750614	197.655	-1270.825897	-220	38.49	11.35
$[UO_2(H_2O)_4(L)]^0$	7.6d	-1270.955819	-1270.749992	199.015	-1270.825793	-219	38.44	11.33
$[UO_2(H_2O)_4(L)]^0$	7.6e	-1270.906167	-1270.701413	201.626	-1270.778209	-95	16.56	2.46
$[UO_2(H_2O)_4(L)]^0$	7.6f	-1270.902883	-1270.697739	198.455	-1270.773326	-82	14.31	1.55
$[UO_2(H_2O)_3(L)\bullet H_2O]^0$	7.6g	-1270.979644	-1270.773266	193.238	-1270.846866	-275	48.13	15.26

C.3. - Chapter 7 - Stability of U^{VI} hydroxamate complexes at pH 11.5: A Computational Investigation

Table C13. Thermodynamic properties of the U^{VI}-hydroxamate complexes at pH 11.5 using the implicit solvation approach. The thermodynamic properties are: Electronic energy (E_e), enthalpy (H), entropy (TS_{total}), Gibbs energy (G).The latter three properties are provided at 298.15 K. The change in Gibbs energy of the reaction ($\Delta_r G$) is also provided for the formation of the U^{VI}-L complexes.

Complex	Figure	Thermodynamics				
		E_e (Ha)	H (Ha)	TS_{tot} (kJ/mol)	G (Ha)	$\Delta_r G$ (kJ/mol)
OH^-	-	-75.944344	-75.932428	51.358	-75.951989	-
L^-	-	-323.264562	-323.164929	100.646	-323.203263	-
$[UO_2(OH)_3(H_2O)]^-$	7.3a	-929.709559	929.629839	141.517	-929.68374	-
$[UO_2(OH)_3(H_2O)_2]^-$	-	-1006.172953	-1006.065819	162.399	1006.127674	-
$[UO_2(OH)_2(H_2O)(L\text{-uni})]^-$ (L trans to H_2O)	7.3b	-1177.011961	-1176.843853	175.692	-1176.91077	+64
$[UO_2(OH)_2(H_2O)(L\text{-uni})]^-$ (L cis to H_2O)	7.3c	-1177.010522	-1176.842466	179.529	-1176.910845	+64
$[UO_2(OH)_3(L\text{-uni})]^{2-}$	7.3d	-1176.543423	-1176.388648	169.834	-1176.453334	-20
$[UO_2(OH)(H_2O)L]^0$	7.3e	-1101.023247	-1100.868965	164.680	-1100.931688	+135
$[UO_2(OH)_2L]^-$	7.3f	-1100.569299	-1100.428335	158.772	-1100.488808	+13
$[UO_2(H_2O)L(L\text{-uni})]^0$	7.3g	-1348.323434	-1348.081086	211.105	-1348.161492	+191
$[UO_2(OH)L(L\text{-uni})]^-$	7.3h	-1347.870242	-1347.640973	198.501	-1347.716578	+74
$[UO_2L_2]^0$	7.3i	-1271.879949	-1271.664601	182.820	1271.734233	+154

Table C14. Thermodynamic properties of the U^{VI}-hydroxamate complexes at pH 11.5 using the mixed solvation approach. The thermodynamic properties are: Electronic energy (E_e), enthalpy (H), entropy (TS_{total}), Gibbs energy (G). The latter three properties are provided at 298.15 K. The change in Gibbs energy of the reaction ($\Delta_r G$) is also provided for the formation of the U^{VI}-L complexes. All OH^- and H_2O are $[OH(H_2O)]^-$ and $(H_2O)(H_2O)_2$. L-uni has one additional H_2O molecule (i.e. $L(H_2O)$)

Complex	Figure	Thermodynamics				
		E_e (Ha)	H (Ha)	TS_{tot} (kJ/mol)	G (Ha)	$\Delta_r G$ (kJ/mol)
$[OH(H_2O)]^-$		-152.416048	-152.378877	76.846	-152.408146	-
$[L(H_2O)_2]^-$		-476.192801	-476.039144	151.163	-476.096719	-
$[UO_2(OH)_3(H_2O)]^-$	7.4a	-1311.990325	-1311.773896	276.506	-1311.879212	-
$[UO_2(OH)_3(H_2O)_2]^-$ (water molecules cis)	-	-1541.387301	-1541.087872	300.084	-1541.202168	-
$[UO_2(OH)_3(H_2O)_2]^-$ (water molecules trans	-	-1541.398652	-1541.099101	280.817	-1541.206058	-
$[UO_2(OH)_2(H_2O)(L\text{-uni})]^-$ (L cis to H_2O)	7.4b	-1559.299442	-1558.994599	309.057	-1559.112313	+37
$[UO_2(OH)_2(H_2O)(L\text{-uni})]^-$ (L trans to H_2O)	7.4c	-1559.303983	-1558.998884	293.384	-1559.110628	+41
$[UO_2(OH)_3(L\text{-uni})]^{2-}$	7.4d	-1482.364267	-1482.100229	286.210	-1482.209241	+3
$[UO_2(OH)(H_2O)L]^0$	7.4e	-1330.40213	-1330.165764	240.913	-1330.257523	+51
$[UO_2(OH)_2L]^-$	7.4f	-1253.477406	-1253.281719	216.256	-1253.364086	-9
$[UO_2(H_2O)L(L\text{-uni})]^0$	7.4g	-1577.705281	-1577.380734	275.642	-1577.485721	+100
$[UO_2(OH)L(L\text{-uni})]^-$	7.4h	-1500.791987	-1500.507573	231.044	-1500.595573	+32

Appendix D – Structural data from DFT calculations

D.1. - Chapter 5 - Establishing a Cost Effective Density Functional Theory Protocol for Calculating log β Values of Geochemically Relevant Uranium Organic Ligand Complexes

Table D1. Average bond lengths (Å) and angles (°) excluding acetate used in the ligand training set which is presented in Chapter 5. The structures highlighted in bold are used in the fitting set. The remaining structures are less energetically stable conformers. These are provided in the same order as in the corresponding thermodynamic Table B. AHA, Sal and Cat are acetohydroxamate, salicylate and catecholate respectively.

Complex	U=O	O=U=O	U-O_{water}	U-OH	U-O(C)
$[UO_2(H_2O)_3(glycolate)]^+$	1.773	177	2.501	-	2.289
$[UO_2(H_2O)(glycolate)_2]^0$ (ligands trans)	**1.781**	**179**	**2.510**	**-**	**2.341**
$[UO_2(H_2O)(glycolate)_2]^0$ (ligands cis)	1.781	177	2.534	-	2.327
$[UO_2(glycolate)_3]^-$ (water trans)	**1.788**	**179**	**2.533**	**-**	**2.360**
$[UO_2(glycolate)_3]^-$ (water cis)				-	
$[UO_2(H_2O)_3(oxalate)]^0$	1.784	175	2.538	-	2.310
$[UO_2(H_2O)(oxalate)_2]^{2-}$	1.800	179	2.572	-	2.390
$[UO_2(oxalate)_3]^{4-}$	1.807	179	-	-	2.394
$[UO_2(H_2O)_3(AHA)]^+$	**1.782**	**174**	**2.507**	**-**	**2.362**
$[UO_2(H_2O)_4(AHA)]^+$ (Fig 6.5b)	1.781	177	2.524	-	2.210
$[UO_2(H_2O)_4(AHA)]^+$ (Fig 6.5c)	1.784	178	2.538	-	2.176
$[UO_2(H_2O)_4(AHA)]^+$ (Fig 6.5d)	1.783	177	2.571	2.213	2.376
$[UO_2(H_2O)_3(L\text{-}glycine)]^+$	1.768	178	2.462	-	2.465
$[UO_2(H_2O)_3(Sal)]^0$ (catecholate O atoms)	**1.795**	**173**	**2.568**	**-**	**2.239**
$[UO_2(H_2O)_3(Sal)]^0$ (catecholate + carbonyl O atoms)	1.780	177	2.558	-	2.370
$[UO_2(H_2O)_3(Cat)]^0$	1.794	173	2.600	-	2.299
$[UO_2(H_2O)_4(Formate)]^+$	1.773	177	2.503	-	2.292
$[UO_2(H_2O)_3(Nicotinate)]^{2+}$	1.769	178	2.467	-	2.466
$[UO_2(H_2O)_4(Nicotinate)]^{2+}$	1.770	177	2.496	-	2.315

D.2. - Chapter 6- Determining the Relative Stability of U^{VI} Complexes with Siderophore Functional Groups in Acidic Solutions using Density Functional Theory

Table D2. Average bond lengths (Å) and angles (°) of the catecholate (CAT) complexes and $[UO_2(H_2O)_5]^{2+}$

Complex	Figure	U=O	O=U=O	U-O_{water}	U-OH	U-$O(C)_1$	U-$O(C)_2$
$[UO_2(H_2O)_5]^{2+}$	-	1.761	179	2.470	-	-	-
$[UO_2(H_2O)_3(L)]^0$	Fig 6.1a	1.794	173	2.600	-	2.296	2.301
$[UO_2(H_2O)_3(OH)(HL)]^0$	Fig 6.1b	1.800	174	2.608	2.235	2.198	-

Table D3. Average bond lengths (Å) and angles (°) of the hydroxamate complexes.

Complex	Figure	U=O	O=U=O	U-O_{water}	U-OH	U-O(C)	U-O(N)
$[UO_2(H_2O)_3(L)]^+$	Fig 6.2a	1.784	173	2.513	-	2.394	2.296
$[UO_2(H_2O)_4(L)]^+$	Fig 6.2b	1.783	175	2.523	-	-	2.200
$[UO_2(H_2O)_4(L)]^+$	Fig 6.2c	1.786	173	2.538	-	-	2.154
$[UO_2(H_2O)_4(L)]^+$	Fig 6.2d	1.784	174	2.538	-	-	2.162
$[UO_2(H_2O)_4(L)]^+$	Fig 6.2e	1.784	174	2.527	-	2.202	-
$[UO_2(H_2O)_3(OH)(HL)]^+$	Fig 6.2f	1.789	175	2.564	2.217	2.343	-

Table D4. Average bond lengths (Å) and angles (°) of the α-hydroxycarboxylate (HC) complexes. U-O(C)$_1$ is the O cis to the α-hydroxy group while U-O(C)$_1$ is the O trans to the α-hydroxy group.

Complex	Figure	U=O	O=U=O	U-O$_{water}$	U-OH	U-αO(C)	U-O(C)$_1$	U-O(C)$_2$
$[UO_2(H_2O)_3(L)]^0$	Fig 6.3a	1.798	172	2.569	-	2.179	2.364	-
$[UO_2(H_2O)_3(L)]^0$	Fig 6.3b	1.778	177	2.529	-	-	2.338	2.397
$[UO_2(H_2O)_4(L)]^0$	Fig 6.3c	1.793	172	2.765	-	2.115	-	-
$[UO_2(H_2O)_4(L)]^0$	Fig 6.3d	1.796	174	2.548	-	-	2.241	
$[UO_2(H_2O)_4(L)]^0$	Fig 6.3e	1.782	175	2.542	-	-	-	2.17
$[UO_2(H_2O)_3(OH)(HL)]^0$	Fig 6.3f	1.792	175	2.607	2.198	-	2.283	-

Table D5. Average bond lengths (Å) and angles (°) of the α-aminocarboxylate (AC) complexes.

Complex	Figure	U=O	O=U=O	U-O$_{water}$	U-O(C)$_1$	U-O(C)$_2$	U-N
$[UO_2(H_2O)_3(HL)]^{2+}$	Fig 6.4a	1.768	178	2.462	2.456	2.474	-
$[UO_2(H_2O)_4(HL)]^{2+}$	Fig 6.4b	1.770	176	2.491	2.324	-	-
$[UO_2(H_2O)_4(HL)]^{2+}$	Fig 6.4c	1.770	176	2.489	2.324	-	-
$[UO_2(H_2O)_3(L)]^{+}$	Fig 6.4d	1.778	176	2.511	2.265	-	2.592
$[UO_2(H_2O)_4(L)]^{+}$	Fig 6.4e	1.770	171	2.539	-	-	2.509

Table D6. Average bond lengths (Å) and angles (°) of the hydroxy-phenyloxazolonate (HPO) complexes.

Complex	Figure	U=O	O=U=O	U-O_{water}	U-OH	U-O(C)	U-O(oxazolone)	U-N
$[UO_2(H_2O)_3(HPO)]^+$	Fig 6.5a	1.784	174	2.544	-	2.198	-	2.518
$[UO_2(H_2O)_3(HPO)]^+$	Fig 6.5b	1.781	175	2.560	-	2.165	2.634	-
$[UO_2(H_2O)_4(HPO)]^+$	Fig 6.5c	1.786	174	2.521	-	2.184	-	-
$[UO_2(H_2O)_4(HPO)]^+$	Fig 6.5d	1.784	174	2.525	-	2.179	-	-
$[UO_2(H_2O)_4(HPO)]^+$	Fig 6.5e	1.779	173	2.526	2.179	-	2.773	-
$[UO_2(H_2O)_4(HPO)]^+$	Fig 6.5f	1.771	173	2.533	-	-	-	2.428
$UO_2(H_2O)_3(HPO)\bullet H_2O]^+$	Fig 6.5g	1.781	172	2.503	-	2.209	2.703	-
$UO_2(H_2O)_3(HPO)\bullet H_2O]^+$	Fig 6.5h	1.784	176	2.592	-	2.209	-	2.546

Table D7. Average bond lengths (Å) and angles (°) of the α-hydroxyimidazolate (HI) complexes.

Complex	Figure	U=O	O=U=O	U-O_{water}	U-OH	U-O(C)	U-N(pyrrole)	U-N(pyridine)
$[UO_2(H_2O)_3(L)]^0$	Fig 6.6a	1.800	171	2.581	-	2.163	-	2.466
$[UO_2(H_2O)_3(OH)(HL)]^0$	Fig 6.6b	1.805	174	2.630	2.182	2.182	-	-
$[UO_2(H_2O)_4(L)]^0$	Fig 6.6c	1.796	173	2.553	-	2.097	-	-
$[UO_2(H_2O)_4(L)]^0$	Fig 6.6d	1.797	171	2.551	-	2.090	-	-
$[UO_2(H_2O)_4(L)]^0$	Fig 6.6e	1.780	178	2.533	-	-	2.329	-
$[UO_2(H_2O)_4(L)]^0$	Fig 6.6f	1.776	175	2.524	-	-	-	2.352
$UO_2(H_2O)_3(L)\bullet H_2O]^0$	Fig 6.6g	1.794	173	2.560	-	2.213	-	2.459

D.3. Chapter 7 - Stability of U^{VI} hydroxamate complexes at pH 11.5: A Computational Investigation

Table D8. Average bond lengths (Å) and angles (°) of the U^{VI}-hydroxamate complexes at pH 11.5 using the implicit solvation model.

Complex	Figure	U=O	O=U=O	U-OH	U-O_{water}	U-O(C)	U-O(N)
$[UO_2(OH)_3(H_2O)]^-$	7.3a	1.828	176	2.228	2.620	-	-
$[UO_2(OH)_3(H_2O)_2]^-$	-	1.818	178	2.251	2.676	-	-
$[UO_2(OH)_2(H_2O)$(L-mono)$]^-$ (L trans to H_2O)	7.3b	1.815	178	2.253	2.671	-	2.284
$[UO_2(OH)_2(H_2O)$(L-mono)$]^-$ (L cis to H_2O)	7.3c	1.822	175	2.218	2.610	-	2.295
$[UO_2(OH)_3$(L-mono)$]^{2-}$	7.3d	1.840	179	2.267	-	-	2.357
$[UO_2(OH)(H_2O)L]^0$	7.3e	1.804	176	2.186	2.511	2.443	2.352
$[UO_2(OH)_2L]^-$	7.3f	1.823	178	2.224	-	2.480	2.414
$[UO_2(H_2O)$L(L-mono)$]^0$	7.3g	1.799	177	-	2.541	2.403	2.299
$[UO_2(OH)$L(L-mono)$]^-$	7.3h	1.816	177	2.206	-	2.472	2.342
$[UO_2L_2]^0$	7.3i	1.800	178	-	-	2.336	2.445

Table D9. Average bond lengths (Å) and angles (°) of the U^{VI}-hydroxamate complexes at pH 11.5 using the mixed solvation model. All OH^- and H_2O are $[OH(H_2O)]^-$ and $[H_2O(H_2O)_2]$. L-uni has one additional H2O molecule (i.e. L(H_2O))

Complex	Figure	U=O	O=U=O	U-OH	U-O_{water}	U-O(C)	U-O(N)
$[UO_2(OH)_3(H_2O)]^-$	7.4a	1.837	176	2.229	2.547	-	-
$[UO_2(OH)_2(H_2O)$(L-mono)] (L trans to H_2O)	-	1.833	176	2.236	2.592	-	-
$[UO_2(OH)_2(H_2O)$(L-mono)] (L cis to H_2O)	-	1.848	178	2.213	2.556	-	-
$[UO_2(OH)_2(H_2O)$(L-mono)$]^-$ (L trans to H_2O)	7.4b	1.836	177	2.202	2.497	-	2.312
$[UO_2(OH)_2(H_2O)$(L-mono)$]^-$ (L cis to H_2O)	7.4c	1.829	176	2.206	2.529	-	2.324
$[UO_2(OH)_3$(L-mono)$]^{2-}$	7.4d	1.845	179	2.253	-	-	2.385
$[UO_2(OH)(H_2O)L]^0$	7.4e	1.809	178	2.161	2.490	2.490	2.360
$[UO_2(OH)_2L]^-$	7.4f	1.827	179	2.208	-	2.491	2.421
$[UO_2(H_2O)$L(L-mono)$]^0$	7.4g	1.800	177	-	2.448	2.447	2.303
$[UO_2(OH)$L(L-mono)$]^-$	7.4h	1.815	179	2.192	-	2.483	2.339

Appendix E-Structures used in ligand training set

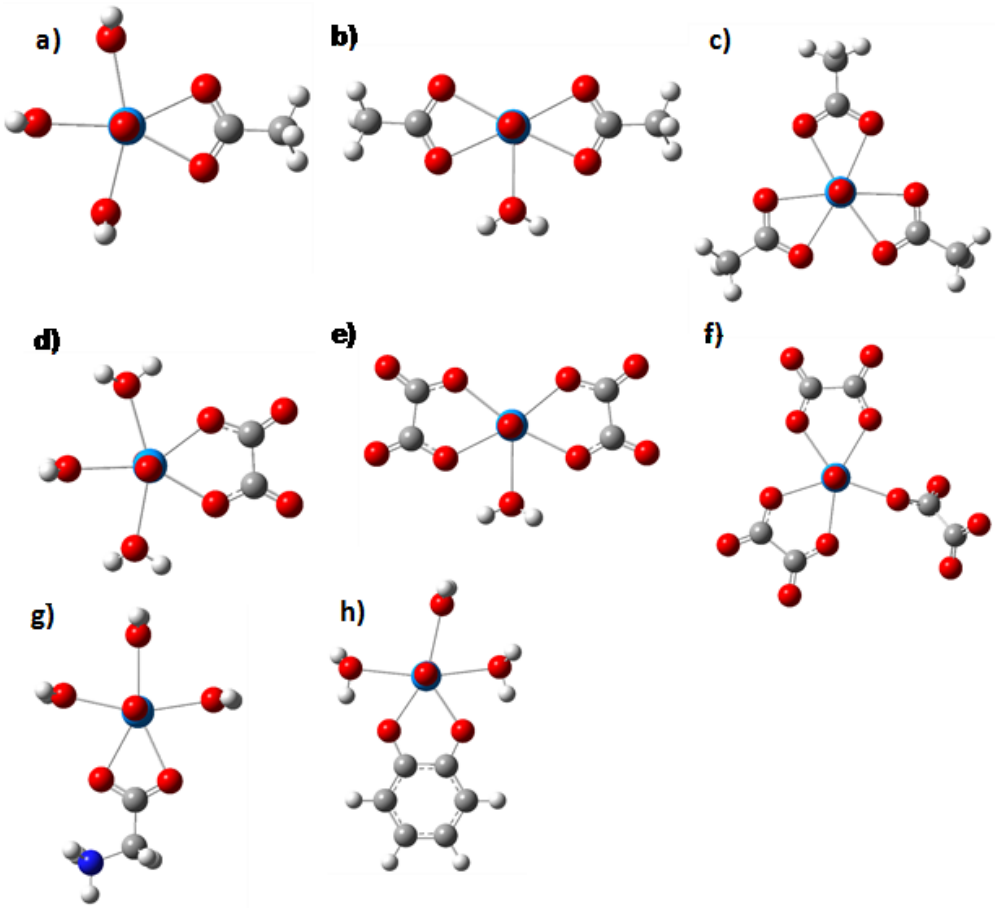

Figure E1. Structures used in the ligand training sets. The white, dark blue, grey red and light blue atoms represent H, N, C, O and U respectively. The structures are: a) acetate (1:1 U^{VI}-L), b) acetate (1:2 U^{VI}-L). c) acetate (1:3 U^{VI}-L) d) oxalate (1:1 U^{VI}-L), e) oxalate (1:2 U^{VI}-L), f) oxalate (1:3 U^{VI}-L), g) L-glycine (1:1 U^{VI}-L), h) catecholate (1:1 U^{VI}-L)

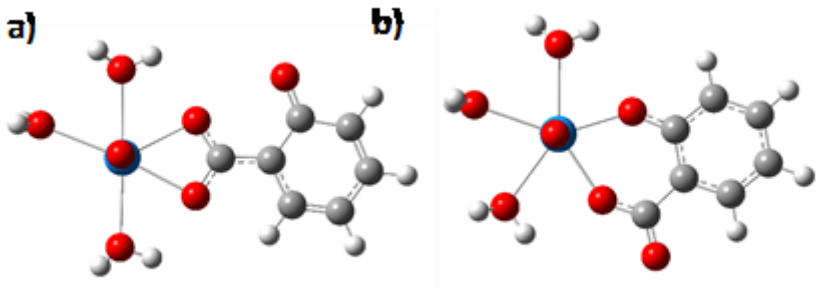

Figure E2. The two possible bidentate complexes between U^{VI} and salycicate. The white, grey, red and light blue atoms represent H, C, O and U respectively. Structure a) is bidentate via carboxylic group, part b) is bidentate via phenyl O atom and a carboxylate O atom. Structure b) is the most energetically favourable structure.

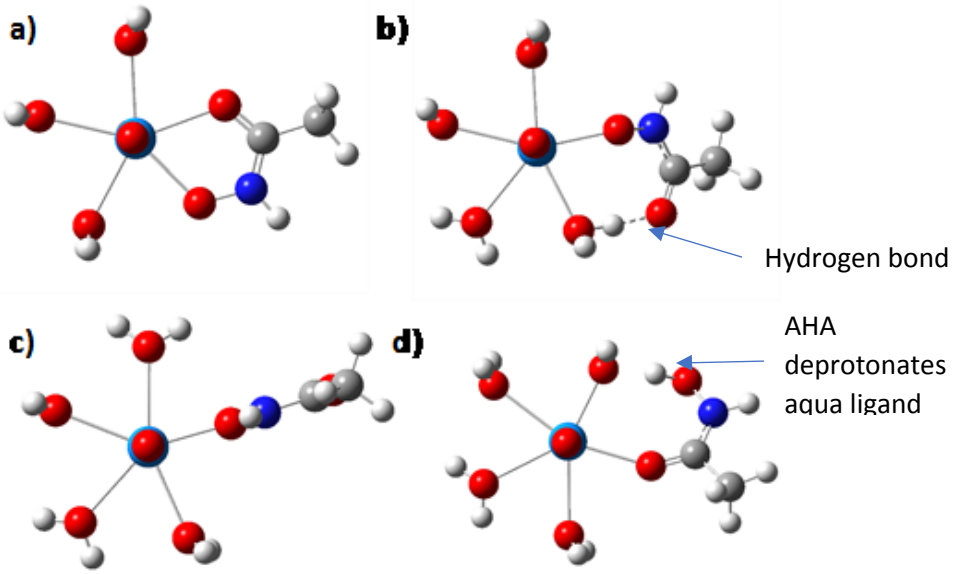

Figure E3. Possible structures for 1:1 U^{VI}-acetohydroxamate complexes. The white, dark blue, grey, red and light blue atoms represent H, N, C, O and U respectively. The structures are: a) bidentate complex, b) monodentate via O(N) atom with AHA oriented in the equatorial plane of U^{VI}, c) monodentate via O(N) atom with AHA oriented in the axial plane of U^{VI}, d) monodentate via O(C) atom with AHA oriented in the equatorial plane. Structure a) is the most energetically favourable and used in the ligand training set.

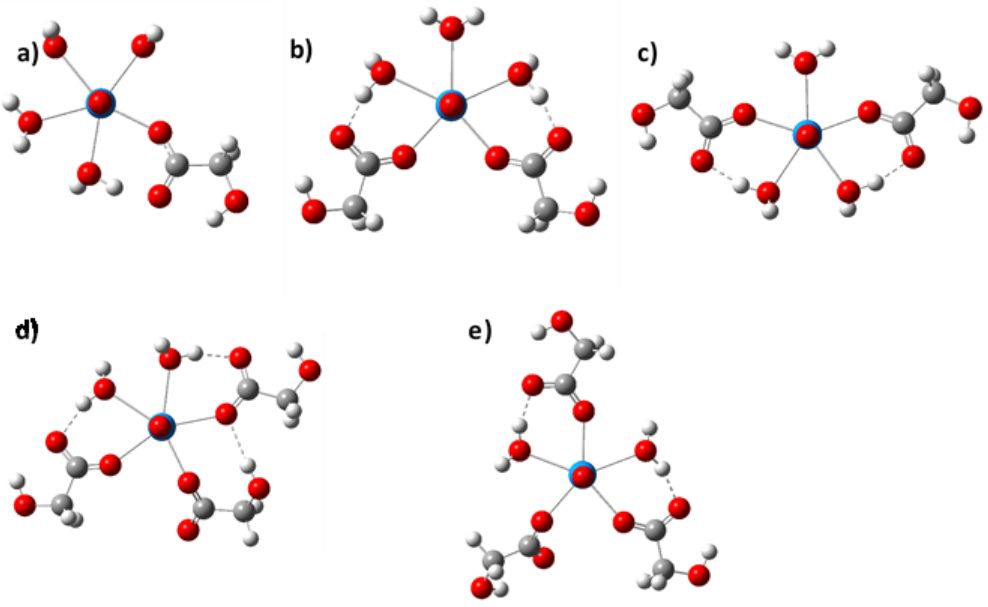

Figure E4. Possible structures for the U^{VI}-glycolate complexes. a) is the 1:1 U^{VI}-L complex, parts b) is the 1:2 U^{VI}-L complex, where the ligand are cis to each other, c) is the 1:2 U^{VI}-L complex, where the ligand are trans to each other, d) is the 1:3 U^{VI}-L complex where the water molecules are cis to each other, e) is the 1:3 U^{VI}-L complex where the water molecules are cis to each other. Structures a), c) and e) are the most energetically favourable structures and used in the training set.

Appendix F - Republication Permissions

1) Kenney J.P.L., Kirby M.E., Cuadros J., Weiss D.J.*, 2017, A conceptual model to predict uranium removal from aqueous solutions in water-rock systems associated with low-and intermediate-level radioactive waste disposal, *RSC Advances*, 7, 7876-7884.

Section 4.3.2 of my thesis was adapted from this paper, including Figures 4.4 and 4.5.

2) Kirby, M.E., Simperler, A., Krevor, S. Weiss, D.J.*, Sonnenberg J.L.*, 2018, Computational Tools for Calculating log β Values of Geochemically Relevant Uranium Organometallic Complexes, *Journal of Physical Chemistry A*, 122, 8007-8019.

Chapter 6 is a slightly altered version of this paper.